



**HAL**  
open science

# A multi-scale modeling approach for diamond tools wear

Adriana Quacquarelli

► **To cite this version:**

Adriana Quacquarelli. A multi-scale modeling approach for diamond tools wear. Mechanics [physics.med-ph]. Université de Lyon, 2021. English. NNT : 2021LYSEI040 . tel-03547633

**HAL Id: tel-03547633**

**<https://theses.hal.science/tel-03547633>**

Submitted on 28 Jan 2022

**HAL** is a multi-disciplinary open access archive for the deposit and dissemination of scientific research documents, whether they are published or not. The documents may come from teaching and research institutions in France or abroad, or from public or private research centers.

L'archive ouverte pluridisciplinaire **HAL**, est destinée au dépôt et à la diffusion de documents scientifiques de niveau recherche, publiés ou non, émanant des établissements d'enseignement et de recherche français ou étrangers, des laboratoires publics ou privés.



# INSA

N°d'ordre NNT : **2021LYSEI040**

**THESE de DOCTORAT DE L'UNIVERSITE DE LYON**  
opérée au sein de  
**INSA Lyon**

**Ecole Doctorale N°162**  
**Mécanique, Energétique, Génie civil, Acoustique**

**Spécialité/ discipline de doctorat :**  
Mécanique

Soutenue publiquement le 06/07/2021, par :  
**Adriana Quacquarelli**

---

## **A multi-scale modeling approach for diamond tools wear**

---

Devant le jury composé de :

FOUVRY, Siegfried	Directeur de Recherche CNRS	LTDS-EC de Lyon	Président
MOLINARI, Jean-François	Professeur	EPFL-Switzerland	Rapporteur
MAGNIER, Vincent	Maître de Conférences HDR	LaMcube-Univ. de Lille	Rapporteur
MEZIANE, Anissa	Professeur	I2M-Univ. de Bordeaux	Examinatrice
FOUVRY, Siegfried	Directeur de Recherche CNRS	LTDS-EC de Lyon	Examineur
FILLOT, Nicolas	Maître de Conférences HDR	INSA de Lyon	Directeur de thèse
MOLLON, Guilhem	Maître de Conférences	INSA de Lyon	Co-directeur de thèse



## Département FEDORA – INSA Lyon - Ecoles Doctorales

SIGLE	ECOLE DOCTORALE	NOM ET COORDONNEES DU RESPONSABLE
<b>CHIMIE</b>	<b><u>CHIMIE DE LYON</u></b> <a href="https://www.edchimie-lyon.fr">https://www.edchimie-lyon.fr</a> Sec. : Renée EL MELHEM Bât. Blaise PASCAL, 3e étage secretariat@edchimie-lyon.fr	<b>M. Stéphane DANIELE</b> C2P2-CPE LYON-UMR 5265 Bâtiment F308, BP 2077 43 Boulevard du 11 novembre 1918 69616 Villeurbanne <a href="mailto:directeur@edchimie-lyon.fr">directeur@edchimie-lyon.fr</a>
<b>E.E.A.</b>	<b><u>ÉLECTRONIQUE, ÉLECTROTECHNIQUE, AUTOMATIQUE</u></b> <a href="https://edeea.universite-lyon.fr">https://edeea.universite-lyon.fr</a> Sec. : Stéphanie CAUVIN Bâtiment Direction INSA Lyon Tél : 04.72.43.71.70 secretariat.edeea@insa-lyon.fr	<b>M. Philippe DELACHARTRE</b> INSA LYON Laboratoire CREATIS Bâtiment Blaise Pascal, 7 avenue Jean Capelle 69621 Villeurbanne CEDEX Tél : 04.72.43.88.63 <a href="mailto:philippe.delachartre@insa-lyon.fr">philippe.delachartre@insa-lyon.fr</a>
<b>E2M2</b>	<b><u>ÉVOLUTION, ÉCOSYSTÈME, MICROBIOLOGIE, MODÉLISATION</u></b> <a href="http://e2m2.universite-lyon.fr">http://e2m2.universite-lyon.fr</a> Sec. : Sylvie ROBERJOT Bât. Atrium, UCB Lyon 1 Tél : 04.72.44.83.62 secretariat.e2m2@univ-lyon1.fr	<b>M. Philippe NORMAND</b> Université Claude Bernard Lyon 1 UMR 5557 Lab. d'Ecologie Microbienne Bâtiment Mendel 43, boulevard du 11 Novembre 1918 69 622 Villeurbanne CEDEX <a href="mailto:philippe.normand@univ-lyon1.fr">philippe.normand@univ-lyon1.fr</a>
<b>EDISS</b>	<b><u>INTERDISCIPLINAIRE SCIENCES-SANTÉ</u></b> <a href="http://ediss.universite-lyon.fr">http://ediss.universite-lyon.fr</a> Sec. : Sylvie ROBERJOT Bât. Atrium, UCB Lyon 1 Tél : 04.72.44.83.62 secretariat.ediss@univ-lyon1.fr	<b>Mme Sylvie RICARD-BLUM</b> Institut de Chimie et Biochimie Moléculaires et Supramoléculaires (ICBMS) - UMR 5246 CNRS - Université Lyon 1 Bâtiment Raulin - 2ème étage Nord 43 Boulevard du 11 novembre 1918 69622 Villeurbanne Cedex Tél : +33(0)4 72 44 82 32 <a href="mailto:sylvie.ricard-blum@univ-lyon1.fr">sylvie.ricard-blum@univ-lyon1.fr</a>
<b>INFOMATHS</b>	<b><u>INFORMATIQUE ET MATHÉMATIQUES</u></b> <a href="http://edinfomaths.universite-lyon.fr">http://edinfomaths.universite-lyon.fr</a> Sec. : Renée EL MELHEM Bât. Blaise PASCAL, 3e étage Tél : 04.72.43.80.46 infomaths@univ-lyon1.fr	<b>M. Hamamache KHEDDOUCI</b> Université Claude Bernard Lyon 1 Bât. Nautibus 43, Boulevard du 11 novembre 1918 69 622 Villeurbanne Cedex France Tél : 04.72.44.83.69 <a href="mailto:hamamache.kheddouci@univ-lyon1.fr">hamamache.kheddouci@univ-lyon1.fr</a>
<b>Matériaux</b>	<b><u>MATÉRIAUX DE LYON</u></b> <a href="http://ed34.universite-lyon.fr">http://ed34.universite-lyon.fr</a> Sec. : Yann DE ORDENANA Tél : 04.72.18.62.44 yann.de-ordenana@ec-lyon.fr	<b>M. Stéphane BENAYOUN</b> Ecole Centrale de Lyon Laboratoire LTDS 36 avenue Guy de Collongue 69134 Ecully CEDEX Tél : 04.72.18.64.37 <a href="mailto:stephane.benayoun@ec-lyon.fr">stephane.benayoun@ec-lyon.fr</a>
<b>MEGA</b>	<b><u>MÉCANIQUE, ÉNERGÉTIQUE, GÉNIE CIVIL, ACOUSTIQUE</u></b> <a href="http://edmega.universite-lyon.fr">http://edmega.universite-lyon.fr</a> Sec. : Stéphanie CAUVIN Tél : 04.72.43.71.70 Bâtiment Direction INSA Lyon mega@insa-lyon.fr	<b>M. Jocelyn BONJOUR</b> INSA Lyon Laboratoire CETHIL Bâtiment Sadi-Carnot 9, rue de la Physique 69621 Villeurbanne CEDEX <a href="mailto:jocelyn.bonjour@insa-lyon.fr">jocelyn.bonjour@insa-lyon.fr</a>
<b>ScSo</b>	<b><u>ScSo*</u></b> <a href="https://edsciencessociales.universite-lyon.fr">https://edsciencessociales.universite-lyon.fr</a> Sec. : Mélina FAVETON INSA : J.Y. TOUSSAINT Tél : 04.78.69.77.79 melina.faveton@univ-lyon2.fr	<b>M. Christian MONTES</b> Université Lumière Lyon 2 86 Rue Pasteur 69365 Lyon CEDEX 07 <a href="mailto:christian.montes@univ-lyon2.fr">christian.montes@univ-lyon2.fr</a>

\*ScSo : Histoire, Géographie, Aménagement, Urbanisme, Archéologie, Science politique, Sociologie, Anthropologie



*Dedicated to Hugo,  
for everything you have done for me,  
and for all the moments I wanted to share with you.*



# Acknowledgments

I want to thank my thesis directors for the originality of the proposed subject, for their help, their essential advice on both the scientific and human level, their meticulous supervision, and their remarkable availability, without which this work would not have been the same. I personally thank Guilhem Mollon for having chosen me first for an internship and then for the Ph.D. To him, I owe all my gratitude for having guided me to the world of research. I thank Nicolas Fillot for making me more enterprising in my work.

My deepest gratitude goes to Umicore, who supported this work. In particular, special thanks go to Thierry Commeau, without whom this thesis would not have been possible. I am highly grateful to him for all he has taught me on a more practical and industrial level at Umicore.

Profound thanks go to the rapporteurs J.F. Molinari and V. Magnier for dedicating their time to read and judge my work. I also thank the examiners A. Meziane and S. Fouvry for agreeing to participate in the jury and especially S. Fouvry for doing me the honor of chairing the PhD. defense.

A big “thank you” to all my colleagues who welcomed me and never made me feel uncomfortable despite my somewhat imprecise French. I would like to thank Marjolaine, Sarra, and Ruibin, with whom it was a pleasure to share the office. In particular, I would like to thank Marjo for making my working days lighter, for her deep sensitivity and altruism. I would also like to thank Nathalie for all the extra-work activities and for being a good friend. A sincere thanks to Pierrick, colleague and friend since the very first day of my internship.

Thanks to Fabio and Valerio, for being present in the darkest moments as well as all the Italian mets at the lab.

I would like to thank Daniele, who supported me in embarking on this adventure and, despite the fact that our paths took different directions, he continued to be there, almost like an old friend.

I want to thank my family, who believed in me and who has always been close to me despite the distance and difficulties due to the pandemic.

A heartfelt thanks go to Gianluigi, for all the kindness and sincerity and for being with me every day. Thanks for making me discover my most determined self, which enabled me to

achieve this important goal. You were the most accidental but also the luckiest meet I've had at the lab (or rather just outside)!

Finally, I would like to thank Hugo, the best friend I ever had: this thesis is dedicated to you.

# Contents

<b>Acknowledgments</b> .....	<b>vii</b>
<b>Contents</b>	<b>ix</b>
<b>Nomenclature</b> .....	<b>xiii</b>
<b>List of tables</b> .....	<b>xxi</b>
<b>List of figures</b> .....	<b>xxiii</b>
<b>Résumé étendu</b> .....	<b>1</b>
Introduction.....	1
Objectifs .....	1
Partie A : État de l'art et mise en œuvre d'une stratégie de modélisation.....	2
État de l'art.....	2
Démarche numérique .....	4
Partie B: Wear prediction at the macroscopic scale .....	6
Données expérimentales préliminaires et modélisation de l'écoulement du troisième corps .....	6
Modélisation de l'usure abrasive .....	7
Résultats et discussion .....	9
Conclusions.....	12
Partie C : Description de l'usure à l'échelle mésoscopique.....	12
L'usure de la matrice à l'échelle locale : Modélisation.....	13
L'usure des matrices à l'échelle locale : Premiers résultats et discussion .....	15
Vers une approche quantitative.....	16
Conclusions.....	17
Conclusions générales .....	18
Perspectives .....	19
<b>Abstract</b>	<b>21</b>
<b>General introduction</b> .....	<b>23</b>
Introduction.....	23
Objectives .....	24
Outlines .....	25

<b>Part A.</b>	<b>State-of-the-art &amp; strategy</b> .....	<b>29</b>
A.1	On the history and use of Diamond Impregnated Tools .....	31
A.1.1	Powder metallurgy fabrication.....	32
A.1.2	Metal matrix microstructure .....	33
A.1.3	Diamonds.....	35
A.2	Wear of the matrix by abrasive particles .....	37
A.2.1	Classification of wear.....	38
A.2.2	Conceptual tools for abrasive wear.....	39
A.2.3	Properties of the abrasive particles .....	41
A.2.4	Matrix resistance to abrasive wear .....	43
A.2.5	Effect of diamonds .....	45
A.3	Conclusions and development of a strategy .....	49
A.3.1	Preliminary conclusions.....	49
A.3.2	Development of a strategy.....	50
<b>Part B.</b>	<b>Wear prediction at the macroscopic scale</b> .....	<b>57</b>
B.1	Experimental-numerical strategy at the macroscale and preliminary experimental inputs	59
B.1.1	Experimental observation of the third body flow .....	60
B.1.2	Experimental observation of wear: the multi-pass scratch test .....	64
B.2	Modeling of the third body flow .....	71
B.2.1	The Reynolds equation .....	72
B.2.2	Implementation of the slurry properties .....	76
B.2.3	Geometry and slurry thickness equation .....	77
B.2.4	Boundary conditions .....	79
B.2.5	Dimensionless formulation .....	79
B.2.6	Numerical application .....	80
B.2.7	Conclusions.....	85
B.3	Modeling of the abrasive wear .....	87
B.3.1	From the Archard equation to a multiscale wear law.....	87
B.3.2	Numerical coupling of Reynolds equation and wear equation .....	95
B.3.3	Conclusions.....	96
B.4	Wear analysis of the surface .....	97
B.4.1	Experimental observation of wear around one diamond .....	97
B.4.2	Numerical prediction of wear at the diamond scale.....	104
B.4.3	Comparison of experimental and numerical results .....	107

B.5	Conclusions.....	111
<b>Part C.</b>	<b>Wear description at the mesoscopic scale .....</b>	<b>115</b>
C.1	Matrix wear at the local scale: Modeling.....	117
C.1.1	Description of the model.....	117
C.1.2	Main contact models.....	128
C.2	Matrix wear at the local scale: First results and discussion .....	137
C.2.1	A first parametric sensitivity analysis of the monotonous CZM .....	137
C.2.2	Effect of the fatigue damage rate on the wear process.....	146
C.3	Towards a quantitative approach .....	159
C.3.1	Experimental observation on the $\mu$ -scratch test.....	160
C.3.2	Numerical scratch test.....	161
C.3.3	Comparison between experimental and numerical results .....	165
C.4	Conclusions.....	175
	<b>General conclusions.....</b>	<b>179</b>
	<b>Further possible developments .....</b>	<b>183</b>
	<b>Annex I. Definition of particles sharpness .....</b>	<b>187</b>
	<b>Annex II. Generation of a realistic sample .....</b>	<b>191</b>
	<b>Annex III. The pseudo-code for the solving of the CZM-fatigue contact law.....</b>	<b>195</b>
	<b>Annex IV. Effect of the matrix thickness .....</b>	<b>199</b>
	<b>Bibliography.....</b>	<b>203</b>



# Nomenclature

$\alpha_1$	Shape factor
$\alpha_2$	Degree of wear of the asperity
$\beta_d$	Size of a protruding diamond
$\Gamma$	Cohesion
$\Delta_{nF,1}; \Delta_{nF,2}$	Fourier Spectrum decays
$\Delta H_s$	Coefficient of the exponential fitting for the scratch hardness
$\Delta t$	Critical time step for 2D mesoscale simulations
$\delta$	Gap diamond tip-workpiece
$\tilde{\delta}$	Gap in the node-to-segment contact algorithm (local contact)
$\tilde{\delta}_{max}$	Cut-off gap in the CZM contact law
$\tilde{\delta}_{max}$	Maximum gap even reached in the CZM contact law
$\tilde{\delta}_n$	Gap in the normal direction (local contact)
$\tilde{\delta}_{res}$	Residual gap in the CZM contact law
$\tilde{\delta}_t$	Gap in the tangential direction (local contact)
$E_f$	Frictional work per unit volume of material removed
$E_r$	Energy restored in the impact Mohr-Coulomb contact law
$E_t$	Energy released after the impact in the impact Mohr-Coulomb contact law
$\bar{E}_n$	Energy dissipation rate in the normal direction in the Impact Mohr-Coulomb contact law
$\varepsilon$	Coefficient for the standard Reynolds equation
$\varepsilon'$	Coefficient for the generalized Reynolds equation
$\varepsilon_r$	Residual strain of metals
$\zeta$	Damped parameter of the Mohr-Coulomb contact law
$\eta$	Apparent viscosity
$\eta_0$	Constant plastic viscosity for the Bingham model

$\eta_N$	Newtonian viscosity
$\bar{\eta}$	Dimensionless apparent viscosity
$\theta$	Attack angle
$\theta_d$	Debris attack angle
$\theta_i$	Attack angle during the indentation test
$\theta_s$	Scratch attack angle
$\vartheta_i$	Angle measured to the center for the grain contour discretization
$K$	Material constant in the Hall-Patch equation
$\kappa$	Parameter of the exponential fitting for the scratch hardness
$\dot{\gamma}$	Shear rate
$\dot{\gamma}^*$	Characteristic shear rate
$\dot{\gamma}_{ij}$	Shear rate components in the j-direction in a plane having -i has a normal
$N_m$	Spectrum cut-off parameter
$\lambda_1; \lambda_2$	Rate of decay of amplitude modes of the Fourier spectrum
$\mu$	Coefficient of friction
$\mu_s$	Coefficient of friction measured during the scratch test
$\mu_s^{num}$	Numerical friction coefficient during the scratch -s
$\bar{\mu}_s^{num}$	Mean numerical friction coefficient
$\rho$	Density of a fluid
$\rho_d$	Density of debris grains
$\rho_m$	Density of the metal matrix microstructure
$\rho_w$	Density of water
$\sigma_0$	Material constant in the Hall-Patch equation
$\sigma_u$	Ultimate strength of metals
$\sigma_y$	Yield strength of metals
$\tau$	Current tangential stress
$\tau_{ij}$	Shear stress components in the j-direction in a plane having -i has a normal
$\tau_y$	Yield tangential stress
$\nu_i$	Poisson ratio of the indenter

$\nu_m$	Poisson ratio of the matrix microstructure
$\varphi$	Mohr coulomb friction coefficient
$\phi$	Cone-angle of the rheometer
$\chi_1, \chi_2$	Coefficients of the power law fitting wear rate ws. Fatigue damage rate
$\Omega$	3D domain
$\partial\Omega$	Boundary domain
$\omega$	Rotational velocity on the rheometer
$A_c$	Contact Area
$A_n, B_n$	Fourier coefficients
$a_i, a_s, a_d$	Half contact width for the case of indentation and scratch test and debris scratching
$B$	Bingham number
$b$	Scalar parameter to define dimensionless domain size
$C$	Consistency index
$Cl_i$	Clearance height at the time $i^{\text{th}}$
$CV$	Coefficient of variation
$CV_t$	Target coefficient of variation
$C_u$	Coefficient of uniformity
$CWR$	Clearance wear rate
$D$	Body Damage parameter
$D_n$	Fourier descriptors
$D_{saw}$	Saw diameter
$dD_f$	Fatigue damage evolution parameter
$d_d$	Equivalent diameter of debris grains
$d_i$	Diamond tip height at the time $i^{\text{th}}$
$d_m$	Equivalent diameter of matrix grains
$d_{nodes}$	Minimum distance between nodes of the degradable microstructure mesh
$E^*$	Effective Young Modulus

$E^{*2D}$	2D Effective Young modulus
$E_i$	Young modulus of the indenter
$E_m$	Young modulus of the metal matrix microstructure
$e_r$	Relative error
$F_c$	Critical load measured experimentally from the scratch test
$F_d$	Load applied to a debris grain
$F_{tool}$	Load applied to the machine
$F_{n,tool} F_{t,tool}$	Normal and tangential components of the load applied to the machine
$F_i$	Applied normal load for the case of indentation test
$F_n$	Normal force
$F_s$	Applied normal load for the case of scratch test
$F_{sturry}$	Normal load carried by the debris flow per unit sliding distance
$F_s^{num}$	2D normal force applied in the numerical scratch test
$F_t$	Frictional force
$F_t^{2D}$	2D tangential force computed from the numerical scratch test
$f_n$	Contact force in normal direction
$f_t$	Contact force in tangential direction
$f$	Shear strength of the wearing material
$G_{c,I}; G_{c,II}$	Critical fracture energy in normal and tangential direction, respectively
$H$	Material hardness
$HB$	HB number
HV10	Vickers hardness
$H_s$	Scratch hardness
$H_s^*$	Characteristic scratch hardness
$h$	Gap thickness
$\bar{h}$	Dimensionless gap thickness
$h_0$	Initial gap thickness
$h_b$	2D depth of the non-degradable material
$h_{c,i}$	Height of clearance computed at the instant $i^{\text{th}}$

$h_D$	Cartesian equation of the protruding diamond
$h_d$	Wear depth caused by a debris grain indentation
$h_m$	2D depth of the degradable material
$h_{p,i}$	Height of protrusion computed at the instant $i^{\text{th}}$
$h_{p,s}$	Penetration depth during the scratch test
$h_{r,s}$	Residual depth during the scratch test
$\bar{h}_{r,s}$	Mean residual depth during the scratch s
$\bar{h}_{p,s}$	Mean indentation depth during the scratch s
$h_s^{num}$	Numerical Indentation during the scratch -s
$\bar{h}_{s-1}^{num}$	Numerical mean indentation depth during the scratch s respect to the mean value of the first scratch
$\bar{h}_s^{num}$	Numerical mean indentation depth during the scratch s
$h_{TB}$	Thickness of the third body debris flow
$K_{ab}$	Archard coefficient and specific wear rate for abrasive wear
$K_{ad}$	Archard coefficient and specific wear rate for adhesive wear
$k_0$	Numerical contact stiffness used in the CZM contact law
$k_n^+; k_n^-$	Normal stiffness during loading (+) and unloading (-) in Mohr-Coulomb contact law
$k_w$	Specific wear rate
$I$	Inertia number
$L_D$	Diamond dimension
$L_i$	Length of the indenter tip
$L_s$	Length of a scratch
$L_x$	Length of the 2D domain
$LWR$	Lateral wear rate
$l_{de}$	Deactivation length
$M_i$	Mass of material within the contact zone
$M_d$	Mass of debris grains in the slurry
$M_w$	Mass of water in the slurry

$m$	Regularization parameter
$m_x, m_y$	Mass flow rate in the x and y-direction, respectively
$N_{debris}$	Number of debris grains in DEM simulations
$NT_{ratio}$	Ratio between tensile and tangential quantities in the CZM contact law
$n$	Flow index
$n_i$	Number of filling circles/spheres of an irregular particle
$n_s$	Number of scratch pass
$P$	Points discretizing a grain contour
$Pr_i$	Protrusion height at the time $i^{th}$
$PWR$	Protrusion wear rate
$p$	Fluid pressure
$p_m$	Mean contact pressure
$p_{max}^{2D}$	Maximum Hertz contact pressure in 2D
$p_{max}^{3D}$	Maximum Hertz contact pressure in 3D
$p_n$	Normal pressure applied in the mesoscopic model
$\tilde{p}$	Contact pressure in MELODY contact algorithms
$\tilde{p}_f$	Pressure threshold for fatigue damage,
$\tilde{p}_{lim}$	Ultimate stress in the CZM contact law
$\tilde{p}_{res}$	Residual cohesion when the bond is broken
$Q^e$	Ejection flow
$Q^r$	Recirculation flow
$Q^s, Q_m^s, Q_{wp}^s$	Total internal source flow, detached particles from matrix and workpiece, respectively
$Q^w$	Wear flow
$Q_m^d$	Amount of particles detached from the matrix surface
$Q_m^w$	Amount of particles ejected from the matrix surface
$R_a$	Average roughness parameter
$R_d$	Equivalent radius of debris grains
$R_{ku}$	Kurtosis roughness parameter

$R_i$	Radius of the indenter during the indentation test
$R_{inisc}$	Radius of maximum inscribed circle/sphere of an irregular particle
$R_q$	r.m.s. roughness parameter
$R_s$	Radius of the indenter during scratch test
$R_{sk}$	Skewness roughness parameter
$RF$	Roundness factor
$r_d^*$	Characteristic radius asperity
$r_i$	Radii and average distance of a point of the grain contour with respect to the center
$r_{i,d}$	Radius of filling circles/spheres of an irregular particle
$SF$	Solid fraction
$SF_t$	Target solid fraction
$s$	Sliding distance
$TWR$	Tail wear rate
$T$	Torque
$t$	Time
$\tilde{t}$	Time in cutting operations
$t^{cost}$	Time to solve numerically the Reynolds equation
$u_i, v_i, w_i$	Velocity components of the surface $-i$ on the $x$ , $y$ , and $z$ -direction, respectively
$\mathbf{v}$	Vector of the velocity field
$\mathbf{v}_r$	Vector of the relative velocity field
$u_1, u_2$	$x$ -velocity on the lower and upper wall, respectively
$u_d$	Velocity of a grain in contact with the matrix surface
$u_m$	Mean entrainment velocity
$u_r$	Relative velocity in $-x$ direction
$u_t$	Tangential velocity
$u_t^{num}$	Applied velocity in the 2D wear model
$V$	Wear volume

$V_{ab}$	Abrasive wear volume
$V_{ad}$	Adhesive wear volume
$Vol_d, Vol_w$	Volume occupied by debris grains and water, respectively
$V_d$	Volume wear by debris grain per unit sliding distance
$V_{sturry}$	Wear volume by the debris flow per unit sliding distance
$v_{feed}$	Feed rate
$v_s$	Scratching velocity
$v_s^{num}$	Numerical scratching velocity
$v_{tool}$	Peripheral speed of the tool
$v_{waves}$	Velocity of wave propagation in the 2D mesoscale model
$x, y, z$	Space dimensions
$X, Y, Z$	Dimensionless space dimensions
$z'$	Height of the asperity above the mean line in the 3D model
$z_m^d$	Damage level (measured the contact surface) in the mesoscopic model
$z_m^w$	Wear level (measured from the contact surface) in the mesoscopic
$z_m$	Variation of the matrix level in the mesoscopic model

# List of tables

Tab. A-1 Properties of 100 % Cobalt matrix microstructures (HV10=Vickers hardness; $\sigma_y$ =yield strength; $\sigma_u$ =ultimate strength; $\epsilon_r$ =residual strain)[42] .....	34
Tab. B-1 Concentration of slurries in terms of debris/water concentration (d/w) and volumetric solid fraction (FS) .....	61
Tab. B-2 Fitting parameters for the Hershel-Bulkley, Ostwald-de Waele and Bingham model and the respective $R^2$ .....	63
Tab. B-3 Specification of the cobalt metal matrix used in the scratch test and the core-drill test (HV10 Vickers Hardness; $\sigma_y$ = yield strength; $\sigma_u$ = ultimate strength; $\epsilon_r$ = residual strain) .....	66
Tab. B-4 Geometrical parameters and velocities .....	81
Tab. B-5 Statistics of the mesh refinements with numbers of degrees of freedom DOF, peaks of pressure $p_{max}$ and times for the resolution $t_{cost}$ .....	81
Tab. B-6 Rheological parameters .....	82
Tab. B- 7 Parameters used in simulations varying $\delta D/h0c$ .....	85
Tab. B-8 Main standard parameters for a drilling operation [42] .....	97
Tab. B-9 Main debris and matrix parameters for a drilling operation [42] .....	98
Tab. B- 10 Numerical and experimental wear rate in terms of PWR and CWR .....	109
Tab. C-1 Initial roughness parameters of the degradable microstructure.....	124
Tab. C-2 Packing 2D input and output parameters ( $dd$ is in $\mu m$ , the other parameters are dimensionless).....	126
Tab. C- 3 Real and numerical features for the numerical acceleration.....	127
Tab. C-4 User-defined parameters of the CZM-fatigue contact law .....	134
Tab. C-5 CZM fatigue parameters for the matrix-matrix and matrix-base contact used in the sensitivity analysis .....	138
Tab. C-6 Mohr-Coulomb parameters for the matrix debris contact, and Damped Mohr-Coulomb parameters for the debris-debris and debris-workpiece contact used in the sensitivity analysis .....	139
Tab. C-7 CZM parameters for the fatigue damage rate sensitivity .....	146
Tab. C-8 Main features for the application of the Hertz theory at equivalent pressure .....	164
Tab. C-9 CZM fatigue parameters for the matrix-matrix and matrix-base contact .....	166
Tab. C-10 Mohr-Coulomb parameters for the matrix indenter contact .....	166
Tab. C-11 Mohr-Coulomb parameters for the matrix indenter contact .....	168
Tab. C-12 CZM fatigue parameters for the matrix-matrix and matrix-base contact .....	171
Tab. C-13 Coefficients and respective errors of the multiple linear regressions obtained from Eqs. (C.25)-(C.26) .....	172

Tab. II-1 Definition of shape descriptors used in Part C and those obtained from the spectrum	192
Tab. IV-1 Comparison between roughness parameters of metal matrix randomly generated in PACKING2D differing in terms of thickness $hm$	199
Tab. IV-2 CZM fatigue parameters	200
Tab. IV-3 Mohr - Coulomb parameters	200

# List of figures

Fig. 1 (a) Topographie de surface d'un segment après sciage [1]; (b) exemple de la scie circulaire (c) topographie du segment de surface après le carottage [2]; (d) schéma d'un outil de carottage et d'un segment diamanté.....	3
Fig. 2 Stratégie utilisée pour l'analyse de l'usure (les lignes en tirets) sont les perspectives de la stratégie.....	6
Fig. 3 Définition de la vitesse relative $u_r$ selon la direction $x$ entre les débris et la surface de contact. La surface a une vitesse de glissement $u_2$ et le grain de débris se déplace à la vitesse $u_d$ .....	8
Fig. 4 Stratégie multi-échelles pour écrire l'équation d'usure de contact : (a) échelle du contact slurry-surface ; (b) échelle du contact grain de débris-surface et (c) échelle du contact local aspérité des débris-surface (c). La figure centrale (b) montre également la définition de l'angularité et du cercle défini par l'aspérité caractéristique $rd^{**}$ (en noir) considérée dans la figure en bas à droite (c).....	9
Fig. 5 (a) Profil vertical du diamant (bleu) et schématisation de la géométrie utilisée dans le modèle (rouges) avec les indications de la géométrie initial du modèle ( $\beta D$ : aspect ratio du diamant; $LD_2$ : longueur de la protrusion du diamant; $Cl_0$ = « clearance » initiale du diamant, $d_0$ =hauteur initiale du diamant, $hc_0=Cl_0-d_0$ : hauteur initiale de la clearance par rapport à $d_0$ ; en bas : micrographie d'un diamant noyé dans la matrice ; (b) Zones d'usure autour d'un diamant ; (c) Définition de la vitesse de protrusion $PWR$ et de clearance $CWR$ (tirée de [28]) en fonction de l'hauteur de « protrusion » $h_{p,i}$ et de la « clearance » $h_{c,i}$ .....	10
Fig. 6 Comparaison entre la hauteur numérique et expérimentale de la protrusion $h_p$ et de la clearance $h_c$ . Le point expérimental à $t=761$ s n'est pas fiable car le diamant subit des microfissures qui peuvent modifier la référence de la pointe de diamant $d_i$ dans l'évaluation de la longueur d'usure. La comparaison est donc limitée au polishing du diamant (jusqu'à $t=367$ s).....	11
Fig. 7 Cartes d'usure de la surface de la matrice (a) calculée numériquement et (b) observés expérimentalement au microscope optique.....	12
Fig. 8 Modèle à méso-échelle.....	14
Fig. 9 Loi traction-séparation triangulaire dans la direction tangentielle.....	15
Fig. 10 Courbes d'usure pour différentes valeurs de $dD_f$ et zoom sur la phase d'initialisation.....	16
Fig. 11 Modèle de microscratch 2D avec l'indication de l'épaisseur de la matrice $h_m$ et de la base $h_b$ , ainsi que de la force appliquée $F_{snum}$ et de la vitesse $v_{snum}$ sur l'indeteur.....	17
Fig. A-1 Classification of diamond tools [34].....	31

Fig. A-2 <b>(a)</b> Circular saw blade, core-drill and diamond-impregnated segments for sawing and drilling tools; <b>(b)</b> circular sawing; <b>(c)</b> frame sawing on the stone [36].....	32
Fig. A-3 Simplified schema of the contact and the wear.....	40
Fig. A-4 The tribological circuit in the contact matrix-workpiece .....	40
Fig. A-5 Abrasive wear modes [4].....	44
Fig. A-6 Kinematic process of circular sawing in <b>(a)</b> down cutting mode and <b>(b)</b> up cutting mode ( $v_{tool}$ = peripheral speed; $v_{feed}$ = feed rate, $F_{n, tool}$ = normal load; $F_{t, tool}$ = tangential load; $h_{saw}$ = depth of cut ), inspired by [1].....	45
Fig. A-7 Schematic representation of interactions between the saw and the workpiece during the circular sawing operation (inspired by [1]) .....	46
Fig. A-8 Schematic representation of interactions between the saw and the workpiece during the frame sawing operation (inspired by [1]).....	46
Fig. A-9 <b>(a)</b> Surface topography of a segment after sawing [1]; <b>(b)</b> example of circular sawing); <b>(c)</b> surface segment topography after drilling [2]; <b>(d)</b> sketch of a drilling machine; <b>(e)</b> sketch of a particular segment .....	47
Fig. A- 10 <b>(a)</b> Surface of the segment after sawing 44 mm <sup>2</sup> ; <b>(b)</b> height of protrusion vs. cumulative area sawn (from [3]).....	48
Fig. A-11 Main strategy used for the wear analysis (dot lines are the perspectives of the strategy)...	51

Fig. B-1 The workflow of the strategy .....	60
Fig. B-2 Debris grains description [42] <b>(a)</b> SEM micrograph of debris particles; <b>(b)</b> grain size distribution .....	61
Fig. B-3 Cone and plate viscometer.....	62
Fig. B-4 <b>(a)</b> Average flow curves in terms of shear stress $\tau$ vs. shear rate $\dot{\gamma}$ ; <b>(b)</b> apparent viscosity $\eta$ vs. shear rate $\dot{\gamma}$ . The error bars represent the variation of the two samples .....	62
Fig. B-5 Flow curves for the three solid fraction <b>(a)</b> FS =27%, <b>(b)</b> FS =30% and <b>(c)</b> FS =32%, fitted by Ostwald-de Wael model; Hershel-Buckely model and Bingham model .....	64
Fig. B-6 Contact model between a hemispherical tip indenter and a sliding surface <b>(a)</b> during static indentation; <b>(b)</b> during the dynamic scratch; ( $F$ = normal load, $v$ = scratch velocity; $R$ = indenter tip radius; $hr$ = depth of penetration; $a$ =half contact width; $\theta$ : attack angle; index $i$ and $s$ stay for indentation and scratch, respectively).....	65
Fig. B-7 First stage of the scratch test <b>(a)</b> Main quantities measured and definition of critical load $F_c$ ; <b>(b)</b> optical micrograph of the first scratch at the beginning ( $F_s= 0$ N) and when the critical load is reached ( $F_s= 19$ N).....	66
Fig. B-8 Evolution of residual groove $hr, s$ attack angle $\theta_s$ and scratch hardness $H_s$ with the number of repeats scratches $n_s$ .....	68
Fig. B-9 Experimental scratch hardness values and exponential fitting ( $H_s^* = 6.39$ GPa; $\Delta H_s = 4.906$ GPa; $\kappa = 0.227$ ) .....	69
Fig. B-10 Schematic representation of the fluid flow between two moving surfaces.....	73
Fig. B-11 Influence of the regularization parameter $m$ on the Herschel-Bulkley fit for the SF = 32 % .	77
Fig. B-12 Initial vertical profile of the matrix surface (blue) and schematization of the diamond geometry used in the model (red line) with the indication of the initial values of the main geometrical features ( $\beta D$ : diamond aspect ratio; $LD_2$ :length of the protruding diamond; $Cl_0$ =initial clearance,	

$d_0$ =initial diamond height, $h_{c,0} = C_{l0} - d_0$ : initial height of clearance respect to the diamond tip; micrograph of the diamond embedded by the metal matrix (bottom-left) .....	78
Fig. B-13 (a) Dimensionless domain used for the computation (top) and a zoom on the central part of the 3D configuration (bottom) (b) horizontal projection on the plane x-y of the surface (top) and vertical projection on the plane x-z of the surface (bottom).....	79
Fig. B-14 Peak of pressure as a function of the mesh refinement .....	81
Fig. B-15 Pressure profile (for $p > 0$ MPa) as a function of the debris content SF and initial geometry profile $h_0$ in the xz section.....	82
Fig. B-16 1D Pressure profile (for $p > 0$ Pa) for a Newtonian and non-Newtonian fluid with SF = 32% and initial geometry profile $h_0$ in the xz section .....	83
Fig. B-17 Fields of viscosity (top) and velocity $u$ (bottom) along the plane xz for $y = 0$ for (a) the Newtonian case (left) and (b) non-Newtonian case (right) .....	84
Fig. B-18 Variation of the peak of pressure on the diamond surface with the dimensionless gap $\delta D/h_{c,0}$ .....	85
Fig. B-19 (a) A schematization of the geometry of the contact between a cone and a surface: perspective view; (b) vertical section ( $hp$ depth of penetration ; $a$ : half contact width; $\theta$ : attack angle). (Inspired by [7]) .....	87
Fig. B-20 Definition of the relative velocity $ur$ between debris and the contact surface. The surface has a sliding velocity $u_2$ and the grain of debris is moving with velocity $ud$ .....	89
Fig. B-21 Multiscale strategy for the wear equation: (a) the contact debris flow-surface; (b) the contact of debris grains-surface; (c) the local contact of the debris asperity and the surface. The central figure (b) also shows the definition of the angularity and the circle defined by the characteristic asperity $rd^*$ (in black) considered in the figure at the bottom right (c) .....	90
Fig. B-22 Method to find the characteristic asperity .....	91
Fig. B-23 A Schematization of the contact between a spherical tip and a surface: (a) perspective view; (b) vertical section; (c) transversal section .....	93
Fig. B-24 Flowchart of numerical coupling between the Reynolds equation and the wear equation..	95
Fig. B-25 (a) Wear zones around one diamond during drilling; (b) Definition of PWR and CWR (inspired by [28]) .....	98
Fig. B-26 Segment surface observed by the optical microscope at different time steps during drilling, and indications of the three diamonds analyzed (kindly granted by USPF) .....	100
Fig. B-27 Top: Micrographs of the diamond S1D2 (kindly granted by USPF) from its emerging to the pull-out. Bottom: the evolution of the height of the protrusion $hp$ and clearance $hc$ with time $t$ and sliding distance $s$ (sliding velocity = 2.67 m/s, see Tab. B-8) .....	101
Fig. B-28 Top: Micrographs of the diamond S1D1 (kindly granted by USPF) from its emerging to the pull-out. Bottom: the evolution of the height of the protrusion $hp$ and clearance $hc$ with time $t$ and sliding distance $s$ (sliding velocity = 2.67 m/s, see Tab. B-8) .....	102
Fig. B-29 Top: Micrographs of the diamond S1D3 (kindly granted by USPF) from its emerging to the micro-fracturing of a diamond. Bottom: the evolution of the height of the protrusion $hp$ and clearance $hc$ with time $t$ and sliding distance $s$ (sliding velocity = 2.67 m/s, see Tab. B-8) .....	103
Fig. B-30 Effect of the diamond position on the PWR measured in $\mu\text{m}/\text{cm}^3$ stone cut ((kindly granted by USPF).....	104
Fig. B-31 $t_0 = 0$ s: (a) Pressure profile with the indication of the flow direction; (b) evolution on attack angle $\theta_d$ and specific wear rate $kw$ with pressure .....	105
Fig. B-32 Maps of specific wear rate $kw$ at the time: (a) $t_0 = 0$ s; (b) $t_0 = 367$ s; (c) $t_0 = 761$ s.	106
Fig. B-33 Maps of pressure $p$ at the time (a) $t_0 = 0$ s; (b) $t_0 = 367$ s; (c) $t_0 = 761$ s .....	106

Fig. B- 34 Maps of relative velocity $\mathbf{v}r$ at the time: at the time: <b>(a)</b> $t_0 = 0 s$ ; <b>(b)</b> $t_0 = 367 s$ ; <b>(c)</b> $t_0 = 761 s$ .....	106
Fig. B-35 Wear of the surface of the matrix computed numerically at the time: <b>(a)</b> $t_0 = 0 s$ ; <b>(b)</b> $t_0 = 367 s$ ; <b>(c)</b> $t_0 = 761 s$ .....	107
Fig. B- 36 Comparison between the numerical and experimental length of protrusion $h_p$ and clearance $h_c$ . The experimental point at $t_3 = 761 s$ is not reliable sinc diamond is undergoing microcracking that may change the reference of the diamond tip $p_i$ in the evaluation of the length of wear. The comparison is therefore limited to the diamond polishing ( $t = 367 s$ ).....	108
Fig. B- 37 Comparison between experimental and numerical wear rate in the early stage of cutting .....	108
Fig. C-1 Mesoscale model (at $t = 0 s$ ) with information about the geometry and the mesh of deformable bodies (non-degradable and degradable microstructure) .....	119
Fig. C-2 <b>(a)</b> Microscale model after compaction (at $t = 0.1 s$ ); <b>(b)</b> definition of the boundary condition imposed on the workpiece.....	120
Fig. C-3 <b>(a)</b> SEM micrograph of the microstructure; <b>(b)</b> grain size distribution after sintering [42]...	121
Fig. C-4 Comparison between the experimental (blue) and numerical (red) degradable microstructure .....	122
Fig. C- 5 Microstructure generated in Packing2D applying the IMC method to the Voronoi Tesselation (black) and initial clouds of seeding points (blue).....	122
Fig. C-6 <b>(a)</b> Definition of skewness $Rsk$ and <b>(b)</b> kurtosis $Rku$ together with the respective distribution functions [117] .....	124
Fig. C-7 Example of normalized amplitude spectrum [29] .....	125
Fig. C-8 Voronoi Tesselation for the debris grains generation in Packing2D .....	126
Fig. C- 9 <b>(a)</b> Definition of compliant and rigid bodies (inspired by [20]); <b>(b)</b> Definition of the contact algorithm: I: Broad proximity detection (detected contact are in green and in red); II: close detection; III: Contact detection: a. nodes from $B_1$ to $B_6$ are detected in stage II as close to the segment $A_1A_2$ ; b. definition of the contact box to select nodes ( $B_5$ and $B_6$ are out from the detection box and therefore not considered); c: projection for computing local detection quantities (normal $n$ and tangential $t$ vector, normal $\gamma n$ and tangential gap $\delta t$ , local coordinate $\xi_i$ varying from -1 to 1 from the origin to the extremity of the segment) [20] .....	128
Fig. C- 10 <b>(a)</b> Mohr-Coulomb contact law; <b>(b)</b> Normal contact force vs. overlap; <b>(c)</b> tangential frictional force vs. sliding displacement .....	130
Fig. C-11 <b>(a)</b> Cohesive contact between two grains; <b>(b)</b> Traction – separation law in the tangential direction (the same graph could be plotted for the tensile direction by simply changing the name of the variables).....	131
Fig. C-12 Flowchart of the CZM fatigue algorithm .....	135
Fig. C-13 Bilinear CZM laws: <b>(a)</b> Effect of the ultimate strength $plim$ ( $pres = 0 MPa$ ; $\delta res = 0.002 \mu m$ ); <b>(b)</b> Effect of the residual gap $\delta res$ ( $pres = 0 MPa$ ; $plim = 50 MPa$ ) on the shape of the law (in this chart, the tensile strength is taken as positive) .....	138
Fig. C-14 Schematization of the measure of the damage and wear level ( $zmd$ and $zmw$ ) computed from the contacting surface at <b>(a)</b> $t = t_1$ initial stage of the contact; and <b>(b)</b> $t = t_i$ : after a certain number of passage of the debris flow. Grains start to lose cohesion reaching the maximum damage possible (in crimson, $D = 1$ ) and detaching from the microstructure. This phenomenon leads to a	

variation of the average contact surface and, therefore of the wear level  $z_{mw}$  (in blue,  $l_{de} \geq 1.15 \mu m$ ) and damage level  $z_{md}$  (in yellow,  $D = 1$ ), with respect to the initial profile. Grains in white have been already ejected while the initial profile is plotted in a black dot line ..... 140

Fig. C-15 **(a)** Damage and wear curves obtained for the case:  $plim = 800 MPa$ ;  $\delta_{res} = 0.002 \mu m$ ; **(b)** Damage maps for three different instants of time ( $t_i, t_{II}, t_{III}$ ) representative of the three phases of the wear process I, II, III ..... 141

Fig. C-16 Variation of the roughness parameters: **(a)**  $Ra$ ; **(b)**  $Rq$ ; **(c)**  $Rsk$ ; **(d)**  $Rku$  (in dark red) and the depth of wear  $z_{mw}$  (in blue) with time if  $plim = 800 MPa$  ..... 142

Fig. C-17 **(a)** Damage and wear curves obtained for the case:  $plim = 50 MPa$ ;  $\delta_{res} = 0.002 \mu m$ ; **(b)** Damage maps for three different instant of time representative of the three phases of the wear process I, II, III ..... 143

Fig. C-18 Variation of the roughness parameters: **(a)**  $Ra$ ; **(b)**  $Rq$ ; **(c)**  $Rsk$ ; **(d)**  $Rku$  (in dark red) and the depth of wear  $z_{mw}$  (in blue) with time if  $plim = 50 MPa$  ..... 144

Fig. C-19 Example of stress generated during the onset of the contact ( $plim = 800 MPa$ ;  $\delta_{res} = 0.002 \mu m$ ) **(a)** Von Mises stress; **(b)** tangential xz stress ..... 145

Fig. C-20 Stress on the matrix microstructure generated during the onset of the contact with the first cracking in the microstructure ( $plim = 50 MPa$ ;  $\delta_{res} = 0.002 \mu m$ ) **(a)** Von Mises stress; **(b)** tangential stress ..... 145

Fig. C-21 Wear curves obtained for  $\delta_{res} = 0.002 \mu m$  and  $\delta_{res} = 0.0002 \mu m$ . In both cases  $plim = 50 MPa$  ..... 146

Fig. C-22 Wear curves for different values of  $dDf$  and zoom on the initialization stage. Indications A and B refer to two particular wear depth  $z_{mw}$  of the wear-in: A' and B' are relative to the case  $dDf = 0.001 MPa - 1$ ; A'' and B'' correspond to  $dDf = 0.1 MPa - 1$  ..... 147

Fig. C-23 Example of stress generated during the onset of the contact ( $plim = 800 MPa$ ;  $\delta_{res} = 0.002 \mu m$ ,  $dDf = 0.1 MPa - 1$ ) **(a)** Von Mises stress; **(b)** tangential xz stress ..... 147

Fig. C-24 Steady-state at the point A' corresponding to the time  $t = 30 ms$  and the wear level  $z_{mw} = 2 \mu m$  ( $plim = 800 MPa$ ;  $\delta_{res} = 0.002 \mu m$ ,  $dDf = 0.001 MPa - 1$ ): **(a)** Maps in terms of body damage parameter  $D$ , Magnitude displacement; Von Mises stress and Cauchy -xz stress; **(b)** relative zooms on a microcrack highlighted in the red window. The damage propagates within the matrix microstructure generating cracks within the material. The fracture is characterized by high relative displacement; moreover, damaged grains are subjected to large displacements while the stress concentrates on the surrounding non-damaged material ..... 149

Fig. C-25 Steady-state at the point A'' corresponding to the time  $t = 5.6 ms$  and the wear level  $z_{mw} = 2 \mu m$  ( $plim = 800 MPa$ ;  $\delta_{res} = 0.002 \mu m$ ,  $dDf = 0.1 MPa - 1$ ): **(a)** Maps in terms of body damage parameter  $D$ , Magnitude displacement; Von-Mises stress and Cauchy -xz stress; **(b)** relative zooms on the red windows (same as in Fig. C-25). There are no particular fractures and microcracks within the matrix microstructure. The fracture is localized on the contacting surface . 150

Fig. C-26 "Perturbed" steady-state at the point B' corresponding to the time  $t = 100 ms$  and the wear level  $z_{mw} = 10 \mu m$  ( $plim = 800 MPa$ ;  $\delta_{res} = 0.002 \mu m$ ,  $dDf = 0.001 MPa - 1$ ): **(a)** Maps in terms of body damage parameter  $D$ , Magnitude displacement; Von-Mises stress and Cauchy xz stress; **(b)** relative zooms on the red windows. The damage propagates within the matrix microstructure, generating developing microfracture; however, the presence of the non-degradable microstructure imposes a limit to this phenomenon and to the grains detachment ..... 151

Fig. C-27 Steady-state at the point B'' corresponding to the time  $t = 14.4 ms$  and the wear level  $z_{mw} = 10 \mu m$  ( $plim = 800 MPa$ ;  $\delta_{res} = 0.002 \mu m$ ,  $dDf = 0.1 MPa - 1$ ): **(a)** Maps in terms of body damage parameter  $D$ , Magnitude displacement; Von Mises stress and Cauchy -xz stress; **(b)**

relative zooms on the red windows. Damaged grains are distributed on the contacting surface. Detached grains undergo severe displacements; microcracks emerge on the contacting surface but, since the damage increases quickly, they do not have time to propagate within the material..... 152

Fig. C-28 Grains vertical position vs. Damage parameter **(a)**  $A' dDf = 0.001MPa - 1$ ; **(b)**  $B' dDf = 0.001MPa - 1$ ; **(c)**  $A'' dDf = 0.1MPa - 1$ ; **(d)**  $B'' dDf = 0.1MPa - 1$ ; ..... 153

Fig. C-29 Spatial derivate of the damage parameter  $D$  with the depth of the degradable material  $z_m$  as a function of the wear level  $z_{mw}$  for the cases observed in Fig. C-28..... 154

Fig. C-30 Evolution of the wear rate  $\Delta h_{mt}$  with the fatigue damage rate  $dDf$  fitted by a power law ( $\chi_1 = 2.099$ ;  $\chi_2 = 0.4363$ ;  $R_2 = 0.9099$ ) ..... 154

Fig. C-31 Relationship between damaged particles  $Q_{md} (D = 1)$  and ejected particles  $Q_{mw} (l_{de} \geq d_{g2})$ ..... 155

Fig. C-32 Evolution of the damage profile for two different fatigue damage rate:  $dDf = 0.001 MPa - 1$  (left)  $dDf = 0.1 MPa - 1$  (right) at four different stages of  $Q_{md}$  from Fig. C-25: **(a)**  $Q_{md}=0.17$ ; **(b)**  $Q_{md}=0.4$ ; **(c)**;  $Q_{md}=0.6$ , **(d)**  $Q_{md}=0.8$ ..... 156

Fig. C-33 Measure of **(a)** penetration depth  $h_p, s$ ; **(b)** residual depth  $h_r, s$ ; **(c)** coefficient of friction  $\mu_s$ ; for successive passages  $n_s$  of the indenter along the same the scratch path  $L_s$ ..... 160

Fig. C-34 **(a)** mean values of penetration and residual depth  $h_s$  **(b)** mean value of friction coefficient  $\mu_s$ ..... 161

Fig. C-35 2D Microscratch model with the indication of the thickness of the matrix  $h_m$  and the base  $h_b$ , as well as of the applied normal force  $F_{Snum}$  and velocity  $v_{Snum}$  on the indenter..... 162

Fig. C-36 Comparison between the experimental (blue) and numerical (red) degradable microstructure..... 162

Fig. C-37 Contact laws used in the model: **(a)** CZM contact law with residual strength  $pres \neq 0$ ; **(b)** purely cohesive Mohr-Coulomb with Coulomb friction  $\phi = 0$ ..... 165

Fig. C-38 **(a)** numerical indentation depth  $h_{snum}$ ; **(b)** numerical friction coefficient  $\mu_{snum}$  along the scratch distance  $x$  for different scratch pass  $n_s = 1, 2, 3$  ( $\Gamma = 4.5 MPa$ ) ..... 167

Fig. C-39 Comparison between experimental and numerical results varying the cohesion  $\Gamma$  between the indenter and the matrix: **(a)** mean wear depth  $h_s - 1$ ; **(b)** mean friction coefficient  $\mu_s$ ..... 168

Fig. C-40 Comparison between experimental and numerical results varying the deactivation length  $l_{de}$  in terms pf  $\Delta z$  between the indenter and the matrix: **(a)** wear depth  $h_s - 1$ ; **(b)** mean friction coefficient  $\mu_s$ . The comparison is limited to the first three scratches  $n_s = 1, 2, 3$ ..... 169

Fig. C-41 Von Mises stress distribution at three different times  $t = 1 ms, t = 2 ms, t = 2.5 ms$  for different values of deactivation length  $l_{de}$ : **(a)**  $\Delta z \rightarrow \infty$ ; **(b)**  $\Delta z = dm$ ; **(c)**  $\Delta z = dm/2$  ..... 170

Fig. C-42 Comparison between experimental and numerical mean depth of wear  $h_s - 1$  varying the strength parameters: **(a)** Effect of the ultimate strength parameter  $plim$  considering the residual depth  $pres = 6 GPa$ ; **(b)** Effect of the ultimate strength parameter  $plim$  considering the residual depth  $pres = 9 GPa$  (in both cases  $\Gamma = 4.5 GPa$ ;  $l_{de} = \Delta z = dm$  ..... 171

Fig. C-43 Comparison between experimental and numerical mean friction coefficient  $\mu_s$  varying the strength parameters: **(a)** Effect of the ultimate strength parameter  $plim$  considering the residual depth  $pres = 6 GPa$ ; **(b)** Effect of the ultimate strength parameter  $plim$  considering the residual depth  $pres = 9 GPa$  (in both cases  $\Gamma = 4.5 GPa$ ;  $l_{de} = \Delta z = dm$ )..... 171

Fig. C-44 Multiple linear regression applied on numerical results of the wear depth and comparison with the experiments: -Experimental results; -Multiple regression applied on numerical results: ●  $pres = 9 GPa = 9$ ; ▲  $pres = 6 GPa$ : **(a)**  $n_s - 1 = n_2 - n_1$ ; **(b)**  $n_s - 1 = n_3 - n_1$  ..... 172

Fig. C-45 **(a)** Von-Mises stress and **(b)** Cauchy  $xz$  stress at the end of the first, the second, and the third scratch ( $n_s = 1, n_s = 2, n_s = 3$ )..... 174

Fig. IV-1 Qualitative and quantitative comparison between two degradable microstructure of different thickness  $hm$ : **(a)** degradable microstructure  $hm = 10 \mu m$ ; **(b)** non-degradable microstructure  $hb = 20 \mu m$ ; **(c)** Comparison between the experimental (blu) and numerical (red) degradable microstructure  $hm = 10 \mu m$ ; **(d)** Comparison between the experimental (blu) and numerical (red) degradable microstructure  $hm = 20 \mu m$  (same as in Fig. C-4, reported here for the sake of comparison with the matrix  $hm = 10 \mu m$ )..... 200

Fig. IV-2 Effect of the degradable thickness  $hm$  on the wear rate and definition of the instants (a), (b), (c) and (d) ..... 201

Fig.IV-3 Evolution of damage D on the degradable material for **(a)**  $t = 0$  s; **(b)**  $t = 10$  s; **(c)**  $t = 20$  s; **(d)**  $t = 30$  s ..... 201

Figure 1 Perspective of the strategy that can be used for the wear analysis ..... 185

Fig. I-1 Expansion of a sphere along with the normal N at a surface point inside the boundaries of the real particle [108] ..... 188

Fig.I-2 Effect of  $dmin$  of the definition of circles ( $rmin = 0.05 \mu m$ ;  $Pmax = 0.01$ )..... 189

Fig. I- 3 Effect of  $rmin$  of the definition of circles ( $dmin = 0.01 \mu m$ ,  $P_{max} = 0.01$ ) ..... 189

Fig. I-4 Effect of  $P_{max}$  of the definition of circles ( $dmin = 0.01 \mu m$ ;  $rmin = 0.05 \mu m$ )..... 190

Fig. II-1 Measured Fourier spectra and average spectrum (bold black line)..... 192

Fig. II-2 Comparison between the experimental (in blue) and the numerical (in red) grain size distribution of debris grains ..... 193

Fig. II-3 Sample generated from the spectrum analysis..... 193

Fig. IV-1 Qualitative and quantitative comparison between two degradable microstructure of different thickness  $hm$ : **(a)** degradable microstructure  $hm = 10 \mu m$ ; **(b)** non-degradable microstructure  $hb = 20 \mu m$ ; **(c)** Comparison between the experimental (blu) and numerical (red) degradable microstructure  $hm = 10 \mu m$ ; **(d)** Comparison between the experimental (blu) and numerical (red) degradable microstructure  $hm = 20 \mu m$  (same as in Fig. C-4, reported here for the sake of comparison with the matrix  $hm = 10 \mu m$ )..... 200

Fig. IV-2 Effect of the degradable thickness  $hm$  on the wear rate and definition of the instants (a), (b), (c) and (d) ..... 201

Fig.IV-3 Evolution of damage D on the degradable material for **(a)**  $t = 0$  s; **(b)**  $t = 10$  s; **(c)**  $t = 20$  s; **(d)**  $t = 30$  s ..... 201

xxx



# Résumé étendu

## Introduction

Ce sujet prend son origine dans le milieu industriel et en particulier dans la production de poudres métalliques utilisées comme matrices pour les outils diamantés.

Les outils diamantés (DIT) comprennent les outils de carottage, les scies à ruban et circulaires, etc. Ils sont utilisés dans plusieurs applications : la coupe de la pierre, le forage et le sciage de béton et de béton armé, et la réparation de routes. Les DIT sont composés de segments abrasifs fixés sur un support en acier par brasage ou soudage. Les segments sont constitués de diamants orientés et dispersés aléatoirement, noyés dans une matrice métallique par un processus de frittage. Lors des opérations de découpe, la matrice retient les diamants qui, grâce à leur dureté, sont capables de couper la pièce. Des débris du matériau découpé se forment inévitablement et, avec l'eau injectée dans l'entrefer pour les éjecter, ils forment un slurry (suspension dense). Ce flux de débris est très abrasif pour la matrice métallique et peut l'user. Ce processus d'usure est également nécessaire pour renouveler les diamants, mais il doit néanmoins être contrôlé : la matrice doit s'user à un rythme compatible avec la rupture du diamant pour atteindre un équilibre optimal entre durée de vie et aptitude à la découpe.

Généralement, les alliages à base de cobalt sont largement utilisés comme matrice pour leur haute résistance à l'abrasion et leurs excellentes propriétés de rétention. Le prix élevé et les enjeux environnementaux sont les principaux inconvénients du cobalt qui ont poussé les producteurs d'outils diamantés à rechercher des alternatives plus adaptées et moins chères pour remplacer, totalement ou partiellement, la poudre de cobalt.

## Objectifs

Sur la base de la demande industrielle et considérant que les mécanismes impliqués dans l'usure de la microstructure de la matrice métallique ne sont pas encore bien compris, cette thèse vise à analyser et prédire l'usure lors d'un essai de carottage. Dans le cadre scientifique plus général, la contribution principale de ce travail consiste en l'élaboration d'une stratégie pour étudier l'usure abrasive d'une surface due au passage continu d'un flux de débris.

L'accès difficile aux grandeurs locales dans le processus de découpe nécessite une approche numérique pour son analyse. Cette approche a l'avantage de décrire des mécanismes non observables expérimentalement et de prédire le comportement à l'usure (dans certaines conditions bien définies) de nouveaux matériaux. La demande industrielle vise tout d'abord à appliquer une telle stratégie sur une matrice métallique de cobalt pur déjà étudiée expérimentalement; cela permet de valider la stratégie et de l'utiliser pour approfondir les études sur différents matériaux. Une approche multi-échelle est proposée, basée sur deux modèles qui représentent deux échelles différentes pour donner des informations complémentaires et répondre à différentes questions :

- Le modèle macroscopique : L'objectif est prédire l'usure à l'échelle du diamant. Ce modèle considère une partie d'un segment constituée d'un diamant et de la matrice alentour.
- Modèle mésoscopique : L'objectif est de décrire et de comprendre les phénomènes locaux d'usure, tels que la décohésion des grains de la matrice, qui ne sont pas observables à l'échelle du modèle macroscopique. Ce modèle considère un élément de volume représentatif à l'échelle des débris. Il tiendra compte de la nature des grains de débris et de la microstructure polycristalline de la matrice métallique.

Les deux modèles seront étudiés respectivement dans les parties B et C, tandis que la partie A introduit le problème industriel, l'état de la l'art scientifique et les outils conceptuels pour atteindre ces objectifs.

## Partie A : État de l'art et mis en œuvre d'une stratégie de modélisation

### Etat de l'art

Les opérations de carottage et de sciage sont souvent effectuées en injectant un fluide (généralement de l'eau) pour refroidir le système et éjecter les grains de débris à travers l'espace entre les segments. Dans les deux opérations, la direction de coupe constante amène à la formation d'un sillage de matrice derrière le diamant et une sorte de cratère devant celui-ci. Par conséquent, le protocole expérimental le plus basique pour la quantification de l'usure consiste en des observations non destructives d'échantillons issus du carottage (plus simple que le sciage en termes d'opération de coupe).

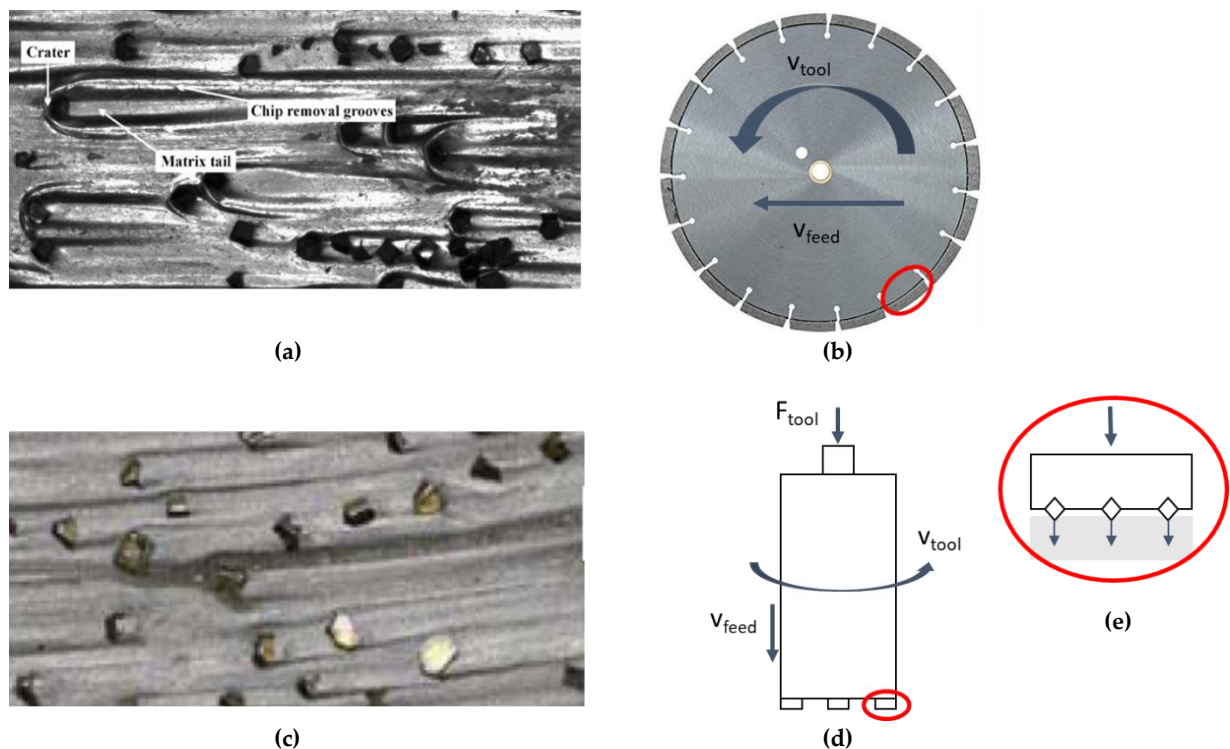


Fig. 1 (a) Topographie de surface d'un segment après sciage [1]; (b) exemple de la scie circulaire (c) topographie du segment de surface après le carottage [2]; (d) schéma d'un outil de carottage ; (e) schéma d'un segment diamanté ( $F_{tool}$ = charge appliquée à la machine ;  $v_{tool}$  = vitesse périphérique de l'outil ;  $v_{feed}$ = vitesse d'alimentation)

L'interaction diamant-débris-matrice est responsable des mécanismes d'usure de la surface de la matrice. Un tel processus dépend de plusieurs aspects tels que :

- Le type de roche : le marbre, le granit, le béton et le béton armé se comportent différemment lors du traitement et génèrent un flux de débris avec des propriétés différentes en termes de granulométrie, de forme des grains, de composition minérale, de dureté et de propriétés de clivage.
- Les spécifications du segment : le nombre et la surface du segment (à l'échelle de l'outil), la concentration en diamant (nombre et taille des diamants à l'échelle du segment), et les propriétés microstructurales de la matrice (à l'échelle de la matrice) modifient l'usure. En particulier, à l'échelle du segment, la présence des autres diamants influence l'usure autour d'un seul diamant; un diamant proche peut offrir une protection et réduire le taux de saillie tandis que, lorsque le même diamant n'est pas protégé par un autre, il est totalement exposé à l'usure [3]. Concernant la microstructure de la matrice, l'usure dépend fortement de la dureté de son matériau.
- Les paramètres opératoires: vitesse et force appliquée et efficacité de refroidissement (c'est-à-dire type de liquide de refroidissement et débit) contrôlent aussi l'usure.

L'usure causée par l'écoulement des débris est définie comme une usure abrasive et peut se produire de différentes manières : labourage, coupe, fissuration [4]–[6]. D'autres mécanismes d'usure importants peuvent être l'érosion [7][8] et l'usure par fatigue [5]. Dans les outils diamantés, ils peuvent se produire simultanément et à des pourcentages différents dans les zones autour du diamant.

Plusieurs tentatives ont été faites pour corrélérer l'usure abrasive aux propriétés des particules abrasives (forme et taille) [9]–[13]. Cependant, dans tous ces cas, le processus d'usure se déroule dans un environnement contrôlé, et les modèles sont strictement liés au test expérimental reproduit. Dans la cadre des utiles diamantés, plusieurs études ont été également réalisées pour analyser, au moins qualitativement, l'usure de la surface en termes de rétention du diamant après le processus de fabrication [14]–[16] et pendant les conditions de travail [17] alors que les mécanismes impliqués dans l'usure de la matrice ne sont pas encore bien compris.

## Démarche numérique

Pour aller plus loin dans l'étude de l'usure par abrasion dans le contexte des outils diamanté, l'approche utilisée est basée sur le concept de circuit tribologique [18] : la matrice métallique et la pièce à découper représentent les premiers corps du système tribologique, tandis que les débris de la pièce sont le troisième corps. Etant donné que des débris sont produits en continu pendant le procédé de coupe, tandis que les grains de matrice métallique sont expulsés rapidement du système, on fera l'hypothèse que l'usure est causée par les débris et non par les grains de matrice eux-mêmes.

Le modèle macroscopique représente une géométrie 3D réaliste avec un coût de calcul raisonnable. Le modèle construit à l'échelle des diamants offre des résultats à la même échelle que l'application industrielle et donne des connaissances qualitatives et quantitatives sur la résistance à l'usure de la matrice, traitant le slurry comme un continuum décrit par sa loi rhéologique.

Cependant, il est impossible d'extraire des informations sur les propriétés d'écoulement du troisième corps à partir de l'application industrielle. Les interactions tribologiques impliquées sont complexes et imposent une stratégie de modélisation basée sur un couplage expérimental / numérique. La viscosité de la suspension influe sur les propriétés d'écoulement, qui sont les principales causes du processus d'usure, et pour cette raison, des tests rhéologiques sont effectués sur un troisième corps modèle, hors du contact industriel.

Les propriétés mécaniques de la matrice offrent une résistance au processus d'usure. Cependant, le test de carottage ne peut pas séparer les différents phénomènes en jeu lors du processus d'usure. Par conséquent, des données supplémentaires sur la résistance à l'abrasion de la microstructure métallique sont obtenues par un scratch test à passes multiples. De cette

façon, le modèle macroscopique est basé sur un setup expérimental indépendant du test du carottage (Fig. 2).

Pour autant, ce modèle macroscopique ne décrit pas la complexité de la dégradation locale de la matrice, et se retrouve dans l'incapacité de rendre compte des mécanismes micromécaniques impliqués, et l'hétérogénéité et la discontinuité du troisième corps. Pour cela, un modèle complémentaire est nécessaire : le modèle mésoscopique.

Ce modèle mésoscopique est intégré dans le code open-source MELODY2D [19], [20], qui couple la méthode Eléments Discrets, généralement utilisée pour étudier l'usure au niveau locale [21]–[23], à la technique Meshfree, qui est une alternative récente aux Eléments Finis [24] pour gérer une géométrie complexe et des corps déformables. De cette manière, les relations contraintes-déformations sont implémentées à l'échelle du grain et les contacts entre les grains sont contrôlés par des lois de contact. Le code est actuellement limité aux problèmes de déformation plane 2D. Dans cette approche, chaque grain peut être un corps rigide ou déformable. La microstructure dégradée et les propriétés des grains de débris sont générées en contrôlant leur forme réelle et leur distribution de taille, surmontant ainsi la limitation des approches discrètes traditionnelles.

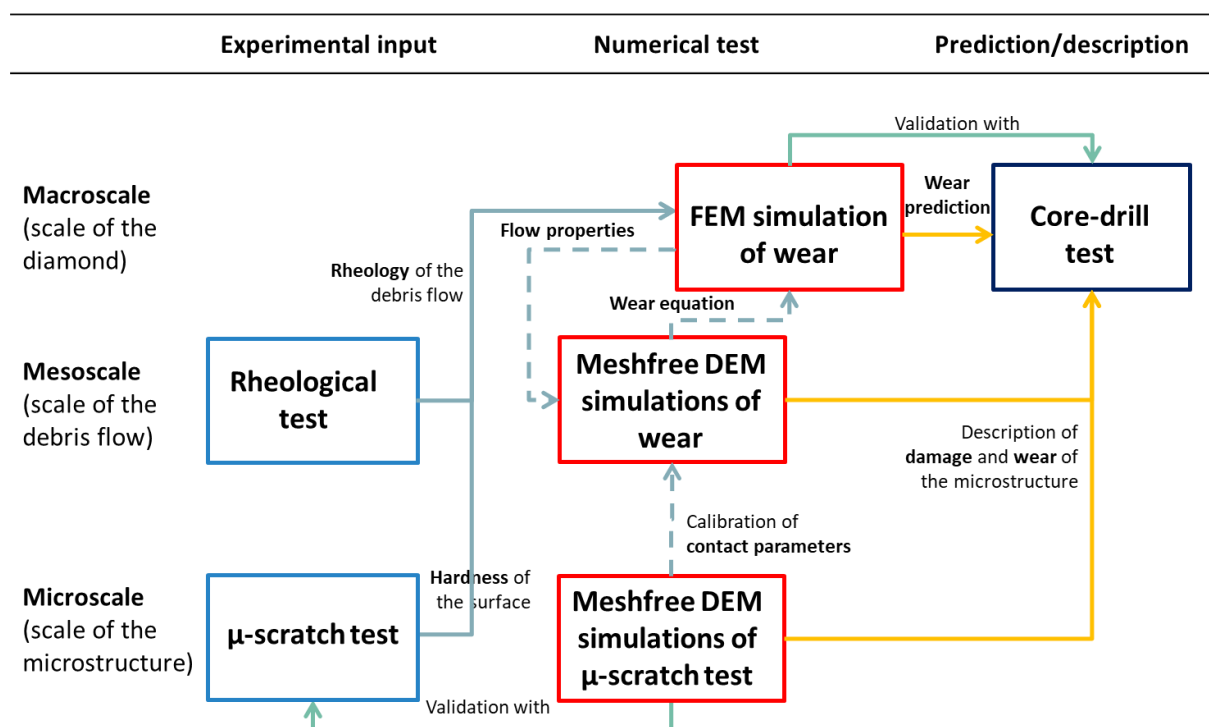


Fig. 2 Stratégie utilisée pour l'analyse de l'usure (les lignes en tirets sont les perspectives de la stratégie)

Les simulations à la méso-échelle font intervenir un grand nombre de grains et de corps déformables, ce qui exige un temps de calcul considérable et la détermination de plusieurs paramètres qui nécessitent une calibration préalable. Une façon simple de la faire consiste à effectuer des simulations numériques du  $\mu$ -scratch test, où la microstructure est abrasée par

une pointe sphérique. Dans les deux cas (le  $\mu$ -scratch test numérique et le modèle à méso-échelle ou les débris abrasent la matrice), la matrice est générée en contrôlant la distribution de la taille des grains et en considérant la même loi de contact. Cette procédure permet la comparaison directe entre les résultats expérimentaux et numériques, ce qui permet de définir les principaux paramètres de la loi de contact inter-granulaire cohésive utilisée.

## Partie B: Wear prediction at the macroscopic scale

La partie B décrit en détail le modèle macroscopique, dont la démarche a été introduite dans la partie A.

### Données expérimentales préliminaires et modélisation de l'écoulement du troisième corps

Ce modèle utilise des informations complémentaires qui ne sont pas accessibles par le carottage et qui sont obtenues en réalisant :

- Un test rhéologique : effectué sur trois suspensions à différentes fractions solides (préparées en mélangeant les débris avec de l'eau). Celles-ci ont un comportement viscoplastique qui devient de plus en plus non newtonien à mesure que la fraction solide augmente et leur rhéologie est bien représentée par le modèle de Hersley Bulkley (HB) :

$$\tau = \tau_y + C|\dot{\gamma}|^n \quad (1)$$

Où  $\tau_y$  est la contrainte à laquelle le fluide commence à s'écouler,  $C$  est l'indice de consistance qui est une simple constante de proportionnalité, et  $n$  est l'indice d'écoulement, qui caractérise un régime rhéofluidifiant ( $n < 1$ ) ou rhéoépaississant ( $n > 1$ ). Les trois cas étudiés montrent un régime rhéofluidifiant.

- Une étude multi-échelle pour définir l'équation d'usure. Cette étude part de l'hypothèse d'une dureté équivalente entre le scratch test à passages multiples et le passage continu de débris sur la surface. Pendant ce test, un pénétrateur à pointe sphérique est déplacé dans la direction horizontale sous une charge verticale et une vitesse horizontale constante, et il parcourt un nombre de passes  $n_s = 10$ . La dureté caractéristique  $H_s^*$  est calculée en effectuant une régression exponentielle des données

expérimentales et elle est définie comme la valeur atteinte après un grand nombre de passages. Cette définition pourrait être améliorée en effectuant un nombre de passages  $n_s > 10$ .

L'information rhéologique est implémentée dans le model pour résoudre l'équation de Reynolds généralisée [25], qui introduit les effets non-newtoniens par rapport à l'équation classique de Reynolds [26]. L'influence de la rhéologie non-newtonienne est discutée en termes de propriétés d'écoulement : en augmentant la concentration en solides du slurry (de SF = 28% à SF = 32%), le fluide devient plus visqueux et montre une augmentation du champ de pression.

## Modélisation de l'usure abrasive

L'équation d'usure est écrite selon un formalisme d'Archard [27], incluant les complexités observées à l'échelle locale pour fournir une description qualitative et quantitative de l'usure à l'échelle du diamant. L'usure est mesurée en termes de profondeur de matière enlevée dans le temps et est égale au produit de la pression de contact calculée à partir de l'équation de Reynolds ( $p = p(x, y)$ ), du module de la vitesse de glissement relative  $\|\mathbf{v}_r\|$  et d'un taux d'usure spécifique  $k_w$  :

$$\frac{dh}{dt} = k_w \cdot p \cdot \|\mathbf{v}_r\| \quad (2)$$

L'une des principales hypothèses sur lesquelles repose l'équation de Reynolds est la condition de non-glissement, c'est-à-dire qu'au niveau de la surface de contact, la suspension (du point de vue de la mécanique des milieux continus) a la même vitesse que la surface de contact. En revanche, localement, un débris dont le centre suit le champ de vitesse continu, n'adhère pas à la matrice avec laquelle il est en contact, mais glisse sur celle-ci. Pour tenir compte de l'effet du glissement relatif entre la surface métallique et le flux de débris, la vitesse relative  $\|\mathbf{v}_r\|$  est alors calculée comme la différence entre la vitesse au centre d'un grain en contact avec la surface et la vitesse de la surface elle-même, comme schématisé à la Fig. 3 pour la composante  $u$  de la vitesse dans la direction  $x$ .

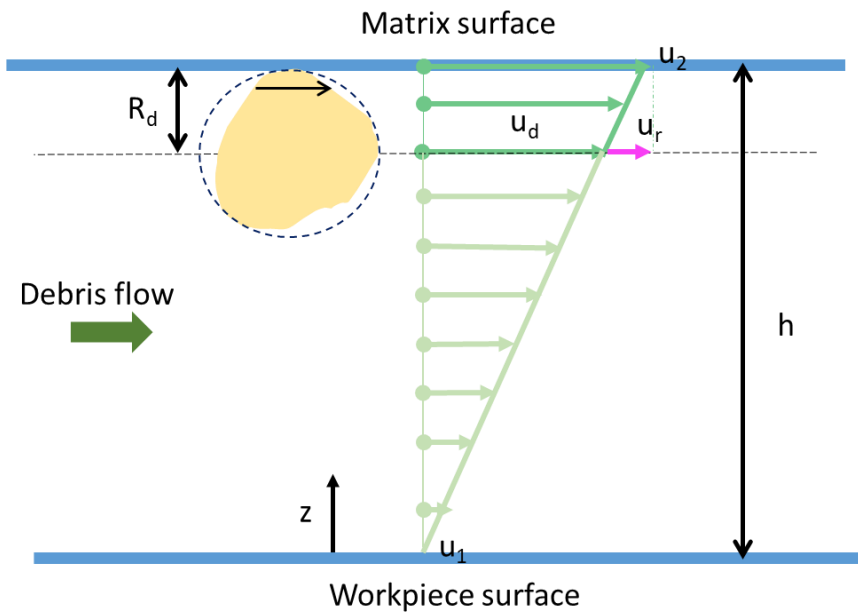


Fig. 3 Définition de la vitesse relative  $u_r$  selon la direction  $x$  entre les débris et la surface de contact. La surface a une vitesse de glissement  $u_2$  et le grain de débris se déplace à la vitesse  $u_d$

La nouvelle définition de vitesse d'usure spécifique  $k_w$  dérive des observations à l'échelle de l'aspérité et introduit le rôle de la forme des débris dans le processus d'usure. Considérant le flux de débris en contact avec la surface métallique (Fig. 4 (a)), un grain caractéristique est défini par le rayon  $R_d$  égal au rayon moyen des grains de la population testée (Fig. 4.(b)) et par le rayon  $r_d^*$  de l'aspérité caractéristique (Fig. 4 (c)). Le taux d'usure spécifique peut être défini à l'échelle du contact entre un tel grain et la surface. De cette manière, la vitesse d'usure spécifique  $k_w$  varie avec l'angle d'attaque  $\theta_d$  responsable des mécanismes d'usure, qui dépend du champ de pression exercé par le flux de débris à proximité du diamant. Ensuite, en supposant que le processus d'usure global est la somme des contributions dues à chaque particule, le taux d'usure spécifique est projeté à l'échelle de l'interface. Ici, l'équation d'usure (2) est écrite en termes de profondeur de matière enlevée dans temps. La Fig. 4 (c) montre que la rugosité d'un grain de débris est comparable à la pointe sphérique d'un indenter. Par analogie avec le processus d'usure généré lors du scratch test, on suppose donc que la matrice métallique atteint la même dureté que celle présentée au début de la partie B comme dureté caractéristique  $H_s^*$ .

Enfin, l'équation d'usure s'écrit :

$$\frac{dh}{dt}(x, y) = k_w(x, y) p(x, y) \|\mathbf{v}_r(x, y, \mathbf{h} - \mathbf{R}_d)\| \quad (3)$$

Où :

$$k_w = \frac{(2\theta_d - \sin 2\theta_d)}{\pi \cdot \sin^2 \theta_d} \cdot \frac{1}{H_s^*} \quad (4)$$

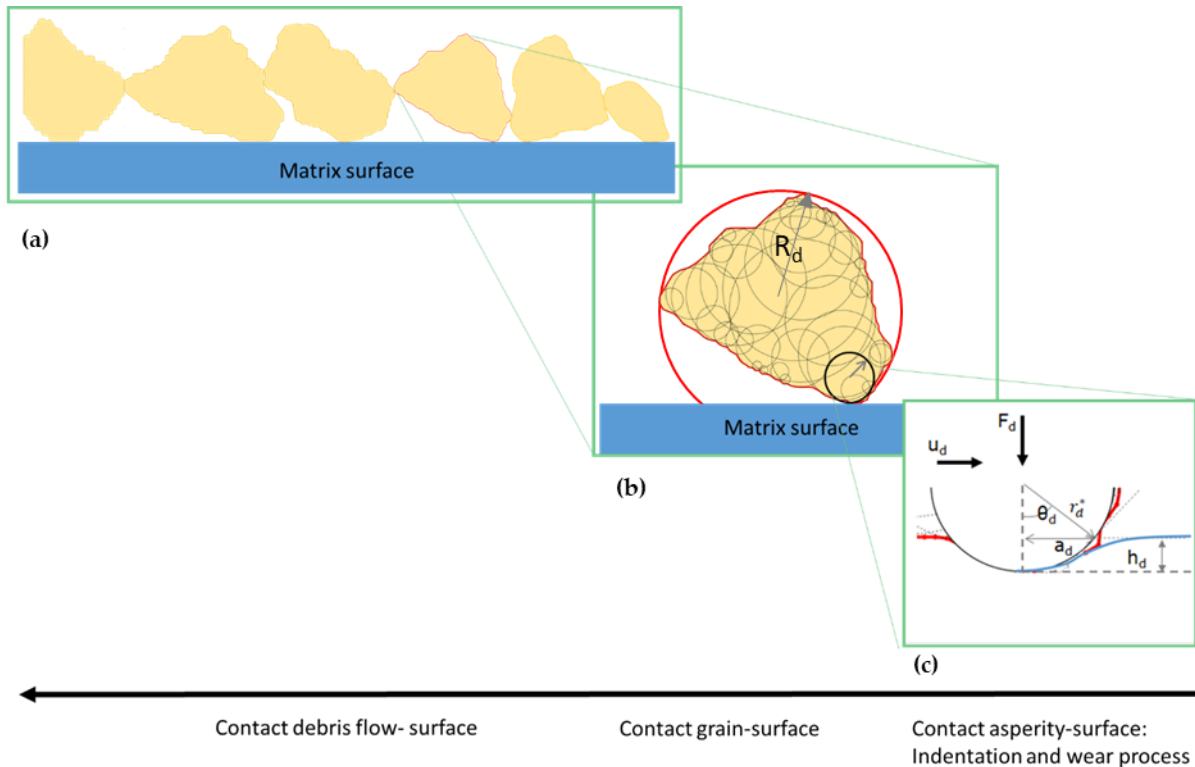


Fig. 4 Stratégie multi-échelles pour écrire l'équation d'usure de contact : (a) échelle du contact slurry-surface ; (b) échelle du contact grain de débris-surface et (c) échelle du contact local aspérité des débris-surface (c). La figure centrale (b) montre également la définition de l'angularité et du cercle défini par l'aspérité caractéristique  $r_d^*$  (en noir) considérée dans la figure en bas à droite (c)

## Résultats et discussion

La validation du modèle est réalisée en comparant les résultats numériques avec les résultats expérimentaux obtenus par carottage. Comme les diamants sont dispersés et orientés de façon aléatoire sur le segment, on choisit un diamant particulier qui n'est pas protégé par les autres et qui se trouve donc dans une configuration plus proche de celle de la simulation numérique. La configuration initiale est illustrée à la Fig. 5 (a).

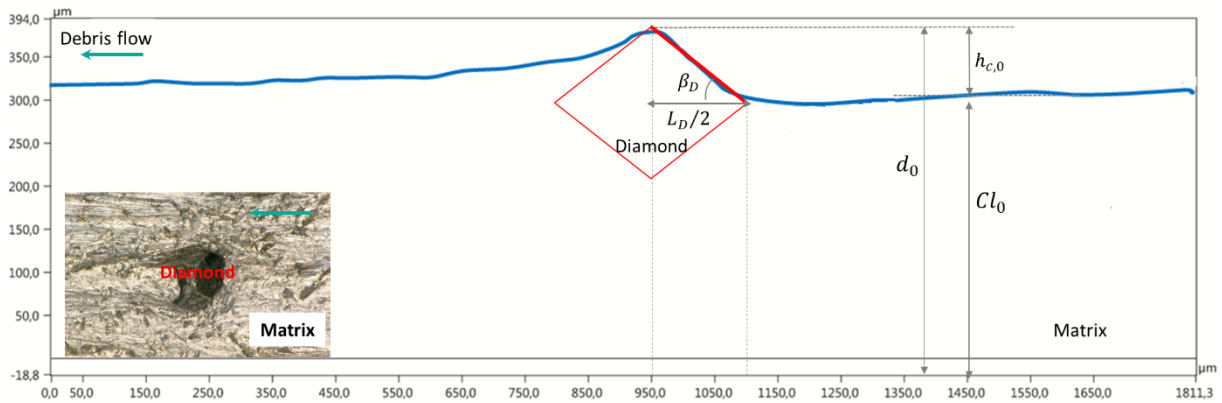
L'usure est mesurée en termes de hauteur de « clearance » et de « protrusion » relatives. La première est mesurée « loin » du diamant comme la différence entre la hauteur de « clearance »  $Cl_i$  et la hauteur de la pointe du diamant  $d_i$  à l'instant  $i$  (Fig. 5) :

$$h_{c,i} = |Cl_i - d_i| \quad (5)$$

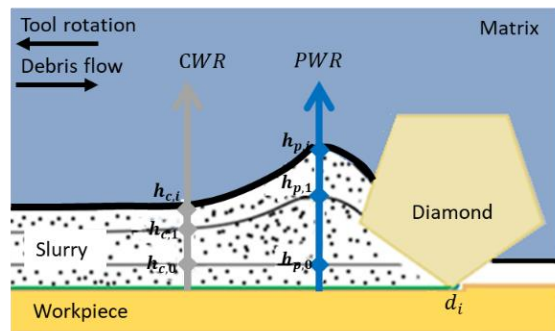
Son évolution dans le temps représente le taux d'usure pour un flux linéaire de débris. La hauteur relative de la protrusion est mesurée au niveau du cratère (Fig. 1(a) et Fig. 5 (b)) creusé devant le diamant. Il est mesuré de la même manière que la clearance, c'est-à-dire comme la

différence entre la hauteur maximale de la protrusion  $Pr_i$  et la pointe du diamant  $d_i$  à l'instant  $i$  :

$$h_{p,i} = |Pr_i - d_i| \quad (6)$$



(a)



(b)

Fig. 5 (a) Profil vertical du diamant (bleu) et schématisation de la géométrie utilisée dans le modèle (rouges) avec les indications de la géométrie initiale du modèle ( $\beta_D$ : aspect ratio du diamant;  $L_D/2$ : longueur de la protrusion du diamant;  $Cl_0$ = « clearance » initiale du diamant,  $d_0$ =hauteur initiale du diamant,  $h_{c,0} = |Cl_0 - d_0|$ : hauteur initiale de la clearance par rapport à  $d_0$  ; en bas : micrographie d'un diamant noyé dans la matrice ; (b) Définition de la vitesse de protrusion PWR et de clearance CWR (tirée de [28]) en fonction de l' hauteur de « protrusion »  $h_{p,i}$  et de la « clearance »  $h_{c,i}$  dans les instants  $i$  du temps  $t$

De cette façon, la Fig. 6 compare les résultats numériques aux résultats expérimentaux. Le taux d'usure est alors mesuré comme la variation de  $h_c$  et de  $h_p$  dans le temps  $t$  ou selon la distance de glissement  $s$ . La comparaison montre que le modèle représente bien l'usure autour du diamant.

La validation est également vérifiée qualitativement en comparant les cartes de hauteur obtenues numériquement avec les observations microscopiques expérimentales à des points de temps  $t$  particuliers (Fig. 7).

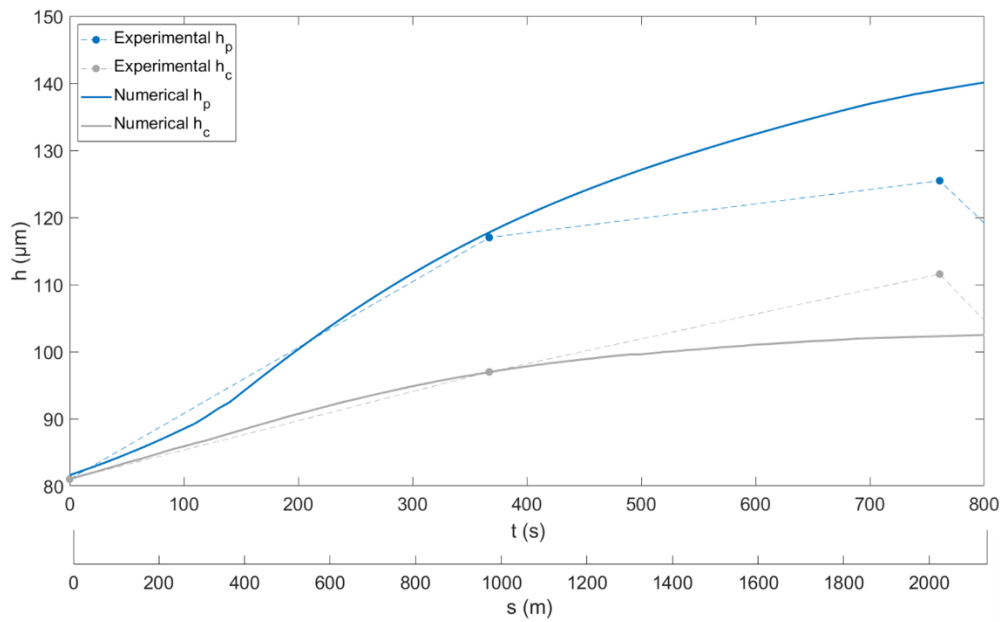


Fig. 6 Comparaison entre la hauteur numérique et expérimentale de la protrusion  $h_p$  et de la clearance  $h_c$ . Le point expérimental à  $t=761$  s n'est pas fiable car le diamant subit des microfissures qui peuvent modifier la référence de la pointe de diamant  $d_t$  dans l'évaluation de la longueur d'usure. La comparaison est donc limitée à *polishing* du diamant (jusqu'à  $t = 367$  s).

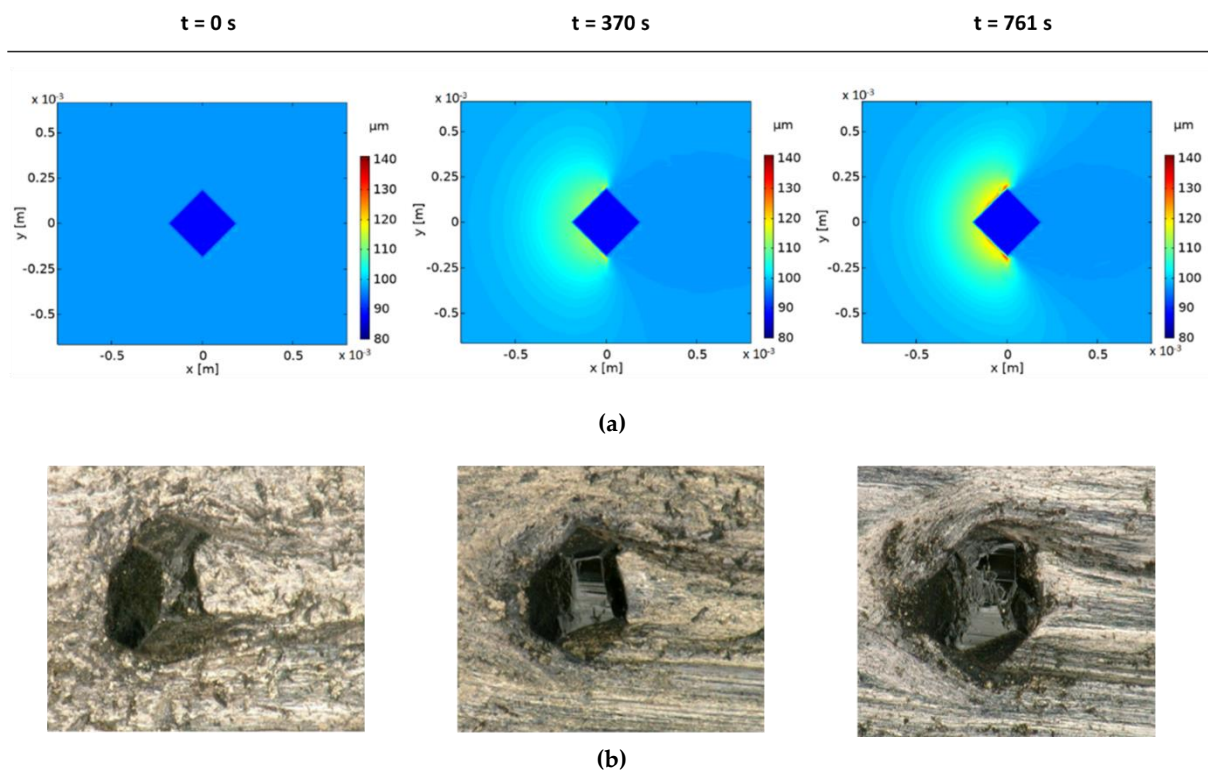


Fig. 7 Cartes d'usure de la surface de la matrice (a) calculée numériquement et (b) observés expérimentalement au microscope optique

## Conclusions

Le modèle numérique présentés ici permet d'analyser les propriétés d'écoulement des débris et l'usure de la surface de la matrice.

Les résultats obtenus sur un alliage à base de cobalt sont en bon accord avec l'observation expérimentale de la surface du matériau après le processus de carottage. Cette correspondance est à la fois qualitative en termes de motifs d'usure sur la surface et quantitative en termes de taux d'usure sur la zone de « protrusion » et de « clearance ». Cela prouve qu'à partir d'un dispositif expérimental indépendant comprenant un scratch test, un test rhéologique, une caractérisation morphologique et des changements d'échelle physiquement valables, il est possible de décrire et de prévoir l'usure à l'échelle d'une application industrielle.

## Partie C : Description de l'usure à l'échelle mésoscopique

Certains phénomènes importants contrôlant l'usure ne sont pas accessibles à l'échelle du diamant et doivent être étudiés à une échelle plus petite. Dans ce but, un modèle numérique tenant compte de la nature des grains des débris et de la microstructure polycristalline de la matrice métallique doit être envisagé. De cette façon, l'usure de la microstructure peut être étudiée de manière appropriée en fonction des cycles de contrainte induits par le passage continu des débris et en termes de décohésion intergranulaire et de fracture de la matrice. De plus, la nature déformable de la matrice sera prise en compte.

Comme présenté dans la Partie A, les méthodes d'éléments discrets couplées aux techniques *meshfree* permettent de traiter dans un cadre unique plusieurs grains, à la fois rigides (les grains de débris et la pièce) et déformables (la microstructure de la matrice métallique). Le code MELODY2D<sup>1</sup> [19] est donc utilisé pour répondre à ces besoins. Dans ce contexte, les frontières des grains de la matrice métallique sont des points de faiblesse, définissant des chemins préférentiels pour l'initialisation et la propagation des fissures. Cette partie vise à décrire et à mieux comprendre le processus d'usure à l'échelle méso, c'est-à-dire à l'échelle du contact entre la surface de la matrice et le flux de débris. Les simulations sont réalisées en considérant un élément de volume représentatif (RVE) extrait d'un segment de diamant, qui rend compte du contact entre la matrice et les grains de débris. Le code est actuellement limité à la 2D. Malgré cette simplification de la réalité et sachant que le processus d'usure est clairement 3D, le code peut surmonter ces limitations par une désactivation artificielle des grains dont les

---

<sup>1</sup> Multibody ELeMent-free Open code for DYnamic simulations in 2D

déplacements sont suffisamment grands pour les considérer comme éjectés (*cutting mode*) ou déplacés sur les côtés latéraux (*ploughing mode*).

Le premier chapitre, décrit les outils numériques utilisés pour la génération des grains et les simulations dynamiques ainsi que les lois de contact par lesquelles les corps interagissent. Le processus d'usure est ensuite analysé numériquement dans le deuxième chapitre, en termes d'endommagement, de détachement et d'éjection des grains, en considérant également les effets de la fatigue. Ensuite, une amélioration du modèle est poursuivie dans le troisième chapitre. Cette dernière section conduit à la calibration des paramètres de contact entre les grains de la matrice en simulant le  $\mu$ -scratch test et en comparant les résultats avec les résultats expérimentaux.

## L'usure de la matrice à l'échelle locale : Modélisation

Le modèle considère la matrice comme un matériau polycristallin dégradable, où la taille des grains et leur distribution sont choisies en fonction des observations expérimentales. Les grains de la matrice sont en contact avec les grains des débris, qui sont aussi modélisés avec des formes et des tailles réalistes en utilisant le même code (PACKING2D [29]) que pour la matrice. La partie dégradable est limitée en haut par un support non dégradable, nécessaire pour réduire le coût numérique de la simulation, son épaisseur est choisie de manière à assurer la continuité entre les deux parties. La géométrie du modèle est montrée dans la Fig. 8. Une pression normale  $p_n$  et une vitesse tangentielle  $u_t$  sont appliquées à la base inférieure de la pièce. La surface supérieure de la base non dégradable est fixée, tandis que des conditions limites périodiques sont appliquées latéralement.

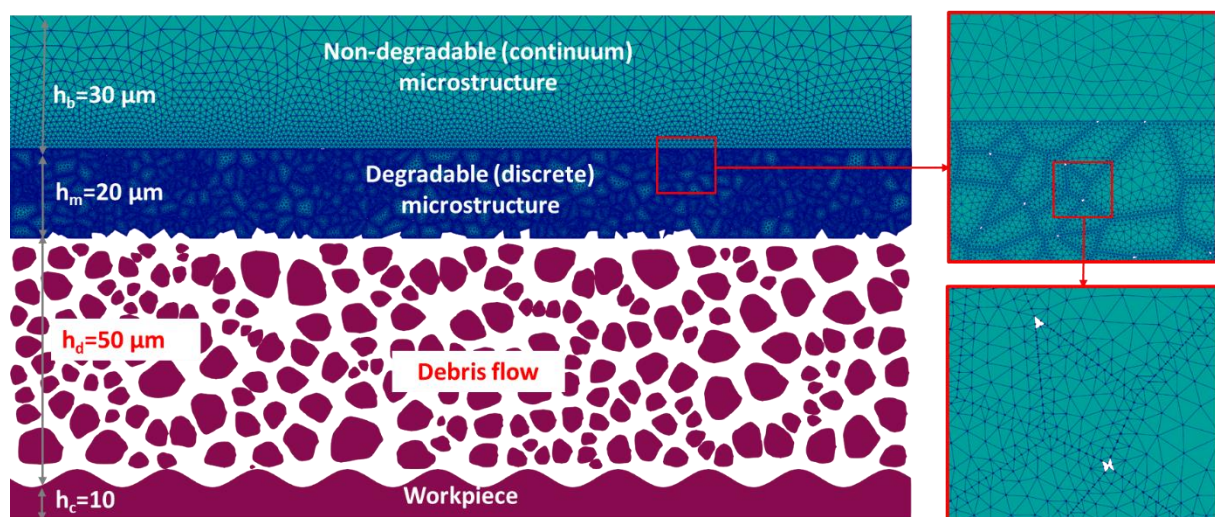


Fig. 8 Modèle à méso-échelle

Les corps rigides (grains de débris et pièces de travail) et les corps déformables (matrice dégradable et non dégradable) sont définis comme un ensemble de nœuds placés sur la frontière et les lois de contact sont donc les mêmes dans les deux cas. Les corps rigides suivent

la formulation classique de la DEM et sont caractérisés par une masse, un centre de masse et une inertie de rotation et comportent trois degrés de liberté (2 déplacements et une rotation). Les corps déformables, quant à eux, ont besoin d'autres nœuds comprenant plusieurs degrés de liberté comme dans la formulation FEM classique. Dans ce modèle, les lois de contact suivantes sont utilisées :

(a) Mohr-Coulomb : pour le contact entre les grains de débris et les grains de la microstructure dégradable.

(b) "Impact Mohr-Coulomb" pour le contact entre les grains de débris et la pièce à usiner et le contact entre les grains de débris eux-mêmes.

(c) "CZM" avec fatigue pour le contact dégradable et non dégradable et le contact entre les grains du matériau dégradable. Cet modèle est généralement utilisé pour la fracture des matériaux polycristallins [30]–[33], en tenant compte de l'influence de la microstructure. Cette loi contrôle le processus d'endommagement et donc d'usure de la matrice métallique, dont les grains se détachent en raison de la perte de cohésion. Le paramètre d'endommagement  $D$  contrôle ce processus et prend la valeur  $D = 0$  si le contact est intact,  $D = 1$  s'il est rompu. La loi est représentée dans la Fig. 9 dans la direction tangentielle (indice  $t$ ). Les paramètres  $\tilde{p}_{lim}$  et  $\tilde{\delta}_{res}$  sont les paramètres de résistance qui contrôlent la forme de la loi. Si la pression de contact  $\tilde{p}$  atteint la valeur limite  $\tilde{p}_{lim}$  et donc le gap  $\tilde{\delta} > \tilde{\delta}_{lim}$ , la rupture se produit de manière monotone ; si la pression du contact dépasse le seuil de fatigue ( $\tilde{p} \geq \tilde{p}_f$ ) et la pression du contact  $\tilde{p}$  n'atteint pas la valeur limite  $\tilde{p}_{lim}$ , le dommage peut également augmenter en raison de la fatigue et il est contrôlé par le paramètre d'évolution de l'endommagement par fatigue  $dD_f$ .

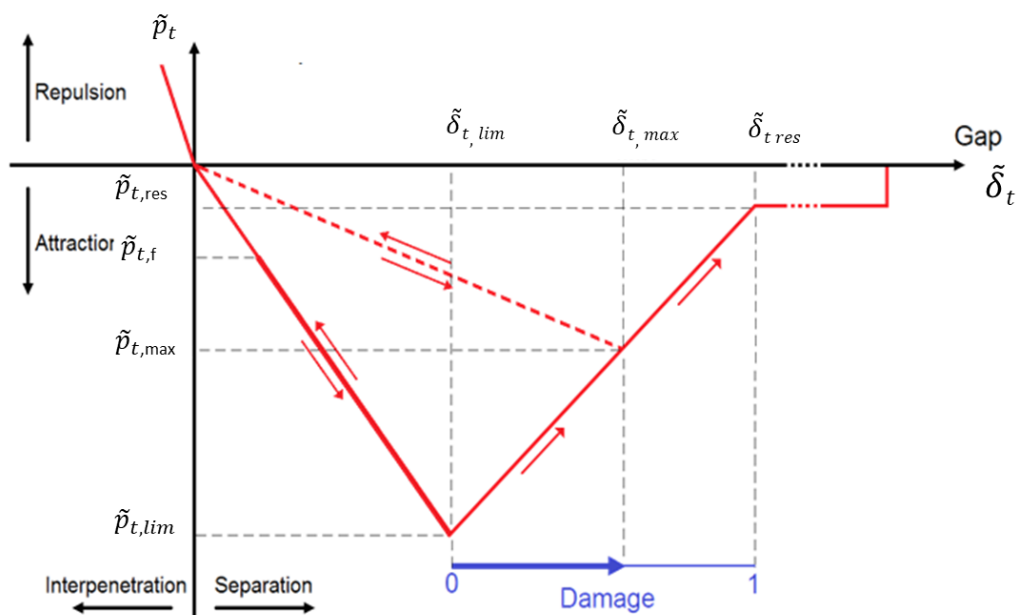


Fig. 9 Loi traction-séparation triangulaire dans la direction tangentielle

## L'usure des matrices à l'échelle locale : Premiers résultats et discussion

La variable  $D$  peut donc augmenter de façon monotone ou par fatigue, en fonction du paramètre de résistance à la rupture, défini  $\tilde{p}_{lim}$  en Fig. 9 (ayant fixé la pression appliqué  $p_n$ ).

Si la résistance à la rupture  $\tilde{p}_{lim}$  est trop faible, l'usure se produit principalement de manière monotone. C'est un processus très rapide, les grains de la matrice qui se détachent restent dans le système et peuvent eux-mêmes être la cause de l'usure. L'usure étant physiquement un processus plutôt lent et progressif, la fatigue doit être prise en compte et l'effet du paramètre d'évolution de l'endommagement par fatigue  $dD_f$  sur l'usure est étudié.

La Fig. 10 montre que la courbe d'usure est caractérisée par trois phases :

- I. Initialisation : la matrice commence à s'endommager mais l'usure est encore négligeable
- II. État stationnaire : le taux d'usure est approximativement constant et est fonction de la propagation de l'endommagement dans la matrice.
- III. État stationnaire perturbé : les grains de la matrice se détachent lentement en raison de la proximité de la partie non dégradée. Cette troisième phase devient de plus en plus importante à mesure que le paramètre d'évolution de l'endommagement par fatigue  $dD_f$  est faible. Cependant, cette troisième phase n'a pas de signification physique particulière puisque la partie non dégradée est un artefact numérique pour accélérer le calcul.

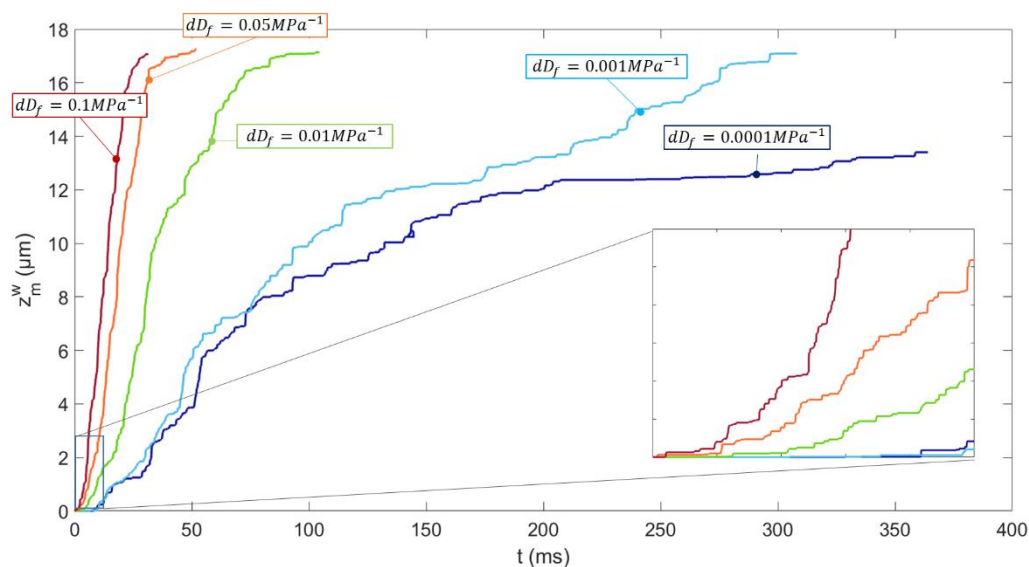


Fig. 10 Courbes d'usure pour différentes valeurs de  $dD_f$  et zoom sur la phase d'initialisation

Ces premiers résultats montrent que le modèle parvient à décrire le processus d'usure à une échelle locale. En particulier, l'usure par fatigue joue un rôle essentiel dans l'endommagement et le détachement des grains. Cette analyse montre également qu'il existe une grande relation entre l'évolution de la topographie de surface, les paramètres de la loi de contact et le processus d'usure. Cependant, il n'est toujours pas clair si la rugosité de surface est directement liée aux paramètres de la CZM et est donc elle-même une cause d'usure, ou si elle en est une conséquence. Ces observations doivent donc être validées en considérant une matrice dégradable plus profonde afin de minimiser l'effet de la troisième phase montrée dans la Fig. 10 même pour des valeurs plus faibles du paramètre  $dD_f$ .

## Vers une approche quantitative

Le paramètre de la loi de contact CZM utilisé dans le chapitre précédent ne correspond à aucune mesure effectuée sur la microstructure concernée. La réalisation d'une calibration basée sur le modèle mésoscopique est possible mais coûteuse car elle nécessite de réaliser des simulations de fatigue, incluant un grand nombre de grains et un long processus d'usure. De plus, la comparaison avec l'essai expérimental peut ne pas être aussi évidente.

L'idée de ce chapitre est de calibrer la résistance ultime  $\tilde{p}_{lim}$  et la contrainte résiduelle  $\tilde{p}_{res}$  de la loi CZM, en réalisant un modèle numérique de *scratch test* multi passages dont les résultats peuvent être comparés aux expériences présentées au chapitre B.1. Comme MELODY est restreint à une cinématique de déformation plane, l'intention est limitée à la calibration. Malgré sa simplicité, le modèle peut cependant décrire des phénomènes micromécaniques tels que les déformations irréversibles et les contraintes résiduelles induites par le scratch. La calibration est effectuée en comparant les résultats numériques et expérimentaux en termes de coefficient de frottement  $\bar{\mu}_s$  et de profondeur d'indentation du scratch  $\bar{h}_{s-1}$ .

Le modèle est illustré à la Fig. 11.

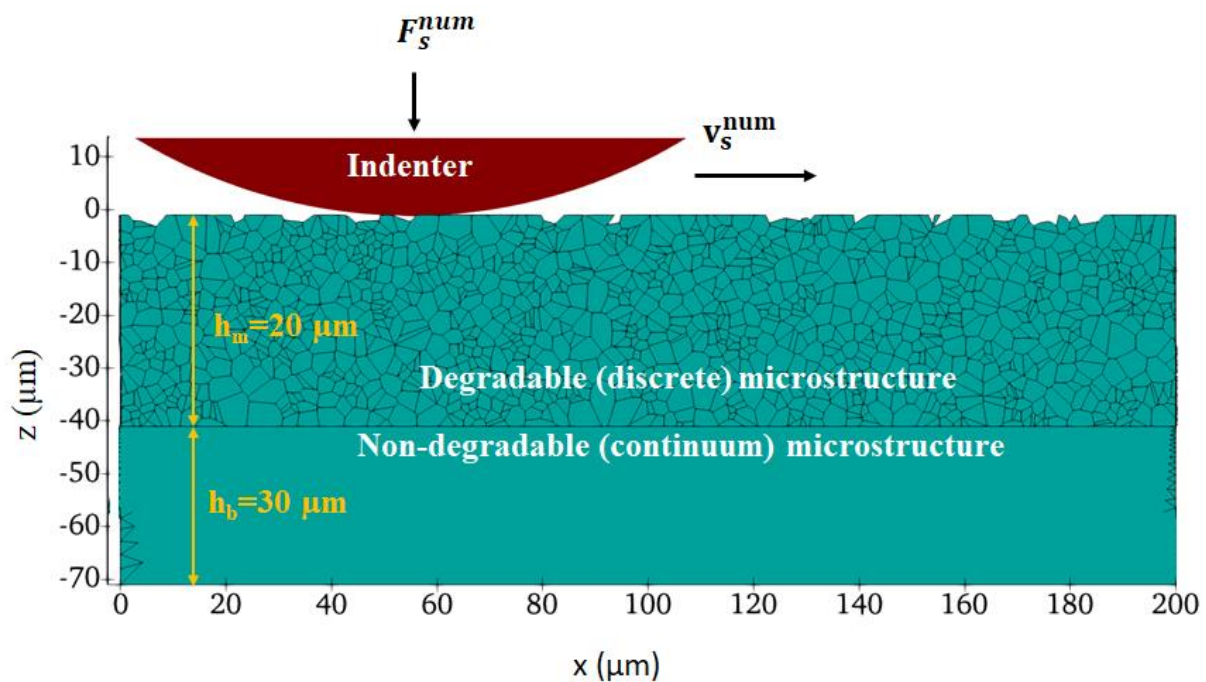


Fig. 11 Modèle de microscratch 2D avec l'indication de l'épaisseur de la matrice  $h_m$  et de la base  $h_b$ , ainsi que de la force appliquée  $F_s^{num}$  et de la vitesse  $v_s^{num}$  sur l'indeteur.

## Conclusions

Le cadre décrit dans cette partie C vise à décrire l'usure à l'échelle locale. Les débris et les grains de la matrice métallique sont modélisés avec une forme et une taille réalistes à l'aide d'un logiciel 2D couplant les techniques de maillage libre et d'éléments discrets (MELODY2D).

Bien que le code soit limité à 2 dimensions et malgré le grand nombre de paramètres définis par l'utilisateur intervenant dans les lois de contact entre corps discrets, il constitue un outil utile pour la compréhension de phénomènes non accessibles à l'échelle des applications industrielles. Quels que soient les paramètres de contact choisis, le processus d'usure décrit par l'outil numérique semble toujours être défini par trois étapes principales : l'initialisation, l'état d'équilibre et l'état d'équilibre perturbé. La durée de chacune d'entre elles et la tendance plus ou moins linéaire de la seconde phase dépendent des paramètres CZM choisis.

Pour optimiser le coût de la simulation, les paramètres du CZM peuvent être calibrés sur un modèle différent représentant l'usure par abrasion causée par le passage de particules plus dures. Ainsi, la calibration réalisée par un  $\mu$ -scratch test montre que la profondeur d'usure dépend principalement des paramètres de résistance de la loi CZM (si la cohésion entre la matrice et le pénétrateur est correctement choisie).

## Conclusions générales

Ce travail vise à développer une stratégie pour modéliser l'usure de la matrice métallique utilisée comme liant dans les outils diamantés pour la coupe de la pierre. Le processus d'usure est causé par le flux de débris abrasifs (composé de copeaux de la pièce et de l'eau utilisée pour les évacuer) et doit être contrôlé pour optimiser la durée de vie de l'outil.

En raison de la nature multi-échelle du problème et du grand nombre de variables impliquées, une nouvelle approche numérique satisfait la demande industrielle, impliquant deux objectifs principaux, réalisés grâce à deux modèles :

- Un modèle macroscopique permet la prédiction de l'usure de la matrice à l'échelle du diamant
- Un modèle mésoscopique permet la description des mécanismes d'usure locaux à l'échelle du flux de débris.

A terme, le modèle se vaudra suffisamment général pour s'adapter à tous types de matériaux de la matrice métallique (monophasée, biphasée, triphasée). Dans ce travail, les deux modèles sont appliqués à une microstructure de matrice métallique de cobalt (monophasé, 100% Cobalt) dont la réponse mécanique est, au moins à l'échelle macroscopique, connue qualitativement et quantitativement, permettant la validation d'une telle modélisation.

Dans le modèle macroscopique, un seul diamant est considéré, qui reste intact pendant tout le processus. Ceci n'est pas réellement vérifié dans la littérature puisque l'usure de la matrice est également affectée par la taille et la distribution des diamants ; de plus, les diamants peuvent subir plusieurs fractures pendant le traitement. Cependant, le choix d'un "diamant isolé" (non protégé par les autres) et la prise en compte de la seule première étape du processus de coupe (où la matrice subit une usure et où le diamant est encore intact) permettent une comparaison quantitative entre le modèle numérique macroscopique et les résultats expérimentaux obtenus.

Pour une bonne optimisation de la microstructure de la matrice, son comportement micromécanique à l'usure doit être considéré à l'échelle du contact avec les débris. Le modèle mésoscopique décrit ainsi les phénomènes locaux d'endommagement et d'usure à cette échelle. Les simulations sont réalisées à l'aide d'un code open source développé au laboratoire et en considérant un élément de volume représentatif (RVE) extrait d'un segment de diamant. Ici, les grains de débris sont représentés comme des corps rigides dont la forme et la taille sont contrôlées, tandis que la matrice est définie de manière réaliste comme un matériau polycristallin déformable. L'usure de la microstructure est étudiée en fonction des cycles de contraintes induits par le passage continu de débris et de particules.

# Perspectives

L'approche multi-échelle proposée nécessite des développements supplémentaires qui concernent les deux modèles indépendamment (le modèle macroscopique et le modèle mésoscopique) et leur interconnexion. Les développements attendus sont détaillés ci-dessous :

- Contexte : des améliorations sont nécessaires dans les deux modèles :
  - o Les deux expériences (rhéologie et  $\mu$ -scratch test) sur lesquelles le modèle macroscopique est basé pourraient mieux représenter les conditions industrielles en adaptant les conditions opératoires.
  - o Le modèle mésoscopique dans son état actuel comporte un nombre assez important de paramètres qui doivent être choisis par l'utilisateur. Après l'analyse de sensibilité réalisée dans cette thèse, l'adaptation du modèle au cas particulier de l'étude permettrait de valider l'approche. Pour ce faire, la calibration effectuée sur le scratch test permet de définir les paramètres de résistance de la loi cohésive, tandis que les paramètres de fatigue doivent être choisis correctement sur la base des résultats déjà obtenus au chapitre C. De plus, les conditions aux limites appliquées à la matrice modélisée peuvent être choisies en considérant le modèle macroscopique.
- Validation à consolider : le modèle macroscopique est construit en considérant l'usure d'une microstructure de matrice de cobalt autour d'un diamant spécifique. Par conséquent, le modèle doit être validé en considérant d'autres diamants retenus par la même microstructure afin de considérer l'effet de la taille et de l'orientation du diamant dans le processus d'usure.
- Extension : Une fois le modèle macroscopique validé, l'étude doit être étendue à d'autres microstructures à matrice métallique. D'autres microstructures peuvent également être étudiées numériquement à la méso-échelle.
- Couplage entièrement numérique : Il s'agit d'un domaine important de développement qui peut être réalisé une fois que les deux modèles sont établis et validés. L'approche numérique couplée partira du même dispositif expérimental composé du scratch test et du test rhéologique. Le premier sera utilisé pour calibrer les paramètres de la loi CZM du modèle mésoscopique, tandis que le second est utile pour définir la rhéologie du flux de débris utilisé dans le modèle macroscopique, qui à son tour donne les propriétés d'écoulement qui peuvent être mises en œuvre comme conditions limites dans le modèle mésoscopique.



# Abstract

Diamond-Impregnated Tools (DIT: core drills, wire saws, circular and frame saw blades) are widely used to process and size brittle materials. DITs are composed of abrasive diamond crystals embedded in a metallic matrix by sintering. During the cutting operations, the matrix retains the diamonds, which, due to their hardness, can indent the workpiece. Debris from the cut material are formed, defining, together with water used to carry them out, a slurry. This slurry flow is highly abrasive for the metal matrix and can wear it. Although this wear process is necessary to renew worn diamonds, it must be controlled in terms of wear rate to attain an optimum balance between service life and free-cutting ability. While several attempts have been made to analyze the wear of the diamonds, the wear process involving the matrix is not yet well understood. Because experimental analyses do not bring all the necessary insights on this problem, the principal aim here is to build a multiscale numerical strategy to describe the abrasive wear accounting for the complex tribological interactions involving matrix, diamonds, and debris flow. This strategy is based on two main models: (1) the macroscopic model, built at the scale of the diamond and solved by Finite Elements Method (FEM); the mesoscopic model (2), built at the scale of the debris grains and solved using a deformable discrete elements code to study wear locally, accounting for the discrete nature of the debris grains and the polycrystalline deformable microstructure of the metal matrix. In the context of the industrial demand, the macroscopic model (1) gives encouraging results in terms of wear rate and can be used as a predictive model in the metal matrix selection. The mesoscopic model (2) describes the main phenomena controlling wear that are not accessible at a higher scale.



# General introduction

## Introduction

Diamond Impregnated tools (DIT) include core drills, wire saws, circular and frame saws, used in various applications such as extraction, sizing and processing of natural stones, drilling and sawing of concrete and reinforced concrete, and road repair.

DITs are composed of abrasive segments fixed to a steel support by brazing or welding. Segments consist of randomly oriented and randomly dispersed diamond crystals embedded in a metallic matrix by a sintering process. During the cutting operations, the matrix retains the diamonds, which, due to their hardness, are able to indent the work-piece. Debris from the cut material will inevitably be formed, defining, together with water used to carry them out, a slurry. This debris flow is highly abrasive for the metal matrix and can wear it. This wear process is also necessary to renew diamonds, but it must nevertheless be controlled in terms of wear rate: the matrix has to wear at a rate compatible with the diamond breakdown to attain an optimum balance between service life and free-cutting ability. For these reasons, the wear resistance of the matrix has to be adjusted to the wear speed of the diamonds: if the matrix is too soft, it wears too fast, and the diamond capacity is not completely used with a premature diamond pull-out; if it wears more slowly than diamonds then the slurry cannot be carried out correctly, and the segment will continuously lose the ability to cut.

Generally, cobalt-based alloys are widely used as a matrix for their high abrasive resistance and great retention properties. The high and unstable price and the environmental issues are the main drawbacks of cobalt that induced producers of diamond-impregnated tools to look for more suitable and cheaper alternatives to replace, totally or partially, the cobalt powder.

# Objectives

Based on the industrial demand and considering that the mechanisms involved in the wear of the metal matrix microstructure are not yet well understood, this thesis aims to analyze and predict wear during a drilling test. In a more scientific general framework, the main contribution of this work consists of the development of a strategy to study the abrasive wear of a surface due to the continuous passage of a debris flow.

Considering the large number of variables involved, the proposed strategy is to mimic the behavior of a diamond segment (or a part of it), by numerical simulations. The numerical approach has the advantage of understanding mechanisms that cannot be observed experimentally and predicting the wear behavior (under certain well-defined conditions) of new materials without going through experimental tests, thereby reducing development costs. In this way, the industrial demand is met by applying such a strategy on a pure cobalt metal matrix already studied experimentally; this allows to validate the strategy and use it to further studies on different materials.

Considering the multiscale nature of the problem, a multiscale approach is pursued. It is based on two different models that look at two different scales : the macroscopic scale (scale of the diamond) and the mesoscopic scale (scale of debris grains). The former aims at being a predictive model of wear around one diamond, to be challenged by experimental observations of worn segments. The second is a descriptive model for the understanding of local phenomena such as decohesion of matrix grains.

The two models are built to give complementary information and answer different questions:

- **Macroscopic model:** The aim is to give a qualitative and quantitative description of wear at the same scale of the industrial application. This model considers a part of a segment consisting of a diamond and the surrounding matrix. A first main objective is to find the field properties (i.e., pressure and velocity at the contacting surface matrix-debris flow) that will allow a prediction of the abrasive wear at the scale of the drilling tool.
- **Mesoscopic model:** The aim is to describe and understand the wear process at the local scale of debris-matrix contact and overcome the limitations imposed by the continuum mechanics frameworks of the previous model. This model will consider a representative volume element at the scale of the contact between the matrix surface. It will account for the nature of the debris grains and the polycrystalline microstructure of the metal matrix. In this way, the wear of the microstructure would be appropriately studied as a function of the stress cycles induced by the continuous passage of debris and in terms of intergranular de-cohesion and fracture of the matrix.

# Outlines

The use of different codes for the multiscale strategy development requires the subdivision through 3 main parts, each of them composed of detailed chapters.

Part A introduces the problem of wear of diamond tools, framing it first in a broader context on the industrial scale and defining the main characters (diamonds and metal matrix microstructures), then contextualizing it in the framework of tribological problems of abrasive wear. Herein, the main conceptual and theoretical tools dealing with abrasive wear are described. Finally, the multiscale strategy necessary to predict wear at the macroscale and comprehend local phenomena at the mesoscale is introduced.

Part B is devoted to the experimental/numerical strategy for wear prediction at the macroscopic scale. Experimental tools are presented to extract local information (non-accessible at the scale of the industrial application) on matrix and slurry. The flow of the abrasive debris is then computed on the basis of Continuum Mechanics. It is coupled to the local properties of the matrix to predict wear of the matrix surface at the diamond scale. The final chapter of this Part deals with the validation of the model, comparing the numerical result with the observations performed on drilling tools.

Part C proposes a mesoscale model to describe and understand local phenomena of wear that are non-accessible experimentally. The numerical tool is discussed and a sensitivity analysis of the abrasive wear is proposed, focusing on the contact between debris and matrix grains and considering their discrete nature. Then, an improvement of the model is proposed based on the calibration of the cohesive properties of the matrix microstructure. As a perspective, it will allow for shifting from the calibration/sensitivity analysis to the modeling of a specific case of study.

A general conclusion is finally drawn on this work, and some ideas for future development as well as links between the described models are proposed.



---

# **Part A.**

## **State-of-the-Art & Strategy**

---



# Part A.

## State-of-the-art & strategy

This first Part aims to describe the industrial case of study concerning the wear of diamond tools and the means useful to analyze it.

The first section gives an overview of the main industrial aspects related to metal bonded tools' production and performance, i.e., the diamond-impregnated tools obtained by metal powder (PM) technology. Starting from the scale of the tool, we go towards an ever-smaller scale, arriving to define the wear of the microstructure caused by the debris flow of material cut during processing.

Chapter 1 describes diamond tools and their components. Chapter 2 deals with the wear of diamond tools contextualized in the general framework of tribological problems dealing with abrasive wear. The key features are then summarized in Chapter 3 before introducing the multiscale approach and the experimental/numerical tools used in this work.

The main idea is to give the basis to understand the problem (i.e., the wear of the metal matrix), what is known about it until now, and the tools we have to describe it.



## A.1

# On the history and use of Diamond Impregnated Tools

Nowadays, diamond tools are widely used in manufacturing processes. Even if the origin of diamond tools dates back to 300 BC, the first diamond saw blade was manufactured in the early 20<sup>th</sup> century to cut limestone and marble.

The development of metal powder (PM) technology and the introduction of synthetic diamonds instead of natural ones led the diamond tool industry to revolutionize the machinery and processing techniques in the stone and construction industries. A classification concerning the manufacturing method involved is given in Fig.A-1.

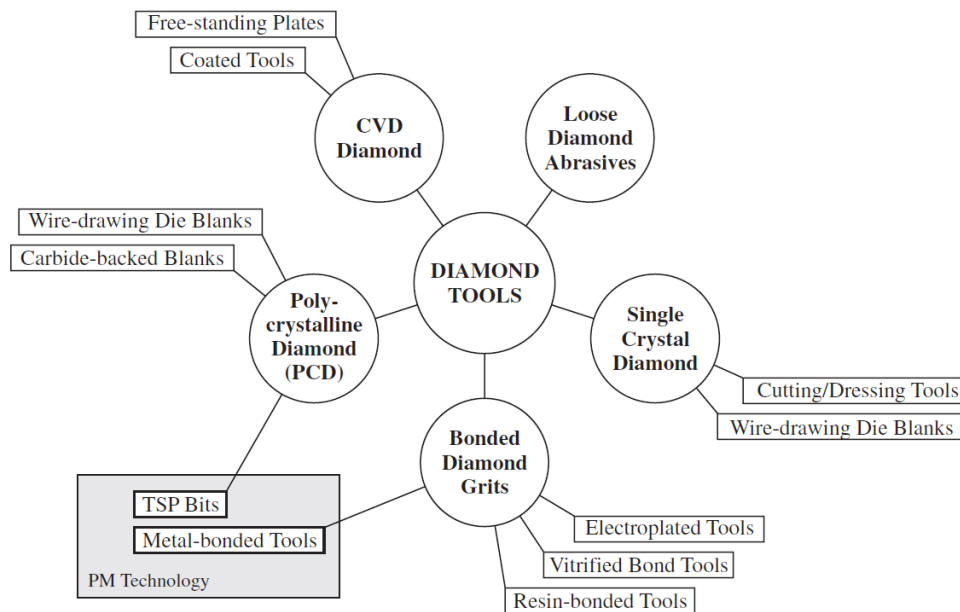


Fig. A-1 Classification of diamond tools [34]

Bonded Diamond Grits, or Diamond Impregnated Tools (DIT), are used in a wide variety of applications. They consist of diamond particles embedded into a metallic or non-metallic matrix by different manufacturing processes.

This work deals with Metal-bonded Tools, obtained with the PM technology and accounting for about two-thirds of the whole bonded diamond grits on the market. They include circular and frame saw blades, wire saws, and core drill for cutting natural stones and construction materials, as well as core bits for drilling in medium to hard rock (Fig. A-2). All of them are composed of abrasive segments fixed to steel support by brazing or laser welding. The support is attached to the machine, gives the right shape to the tool, transmits the kinetic energy from the machine axes to the diamonds, and adsorbs the stress generated during machining. Segments consist of randomly oriented and dispersed diamond grids embedded in the metallic matrix by the aforementioned (PM) techniques [35]–[37].

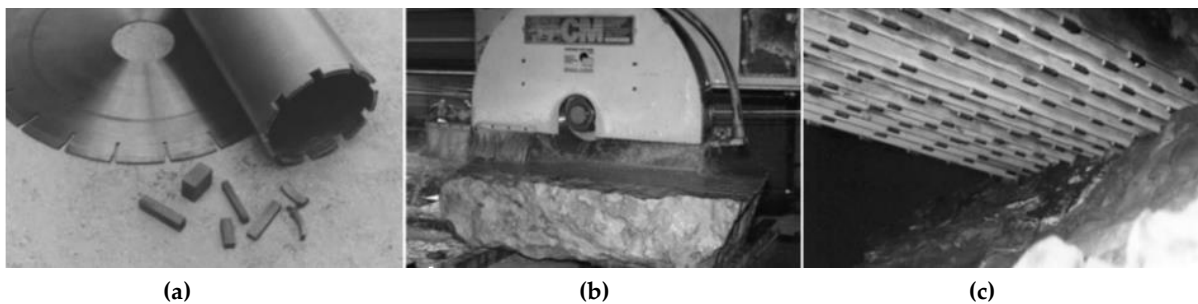


Fig. A-2 (a) Circular saw blade, core-drill and diamond-impregnated segments for sawing and drilling tools; (b) circular sawing; (c) frame sawing on the stone [36]

Diamonds constitute the cutting edges: they are held by the metallic matrix during the cutting process and can indent the material to cut it. The diamond-workpiece contact, generated during diamond indentation, is responsible for the two-body contact between diamond and stone, which can wear diamond own to high mechanical and thermal loads and the hardness of the workpiece itself [38]. This contact generates the detachment of particles from the workpiece, which can flow within the contact zone and abrade the metallic surface.

To achieve the required cutting performance and tool life, it is important to properly choose the specification of the cutting tool in terms of the matrix (chemical composition and degree of alloying, main particle size and size distribution, and contents of impurities) and diamonds (shape, size, and thermal stability) [36], [39]. These main properties are controlled by the manufacturing process.

### A.1.1 Powder metallurgy fabrication

The main steps of the powder metallurgy technique are illustrated in Fig. A-3. After the metallic powder's granulation to achieve the desired chemical composition, shape, and size distribution of grains, the powder is mixed with diamond grits. Diamonds are coated with titanium ("Ti-coated") or chromium ("Cr-coated") [17], improving diamond distribution on the segment and guaranteeing better resistance to wear. Then, the cold pressing is applied as a pre-sintering operation before the hot pressing in steel molds. The following hot pressing

consists of the simultaneous application of heat and pressure to obtain a product almost free from internal porosity. The temperature reached during the hot pressing should be controlled to minimize the percentage of diamonds converted into graphene ( $T < 900\text{ }^{\circ}\text{C}$ )

A final operation of deburring is necessary to clean and remove edge residual after consolidation.

Once the PM process is completed, segments are finally attached to the core by laser or welding operations.

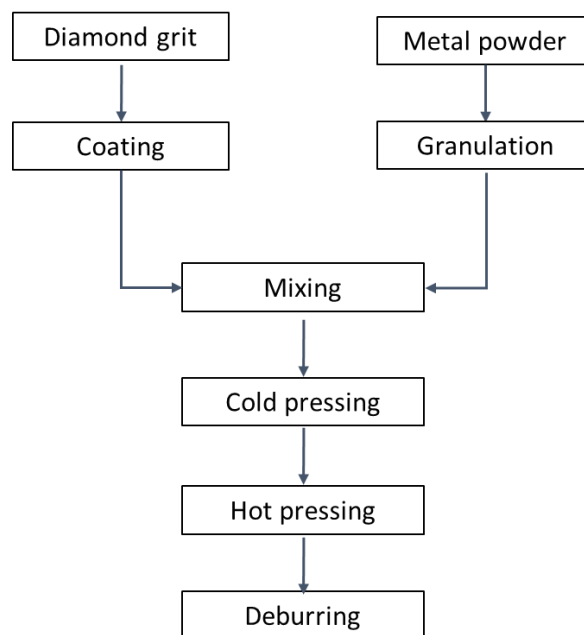


Fig. A-3 Powder Metallurgy process

### A.1.2 Metal matrix microstructure

The two leading roles of the matrix are to hold diamonds and to wear slowly, preventing premature diamond breakdown and protruding new diamond.

Cobalt and cobalt-based alloys are commonly used to produce matrices for diamond impregnated tools for their high abrasive resistance and great retention properties. Unlike other materials, fine cobalt powders can be produced by controlling the shape and size of grains and the chemical purity such that they can be well-adapted to several cutting conditions.

The mean grain size of the starting powder and the needed temperature of hot pressing have a strong influence on the grain size of the matrix microstructure. Finer powders result in smaller grain sizes and hence a higher hardness of the binder. Grain size also controls the mechanical yield strength of the microstructure and, therefore, the retention capacity. The

grain size strengthening is explained in terms of grain boundary strengthening as grain boundaries restrict the movement of dislocations. The Hall-Patch relation [40], [41] explains this effect:

$$\sigma_y = \sigma_0 + Kd_m^{-\frac{1}{2}} \quad (A.1)$$

Where  $\sigma_y$  is the yield strength,  $d_m$  the average diameter of the grains of the microstructure, and  $\sigma_0$  and  $K$  are constants for a given metal.

Another parameter affecting the matrix performance is the porosity of the microstructure after sintering, which should be controlled to avoid premature cracks within the matrix.

Tab.A-1 describes the main properties of the microstructure for three cobalt alloys characterized by different grain sizes [42]. The finer the powder, the lower is the content of pores and the higher the performance. The temperature reached during the hot pressing is 780°C for the CO7106 and CO6101, while it arrives at 960°C for the CO6102.

The high and unstable price and the environmental issues are the main drawbacks of cobalt that induced producers of diamond-impregnated tools to look for more suitable and cheaper alternatives to replace, totally or partially, the cobalt powder.

Tab. A-1 Properties of 100 % Cobalt matrix microstructures (HV10=Vickers hardness;  $\sigma_y$ =yield strength;  $\sigma_u$ =ultimate strength;  $\epsilon_r$ =residual strain)[42]

Label	Grain size before sintering	Grain size after sintering	Porosity	Hardness	$\sigma_y$	$\sigma_u$	$\epsilon_r$
	[ $\mu\text{m}$ ]	[ $\mu\text{m}$ ]	[%]	[HV10]	[MPa]	[MPa]	%
CO6102	2	2.3	0.18	299	450	700	2
CO6101	1.5	2	0.20	308	650	825	1
CO7106	2	2,3	0.13	336	800	950	0.5

Replacing cobalt with iron does not affect the hardness of the sinters but leads to a considerable decrease in the material yield strength [36]. Also, at high fabrication temperature, the iron is dangerously reactive with diamonds due to the considerable solubility of carbon in austenite. However, moderate iron addition to cobalt improves its ductility. In addition to iron, copper, tin, pre-alloyed bronzes, tungsten, and tungsten carbides are used extensively as additives or partial substitutes of cobalt with the idea to aid the manufacturing process and to modify the matrix wear and retention characteristics [36].

Tungsten is one of the strongest and most rigid materials with a strong atomic bonding affinity for carbon, resulting in a thin film of tungsten carbide at the interface between the tungsten and the diamond. It is also used to increase the matrix resistance to wear as the addition of

tungsten to the powder mixture increases the material hardness by 30%; while when tungsten is added to a mixture of cobalt and iron, the material hardness and yield strength increase to 40% and 45% respectively [43]. However, it makes the consolidation process more complicated since it requires high temperature and pressures, up to 980° and 50 MPa, respectively, to produce sintered with low porosity (< 5%).

Additives as pre-alloyed and premixed bronze powders, elemental copper, and tin usually assist the matrix densification but reduce wear resistance, thus rendering the tool more suitable for processing less abrasive materials.

### A.1.3 Diamonds

The main diamonds properties affecting the performance of the cutting process are the size, shape, and concentration.

Nowadays, synthetic diamonds have almost totally replaced the natural ones with an essential economic advantage. The major differences between natural and synthetic diamonds are the impurity contents and the particle shape. Natural grits are free from metallic inclusions, leading to high thermal stability, while the irregular surface topology gives rise to excellent bonding characteristics. On the other side, synthetic diamonds can be designed and manufactured to satisfy specific application requirements [36].

In addition to the previously introduced coating, the size must be controlled. It should be chosen as a function of the particular tool application as large diamonds protrude faster from the matrix, and allow faster ejection of the debris flow [35]. A 40/50 US mesh (400/297  $\mu\text{m}$ ) is generally used in circular sawing, drilling and milling of stone (granite, diorite, gabbro, less abrasive sandstone, limestone, dolomite, and marble), concrete and refractory materials, wire sawing of stone and construction materials, calibrating of stone slabs [36].

Finally, the number of diamonds in the segment is measured in terms of concentration: at the concentration 100 corresponds to 4.4 carat·cm<sup>-3</sup> ([100] = 4.4 carat·cm<sup>-3</sup>, equal to the 25 % vol.)<sup>2</sup>. The diamond concentration should be adequately chosen: the higher the abrasiveness of the workpiece, the larger the diamond concentration should be.

---

<sup>2</sup> 1 carat = 0.0002 kg



## A.2

# Wear of the matrix by abrasive particles

The wear of the matrix is related to the abrasiveness of debris grain detached from the workpiece. It is necessary to renew diamonds, but this wear rate must nevertheless be controlled: the matrix has to wear at a rate compatible with the diamond particle breakdown to attain an optimum balance between service life and free-cutting ability. For these reasons, the wear resistance of the matrix has to be adjusted to the wear speed of the diamonds: if the matrix is too soft, it wears too fast, and the diamond capacity is not completely used with a premature diamond pull-out; if it wears more slowly than diamonds then the slurry cannot be carried out correctly, and the segment will continuously lose the ability to cut.

The binder has a fundamental role in the performance of diamond tools. In particular, metal matrices are widely used for their high bond strength, good formability, and long service life [15]. The diamond retention capacity of the matrix strongly depends on its mechanical properties, i.e., Young's modulus, yield strength, toughness modulus, and material hardness. Fixing all the cutting operations (tool, cutting parameters, diamond specifications), the wear process to which the matrix is subjected during cutting depends not only on the matrix itself but also on the type of workpiece, the abrasiveness of the debris grains formed, the liquid used to carry them out and the debris ejection.

Several works have been done to study the holding of diamonds after the manufacturing process [14]–[16] and during the working conditions [17]. In contrast, the complexity of the processes and the important number of involved variables make it difficult to perform laboratory tests and wear modeling. The wear and breakdown of diamonds are documented in the literature [3], [44], [45], while the wear of the matrix is not clear.

To better understand the interactions involved in the wear process and how to model it, section A.2.1 introduces the definition of abrasive wear in a larger framework. Section A.2.2 gives the fundamental tribological concepts and numerical tools already developed in the literature to solve wear problems and how they can be used as starting points for building the strategy proposed in Chapter A.3. Looking into more details at the abrasion process, section A.2.3 deals with properties of abrasive particles, while A.2.4 is about the resistance of contacting surface (i.e., the metal matrix in this case of study). In the end, section A.2.5 analyzes the effect of diamonds on the wear process in the particular case of DIT.

## A.2.1 Classification of wear

Wear is not a material property but the response of the system under certain contacting conditions [6], [46]. The wear rate can change in a wide range depending on contact conditions (i.e., contacting materials, contact pressure and sliding velocity, the shape of abrasives, environmental conditions, lubricant properties, etc.) [6], thus makes the wear description and prediction a challenging study. Wear can occur in different types, which can also play simultaneously:

- i. Adhesive wear;
- ii. Abrasive wear;
- iii. Fatigue wear;
- iv. Corrosive wear.

Adhesive and abrasive wear are caused by plastic contact. Adhesive wear occurs when two solid surfaces slide over each other and there is enough adhesive bonding at the interface. This kind of wear is related to strong plastic deformations in the contact region defined by the asperity-asperity contact and causing crack initialization and propagation and is generally estimated in terms of wear volume  $V_{ad}$  by the Archard Equation [27]:

$$V_{ad} = \frac{K_{ad}F_n}{H}s \quad (A.2)$$

Where  $F_n$  is the applied normal load,  $s$  is the sliding distance,  $H$  is the material hardness and  $K_{ad}$  is named Archard coefficient, introduced to accommodate several aspects such as the probability of wear particle generation, the size of the wear particle to the size of the contact, microstructure of the material in the contact zone [46]. The ratio  $\frac{K_{ad}}{H}$  is generally named specific wear rate  $k_w$  :

$$k_w = \frac{K_{ad}}{H} \quad (A.3)$$

and is measured in  $mm^3N^{-1}m^{-1}$ .

Assuming frictional forces proportional to the normal load by the friction coefficient  $\mu$  ( $F_t = \mu F_n$ ), wear can be defined in terms of frictional work expended per unit volume  $V$  of material removed:

$$E_f = \frac{\mu F_n s}{V} = \frac{\mu}{k_w} \quad (A.4)$$

The energetic approach assumes that the wear volume  $V$  is proportional to the frictional forces too [47]:

$$V \propto F_t s$$

This energetic approach is introduced by Fouvry and co-workers [48], [49] as a more stable quantification of the wear response of fretting. However, it is based on the same assumptions and parameters of the Archard equation.

One limitation of Eq. (A.2) is that the specific wear rate needs to be evaluated by specific experimental tests and is strictly dependent on the parameters defined. The same wear equation -Eq.(A.2)- can be obtained starting from different assumptions for abrasive wear [7], which occurs if there is a hard material indenting a surface [50]. The abrasive wear will be introduced in section A.2.4.

The other two wear mechanisms (i.e., the fatigue wear and the corrosive wear) can happen both in elastic and plastic contact. The fatigue wear mode consists of removing material by cyclic loading due to the continuous passage of abrasive particles causing the plastic flow accumulation at the surface [5]. Corrosive wear is mostly due to chemical reactions generally activated by frictional deformation [46], [51]. Adhesive, abrasive, and fatigue wear are generally defined as mechanical wear since they manifest as ductile, brittle, or fatigue fracture on the surface induced by stress and strain [46].

This work deals with the abrasive and fatigue wear process since debris grains are harder than the matrix surface and, even carrying a small load, they can indent the material (abrasive wear) under repeated cycles of contact (fatigue wear). As introduced in Chapter A.1, the matrix microstructure is a polycrystalline material with well-defined mechanical properties. However, it is characterized by grain boundaries and inclusions that are preferential zones for stress localization and accumulation, defining the fatigue fracture.

The remainder of this chapter introduces the conceptual tools for wear modeling and enters into more detail on the wear process involved in this study.

## A.2.2 Conceptual tools for abrasive wear

As introduced before, this work deals with abrasive wear characterized by abrasive particles free to slide and roll between two sliding surfaces and defining the “third body” of the tribosystem. The third body concept was introduced by Maurice Godet [52] as a transposition of the lubrication theory to the dry contact between two solid surfaces. In the lubrication theory, it is a fluid, while in dry contact, it consists of a set of solid particles of different shapes and sizes. In any case, the third body is an operator working to support the load applied to the contact and separating the two first bodies, thereby limiting their direct contact [53].

In this framework, the diamond indentation within the workpiece is the first stage of wear and is an example of two-body wear (i.e., diamond-workpiece contact), leading to the wear of the workpiece and the chip formation. Then, debris grains circulate between the matrix surface and the workpiece defining the third body of the system, able to abrade the metallic surface (three-body wear), as illustrated in Fig. A-3.

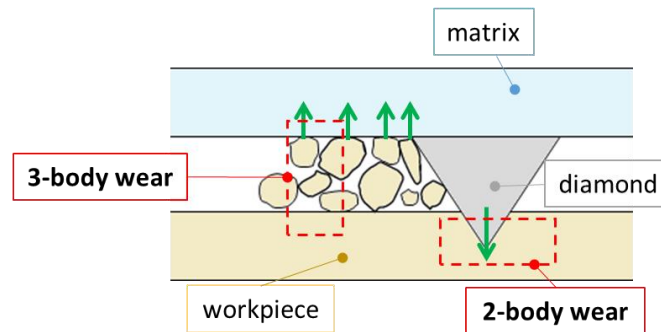


Fig. A-3 Simplified schema of the contact and the wear

According to the third body concept, the tribological circuit was first introduced by Berthier [18] as a useful tool to establish the mass balance within the contact and to analyze wear. Based on this model, as both the metallic surface and the workpiece are degradable materials, detached particles from the two surfaces define the internal source flow  $Q^s$  of the tribological circuit. Then, particles can be ejected from the system characterizing the ejection flow  $Q^e$ . Defining wear no longer as the loss of mass from one material but as the loss of mass from the whole contact [18], the wear flow  $Q^w$  is the amount of particles of  $Q^e$  that definitely leave the system, while the remaining part of  $Q^e$  defines the recirculation flow  $Q^r$  and is reintroduced in the system. Considering the mass equilibrium of the system, the amount of particles  $M$  of the third body per unit time ( $dM/dt$ ) should be equal to the difference  $Q^s - Q^w$  [22]. The adaptation of the tribological circuit to the case of study is illustrated in Fig. A-4.

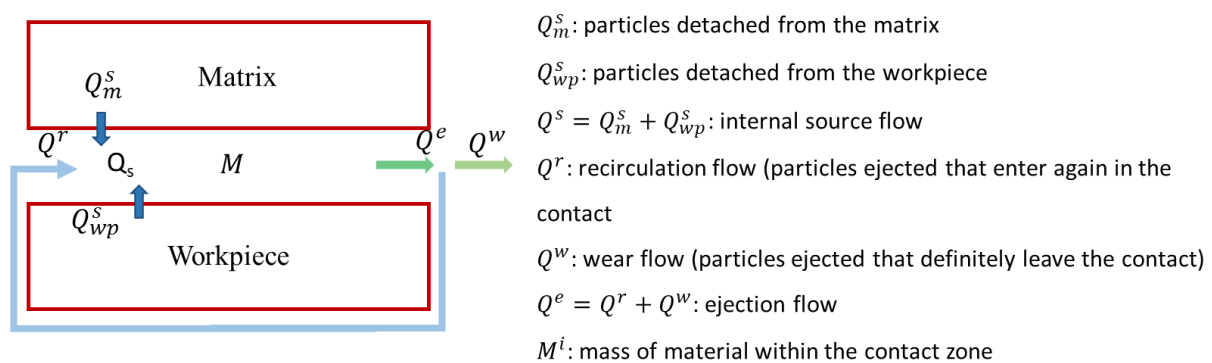


Fig. A-4 The tribological circuit in the contact matrix-workpiece

In the optimum cutting conditions, the workpiece wears faster than the metallic surface, such that particle detached from the workpiece  $Q_{wp}^s$  are present in a larger quantity than the particles detached from the matrix  $Q_m^s$ . Also, after the diamond indentation into the workpiece,

debris grains from the workpiece are continuously renewed during the cutting process, such that each ejected particle is immediately replaced by new particle detachment and by the recirculation flow. This means that a steady state is reached fast ( $Q_{wp}^S = Q_{wp}^W$ ) and the total mass of the third body inside the contact remains almost constant [22], [23]. This equilibrium is also guaranteed to the tail formed behind the diamond giving the right support.

For these reasons, the wear of the matrix does not depend on the metallic grains themselves but is only due to the slurry, which characterizes the third-body of our tribosystem and whose grains have strong abrasive power.

### A.2.3 Properties of the abrasive particles

During the processing of rocks and concretes, the load is almost fully transferred from the machine to diamonds to indent the material, guaranteeing a long life to the metallic surface. However, grains detached from the workpiece have strong abrasive power because of the intrinsic properties of the processed material and the imposed operation conditions. The characteristic hardness, shape, and size of debris grains play a key role in the abrasion of the surface; while interacting with the water coolant in the process, debris grains form the slurry, whose rheological properties are those of a complex fluid.

#### *Particle hardness*

Rock properties play a key role in the abrasive capacity of debris particles, defining the working condition of the tool [54].

The hardness of rocks depends on the size, shape, and amount of different mineral constituents and the bond strength between mineral grains. The 2-body wear is mostly controlled by the porosity and the consequent brittleness of the rock, while the content of hard minerals is the predominant factor of abrasive wear in 3-body conditions [55]. Silicate minerals are generally more abrasive than the others [54]. Marble, granite, concrete, and reinforced concrete behave differently during processing [56]; therefore, while the cutting of hard rocks (e.g., marble and granite) is controlled by the diamond fracture and pull-out, in soft materials as sandstone and porous ceramics, the wear resistance of the matrix is the main character responsible for the tool life. This explains why the cutting and wear process is related to the nature and fracturing of the workpiece.

It is worth noting that, whatever is the type of rock processed, it is always harder than the matrix surface, otherwise the matrix will be unable to retain diamonds, reducing the life of the tool. Particles with hardness lower than that of the surface cause much less wear than harder particles [55]; while for particles significantly harder than the surface, the exact value of their hardness matters much less [7].

*Particle shape and size*

The mineral composition and the cutting conditions affect the size and shape of debris particles, defining their abrasive power.

The particle size effect denotes the increase of the wear rate with the average grain size up to a critical value [7], [57], [58] that is often about 100  $\mu\text{m}$  [9]. Several explanations are given in the literature to describe this phenomenon. According to the Larsen-Badse theory [59], the small grains only have elastic interactions with the surface without any material removal contributions. Misra & Finnie [9] defined a hard surface layer responsible for the size effect since small particles lead to shallow penetration while large abrasive particles are able to wear through that layer.

Another important aspect to consider is the role of the shape in the particle size effect, as the pattern of the deformation caused by the particle depends on its depth of indentation into the surface [7], [10].

The shape of abrasives depends on the properties of the original material (i.e., the mineral composition) and how they are carried away (freshly fractured material generates abrasives with several cutting edges). This, in turn, affects the wear rate since angular particles cause more significant wear than rounded particles [7], [60], [61]. However, it is not easy to identify the shape of irregular particles and relate it to wear. A widely used parameter is the roundness factor or circularity  $RF$  defined as the ratio between the actual area of the 2D projection and the area of a circle with the same parameter  $RF$  as the projection. Departing from  $RF = 1$ , such a parameter gives a measure of the deviation of the particle from a sphere. Abrasive wear rate has been easily correlated with the roundness factor. Although it can be computed quickly, it does not consider the sharpness of the corners of the particle, giving only a global description of the shape.

Different methods are proposed in the literature to describe the sharpness of a particle [60], [62], [63] and correlate it to abrasive wear. A sharp grain is expected to penetrate more into the material surface, causing more wear. To explain this phenomenon, Woldman and co-workers [63] attempted to extract a local parameter (sharpness) based on a visual inspection and correlate it to the specific wear rate  $k_w$  calculated according to the Archard formulation [27]. They observed that the wear rate increases with sharpness but that the sharpness parameter is not a sufficient indicator as the combination of size and shape might be considered.

*Flow properties of the slurry*

Using water as a coolant facilitates the grains ejection from the system in core drilling application, improving the cutting performance. Debris grains together with water form a slurry. The slurry can be defined in terms of mass ratio water/debris or solid fraction  $SF$ , and

it is able to flow within the contact zone, exercising pressure to the matrix surface as a function of its rheology and initial clearance. The debris flow rheology depends on the aforementioned solid fraction: higher contents of debris grains lead to more viscous slurries and higher contact pressure and abrasive power of debris grains. The relation between the solid fraction and the viscosity was described quantitatively by [64]. For a viscous slurry, the rotation of grains is negligible due to their interlocking and angular shape, causing a slip velocity in contact with the matrix surface with a strong influence on the wear rate.

### A.2.4 Matrix resistance to abrasive wear

The wear of the matrix involves removing the material by plastic deformation caused by the continuous passage of debris grains.

The simplest model to describe abrasive sliding wear is the Archard equation defined as in Eq. (A.2) for adhesive wear. One limitation of Eq. (A.2) is that the specific wear rate needs to be evaluated by specific experimental tests. Moreover, the wear rate should be inversely proportional to hardness  $H$ . In other words, the hardness of the material is an indicator of the material resistance. As explained in the previous section, wear occurs only if the matrix surface is softer than the abrasive particles in contact; however, during the wear process, the surface undergoes several plastic deformations that might lead to a strain-hardening, and therefore, the material hardness might be different from the bulk hardness [7][5]. The definition of material hardness will be discussed in Part B in writing the wear equation.

Another problem with the Archard model is that all the material displaced is ejected from the contact. However, in practice, particles can deform the surface differently as a function of their shape and size, leading to removing only part of the material displaced from the groove or even removing no material at all [7]. In three-body abrasion, only a small proportion of abrasives cause wear, depending on their angle of attack on the surface [4]. Three main abrasive wear modes can be observed [4]–[6] (Fig.A-5):

- i. Microploughing: No material is removed from the surface, but it flows down beneath the abrasive particles. A plow is formed ahead of the abrading particle, and material is continually displaced, forming ridges on the side of the groove. Ploughing can occur during the passage of many abrasive particles acting simultaneously or successively.
- ii. Micro-cutting: All the material displaced by abrasive particles is removed and flows up the front face of the particle.
- iii. Micro-cracking: Highly concentrated stresses are imposed by abrasive particles. Grains are detached from the surface due to crack formation and propagation.

The repeated displacing of material by ploughing may lead to the wear and breakdown of the material by fatigue. A three-dimensional representation of the wear modes is illustrated in Fig. A-5. Another important form of wear caused by hard particles is erosion. Here abrasive particles strike the softer surface resulting in plastic deformations, which manifest as small craters on the surface [7][8].

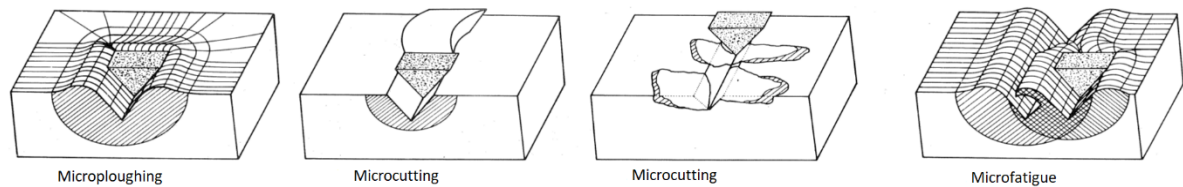


Fig. A-5 Abrasive wear modes [4]

A specific model for abrasion accounting for the abrasive wear modes was proposed by Hokkirigawa and co-workers [65] [6], considering the scratching of an asperity on the surface. This model has the same form of the Archard law where the wear volume  $V_{ab}$  is proportional to the normal load  $F_n$ , the sliding distance  $s$  and inversely proportional to the hardness  $H$  of the material surface. Instead of the coefficient  $K_{ab}$  two main parameters ( $\alpha_1$  and  $\alpha_2$ ) need to be defined) :

$$V_{ab} = \alpha_1 \alpha_2 \frac{F_n s}{H} \quad (A.5)$$

$\alpha_1$  is a shape factor of the asperity (experimentally test to 0.1 [6]), and  $\alpha_2$  is the degree of wear with values varying from 0.1 to 1 as a function of the mechanical properties and the shear strength of the wearing material  $f$ , and the angle of attack  $\theta$  of the abrasive particles [6]. The critical angle of attack describes the severity of wear and the transition between the microploughing and the micro-cutting. For high values of attack angle and shear strength  $f$  (defined as the ratio between the shear stress and the shear yield stress of the plastically deforming material), the transition from ploughing to cutting occurs passing from the micro-cracking that can be seen as an intermediate wear mode between the two formers [66].

Eq. (A.5) well describes the abrasive wear, but it is still related to the experimental test. The definition of parameters  $\alpha_1$  and  $\alpha_2$  may be not so evident at the scale of the industrial application where different wear zones can be defined and all the wear modes described may occur simultaneously and in different proportions as a function of the cutting conditions, the pressure generated during processing, and the reciprocal position of diamonds.

## A.2.5 Effect of diamonds

The diamond protrusion above the matrix is not only a necessary process to optimize the cutting condition but is also needed to protect the matrix from direct contact with the workpiece by developing the clearance space between them.

During the cutting operation, the load is fully transferred from the machine to the diamonds to cut the workpiece. The various cutting tools (circular sawing, frame sawing and core drill) are different in terms of force and velocity applied on the segments as each particular tool needs the right combination of normal load and feed velocity to achieve the best cutting ability and working conditions.

### *Effect of diamonds in circular sawing*

In circular sawing, the blade rotates in a constant direction at high peripheral speed ( $v_{tool} > 25 \text{ m/s}$ ) in the upwards or downwards direction: in down cutting, the maximum depth of cut  $h_{saw}$  is reached at the beginning of the contact; while in up cutting, the chip thickness increases from zero to the maximum at the end of the contact. The relative orientation of the resultant cutting force  $F_{saw}$  is different in the two cases, as illustrated in Fig. A-6.

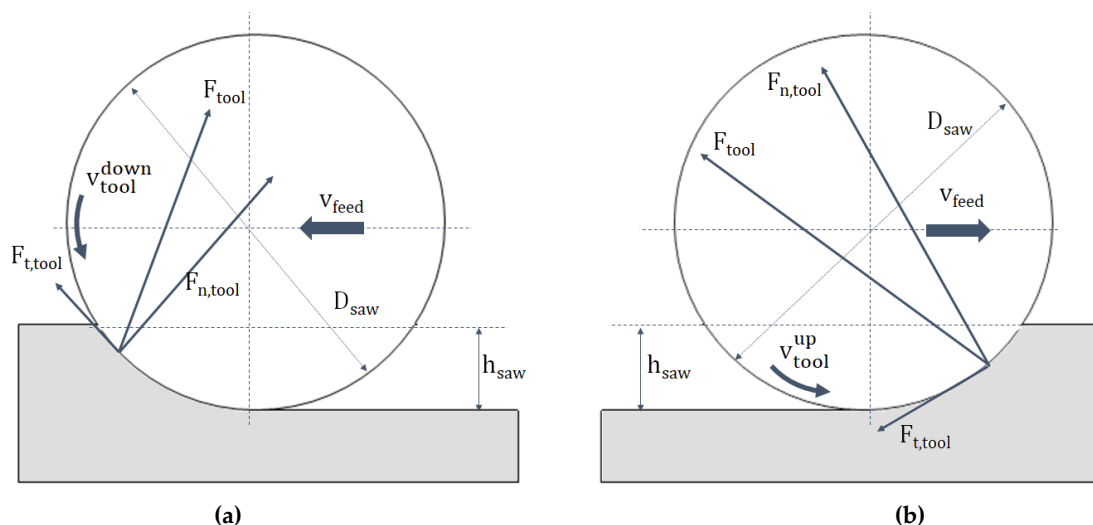


Fig. A-6 Kinematic process of circular sawing in (a) down cutting mode and (b) up cutting mode ( $v_{tool}$  = peripheral speed;  $v_{feed}$  = feed rate,  $F_{n,tool}$  = normal load;  $F_{t,tool}$  = tangential load;  $h_{saw}$  = depth of cut), inspired by [1]

The cutting mode has a strong influence in terms of the rate of material removal. Whatever the process kinematics, it will always lead to the development of a tail of matrix behind each diamond acting as a support during cutting, and a sort of crater in front of it, defined by the protrusion height of the diamond [67] (Fig. A-7).

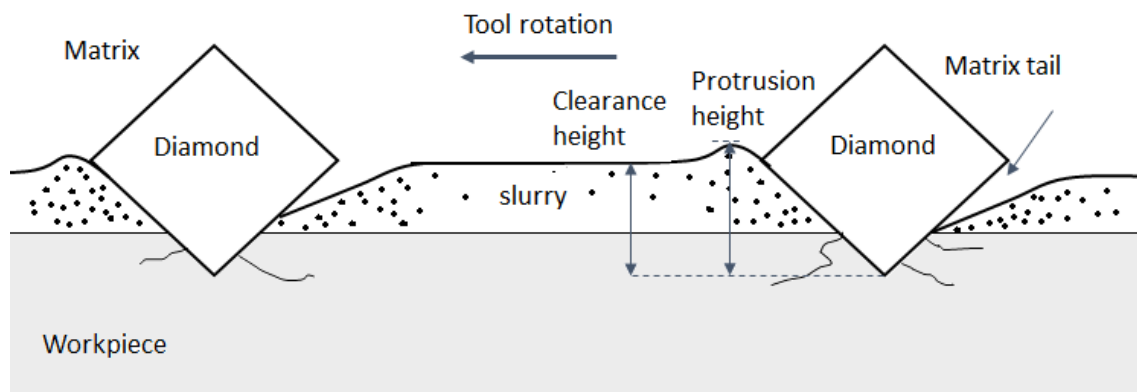


Fig. A-7 Schematic representation of interactions between the saw and the workpiece during the circular sawing operation (inspired by [1])

### *Effect of diamonds in frame sawing*

In frame sawing, the blade is subjected to a reciprocal sawing action at slow sinusoidal speed with a maximum of around 2 m/s.

These conditions make difficult the removal of debris grains and creates severe wear conditions for the matrix leading to a premature diamond pull-out since there is no build-up of matrix tail and forces act on diamond particles in alternate directions [1], [67] (Fig. A-8)

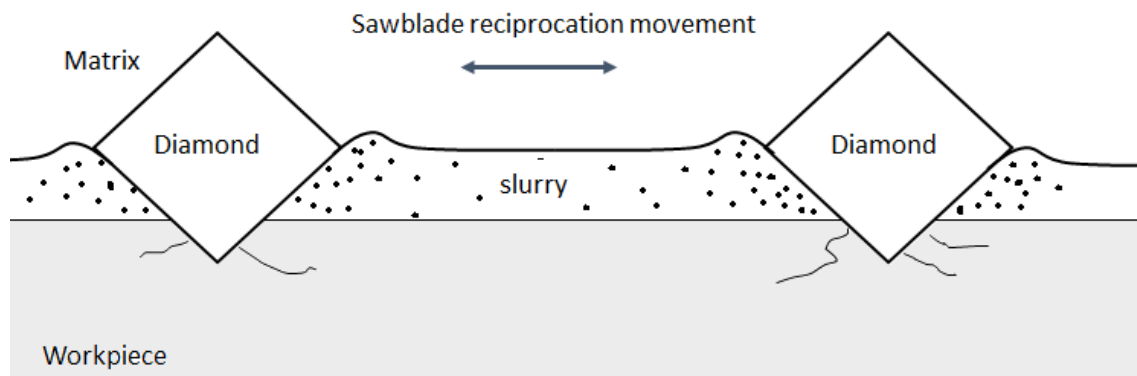


Fig. A-8 Schematic representation of interactions between the saw and the workpiece during the frame sawing operation (inspired by [1])

### *Effect of diamonds in core drill*

In a core drill, the tool is subjected to low and constant peripheral speed ( $v_{tool} = 1 - 10 \text{ m/s}$ ) and a high normal load that is fully transmitted to diamonds. Cutting is performed with a constant direction of rotation. Although the kinematic conditions of chip formation are relatively simple compared to those observed in sawing techniques, the wear process of the matrix is almost the same as observed in circular sawing (Fig. A-9)

The comparison between surface topographies after sawing and core drill is illustrated in Fig. A-9 together with the schematization of the two cutting tools.

The drilling and sawing operations are always performed while pumping a fluid (usually water) to cool the system and eject debris grains through the space between the segments. In both cases, the constant cutting direction allows the formation of a matrix tail behind the diamond protected by the diamond itself, and the surface is struck by the debris grains showing only signs of erosion and no wear by abrasion.

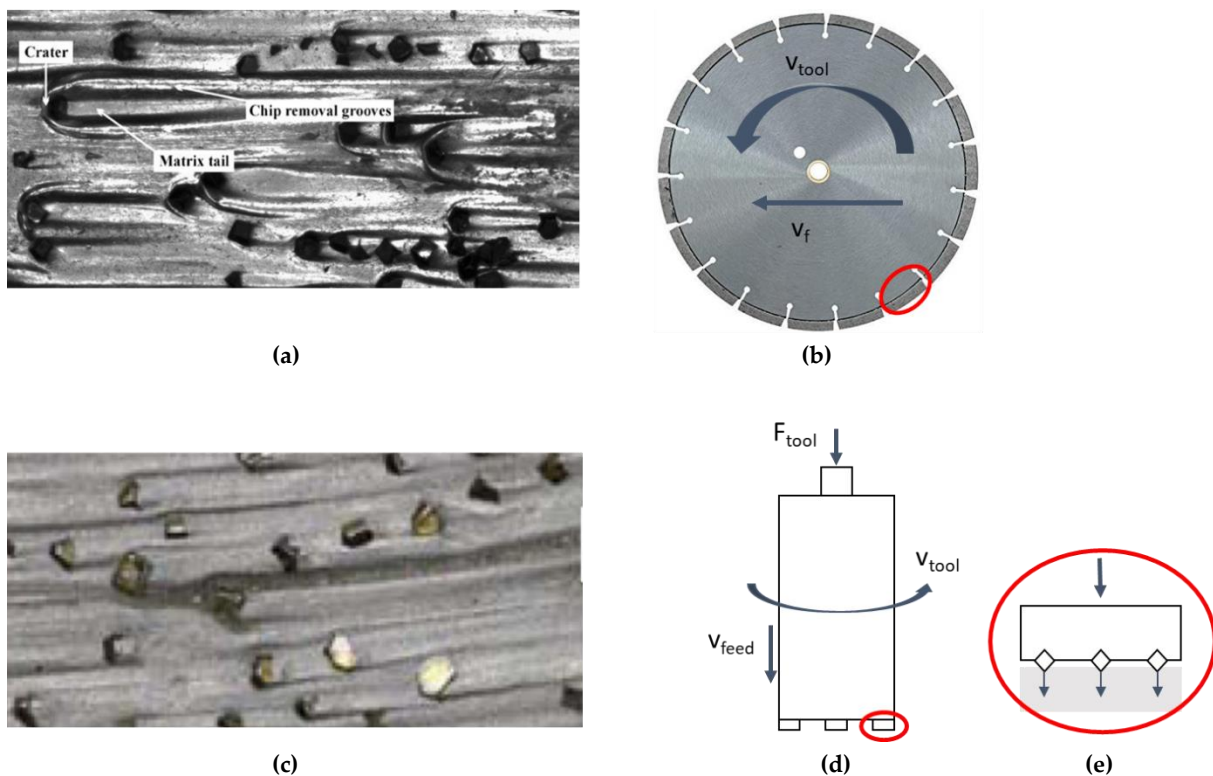


Fig. A-9 (a) Surface topography of a segment after sawing [1]; (b) example of circular sawing); (c) surface segment topography after drilling [2]; (d) sketch of a drilling machine; (e) sketch of a particular segment

### *Effect of diamond distribution*

The diamond distribution is another important aspect affecting the wear of the matrix. Wright and co-workers [3] observed experimentally that protrusion height might change if the diamond is shielded or not by other diamonds present on the interface. Diamond 1 in Fig. A-10 is shielded by two diamonds in front of it. The lateral debris flow of one of them ends at the right-hand side of Diamond 1, while the left-hand side is covered by the closer one. This evidence results in relatively slow wear of protrusion as the diamond is protected. Diamond 2 in Fig. A-10 is fully exposed; therefore, the peak of the height of the protrusion is reached faster with earlier breakdown than diamond 1.

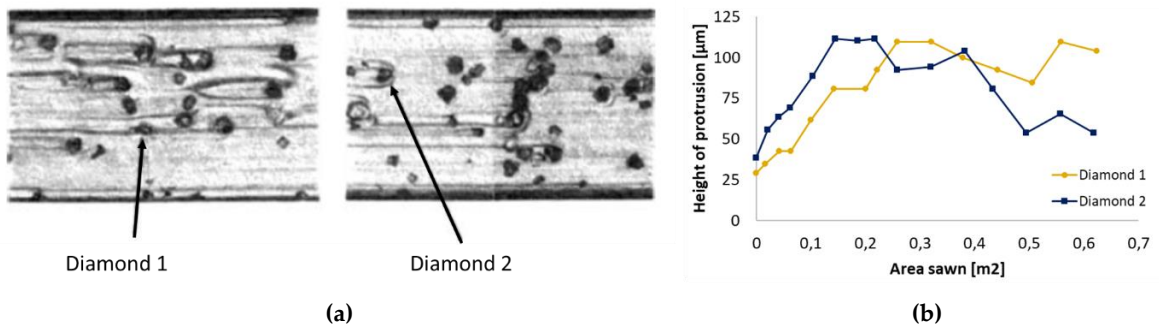


Fig. A- 10 (a) Surface of the segment after sawing 44 mm<sup>2</sup>; (b) height of protrusion vs. cumulative area sawn (from [3])

## A.3

# Conclusions and development of a strategy

The wear of the matrix surface described in Chapter A.2 falls within interaction and contact problems between surfaces described briefly in Section A.2.2.

This chapter outlines the key points of the wear of the matrix (Section A.3.1). It also introduces an experimental-numerical multiscale strategy (Section A.3.2) starting from what is already done in literature in the framework of wear, ruling out the alternatives, and defining an innovative and integrated experimental-numerical approach.

### A.3.1 Preliminary conclusions

The particular diamond-debris-matrix interaction is responsible for the complex wear mechanisms of the matrix surface. Such a wear process of the metallic surface depends on several aspects as:

- i. rock type: marble, granite, concrete, and reinforced concrete behave differently during processing and generate a debris flow with different properties in terms of grain size (the wear rate increases with particle size until a critical value is reached, above which the wear rate seems to be independent of the grain size); particle shape (freshly fractured material generates abrasives with several cutting edges able to wear faster); mineral composition and hardness (soft minerals induce slower wear mechanisms, e.g., thermal fatigue and oxidation), and cleavage properties (resistance to fragmentation)
- ii. Segment specifications: the number and surface of the segment (at the scale of the tool), the diamond concentration (number and size of diamonds at the scale of the segment), and the matrix microstructural properties (at the scale of the matrix). In particular, at the scale of the segment, it was seen experimentally that the presence of the other diamonds influences wear around one single diamond; a close diamond may offer protection and reduce the rate of the protrusion while, when the same diamond is not shielded by another one, it is fully exposed to wear. Regarding the microstructure of the matrix, wear strongly depends on its material hardness.

- iii. Operational parameters: feed rate, peripheral speed, force applied, and cooling efficiency (i.e., coolant type and flowrate) [38]. In particular, the processed rock and the used coolant exert control on the slurry rheological properties.

Several studies have been done to analyze, at least qualitatively, the wear of the surface in terms of diamond retention after the manufacturing process [14]–[16] and during the working conditions [17] while mechanisms involved in the matrix wear are not yet well understood.

In the abrasive wear framework, Siniawski et al. [68] defined a simple wear law to describe the kinetics for the abrasion for different material pairs based on pin-on-disk experiments. Bull and Rickerby [69] proposed a model for abrasive wear based on the multi-pass scratch test. The scratch test is nowadays widely used to determine the wear resistance of the surfaces [70]–[72]. Several attempts have been made to correlate the abrasive wear to the properties of the abrasive particles (shape and size) [9]–[13]. Woldman et al. [72] proposed a method for predicting abrasive wear rate and understanding the wear process of machining components operating in sandy conditions. However, in all of these cases, the wear process takes place in a controlled environment, and models are strictly related to the reproduced experimental test.

### A.3.2 Development of a strategy

Despite the differences in terms of the chip formation kinematics, the wear process involved in core drill and circular sawing is almost the same (Fig.A-9). In both cases, the diamond remains in a quasi-continuous contact with the workpiece material, leading to the development of a matrix tail behind each diamond and a sort of crater in front of it. Therefore, the most evident experimental protocol for wear observation and quantification consists of non-destructive observations obtained from the core drill, which is simpler than the sawing in terms of cutting operation. This test is useful for understanding the wear process and is the core of the multiscale experimental-numerical strategy proposed hereafter and illustrated in Fig. A-11. This strategy consists of two main models:

- i) The macroscopic model
- ii) The mesoscopic model (based on a calibration at the microscale)

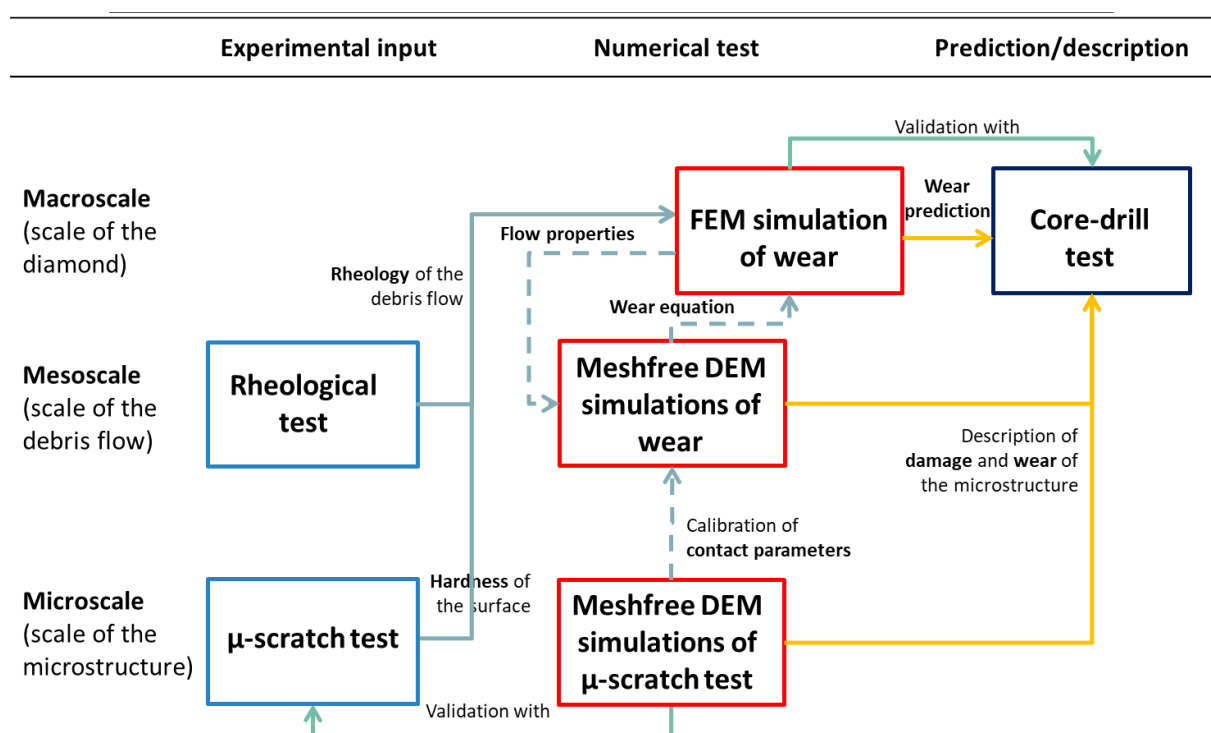


Fig. A-11 Main strategy used for the wear analysis (dot lines are the perspectives of the strategy)

The advantage of running simulations is the possibility to understand mechanisms that cannot be observed experimentally and to predict the wear behavior (under certain well-defined conditions) of new materials without going through experimental tests, thereby reducing development costs. This latter objective can be achieved after the model has been validated with known experimental results.

In the framework of cutting tools, the impossibility of considering all of the aspects involved requires a numerical study able to simplify the real phenomena. Zhou and co-workers [73] studied the behavior of diamond bits under drilling conditions but without considering the damage and failure; Li and co-workers [74] modeled the plastic deformation and residual stress close to diamond during the sintering process. More attention to the wear process is paid by Suh and co-workers [75], who studied the matrix wear with respect to the diamond without considering the debris flow properties on the wear process. At a smaller scale, Xu and co-workers [76] proposed a model to describe the failure mechanism at the diamond-matrix interface in diamond bits during failure and diamond pull-out. Other models are based on mathematical and statistical multiple regressions to analyze the influence of rock properties on the matrix wear rate [54]. These models describe aspects of the wear process and cannot predict wear at the scale of diamond tools.

Notice that the multiscale nature of the problem makes it difficult to model all the features within an individual numerical model. Therefore, the wear process is analyzed here with two

different models looking at two different scales: the macroscopic scale (scale of the diamond) and the mesoscopic scale (scale of debris grains).

The former is a predictive model based on the experimental observation, while the second is a descriptive model for the understanding of local phenomena. The two models give complementary information.

#### *A.3.2.1 The macroscopic model for the multiscale wear analysis at the scale of diamonds*

The macroscopic model accounts for a realistic macroscopic 3D geometry with a reasonable computational cost and a good transferability.

The model built at the scale of the diamonds looks at the same scale as the industrial application giving qualitative and quantitative knowledge about the wear resistance of the matrix and treating the slurry as a continuum described by its rheological law.

The continuum approach has been proved to be valid in solid lubrication [77], [78], where analogies with fluid mechanics and mass, momentum, and energy conservation are guaranteed. Indeed, FEs (Finite Elements) are routinely used to solve numerically Hydrodynamic (HD) or Elasto-HydroDynamic (EHD) contact problems [79] using the Reynolds equation [26]. The advantage is that the third body's pressure profile can be characterized easily as a function of the rheology and the thickness profile, while the wear is usually controlled by an Archard-type wear law [27].

However, the impossibility to extract information on the flow property of the third body from such industrial application and the complex tribological interactions involved need to define a modeling strategy based on an experimental/numerical coupling.

The viscosity of the slurry influences the flow properties, which are the leading causes of the wear process, and for that reason, rheological tests are performed on the third body flow.

In most cases, the third body responsible for wearing a contacting material surface is characterized by particles detached from the degradable surface itself; therefore, its rheology is unknown. However, in this particular case of study, the wear of the metal matrix is caused mostly by the debris grains detached from the workpiece and not by the metallic grains themselves. This evidence allows us to consider the slurry as an artificial third body, analyze its rheology experimentally and independently, and introduce it in the model.

The mechanical properties of the matrix offer resistance to the wear process. Again, the core-drill test cannot separate the effects that cause or oppose the wear process and quantify them, and it is not easy to place some devices measuring such features. Therefore, additional data about the resistance to abrasion of the metallic microstructure is obtained by a multipass

scratch test. The scratch test is widely used to determine the wear resistance [70]–[72]; moreover, performing several scratches in the same directions is representative of the continuous passage of debris grains.

Such a model's limitations consist of the impossibility of understanding local phenomena. It considerably simplifies the micromechanical mechanisms involved in the degradation of the microstructure at the scale of grains and does not consider the heterogeneity and the discontinuity of the third body. For this purpose, a complementary model is necessary.

#### *A.3.2.2 The mesoscopic model for the local wear analysis*

Local wear is often studied by DEM (Discrete Elements Methods) [80]. This approach has been used to model the degradation of the first body ([21]–[23]), and the flow of matter at the interface between continuous first bodies [81]. However, it is limited in treating both the degradable material and the third body as a collection of rigid and spherical grains.

The current trend consists of coupling discrete methods with finite elements [82] or meshfree technique [19], [20] to perform multiscale modeling.

The key purpose is to borrow from continuous modeling the idea of user-defined stress–strains relations implemented at the grain scale but retaining the idea of a discrete description of the material grains interacting through contact [19]. The classical equations of continuum mechanics are solved using a weak formulation as in a typical FEM code, including geometric nonlinearities and inertial terms [20].

The meshfree technique is a recent alternative to FEM [24] with the advantage of handling complex geometry and deformable bodies involving large plastic deformation where the connectivity of the mesh can be difficult to maintain without introducing error into the simulation.

The model discussed here is built using an innovative multibody meshfree technique coupled with a Discrete Element Method (DEM) approach [20]. The code is currently limited to 2D plane-strain problems. In this approach, each grain can be a rigid or deformable body. The displacement field is interpolated on the domain of each of them using a meshfree description based on a certain number of field nodes with two degrees of freedom in displacement each. The degradable microstructure and debris grains properties are generated by controlling their real shape and size distribution, overcoming the limitation of the traditional discrete approaches.

### *A.3.2.3 Towards a fully numerical multiscale approach*

Simulations at the mesoscale involve a large number of grains and deformable bodies, requiring considerable computation time and the determination of several physical parameters.

The parameters involved in the contact law between grains of the microstructure require a preliminary calibration. A simple way to do it consists of running numerical simulations of the  $\mu$ -scratch test, where the microstructure is abraded by a spherical tip. In both cases (i.e., numerical scratch test and mesoscale model), the matrix is generated controlling the grain size distribution and obeying the same contact law. This procedure allows the direct comparison between experimental and numerical results, defining the main strength parameter of the cohesive intergranular contact law that can be used for the mesoscale model.

Then, a challenging problem will be the writing of the wear equation from the mesoscale numerical model implementing all the micromechanical features (fatigue wear, roughness, damage, ...) involved in the wear process.

---

## **PART B**

# **Wear prediction at the macroscopic scale**

---



## Part B.

# Wear prediction at the macroscopic scale

This part analyzes the problem at the macroscopic scale (i.e., the scale of the diamond) using a continuum approach.

The first chapter introduces the experimental-numerical strategy describing the independent experimental set-up and introducing the finite element strategy that is the focus of the subsequent chapters.

Chapter 2 is dedicated to solving the Reynolds equation taking into account the experimental rheological results. Chapter 3 describes the wear modeling at the continuum scale and the coupling with the Reynolds equation. The wear equation is inspired by an Archard formulation and considers the results obtained performing the  $\mu$ -scratch test, described in Chapter 1. Then, in chapter 4, the numerical results of wear are discussed and compared with the experimental ones at the diamond scale.



## B.1

# Experimental-numerical strategy at the macroscale and preliminary experimental inputs

As explained in Part A, the wear of the matrix is a complex multiscale problem. Despite the difficulty accessing the microstructure scale, the wear can be measured experimentally by a core-drill test in terms of the depth of material removed in time (or sliding distance) at the diamond scale. This approach gives a qualitative and quantitative description of the performance of a microstructure used as the binder of the tool under well-defined operating conditions.

However, these observations are not sufficient for a good understanding of the wear process. Therefore, a numerical model is built at the same diamond scale and is validated with the aforementioned experimental evidence. This model deals with solving a wear equation as a function of the local pressure and velocity fields acting on the matrix surface. The influence of these flow properties of the slurry explains why the wear processes become more important in front of the diamond and in its proximity (where the product between the pressure and the velocity is maximum). The simple and efficient way to compute them is the Reynolds equation.

Complementary information that is not accessible by the core drill is obtained by performing a rheological test and a multiscale study that considers the experimental evidence of wear from the  $\mu$ -scratch test and the abrasiveness of debris grains. Therefore the overall experimental set-up consists of:

- i) the rheological test, performed on debris grains detached from the workpiece and that define the third body of the system
- ii) the  $\mu$ -scratch test, performed on the metal microstructure used as the matrix in cutting tools
- iii) the core drill test used to evaluate the performance of cutting tools at the industrial scale

The main experimental-numerical strategy is illustrated in Fig. B-1. The rheological test and the  $\mu$ -scratch test are presented in section B.1.1 and section B.1.2, respectively. The core drill

test, already introduced in Part A, will be discussed in detail in section B.4 considering the experiments performed by Umicore<sup>3</sup>.

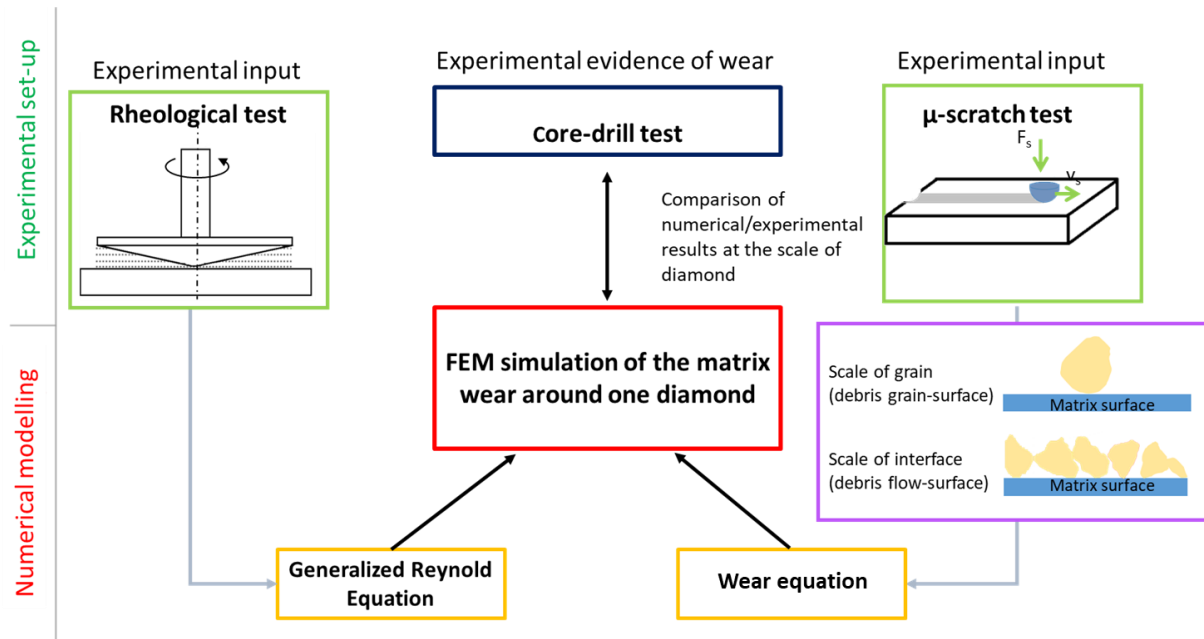


Fig. B-1 The workflow of the strategy

### B.1.1 Experimental observation of the third body flow

Debris grains extracted from the machine after the cutting process are mixed with water to obtain a slurry representative of the one formed with the coolant during the drilling operation. Fig. B-2 shows a micrograph of debris grains of concrete and their particle size distribution. Grains are more or less angular, with 90% of the population between 1  $\mu\text{m}$  and 100  $\mu\text{m}$ . The size distribution is bimodal with modes of 20  $\mu\text{m}$  and 2  $\mu\text{m}$  respectively, with a median value of 10  $\mu\text{m}$ , while the main grain size is 20  $\mu\text{m}$ .

Starting from this grain population, and considering only grains with grain size less than 100  $\mu\text{m}$ , three different slurries with different water content are prepared, which correspond to three different mass ratios debris/water: 50/50, 50/45, and 50/40; each sample is tested twice.

<sup>3</sup> Umicore Specialty Powder France

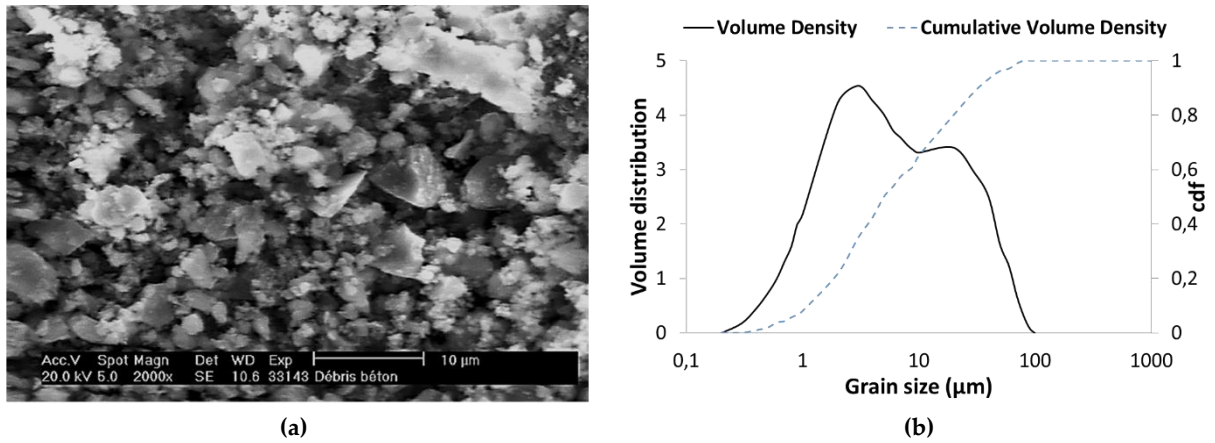


Fig. B-2 Debris grains description [42] (a) SEM micrograph of debris particles; (b) grain size distribution

The debris density is equal to  $\rho_d = 2650 \text{ kg/m}^3$ , therefore the amount of debris grains corresponding to the mass ratio debris/water is computed as:

$$SF = \frac{Vol_d}{Vol_d + Vol_w} \quad (B.1)$$

Where  $Vol_d$  and  $Vol_w$  are the volume occupied by the debris grains and the water respectively, obtained in terms of the ratio between the mass  $M$  and the density  $\rho$ :

$$Vol_d = \frac{M_d}{\rho_d}; \quad Vol_w = \frac{M_w}{\rho_w}$$

Where index  $d$  and  $w$  denote the debris and the water, respectively.

The debris/water mass ratio and the corresponding solid fraction SF are reported in Tab. B-1.

Tab. B-1 Concentration of slurries in terms of debris/water concentration (d/w) and volumetric solid fraction (FS)

	d/w	SF (vol. %)
<b>Slurry 1</b>	40/50	27
<b>Slurry 2</b>	45/50	30
<b>Slurry 3</b>	50/40	32

Then, once the sample is prepared and after shaking to re-suspend particles, the rheological test is performed using a flat cone-plate viscometer<sup>4</sup>, which consists of a flat plate and an inverted rotating cone, thermostatically kept at 25 °C. The slurry is placed in the gap between the cone and plate, as illustrated in Fig. B-3.

<sup>4</sup> RHEONIS Fluid Material Engineering

The angle of the cone  $\phi$  is small, and the rotational velocity  $\omega$  is constant. In those conditions, the shear rate  $\dot{\gamma}$  is uniform at all points in the fluid ( $\dot{\gamma} = \frac{\omega}{\phi}$ ).

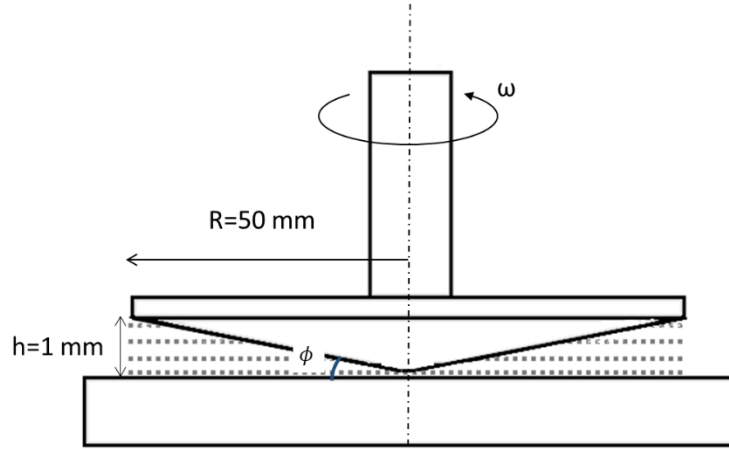


Fig. B-3 Cone and plate viscometer

The test is performed varying the shear rate  $\dot{\gamma}$  from  $0.1 \text{ s}^{-1}$  to  $2000 \text{ s}^{-1}$ , the shear stress  $\tau$  is obtained from the measurement of the corresponding torque  $T$  ( $\tau = \frac{3T}{2\pi R^3}$ , see Fig. B-3) and the apparent viscosity is computed as tangential viscosity in terms of :

$$\eta = \frac{\tau}{\dot{\gamma}} \quad (B.2)$$

Fig. B-4 plots the flow curves with the error bars for the three slurries in terms of shear stress  $\tau$  vs. shear rate  $\dot{\gamma}$  and apparent viscosity  $\eta = \frac{\tau}{\dot{\gamma}}$  vs. shear rate  $\dot{\gamma}$ , respectively. The first important evidence is that the viscosity increases with the solid fraction. This increase was attributed to the frictional forces between particles and the water occlusion [83].

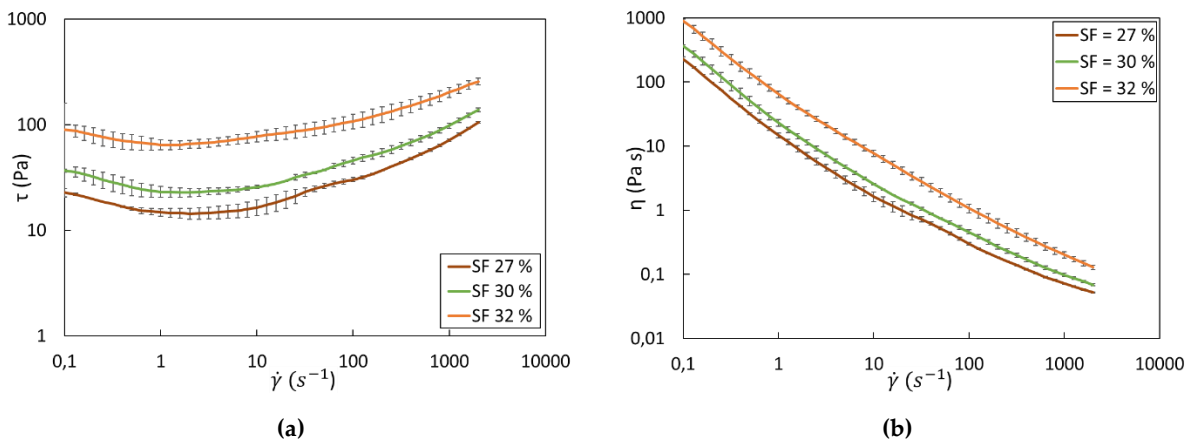


Fig. B-4 (a) Average flow curves in terms of shear stress  $\tau$  vs. shear rate  $\dot{\gamma}$ ; (b) apparent viscosity  $\eta$  vs. shear rate  $\dot{\gamma}$ . The error bars represent the variation of the two samples

A slight thixotropy is observed at the beginning of the test ( $\dot{\gamma} \leq 1 \text{ s}^{-1}$ ), that is due to the rearrangement of the particles in the volume leading to a slight decrease of shear stress with the increase of shear rate since a minimum is reached (equal to 65 Pa for FS = 32 %, 23 Pa for FS = 30 % and 15 Pa for FS = 27 %). Then, the increase of the shear stress with the shear rate being non-linear and in particular is typical of Bingham pseudoplastic fluids characterized by a shear-thinning behavior, i.e., the apparent viscosity ( $\eta = \frac{\tau}{\dot{\gamma}}$ ) decreases under the increase of the shear rate  $\dot{\gamma}$ . This trend is attributed to the rearrangement of particles that facilitates the shearing reducing the resistance to flow. This is also in agreement with cement slurry results [84] and Coal-Water Slurry [85]. However, it is more relevant for the slurry with high concentration where the interaction between particles became evident. Data set corresponding to FS = 27 % and FS = 30 % are close to each other and quite far from FS = 32 %, thus can be attributed to a regime transition in terms of solid fraction: from the data-set corresponding to FS = 27 % to FS = 30 % there is an increase in terms of apparent viscosity  $\eta$  of about 50 %, while an increase up to 280 % is observed from the FS = 30 % to FS = 32 %. Three different empirical fittings are tested to determine the best model describing experimental data: the Ostwald de Waele model, the Herschel-Bulkley model, and the Bingham model. The main parameters of the fitting curves, as well as the  $R^2$  parameter, are reported in Tab. B-2 while the fitting curves for FS =27 % and FS = 30 % are plotted in Fig. B-5.

Tab. B-2 Fitting parameters for the Herschel-Bulkley, Ostwald-de Waele and Bingham model and the respective  $R^2$

SF (%)	Herschel-Bulkley $\tau = \tau_y + C\dot{\gamma}^n$				Ostwald-de Wael $\tau = C\dot{\gamma}^n$			Bingham $\tau = \tau_y + \eta_0\dot{\gamma}$		
	$\tau_y$ (Pa)	$C$ (Pa s <sup>n</sup> )	$n$	$R^2$	$C$ (Pa s <sup>n</sup> )	$n$	$R^2$	$\tau_y$ (Pa)	$\eta_0$ (Pa s)	$R^2$
0.32	61.01	5.26	0.48	0.9988	48.96	0.20	0.9299	82.84	0.11	0.8987
0.30	19.79	2.09	0.53	0.998	10.81	0.32	0.9725	32.64	0.06	0.933
0.28	13.23	1.12	0.58	0.9975	6.03	0.36	0.9718	21.33	0.05	0.9477

For all three samples, the model that best describes the experimental data-set is the Herschel-Bulkley model:

$$\tau = \tau_y + C|\dot{\gamma}|^n \quad (B.3)$$

Where  $\tau_y$  is yield stress, i.e., the stress at which the fluid starts to flow,  $C$  is the consistency index that is a simple constant of proportionality, and  $n$  is the flow index, which measures the degree to which the fluid is shear thinning ( $n < 1$ ) or shear thickening ( $n > 1$ ). The Herschel-Bulkley model (HB) includes the Bingham model and the Ostwald-de Wael model as particular cases considering  $n = 1$  and  $\tau_y = 0$  respectively.

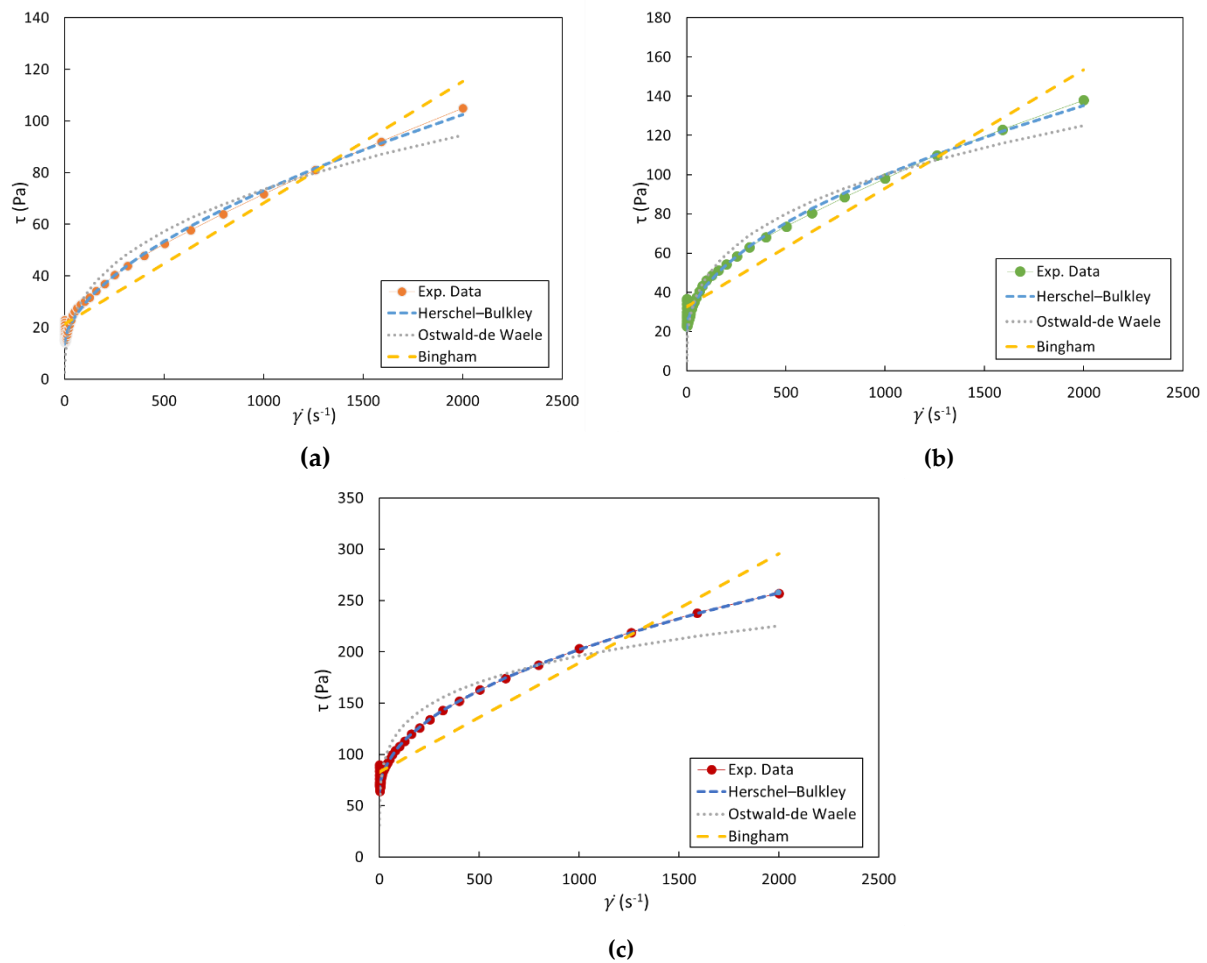


Fig. B-5 Flow curves for the three solid fraction (a) FS =27%, (b) FS =30% and (c) FS =32%, fitted by Ostwald-de Wael model; Hershel-Buckely model and Bingham model

The yield stress  $\tau_y$  in the Herschel-Bulkley and Bingham model is the stress necessary for the slurry to flow and below which the behavior is plastic. The yield stress is higher for the more concentrated fluid, which means that higher initial energy is necessary before the fluid starts to flow.

### B.1.2 Experimental observation of wear: the multi-pass scratch test

In this study, the scratch test is implemented in the strategy as a means to quantify the wear resistance of the microstructure, and it is used for the writing of the wear equation, giving additional information that is not accessible from the core-drill test. Therefore it is used as an experimental tool operating independently from the drilling machine.

In a general framework, a scratch test is a simple method to determine the wear properties of materials and coating. Fig. B-6 compares the indentation and scratch process: by definition,

the scratch test can be regarded as a tangential indentation [86] where the indenter is moving and therefore is in contact only over its front surface [7]. This is roughly the same wear process involved during the cutting operation where a single debris grain can abrade the surface under a normal load and move in the tangential direction.

In the first stage of the test, a conical Rockwell diamond indenter with a spherical tip radius of  $R_s = 100 \mu\text{m}$  penetrates in the metallic surface under a progressive load from 0.020 N to 30 N and with a scratch speed  $v_s$  of 10 mm/min for a scratch distance  $L_s$  of 5 mm. The machine allows acquiring normal and tangential force (and therefore the friction coefficient  $\mu_s$ ) and the depth of the scratch. During the actual indentation, the penetration depth  $h_{p,s}$  is measured by depth sensors. When the load is released, post-scan observations allow defining the residual depth  $h_{r,s}$ : the equipment carries out a contact-sensor scan of the surface (in the same direction as the scratch) by applying a contact force as low as possible (10 mN), measuring the residual depth (always less than the depth of penetration), and giving the elastic return of the material  $\frac{h_{p,s}-h_{r,s}}{h_{p,s}}$ .

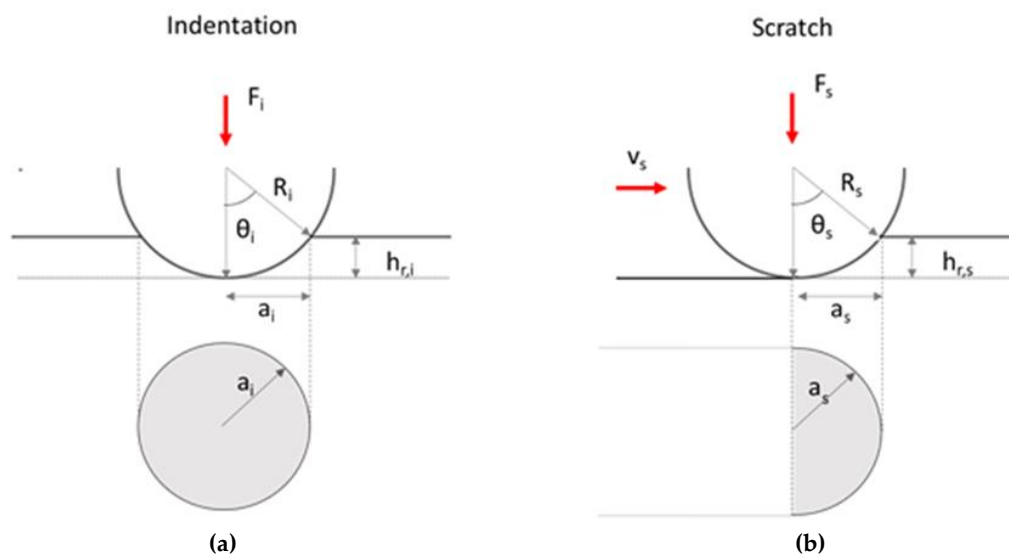


Fig. B-6 Contact model between a hemispherical tip indenter and a sliding surface (a) during static indentation; (b) during the dynamic scratch; ( $F$  = normal load,  $v$  = scratch velocity;  $R$  = indenter tip radius;  $h_r$  = depth of penetration;  $a$  = half contact width;  $\theta$ : attack angle; index  $i$  and  $s$  stay for indentation and scratch, respectively).

The onset load for cracking initiation and change in wear regime is defined as the critical load  $F_c$ . The module of critical load, as well as the wear mechanism involved, change with the mechanical properties of the material tested. Here a 100% cobalt alloy is tested. The mechanical properties are listed in Tab. A-1 and are here reported in Tab. B-3. The same material is used as a binder for the core drill test, discussed in Section B.1.3.2.

Tab. B-3 Specification of the cobalt metal matrix used in the scratch test and the core-drill test (HV10 Vickers Hardness;  $\sigma_y$  = yield strength;  $\sigma_u$  = ultimate strength;  $\varepsilon_r$  = residual strain)

Label	Grain size before sintering	Grain size after sintering	Porosity	Hardness	$\sigma_y$	$\sigma_u$	$\varepsilon_r$
	[ $\mu\text{m}$ ]	[ $\mu\text{m}$ ]	[%]	[HV10]	[MPa]	[MPa]	%
CO6102	2	2,3	0,056	299	450	700	2

The main quantities measured in the test and the optical micrographs of the scratched surface are defined in Fig. B-7. The critical load is determined by optical microscopy observations and measurements of  $\mu_s$ . For  $F_s = 19$ , cracks start to propagate perpendicular to the direction of scratching.

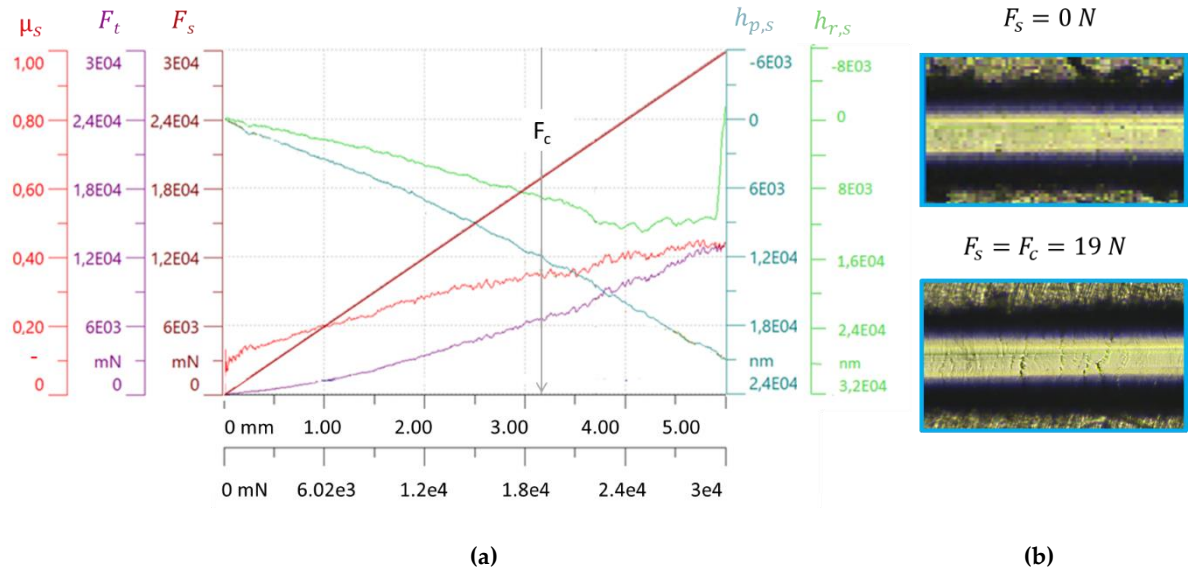


Fig. B-7 First stage of the scratch test (a) Main quantities measured and definition of critical load  $F_c$ ; (b) optical micrograph of the first scratch at the beginning ( $F_s = 0 \text{ N}$ ) and when the critical load is reached ( $F_s = 19 \text{ N}$ )

In the second stage, multiple scratches are performed in the same direction under constant normal load  $F_s = 10 \text{ N}$  ( $F_s < F_c$ ) and constant scratch velocity  $v_s = 10 \text{ mm/min}$ .

For each scratch, measuring the profile of the indentation depth  $h_{p,s}$  and the residual depth  $h_{r,s}$ , as well as the coefficient of friction  $\mu_s$ , it is possible to compute their respective mean values. From the residual depth  $h_{r,s}$  looking at the schematization in Fig. B-6 b., the half contact width is defined as:

$$a_s = \sqrt{2R_s h_{r,s} - h_{r,s}^2} \quad (B.4)$$

An indicator of the severity of the wear process is the attack angle  $\theta_s$  (Fig. B-6) between the front of the indenter and the surface of the material being scratched [87]. Neglecting the ridges of material in front of and to the sides of the indenter, assuming that the height of the ridge in front of the indenter is the same as the ridge to the sides of the indenter, the contact area is half a circle and the attack angle is defined as:

$$\sin \theta_s = \frac{a_s}{R_s} \quad (B.5)$$

The attack angle is an important indicator of the abrasive wear mechanisms involved during scratching, several authors have estimated the transition from the ploughing wear to the cutting wear as a function of a critical value of  $\theta_s$  [65], [70], [87].

Another indicator providing a good estimation of the wear resistance under the continuous passage of an abrasive particle is the scratch hardness, defined as:

$$H_s = \frac{F_s}{\frac{\pi a_s^2}{2}} \quad (B.6)$$

Performing multi-scratches along the same scratch path and in the same direction provides much more information than the single scratch event in terms of damage and repeated abrasion. Also, the indentation test, as well as the single scratch test, are performed at high load leading to a high-stress abrasion process, while in the multi-scratch test the load is much lower, causing less fracture damage and a low-stress abrasion process [56][55], which is more similar to what is expected in industrial conditions. For this purpose, the scratch hardness is more representative than Vickers's hardness in terms of wear resistance and damage.

Fig. B-8 plots the mean values of residual depth  $h_{r,s}$ , attack angle  $\theta_s$  and scratch hardness  $H_s$  as a function of the number of scratches. Notice that both the attack angle  $\theta_s$  and the scratch hardness  $H_s$  are computed from the measured residual depth  $h_{r,s}$  by Eqs. B.4-6. How the mean residual depth is estimated will be discussed in section C.3 since it will be used to model the scratch test. The behavior under the first scratch may be affected by initial conditions and may not represent the real behavior of the surface. During multi-scratches, the degree of penetration increases with the number of cycles own to the increase of the measured depth of the groove  $h_{r,s}$ . For the same reason, an increase in terms of contact width is expected; as the load is constant, such behavior provides a decrease in terms of scratch hardness  $H_s$ . However, whatever the feature is, the behavior is not linear, as early scratches produce a large effect in terms of residual depth and scratch width. Then, the higher the number of scratches, the smaller the effect of scratching. Hence, the cumulative effect seems less important when increasing the number of scratches [88]. An explanation of this trend may be the formation of an altered surface layer that characterizes the third body layer of wear particles and is able to

resist further surface damage than the original material. This behavior may also be related to the plastic deformation process, such as work hardening, which contrasts with the fatigue effect due to the multi-passing, or by the mechanical compaction of crushed material at the surface [88].

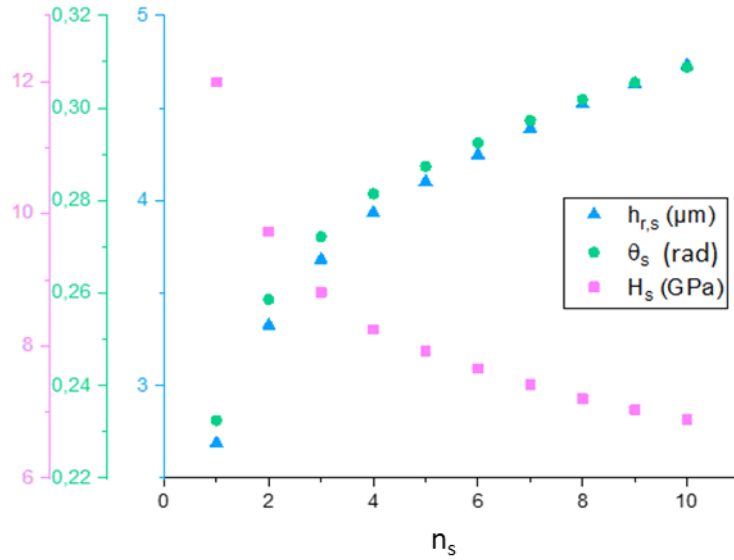


Fig. B-8 Evolution of residual groove  $h_{r,s}$  attack angle  $\theta_s$  and scratch hardness  $H_s$  with the number of repeats scratches  $n_s$

Ignoring the first pass and considering that the behavior of the metal matrix under the cutting process is similar to what may be observed under a higher number of scratches ( $n > 10$ ), the characteristic scratch hardness is calculated by performing a non-linear regression of the experimental data-set. For instance, the exponential law well fits the experimental points ( $R^2 = 0.9965$ ), as displayed in Fig. B-9:

$$H_s = H_s^* + \Delta H_s e^{-\kappa n_s} \quad (B.7)$$

Where  $H_s^* = 6.39 \text{ GPa}$  is the characteristic scratch hardness reached after many scratch repetitions and will be considered in Chapter C.3.

A better estimation can be obtained by performing a large number of scratches ( $n > 10$ ) and is an interesting perspective for a deeper understanding of the material behavior under a large number of scratch cycles.

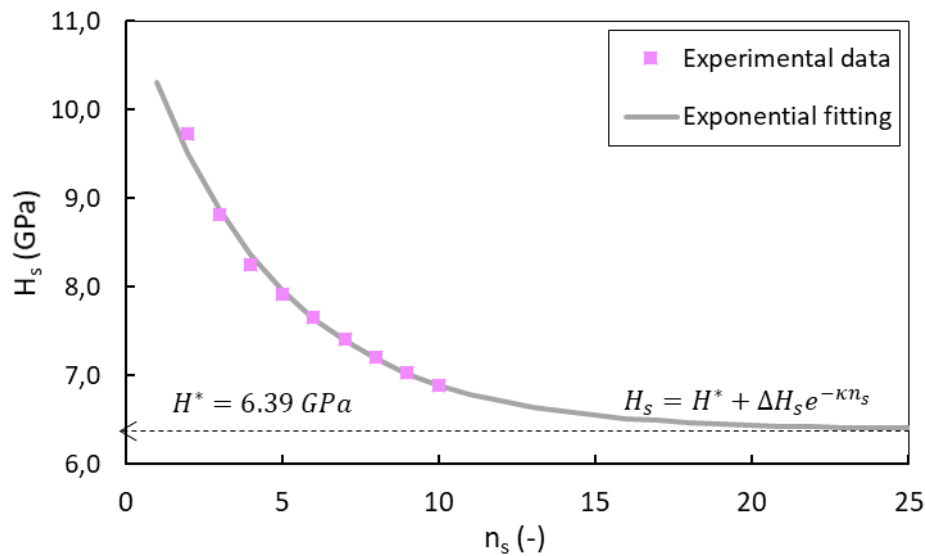


Fig. B-9 Experimental scratch hardness values and exponential fitting ( $H_s^* = 6.39$  GPa;  $\Delta H_s = 4.906$  GPa;  $\kappa = 0.227$ )

The micro scratch test is widely used to test hard metals [65], [70], [88]–[90], and this is why it is chosen to test cobalt and other alloys used as a metal matrix in DIT. However, the effect of the indenter tip radius on the scratch hardness is not yet well understood. Performing a single scratch pass test, different studies [91], [92] observed that the scratch hardness increases with the reduction of the tip size, keeping the load constant. However, the scratch hardness  $H_s^*$  changes if a multipass test is performed. In this case of study, the scratch hardness is defined as the constant value reached after several passes of the indenter and the value obtained is smaller than the one after the first scratch. This procedure allows us to consider  $H_s^*$  as an intrinsic property of the material, assuming that the metallic surface reaches a constant hardness. In other words, we assume that an indenter with a tip radius equal to the characteristic asperity and under different operating conditions will reach the same value  $H_s^*$  after a certain number of passes. This assumption allows for shifting from the scale of the experimental test to the industrial application scale.



## B.2

# Modeling of the third body flow

The Reynolds equation [26] is widely used in the fluid lubrication theory [93]–[99]. Pioneering works have been performed to implement non-Newtonian effects [25], [100], and the slip at the bearing surface [101].

In the following, the 3<sup>rd</sup> body is considered a non-Newtonian fluid (continuum scale) able to flow into a narrow gap (the clearance) between the segment and the workpiece and characterized by abrasive properties. Such a fluid is modeled, solving the Generalized Reynolds equation [25] numerically in a 3D domain, obtaining the flow properties (pressure field and fluid velocity) as a function of the rheology of the slurry and the initial clearance (i.e., the initial film thickness).

The Reynolds equation is first introduced starting from the classical formulation and then is applied to this case of study with particular attention to the rheology of the slurry and the geometry of the segment surface.

As the pressure variation is instantaneous compared to the time required to the surface to adapt to the new configuration in the wearing condition, the Reynolds equation is solved in a stationary case. Results are then implemented in the wear law; this numerical coupling is explained in section B.3.2.

## B.2.1 The Reynolds equation

The non-Newtonian effects can be introduced in the Reynolds equation in a modified form derived from the classical formulation.

### B.2.1.1 The Reynolds equation: classical formulation

The classical Reynolds equation [26] derives from the Navier-Stokes equations under the following simplifying assumptions:

1. thin film geometry compared to the dimension of the contact
2. constant pressure across the film thickness
3. constant density and viscosity across the film thickness
4. Newtonian fluid
5. the fluid is considered in an isothermal and stationary regime (transient phenomena are negligible)
6. negligible body force
7. no-slip boundary conditions
8. the flow is laminar (low Reynolds number)
9. inertia and surface forces are negligible with respect to the viscous forces

Under these assumptions and considering the  $z$ -direction as the direction of the gap  $h$  (Fig. B.-1-10) the conservation of momentum equation becomes:

$$\begin{aligned}\frac{\partial p}{\partial x} &= \frac{\partial \tau_{zx}}{\partial z} \\ \frac{\partial p}{\partial y} &= \frac{\partial \tau_{zy}}{\partial z} \\ \frac{\partial p}{\partial z} &= 0\end{aligned}\tag{B.8}$$

with:

$$\tau_{zx} = \eta_N \dot{\gamma}_{zx} = \eta_N \frac{\partial u}{\partial z} \quad \text{and} \quad \tau_{zy} = \eta_N \dot{\gamma}_{zy} = \eta_N \frac{\partial v}{\partial z}\tag{B.9}$$

Where  $\eta_N$  is the (Newtonian) viscosity of the fluid,  $u$  and  $v$  are the velocity field components in the  $x$  and  $y$ -direction, respectively.

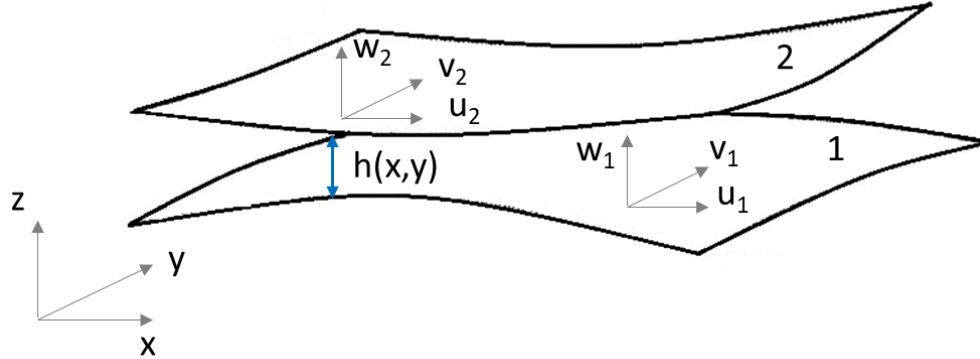


Fig. B-10 Schematic representation of the fluid flow between two moving surfaces

Looking at Fig. B-10, the no-slip boundary conditions at the lower and upper surface write respectively:

$$u = u_1; \quad v = v_1; \quad w = w_1 \quad (B.10a)$$

$$u = u_2; \quad v = v_2; \quad w = w_2 \quad (B.10b)$$

Moreover, considering  $z = 0$  at the lower surface and  $z = h$  at the upper surface, two successive integrations of the momentum equation (Eqs. (B.8)) give the velocity fields along the vertical direction ( $z$ -direction):

$$\begin{cases} u(z) = \frac{1}{2\eta_N} \frac{\partial p}{\partial x} z(z-h) + \frac{h-z}{h} u_1 + \frac{z}{h} u_2 \\ v(z) = \frac{1}{2\eta_N} \frac{\partial p}{\partial y} z(z-h) + \frac{h-z}{h} v_1 + \frac{z}{h} v_2 \end{cases} \quad (B.11)$$

The no-slip boundary condition means that the velocities with indices 1 and 2 are the velocity of the material surface 1 and 2, respectively, as noted in Fig. B-10.

In a steady-state condition, the mass continuity equation for a compressible flow writes:

$$\frac{\partial m_x}{\partial x} + \frac{\partial m_y}{\partial y} = 0 \quad (B.12)$$

With:

$$m_x = \int_0^h \rho u(z) dz \quad \text{and} \quad m_y = \int_0^h \rho v(z) dz$$

Replacing  $u(z)$  and  $v(z)$  with (Eqs. B.11) (with  $v = 0$  on both the lower and upper surfaces, one finds the Reynolds equation in a stationary condition that describes the pressure variation of a thin viscous layer of fluid between two surfaces as a function of the operating conditions and the geometry defined by the film thickness  $h$ :

$$\frac{\partial}{\partial x} \left( \frac{\rho h^3}{\eta_N} \frac{\partial p}{\partial x} \right) + \frac{\partial}{\partial y} \left( \frac{\rho h^3}{\eta_N} \frac{\partial p}{\partial y} \right) = 12u_m \frac{\partial}{\partial x} (\rho h) \quad (B.13)$$

Where  $u_m = \frac{u_1 + u_2}{2}$ .

The left side terms of Eq. (B.12) are the Poiseuille terms and are related to the Poiseuille flow that is pressure-induced, while the right side term is the Couette term and refers to the Couette flow driven by drag force acting on the fluid between the two surfaces.

The Reynolds equation can be written in a more compact form:

$$\nabla \cdot (\varepsilon \nabla p) = \frac{\partial (\rho h)}{\partial x} \quad (B.14)$$

with:  $\varepsilon = \frac{\rho h^3}{12u_m \eta_N}$

### B.2.1.2 The Generalized Reynolds equation

The Reynolds equation is dedicated to Newtonian fluids, i.e., fluids obeying Newton's law between the shear stress and the shear rate that is a linear relation. Thus, the viscosity of the fluid is independent of the shear rate and can be easily defined as  $\eta_N = \tau / \dot{\gamma}$ . However, slurries analyzed in Section B.1.2 show a non-Newtonian behavior.

The generalized Reynolds equation was introduced by Dowson [25] to extend the classical formulation to non-Newtonian fluids and consider the effect of the viscosity (and density) variation along the gap thickness  $h$ . Therefore, assumptions 3. And 4. listed in section B.2.1.1. are not required anymore. It is obtained in a similar way integrating the simplified Navier-Stokes equation (Eqs. (B.8)) and considering the following constitutive relations obtained by substituting the apparent viscosity  $\eta$  to the Newtonian viscosity  $\eta_N$  of Eqs. (B. 9):

$$\tau_{zx} = \eta \dot{\gamma}_{zx} = \eta \frac{\partial u}{\partial z} \quad (B.15a)$$

$$\tau_{zy} = \eta \dot{\gamma}_{zy} = \eta \frac{\partial v}{\partial z} \quad (B.15b)$$

Where  $\eta$  should be characterized by performing rheological tests. Note that in this case,  $\eta$  can vary along and across the gap thickness as  $\eta = \eta(p, \dot{\gamma})$  while the Newtonian viscosity  $\eta_N$  may be defined as  $\eta_N = \eta_N(p)$  only [102], [103].

Integrating the momentum equation Eq. (B.8) twice and using the condition of no-slip at the wall boundary, the velocity profile along the vertical direction, z-direction, Eq. (B.11), became:

$$\begin{cases} u(z) = \frac{\partial p}{\partial x} \left( \int_0^z \frac{z}{\eta} dz - \frac{\eta_e}{\eta'_e} \int_0^z \frac{dz}{\eta} \right) + \eta_e (u_2 - u_1) \int_0^z \frac{dz}{\eta} + u_1 \\ v(z) = \frac{\partial p}{\partial y} \left( \int_0^z \frac{z}{\eta} dz - \frac{\eta_e}{\eta'_e} \int_0^z \frac{dz}{\eta} \right) \end{cases} \quad (B.16)$$

Where:

$$\frac{1}{\eta_e} = \int_0^h \frac{dz}{\eta}; \quad \frac{1}{\eta'_e} = \int_0^h \frac{z}{\eta} dz; \quad \frac{1}{\eta''_e} = \int_0^h \frac{z^2}{\eta} dz \quad (B.17)$$

The norm of the velocity field is therefore defined:

$$\|\mathbf{v}\| = \sqrt{u^2 + v^2} \quad (B.18)$$

The components  $\dot{\gamma}_{zx}$  and  $\dot{\gamma}_{zy}$  of the shear rate  $\left( \dot{\gamma} = \sqrt{\dot{\gamma}_{zx}^2 + \dot{\gamma}_{zy}^2} \right)$  are obtained by deriving velocity components along z. Then, the general non-linear equation for non-Newtonian fluid writes:

$$\dot{\gamma}^2 = \frac{1}{\eta^2} \left\{ \left[ \frac{\partial p}{\partial x} \left( z - \frac{\eta_e}{\eta'_e} \right) + \eta_e (u_2 - u_1) \right]^2 + \left[ \frac{\partial p}{\partial y} \left( z - \frac{\eta_e}{\eta'_e} \right) \right]^2 \right\} \quad (B.19)$$

Where the surface velocities  $u_1$  and  $u_2$  define the kinematic boundary conditions on the lower and upper surface, respectively.

In the same way as the classical Reynolds equation, replacing the field velocity, Eqs. (B.16), in the continuum equations, Eq. (B.12), gives the final Reynolds equation, which is named as Generalized Reynolds equation and is valid whatever the behavior of the fluid across and along the film thickness:

$$\nabla \cdot (\varepsilon' \nabla p) - \frac{\partial \left[ \rho h \left( u_2 - \frac{\eta_e}{\eta'_e} \left( \frac{u_2 - u_1}{h} \right) \right) \right]}{\partial x} = 0 \quad (B.20)$$

Where  $\varepsilon' = \rho \left( \frac{1}{\eta_e''} - \frac{\eta_e}{\eta_e'^2} \right)$ .

If the apparent viscosity  $\eta = \eta_N$ , Eq. (B.20) reduces to the classical Reynolds equation (Eq. B.14).

## B.2.2 Implementation of the slurry properties

The slurry's properties analyzed experimentally in section B.1.2 are now implemented in the generalized Reynolds equation.

### B.2.2.1 An incompressible fluid

The slurry is assumed as an incompressible fluid; thus, the density does not influence the flow properties. Under this assumption, the mass-conservation equation, Eq. (B-12), simplifies in:

$$\frac{\partial u}{\partial x} + \frac{\partial v}{\partial y} + \frac{\partial w}{\partial z} = 0 \quad (B.21)$$

Moreover, the generalized Reynolds equation can be simplified as follow:

$$\nabla \cdot (\varepsilon' \nabla p) - \frac{\partial \left[ h \left( u_2 - \frac{\eta_e}{\eta_e'} \left( \frac{u_2 - u_1}{h} \right) \right) \right]}{\partial x} = 0 \quad (B.22)$$

Where  $\varepsilon' = \left( \frac{1}{\eta_e''} - \frac{\eta_e}{\eta_e'^2} \right)$

### B.2.2.2 The viscosity of the slurry

The three slurries with different solid fraction SF defined in B.1.1 follow shear-thinning behavior. However, the non-differentiability in the mathematical formulation of the constitutive law in Eq. (B.3) leads to some instabilities and convergence problems in the implementation of the Hershel-Bulkley model caused by the change in flow regime for  $\tau = \tau_y$ . To solve this issue, several regularization methods are proposed in the literature [98], [104], [105]. The common idea is to overcome the discontinuity of the change in the flow regime in the yielding point using a single constitutive law holding both the yielded and the unyielded region. Using the Papanastasiou regularization [105], Eq. (B.3) becomes:

$$\tau = C |\dot{\gamma}|^n + \frac{\tau_y (1 - e^{-m|\dot{\gamma}|})}{|\dot{\gamma}|} \cdot \dot{\gamma} \quad (B.23)$$

Where  $m$  is the regularization parameter, which reduces the singularity and makes the shear rate non-zero everywhere. If  $m \rightarrow \infty$  the HBP (Herschel-Bulkley Papanastasiou) model reduces to Eq. (B.3), and if  $m \rightarrow 0$  the model is reduced to the simple power law.

The influence of the regularization parameter is plotted in Fig. B-11 for SF = 32 %.

The verification of the regularization parameter is discussed in Section B.2.4. The relative error  $e_r = \frac{|\tau_{HBP} - \tau_{HB}|}{\tau_{HB}}$  becomes smaller and smaller with the increase of  $m$  and at high values of shear rate. For example, when  $m = 2$ :  $e_r \leq 10^{-2}$  when  $\dot{\gamma} \geq 2 \text{ s}^{-1}$ .

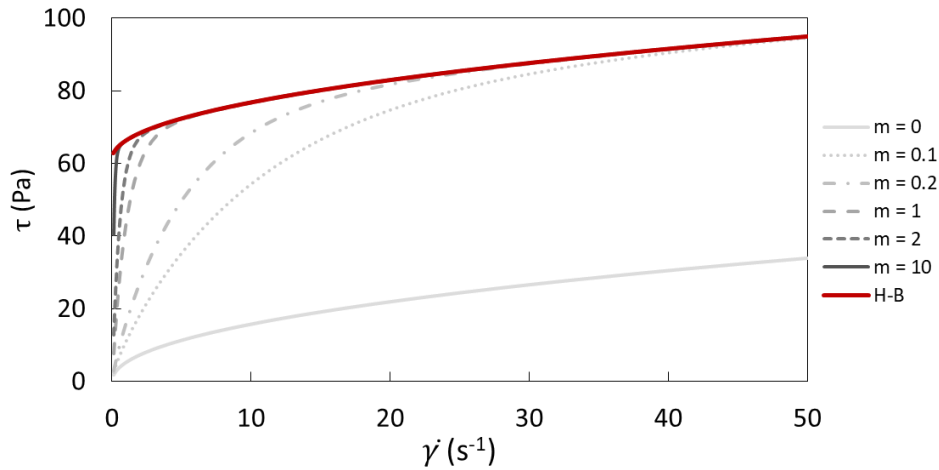


Fig. B-11 Influence of the regularization parameter  $m$  on the Herschel-Bulkley fit for the SF = 32 %

### B.2.3 Geometry and slurry thickness equation

The real shape of diamond crystals ranges from the cube to the octahedron as a function of the synthesis conditions [16]. The main geometrical assumption for building the model is to consider a portion of a segment with a central diamond retained by the metallic matrix. The example shown in this case study refers to a particular diamond observed experimentally, illustrated in Fig. B-12 that is respectful of the assumption mentioned above. The angle  $\beta_D$  in Fig. B-12 defines the size of the protruding diamond ( $L_D/2$ ); it can vary depending on the initial clearance of the diamond on the surface  $h_{c,0}$  (which also affects the ability to cut) defined as the distance between the matrix surface and the diamond tip in the initial configuration. The definition of clearance will be reminded in Chapter B.4 to define the wear rate.

Moreover, a more detailed numerical study (including a sensitivity analysis on the shape, size and orientation of the diamond) is an interesting perspective).

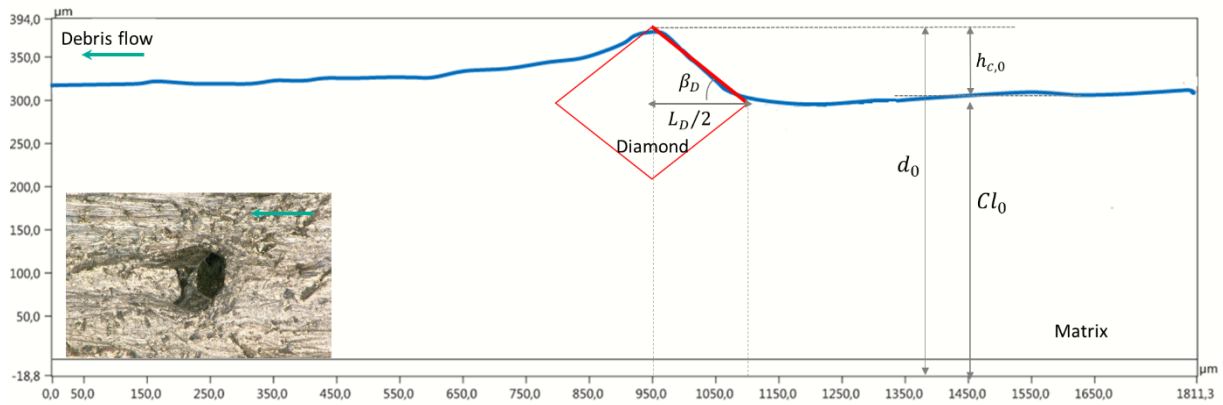


Fig. B-12 Initial vertical profile of the matrix surface (blue) and schematization of the diamond geometry used in the model (red line) with the indication of the initial values of the main geometrical features ( $\beta_D$ : diamond aspect ratio;  $L_D/2$ : length of the protruding diamond;  $Cl_0$ : initial clearance,  $d_0$ : initial diamond height,  $h_{c,0} = |Cl_0 - d_0|$ : initial height of clearance respect to the diamond tip; micrograph of the diamond embedded by the metal matrix (bottom-left))

The geometrical features are represented in Fig. B-13. The domain is a 3D configuration where the upper surface stands for the segment surface (matrix + diamond), while the lower surface is the surface of the workpiece. The matrix is assumed as a flat surface (that will evolve during the wear process), while the diamond has an octahedral shape. This allows writing the equation of the slurry  $h(x, y, t_i)$  in the initial unworn condition (at the time  $t_0 = 0$  s) as:

$$h(x, y, t = 0 \text{ s}) = h_0(x, y) = \min(h_{c,0}, h_D + \delta_D) \quad (B.24)$$

where  $h_{c,0}$  is the above mentioned initial clearance<sup>5</sup>,  $h_D$  is the cartesian equation of the diamond:

$$h_D(x, y) = (|x| + |y|) \tan \beta_D \quad (B.25)$$

Where:

$$\tan \beta_D = h_{c,0} / (L_D/2) \quad (B.25b)$$

defines the size of the diamond, as illustrated in Fig. B-12 (b) and  $\delta_D$  is a small thickness between the tip of the diamond and the workpiece. It can be seen as a numerical parameter; in reality, there is direct contact since the diamond is indenting the workpiece during the overall cutting process; however, it is necessary for the numerical convergence of the solution. The choice of that parameter is discussed in Section B.2.6.

<sup>5</sup> The initial value correspond to the time  $t_0 = 0$  s and is equal to the initial protrusion  $h_{p,0}$ . The definition of clearance and protrusion will be reminder in Chapter B.4

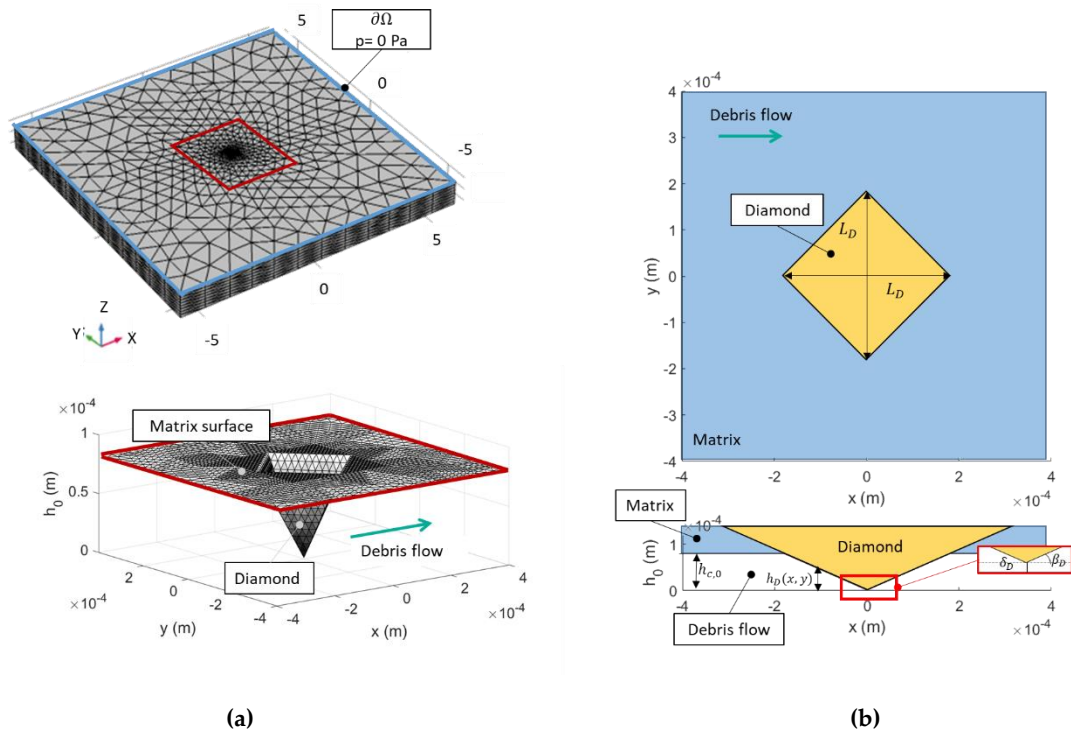


Fig. B-13 (a) Dimensionless domain used for the computation (top) and a zoom on the central part of the 3D configuration (bottom) (b) horizontal projection on the plane x-y of the surface (top) and vertical projection on the plane x-z of the surface (bottom)

## B.2.4 Boundary conditions

The resolution of the Reynolds equation requires the specification of the value of pressure  $p$  on the boundary  $\partial\Omega$  of the domain (Fig. B-13 (a)-top). Here, a Dirichlet boundary condition is imposed as:

$$p = 0 \text{ on } \partial\Omega$$

To avoid results being affected by the imposed value on the boundary, the domain must be much larger than the surface of interest.

## B.2.5 Dimensionless formulation

The dimensionless domain represented in Fig. B-13 (a)-top is independent on the real size of the physical problem; it is defined by the following dimensionless independent variables:

$$X = \frac{x}{b}; Y = \frac{y}{b}; Z = \frac{z}{h} \quad \bar{h} = \frac{h}{h_{c,0}} \quad (B.26)$$

Where  $x$ ,  $y$ , and  $z$  are the independent variables, while  $h(x, y, t_i)$  is the internal variable whose initial value is defined in Eq. (B.24) as  $h(x, y, t = 0 s) = h_0(x, y)$ . The scalar parameter  $b$  is defined as:

$$b = \frac{L_D}{2} \quad (B.27)$$

Considering the definitions in Eq. (B.24) and Eqs. (B.25), the dimensionless  $\bar{h}$  becomes:

$$\bar{h}_0(X, Y) = \min \left( 1, (|X| + |Y|) + \frac{\delta_D}{h_{c,0}} \right) \quad (B.28)$$

In this way, the generalized Reynolds equation (see Eq. (B. 22)) writes:

$$\nabla \cdot (\varepsilon' \nabla p) - \frac{\partial \left[ \bar{h} h_{c,0} \left( u_2 - \frac{\bar{\eta}_e}{\bar{\eta}'_e} \left( \frac{u_2 - u_1}{\bar{h}} \right) \right) \right]}{\partial X} = 0 \quad (B.29)$$

Where:  $\varepsilon' = \left( \frac{1}{\bar{\eta}'_e} - \frac{\bar{\eta}_e}{\bar{\eta}'_e^2} \right)$ ;  $\frac{1}{\bar{\eta}_e} = \int_0^1 \frac{\bar{h} dz}{\bar{\eta}}$ ;  $\frac{1}{\bar{\eta}'_e} = \int_0^1 \frac{\bar{h}^2 dz}{\bar{\eta}}$ ;  $\frac{1}{\bar{\eta}''_e} = \int_0^1 \frac{\bar{h}^3 dz}{\bar{\eta}}$

A dimensionless formulation for the HBP model is offered by [106]:

$$\bar{\eta} = [1 - e^{\bar{m}|\bar{\gamma}|}] \frac{HB}{|\bar{\gamma}|} + |\bar{\gamma}|^{n-1} \quad (B.30)$$

Where:

$$|\bar{\gamma}| = \frac{|\dot{\gamma}|}{\dot{\gamma}^*}; \bar{\eta} = \frac{\eta}{\eta_N}; \bar{m} = m \dot{\gamma}^*; HB = \frac{\tau_y}{\dot{\gamma}^{*n}} \frac{1}{\eta_N}; \eta_N = C \dot{\gamma}^{*n-1}$$

$\dot{\gamma}^*$  is the characteristic shear rate, taken as:  $\dot{\gamma}^* = \frac{u_2 - u_1}{h/2}$ ; and HB is the Hershey-Buckley number that converges to the Bingham number  $B = \frac{\tau_y}{\dot{\gamma}^*} \frac{1}{\eta_N}$  if  $n = 1$ .

## B.2.6 Numerical application

The Reynolds equation is solved numerically by FEM (Finite Elements methods) in the commercial software COMSOL Multiphysics. A preliminary sensitivity analysis is performed to calibrate the mesh size.

### B.2.6.1 Mesh refinement

In solving finite elements, the accuracy of the solution is linked to the mesh size. A finer mesh leads to a more accurate solution that moves toward the exact solution.

However, the choice of the mesh is limited by the computational time. As the exact pressure field on the film thickness is unknown, the optimization of the mesh is reached by looking at the variation of the peak of pressure with an increasing mesh fineness. Mesh refinement is performed considering the conditions listed in Tab.B-4, changing the mesh as is Tab.B-5.

Tab. B-4 Geometrical parameters and velocities

$h_{c,0}$	$\delta_D/h_{c,0}$	$L_D$	$u_1$	$u_2$	$\eta_N$
[ $\mu\text{m}$ ]	[-]	[ $\mu\text{m}$ ]	[m/s]	[m/s]	[Pa s]
80	0.01	375	0	2.67	0.02

Tab. B-5 Statistics of the mesh refinements with numbers of degrees of freedom DOF, peaks of pressure  $p_{max}$  and times for the resolution  $t^{cost}$ 

Mesh	Number elements	Min. length size ( $\mu\text{m}$ )	DOF	$p_{max}$ (Pa)	$t^{cost}$ (s)
1	7473	36	73928	2694	10
2	12016	18	112521	5609	13
3	29835	10	272869	8916	35
4	15467	9	144393	10977	26
5	12636	8,33	119225	10963	16
6	29480	8	221788	10981	25
7	46106	6,36	416157	10678	192

Results are plotted in terms of the peak of pressure vs. the minimum element size in Fig. B-14. Up to a certain size, the variation of pressure becomes negligible. The minimum element size is taken as 8  $\mu\text{m}$ , corresponding to 29480 elements in the domain.

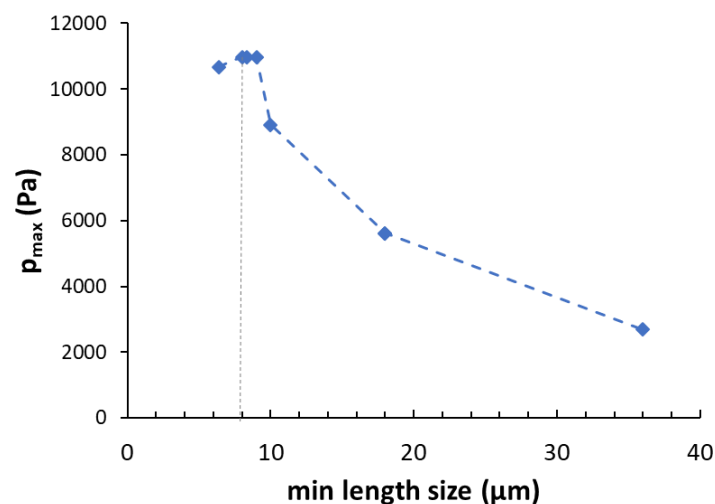


Fig. B- 14 Peak of pressure as a function of the mesh refinement

### B.2.6.2 Effect of rheology on the field of pressure

The small slurry thickness and the relatively high velocity of the cutting process result in shear rates out from the range studied experimentally in a viscometer that varies from  $0.1 \text{ s}^{-1}$  to  $2000 \text{ s}^{-1}$  (see section B.1.1). Assuming that the HB model still describes the behavior of the three slurries introduced in Chapter B.1.1, even for a high shear rate ( $\dot{\gamma} \geq 10^4 \text{ s}^{-1}$ ), the effect of the rheology on the flow properties is discussed here. Numerical simulations are performed, setting the input parameters provided in Tab. B-4 except for the viscosity since it will be no more Newtonian and will vary as in Tab. B-6.

Tab. B-6 Rheological parameters

FS [%]	Herschel–Bulkley modified $\tau = C \dot{\gamma} ^n + \frac{\tau_y(1-e^{-m \dot{\gamma} })}{ \dot{\gamma} } \cdot \dot{\gamma}$			
	$\tau_y$ [Pa]	$C$ [Pa s <sup>n</sup> ]	$n$	$m$
0.32	61.01	5.26	0.48	2
0.30	19.79	2.09	0.53	2
0.27	13.23	1.12	0.58	2

#### Effect of the solid fraction

Fig. B-15 illustrates the pressure profile (for  $p > 0 \text{ Pa}$ ) as a function of the concentration of debris grains in the slurry. As expected, the increase of solid concentration leads to an increase in the pressure field due to the increase of the apparent viscosity  $\eta$ .

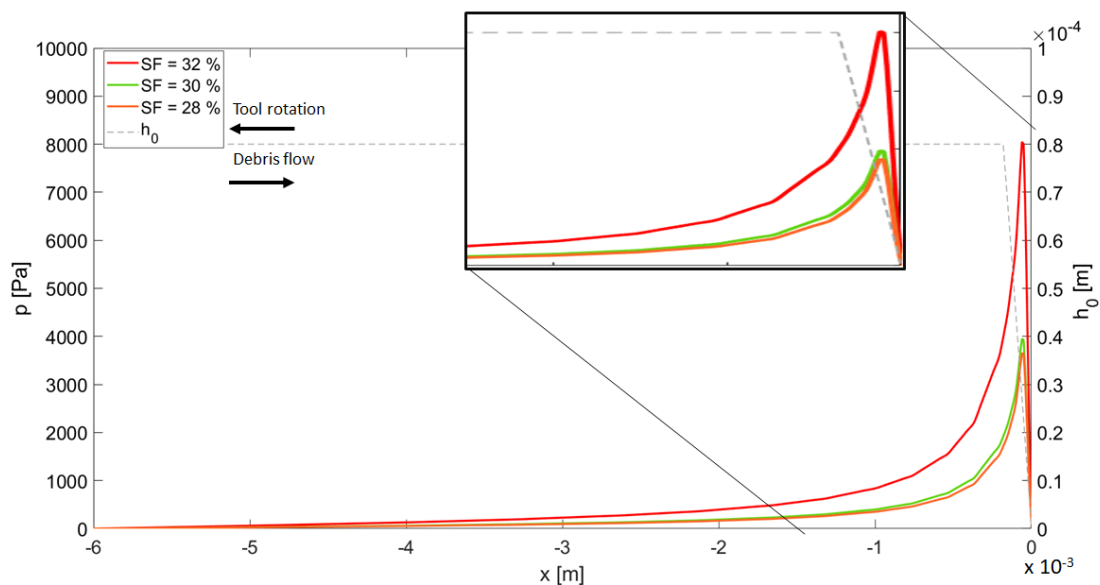


Fig. B-15 Pressure profile (for  $p > 0 \text{ MPa}$ ) as a function of the debris content SF and initial geometry profile  $h_0$  in the xz section

### Effect of Newtonian/Non-Newtonian rheology

Replacing of a Newtonian viscosity such that  $\bar{\eta} = 1$  ( $\eta = \eta_N$ ) in Eq. (B.30) and considering the parameters in Tab. B-6 gives:

$$\eta = \eta_N = k\dot{\gamma}^{*n-1} = 0.0163 Pa s$$

This leads to a sharper field of pressure than the Non-Newtonian case, the overestimation of pressure in correspondence of the diamond, and the underestimation on the matrix surface. This is observed in Fig. B-16 for the slurry with SF = 32 %, where  $\eta_N = 0.0163 Pa s$ .

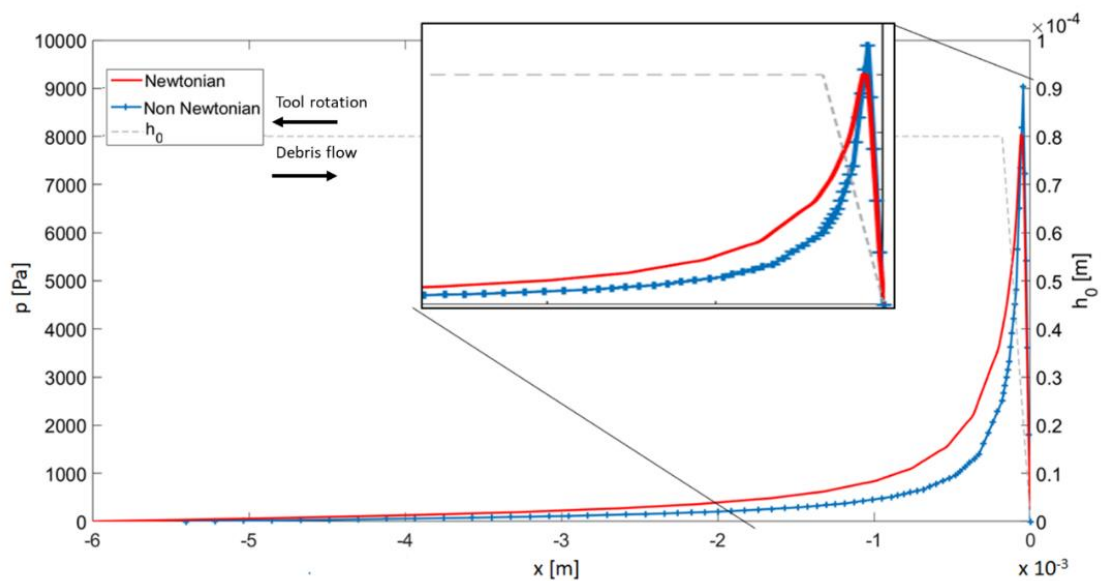


Fig. B-16 1D Pressure profile (for  $p > 0 Pa$ ) for a Newtonian and non-Newtonian fluid with SF = 32% and initial geometry profile  $h_0$  in the  $xz$  section

Fig. B-17 shows the field of viscosity and velocity along the  $xz$ -plane for  $y = 0$  for the Newtonian and the non-Newtonian case. In the latter, the variation of viscosity along and across the gap thickness is more evident in correspondence of the diamond surface, where  $h_0 = h_D(x, y)$ .

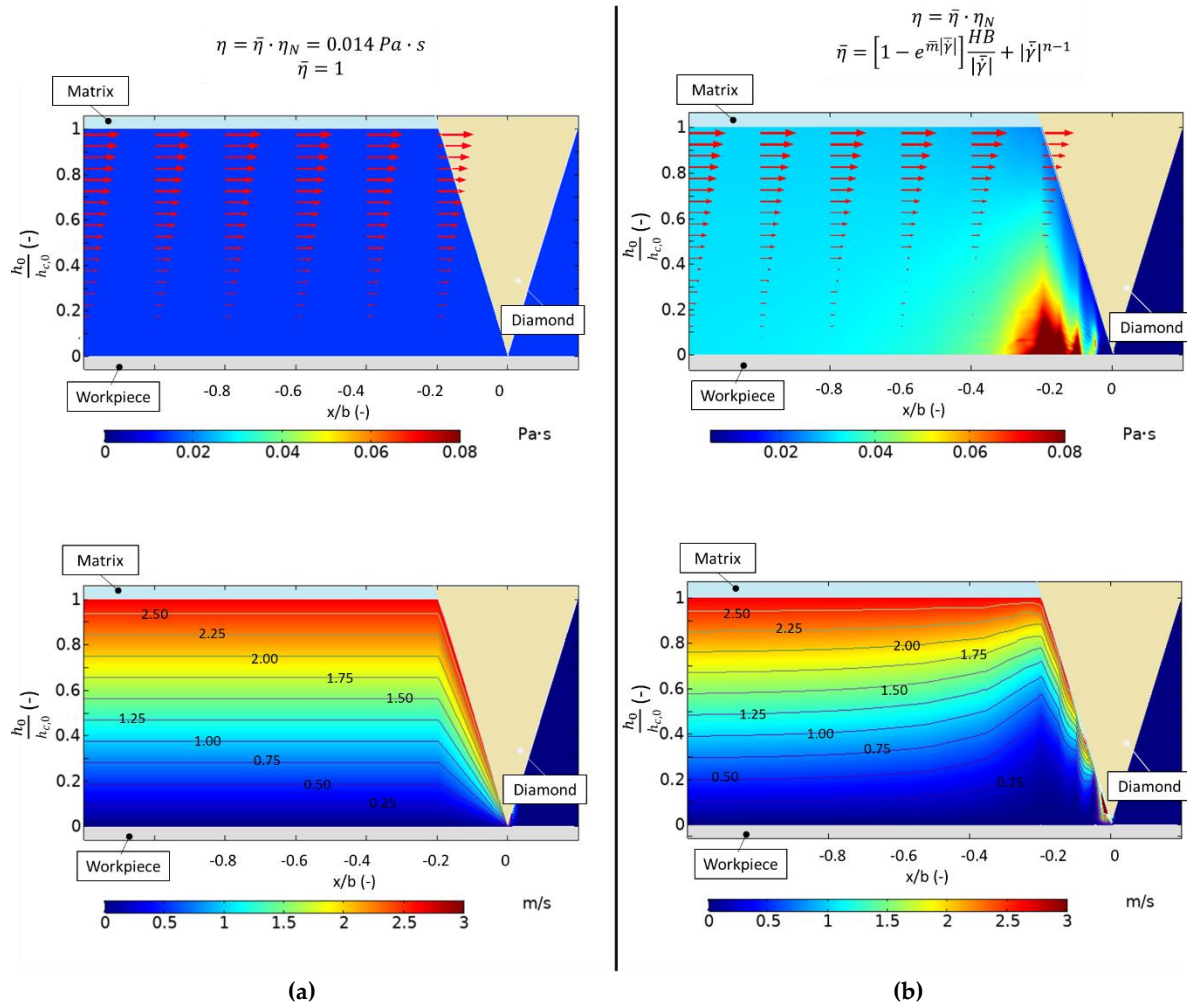


Fig. B-17 Fields of viscosity (top) and velocity  $u$  (bottom) along the plane  $xz$  for  $y = 0$  for (a) the Newtonian case (left) and (b) non-Newtonian case (right)

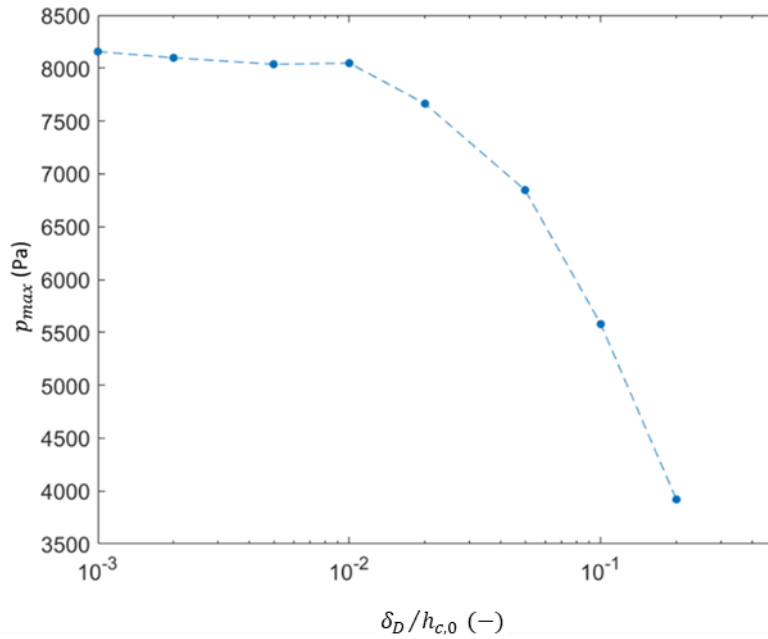
### B.2.6.3 Influence of the small gap thickness $\delta_D$

By definition, the pressure is strongly related to the gap thickness occupied by the slurry, which determines the initial clearance of the diamond. To avoid some numerical issues related to the convergence of the solution, a small gap  $\delta_D$  between the diamond tip and the workpiece is considered, as defined in Eq. (B.24). This gap has to be small enough not to affect the results. A parametric study is run to analyze the pressure profile varying the ratio  $\delta_D/h_{c,0}$  for the slurry with SF = 32 %. The main properties are fixed as in Tab. B-7.

The variation of the pressure profile along the  $x$ -line direction is plotted in Fig. B-18. As expected, the smaller is the ratio  $\delta_D/h_{c,0}$  the higher is the field of pressure up to a certain value below which the reduction of  $\delta_D/h_{c,0}$  does not affect results significantly. Therefore, the ratio  $\delta_D/h_{c,0} = 0.01$  seems to describe with accuracy the pressure field without instability problems and with shorter time-consuming than the smaller values.

Tab. B- 7 Parameters used in simulations varying  $\delta_D/h_0^c$ 

$h_{c,0}$ [ $\mu\text{m}$ ]	$\delta_D/h_{c,0}$ [-]	$L_D$ [ $\mu\text{m}$ ]	$u_1$ [ $\text{m/s}$ ]	$u_2$ [ $\text{m/s}$ ]	$\eta$ [ $\text{Pa s}$ ]			
					$\tau_y$ [ $\text{Pa}$ ]	$C$ [ $\text{Pa s}^n$ ]	$n$ [-]	$m$ [-]
80	Var.	375	0	2.67	61.01	5.26	0.48	2

Fig. B-18 Variation of the peak of pressure on the diamond surface with the dimensionless gap  $\delta_D/h_{c,0}$ 

## B.2.7 Conclusions

A preliminary study is performed to fix the main numerical parameters (i.e., mesh size and regularization parameter of the HB model). The influence of the non-Newtonian rheology is discussed in terms of flow properties. Increasing the solid concentration of the slurry (from SF = 28 % to SF = 32 %), the fluid became more viscous with an increase in the pressure field. A Newtonian fluid instead of the non-Newtonian one leads to a sharper profile of the pressure field and a more linear velocity gradient across the gap thickness than the non-Newtonian case.

These preliminary results are useful for monitoring the flow properties that are not accessible from the experimental test and are also implemented in the wear equation, discussed in Chapter B.3 and applied in Chapter B.4.



## B.3

# Modeling of the abrasive wear

The resolution of the Reynolds equation gives the pressure field at every location of the contact. The pressure field is one parameter of the wear equation, which is the focus of this chapter. This equation is written following an Archard formalism, including complexities observed at the local scale to provide a qualitative and quantitative description of wear at the diamond scale.

### B.3.1 From the Archard equation to a multiscale wear law

As introduced in Part A.2, the Archard wear equation [27] was originally proposed to estimate the removal volume  $V_{ad}$  in the case of sliding contact at a constant speed as a function of the dimensionless wear coefficient  $K_{ad}$ , the supported normal load  $F_n$ , the indentation hardness of the soft material  $H$ , and the sliding distance  $s$  (Eq. A.2). The coefficient  $K_{ad}$  was introduced as a constant of proportionality to describe the severity of the wear. From an engineering point of view, it might be more useful to write the Eq.(A.2) as:

$$V = k_w F_n s \quad (B.31)$$

Where  $k_w$  is the specific wear rate ( $mm^3 N^{-1} m^{-1}$ ) defined as in Eq. (A.3).

The same formulation of Eq. (B.31) is obtained for the abrasive wear under different initial assumptions and considering the contact between a conical abrasive particle and a surface [7] (Fig. B-19). In this particular case, the coefficient  $K_{ab}$  (and the specific wear rate  $k_w$ ) depends on the fraction of material removed and the geometry of the indenter.

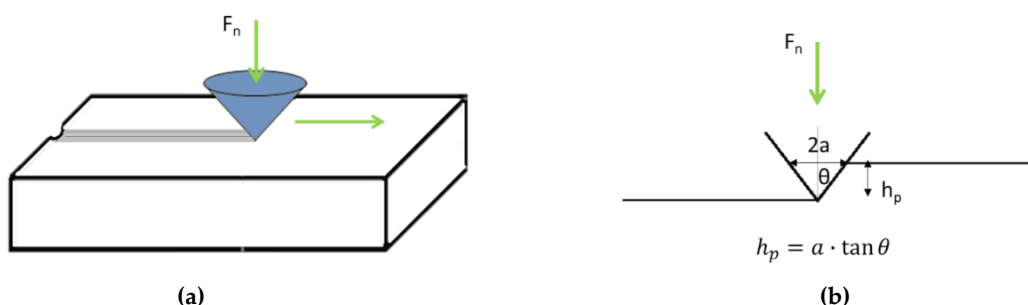


Fig. B-19 (a) A schematization of the geometry of the contact between a cone and a surface: perspective view; (b) vertical section ( $h_p$  depth of penetration ;  $a$ : half contact width;  $\theta$ : attack angle). (Inspired by [7])

Despite its simplicity, this theoretical formulation does not account for local features regarding contact pressure and size of asperity (since the asperities are considered conical). The hardness considered here is the bulk hardness obtained by Vickers or Rockwell indentation tests and is sensitive to the testing conditions that do not include problems where fatigue and multipass processes are relevant.

A local formulation of the wear equation is obtained by dividing the wear equation by the contact area  $A_c$  and deriving in time:

$$\frac{dh}{dt} = k_w \cdot p \cdot \|\mathbf{v}_r\| \quad (B.32)$$

Here, wear is measured in terms of the depth of material removed in time and is proportional to the local contact pressure computed from the Reynolds equation ( $p = p(x, y)$ , Eq. (B.29)) and the modulus of the relative sliding velocity  $\|\mathbf{v}_r\|$  (described in Chapter B.3.1.1) by the specific wear rate  $k_w$  (described in Chapter B 3.1.2).

### B.3.1.1 The relative sliding velocity

One of the main assumptions on which the Reynolds equation is based is the no-slip condition, i.e., at the solid boundary, the slurry has the same velocity as the contact surface. It is straightforward that if the relative velocity is zero, no wear occurs at the surface.

The component of the velocity of the equivalent fluid in the x-direction has been identified in Chapter B.2 as  $u(x, y, z)$ . Each debris grain can be identified as a sphere of radius  $R_d$  and velocity  $u_d$  defined at its center of mass by the equivalent fluid's velocity  $u$  at the same position.

Looking at Fig. B-20 the velocity of the grain in contact with the matrix surface in the x direction is:

$$u_d(x, y) = u(x, y, h - R_d) \quad (B.33)$$

The relative velocity in the x-direction is written locally as the difference between the velocity of the upper surface  $u_2$  and the velocity of such a debris grain  $u_d$

$$u_r(x, y) = u_2 - u_d(x, y, h - R_d) \quad (B.34)$$

This equation assumes that the wear debris rotation is negligible due to their interlocking and their angular shapes. The relative velocity  $v$  in the y-direction  $v_r(x, y)$  is defined in the same way as in Eq. (B.34), considering that  $v_2 = 0$ . Therefore, the modulus of the relative velocity, defined as in Eq. (B.18), is:

$$\|v_r\| = \sqrt{u_r^2|_{z=h-R_d} + v_r^2|_{z=h-R_d}} \quad (B.35)$$

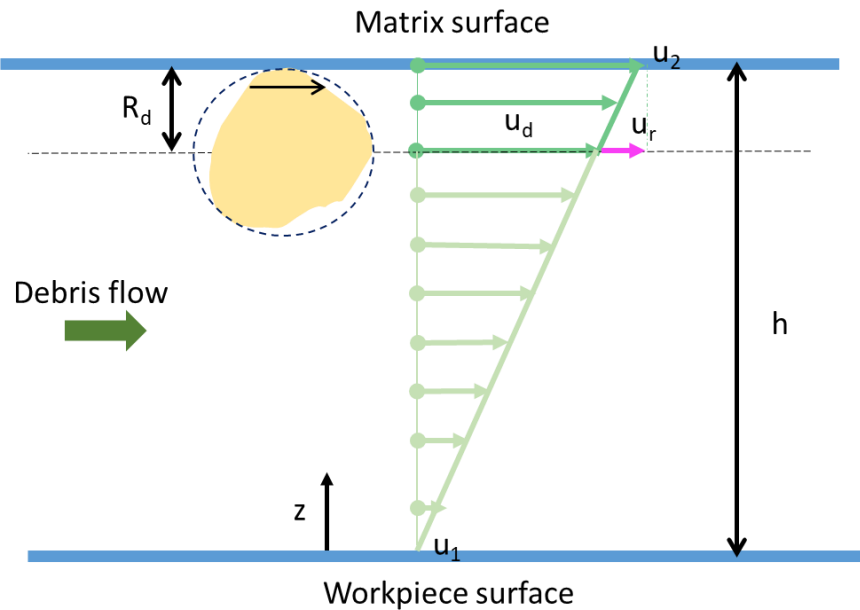


Fig. B-20 Definition of the relative velocity  $u_r$  between debris and the contact surface. The surface has a sliding velocity  $u_2$  and the grain of debris is moving with velocity  $u_d$

### B.3.1.2 On the definition of the specific wear rate

The strict Archard character of Eq. (B.32) is still restricted to the case where  $k_w$  is constant. This might not always be the case, as it is discussed here for the wear of diamond tools. For instance, a multiscale strategy is proposed by Waddad and co-workers [107] to study the thermodynamic behavior of complex systems; herein, the specific wear rate is obtained as a function of the temperature.

In this thesis, the variability of the specific wear rate is also investigated. In particular, it is based on a multiscale approach that, starting from the local contact asperity and by analogy with the multipass scratch test (Chapter B.1.2), defines the wear resistance of the matrix to the continuous passage of debris grains. In this direction,  $k_w$  includes the local properties (size and shape) of abrasive grains, the load distribution, and the microstructure's scratch hardness. The main multiscale strategy first considers the contact between the debris flow and the surface and then uses the definition of the characteristic asperity  $r_d^*$ , it is schematized in Fig. B-21.

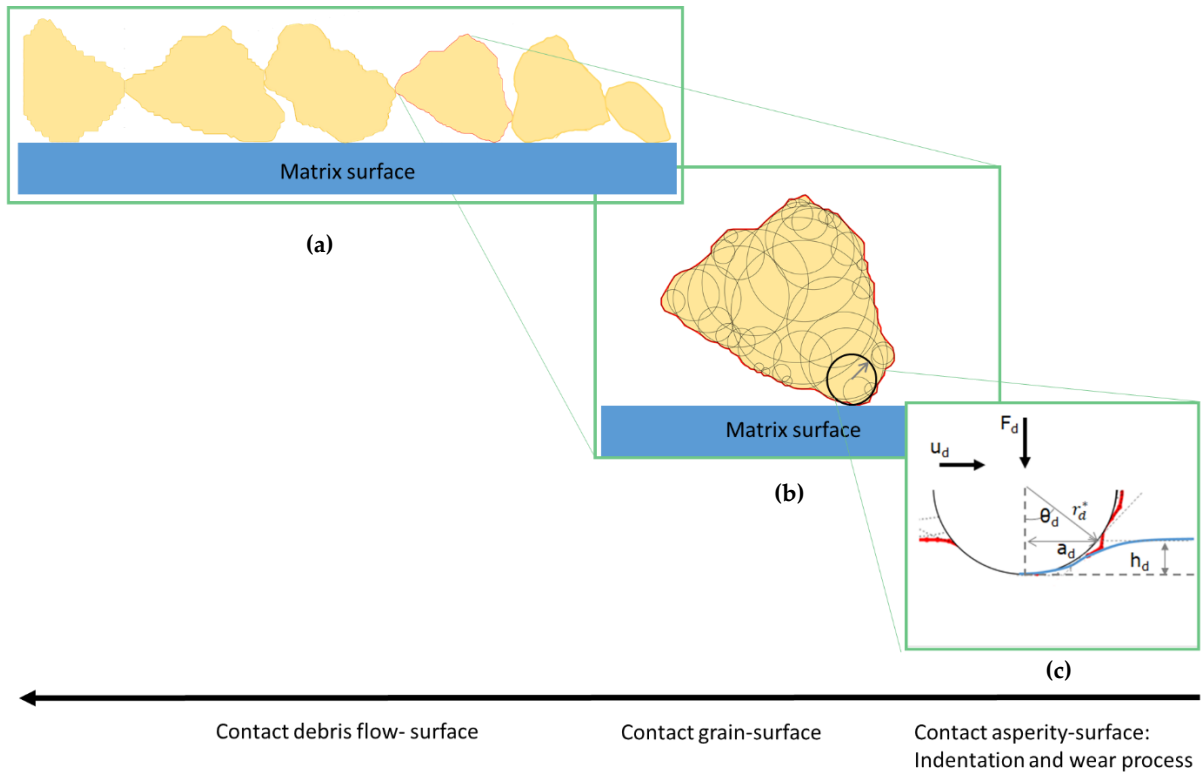


Fig. B-21 Multiscale strategy for the wear equation: **(a)** the contact debris flow-surface; **(b)** the contact of debris grains-surface; **(c)** the local contact of the debris asperity and the surface. The central figure **(b)** also shows the definition of the angularity and the circle defined by the characteristic asperity  $r_d^*$  (in black) considered in the figure at the bottom right **(c)**

### *Effect of angularity of debris grains*

At the scale of the interface debris flow-matrix surface, debris grains are considered perfectly rounded (with a radius equal to the mean radius of the circumscribed circumference  $R_d$ ), neglecting the local features of their shapes (Fig. B-20). This assumption is a useful simplification to compute flow properties. However, grains are not spherical but exhibit some contour irregularities that strongly influence abrasive wear. As introduced in Part A, the shape of abrasives is a characteristic feature of the wear phenomena. Several attempts have been made to quantify and correlate it to the specific wear rate; nevertheless, the impact of grains shape remains a challenge.

Also, there is no unique definition of debris angularity. J.-F. Ferrellec and G.R. McDowell [108] proposed creating complex particle shapes with spheres and using them for DEM simulations. This method consists of filling a particle with  $n_c$  spheres of radius  $r_d$ . Then, Mollon and Zhao [29] defined roundness as:

$$RF = \frac{\sum r_d}{n_c \cdot R_{insc}} \quad (B.36)$$

and used that definition to create realistic 2D samples, substituting spheres with circles ( $R_{inisc}$  is the radius of the maximum inscribed circle). This methodology is useful to describe debris grains with their realistic shape and size and is a topic of Part C.

For the present chapter, this approach is used to define the characteristic asperity of debris grains able to indent and abrade the matrix surface. For this purpose, 34 grains are extracted from Fig. B-2 (a) and analyzed considering their 2D projection. After binarization and the application of a median filter to reduce the influence of noise on the contour, their shape is filled with circles, as explained before. The number of circles describing each grain is controlled by balancing the calculation time and accuracy level. This optimum is reached by defining three main threshold parameters. The complete procedure is described in Annex I.

Sharpness has been defined in [109] as a measure of the capacity of a body to cause material removal in another body by its shape alone. Accordingly, not all the circles that fill the grain represent the abrasiveness, but only those that describe the local asperities. The statistical analysis on the whole radii data-set shows that the sample is represented by a lognormal distribution, whose peak defines the radius of the characteristic asperity carrying the grains' abrasive power  $r_d^* = 0.073 \mu\text{m}$ . The SEM micrograph is reported in Fig. B-22 together with the overall methodology used.

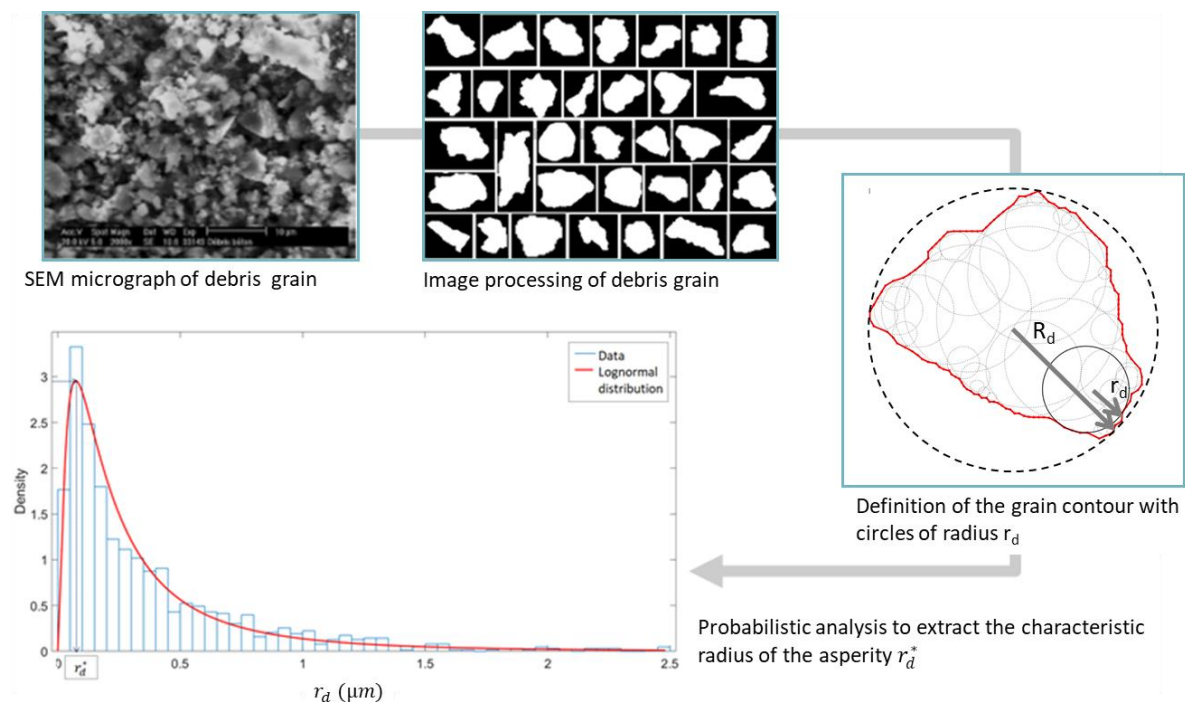


Fig. B-22 Method to find the characteristic asperity

The characteristic radius of the asperity controls the local features of the wear process with significant influence in the macroscopic wear. In particular, assuming the perfectly plastic condition, there is no elastic recovery after the deformation. The wear volume per unit sliding

distance (i.e., the cross-sectional area of the groove) is represented by the equation [13], [88], [89]:

$$V_d = \frac{r_d^{*2}}{2} \cdot (2\theta_d - \sin 2\theta_d) \quad (B.37)$$

Where the local attack angle  $\theta_d$  defined as in Fig. B-21 (c), writes as:

$$\theta_d = \arcsin \frac{a_d}{r_d^{*2}} \quad (B.38)$$

With  $a_d$  the half contact width.

Eq. (B-37) assumes that the shape of the scratch is conformal with the shape of the indenter, for a spherical tip, like a portion of a cylinder (Fig. B-23). In other words, the model assumes that the main abrasive wear mechanism is the cutting, i.e., all the material detached from the matrix surface is worn away and not simply displaced on the lateral edges.

The value of  $a_d$  can be computed considering the characteristic local asperity as an indenter able to scratch the surface under a well-defined load  $F_d$  and moving on the plane direction, such that locally, for those above fully plastic deformation, no load-bearing supports the rear half of the tip [86] therefore, locally, the debris grain is in contact only over its front surface, covering a contact area equal to  $\frac{\pi a_d^2}{2}$ .

$$F_d = p_m \cdot \frac{\pi a_d^2}{2} \quad (B.39)$$

Where  $p_m$  is the mean contact pressure. It was seen experimentally [7] that, in fully plastic conditions,  $p_m$  is almost equal to the indentation hardness. During the scratch test the tip is moving in the tangential direction, this allows to consider the scratch hardness  $H_s^*$  (computed as in Eq. (B.7) and assumed as representative of the hardness during multipass) equal to the mean contact pressure [13].

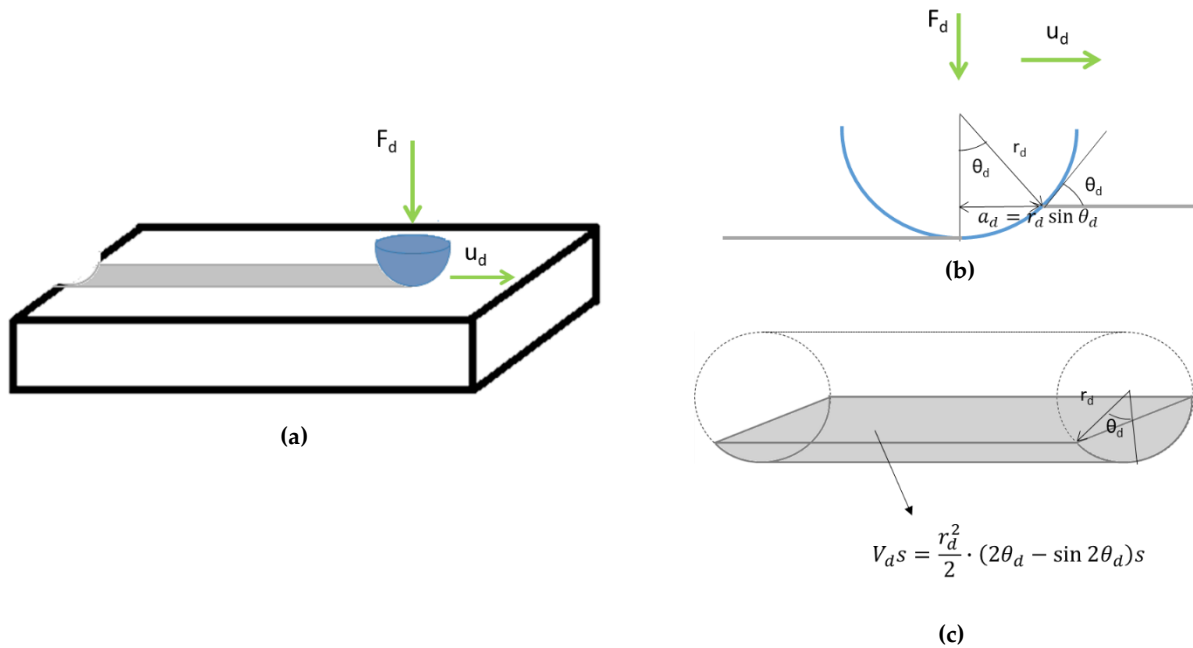


Fig. B-23 A Schematization of the contact between a spherical tip and a surface: (a) perspective view; (b) vertical section; (c) transversal section

### The contact grain-surface

The model described here provides a qualitative and quantitative description of wear at the scale of diamond starting from observations at debris scale.

According to the Archard wear equation, each debris grain is able to abrade the contacting surface removing a volume per unit sliding distance that is proportional to the load transmitted. The proportionality is expressed in terms of specific wear rate  $k_w$ , defined as in Eq. (B.31) with  $V_d$  and  $F_d$  are defined as in Eq. (B.37) and Eq. (B.39), respectively.

The angle of attack  $\theta_d$  and the contact width  $a_d$  are related by Eq. (B.38).

The value of  $\theta_d$  is an indicator of the main abrasive wear mechanisms involved. As already seen, ploughing, cutting, fatigue, and erosion are involved in different percentages in different wear zones. The cutting phenomena are predominant in the protrusion zone. It seems reasonable to introduce the variation of the attack angle as a function of the pressure exerted by the debris flow, which is higher close to the diamond (where a significant wear process occurs). Each debris grain transmits a local normal load  $F_d$  as a function of the contact pressure coming from Eq.(B.25), acting over a characteristic square contact surface  $4R_d^2$ :

$$F_d = p(x, y) \cdot 4R_d^2 \quad (B.40)$$

By substitution of  $F_d$  in Eq. (B.39), it is possible to obtain the value of half contact width  $a_d$  at every contact location and obtain the corresponding values of  $\theta_d$  from the Eq. (B.38).

Under these conditions, the specific wear rate can be written as:

$$k_w = \frac{(2\theta_d - \sin 2\theta_d)}{\pi \cdot \sin^2 \theta_d} \cdot \frac{1}{H_s^*} \quad (B.41)$$

With  $\theta_d = \theta_d(x, y)$ .

It should be noticed here that the scratch hardness is a constant for the matrix, while the angle  $\theta_d$  is varying in space and time as it depends on the field of pressure that is variable along the surface and during the wear process.

The introduction of the pressure in the definition of specific wear rate  $k_w$  leads to an expression of the wear equation that is not a simple Archard formulation but also considers the local effect of the pressure at the scale of debris grains. The specific wear rate obtained has a local character that can be projected to the global scale of the contact interface, i.e., the model's scale. This scale jump is a key step of the model and is possible by the Eq. (B.41), which allows considering the overall wear volume per unit sliding distance  $V_{slurry}$  (own to the total amount of  $n$  individual debris grains of the slurry passing on the surface) equal to the sum of the wear contributions  $V_d$  related to each of them, and the total normal load  $F_{slurry}$  as the sum of the normal loads  $F_d$  carried by each debris particle in contact with the matrix surface, respectively:

$$V_{slurry} = \sum_{d=1}^n V_d \quad (B.42a)$$

$$F_{slurry} = \sum_{d=1}^n F_d \quad (B.42b)$$

$V_d$  and  $F_d$  are related by the specific wear rate  $k_w$  as in eq. (B.31) for the Archard adhesive equation.

The wear of the matrix surface is expressed in terms of the Archard type equation, where the wear rate  $\frac{dh}{dt}$  is related to the pressure  $p(x, y)$  computed in Eq. (B.29) and the modulus of the velocity  $\|\mathbf{v}_r\|$  at the contact surface, Eq. (B.35), by the specific wear rate  $k_w$  (Eq. B-41):

$$\frac{dh}{dt}(x, y) = k_w(x, y) p(x, y) \|\mathbf{v}_r(x, y, \mathbf{h} - \mathbf{R}_d)\| \quad (B.43)$$

### B.3.2 Numerical coupling of Reynolds equation and wear equation

The resolution of the wear equation in time is performed using an implicit Backward Differentiation Formula (BDF) [110], [111], which requires a convergence to attain the solution (due to the high non-linearity of the problem) but is numerically more stable than an explicit solver. The solver uses an adaptive time step with a maximum value equal to 10 s to assure convergence. All the load applied to the machine is carried by the diamonds to cut the workpiece. The debris grains exercise pressure to the contacting surface, studied numerically in terms of the Reynolds equation. The coupling between the Reynolds equation and the wear equation is explained in the flowchart in Fig. B-24. The variation of pressure is instantaneous compared to the time necessary to adapt the surface at the new configuration; therefore, the variation of pressure in time is only due to the variation of the surface profile  $h_i$ .

It is important to notice that, to satisfy the assumption of intact diamond during the process, the wear equation is applied only on the surface of the binder; therefore (see Fig. B-13(c)):

I. on the diamond surface:

$$\frac{dh}{dt} = 0 \quad (B.44a)$$

If:

$$h(x, y, t) \geq h_D(x, y)$$

II. on the matrix surface:

$$\frac{dh}{dt} = k_w(p_i) \cdot p_i \cdot \|\vec{v}_r\| \quad (B.44b)$$

If:

$$h(x, y, t_i) \geq h_{c,0} \quad \text{and} \quad h(x, y, t_i) < h_D(x, y)$$

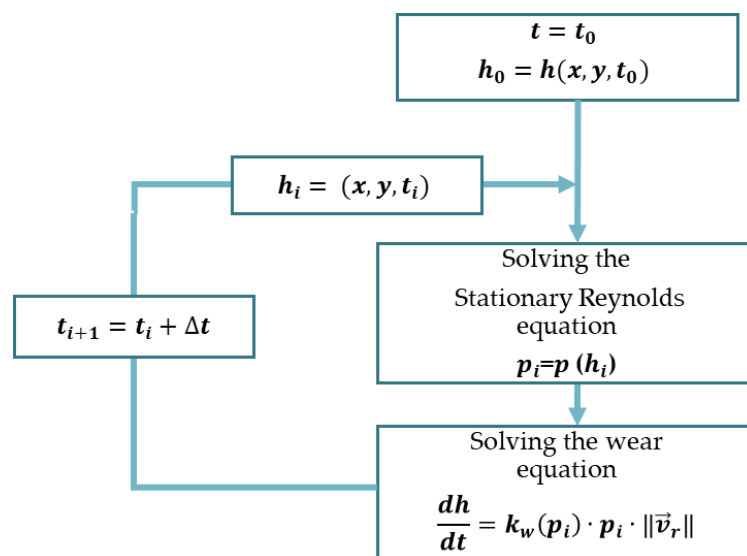


Fig. B-24 Flowchart of numerical coupling between the Reynolds equation and the wear equation

### B.3.3 Conclusions

The wear equation proposed here is based on the Archard wear formulation overcoming its limitations that derive from reducing the specific wear rate to a simple coefficient open to several interpretations. The new definition derives from observations at the single asperity scale and introduces the role of debris sharpness in the wear process. A characteristic grain is defined by the radius  $r_d^*$  of the characteristic asperity and radius  $R_d$  equal to the average grain radius of the population tested. The specific wear rate can be defined at the scale of the contact between such grain and the surface.

The variability of the specific wear rate is given by the angle of attack responsible for the wear mechanisms, which depends on the pressure field exerted by the debris flow close to the diamond. Then, assuming that the overall wear process is the sum of the contributions due to each particle, the specific wear rate is projected at the scale of the interface. Here the wear equation is written in terms of depth of material removed, deriving the classical formulation in time.

Another limit of the standard formulation of the Archard equation is that the hardness does not account for the multipass behavior. The description used here is based on the multipass scratch test that accounts for the low load and the repeated passing of an indenter, simulating the processing observed in the industrial application.

## B.4

# Wear analysis of the surface

The coupling between the Reynolds equation (Chapter B.2) and the wear equation (Chapter B.3), as well as the implementation of the experimental measures (Chapter B.1), allows defining a model able to predict wear at the scale of the continuum. The validation of the model is performed here, starting from experimental evidence of wear from the core drilling test (section B.4.1) and discussing the numerical results (section B.4.2). Finally, section B.4.3 compares the experimental and numerical evidence of wear with relevant conclusions about the model qualitatively and quantitatively.

### B.4.1 Experimental observation of wear around one diamond

The core-drill test is associated with the (initially) non-destructive observation of diamonds on the segment to follow the wear of the metallic matrix during the cutting process. The tool consists of eight diamond segments brazed on a 102 mm diameter steel core barrel [28], [42]. The main cutting and material parameters related to a cutting operation are given in Tab. B-8 and Tab. B-9, respectively.

Tab. B-8 Main standard parameters for a drilling operation [42]

Cutting Parameters		
Tool diameter	102	mm
Metal matrix	Cobalt	
Material to be cut	Concrete	
Volume of material cut	280	cm <sup>2</sup>
Diamond concentration*	30	
Diamond size**	40/50	mesh
Number of diamonds per segment	44	
Segment surface	91	mm <sup>2</sup>
Number of segments	8	
Angular velocity	500	rpm
Linear (drilling) velocity	2,67	m/s
Mean cutting speed	0,4	mm/s
Applied Vertical Force	2,5	kN
Water flow	50	l/h

\* 1,32 carat/cm<sup>3</sup>; \*\* 300/375 μm

Tab. B-9 Main debris and matrix parameters for a drilling operation [42]

Debris and Matrix Parameters		
Water/debris (mass ratio)	40/50	
Debris grain average diameter	20	$\mu\text{m}$
Matrix grain size (before sintering)	2	$\mu\text{m}$
Matrix grain size (after sintering)	2,3	$\mu\text{m}$
Vickers Hardness	299	HV10

Fig. B-25 (a) shows a crater in front of the diamond and a tail behind it. Two main zones characterize the crater: clearance and protrusion zone (C-zone and P-zone, respectively) measured as in Fig. B-25 (b). The clearance was already introduced in Chapter B.2 to define the initial gap thickness occupied by the slurry. More precisely, during the cutting process, the relative height of clearance  $h_{c,i}$  is measured far enough from the diamond and in terms of the clearance  $Cl$  with respect to the height of the diamond tip  $d_i$  at the  $i^{\text{th}}$  time instant:

$$h_{c,i} = |Cl_i - d_i| \quad (C.45)$$

The evolution of the height  $h_{c,i}$  with time during the cutting process (Clearance Wear Rate, or CWR) represents the matrix wear rate under a linear swarf flow. The clearance allows the diamond to penetrate the material and to carry out debris. In the same way as for the clearance, close to the diamond in the upstream direction, the relative protrusion  $h_{p,i}$  is defined as the height of the protrusion  $Pr_i$  with respect to the height of the diamond tip  $d_i$  at the  $i^{\text{th}}$  time instant:

$$h_{p,i} = |Pr_i - d_i| \quad (B.46)$$

The evolution of  $h_{p,i}$  during the cutting process (Protrusion Wear Rate, or PWR) represents the matrix wear rate under a flow disturbed by the presence of the diamond. The definition of CWR and PWR are displayed in Fig. B-25 (b), considering three different times  $t_i$ .

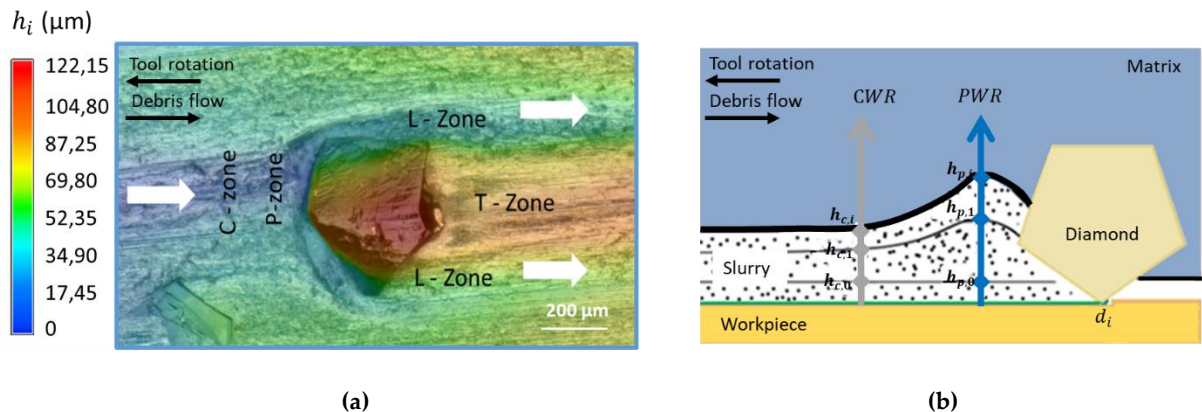


Fig. B-25 (a) Wear zones around one diamond during drilling; (b) Definition of PWR and CWR (inspired by [28])

The slurry can then flow around the diamond, generating a lateral zone of wear and a tail (L-zone and T-zone, respectively, in Fig. B-25 (a)) before being transported out of the segment. The lateral wear rate (LWR) and the tail wear rate (TWR) are defined in the same way as the PWR and the CWR considering as reference height the diamond tip  $d_i$ . In the following, attention is paid to the clearance and protrusion zones, which define a quantitative measure of wear in terms of depth of material removal.

Observation conducted by UMICORE by optical microscope showed different wear mechanisms (micro-cutting, micro-fatigue, micro-ploughing, and erosion, see Section A.2.4) are involved in different proportions in the four wear zones. Micro-cutting, microcracking, micro-ploughing, and micro fatigue are the main mechanisms involved in the clearance zone. In the protrusion zone, the predominant wear modes are micro-cutting, microcracking, and micro fatigue, with some erosion processes own to the debris striking the surface. In the lateral zone, the micro fatigue mode (caused by the continuous passage of debris) and the erosion mechanism are predominant, while the tail is subjected to fatigue and blast erosion. Experimental evidence shows that erosive wear has marginal importance, secondary to the abrasion [112].

The presence of different wear zones can be related to the attack angle of the indenter particle on the surface, which increases going from ploughing to cutting (see section A.2.4). Even if the model proposed here gives a macroscopic response of the material, the wear equation proposed in Eq. (B.43) includes the effect of the attack angle  $\theta_d(p(x, y, t))$  on the measure of wear. Moreover, as explained in A.2.5, diamonds' distribution plays an essential role in the protrusion wear rate.

For a fair comparison with the numerical results described in the next section, isolated diamonds are chosen, i.e., those not shielded by nearby diamonds that can influence the incoming flow. Considering the segment in Fig. B-26, three diamonds are labeled as S1D1, S1D2, and S1D3, respectively. S1D1 and S1D2 are emerging after 380 s, while S1D3 emerges after 747 s from the beginning of the test. The diamonds S1D1 and S1D3 are close to the internal border of the segment, while S1D1 is located in the central part.

The wear process observed is in good agreement with what is observed in literature in terms of diamond retention during sawing and drilling [54]: starting from the emergence of a new diamond on the surface, the main wear phases of the matrix wear around one diamond can be related to the wear process of the diamond itself which follow the entire life of a diamond from the emerging to the pullout and are defined as: the polishing, fracturing, cracking and pull out. They are well defined qualitatively and quantitatively in Fig. B-27 for the diamond S1D2. Here, considering  $t_i = \tilde{t}_i - \tilde{t}_0$ , the reference time is set to  $t_0 = 0$  s in the early emerging of the diamond ( $\tilde{t}_0 = 380$  s after the cutting process in Fig. B-26).

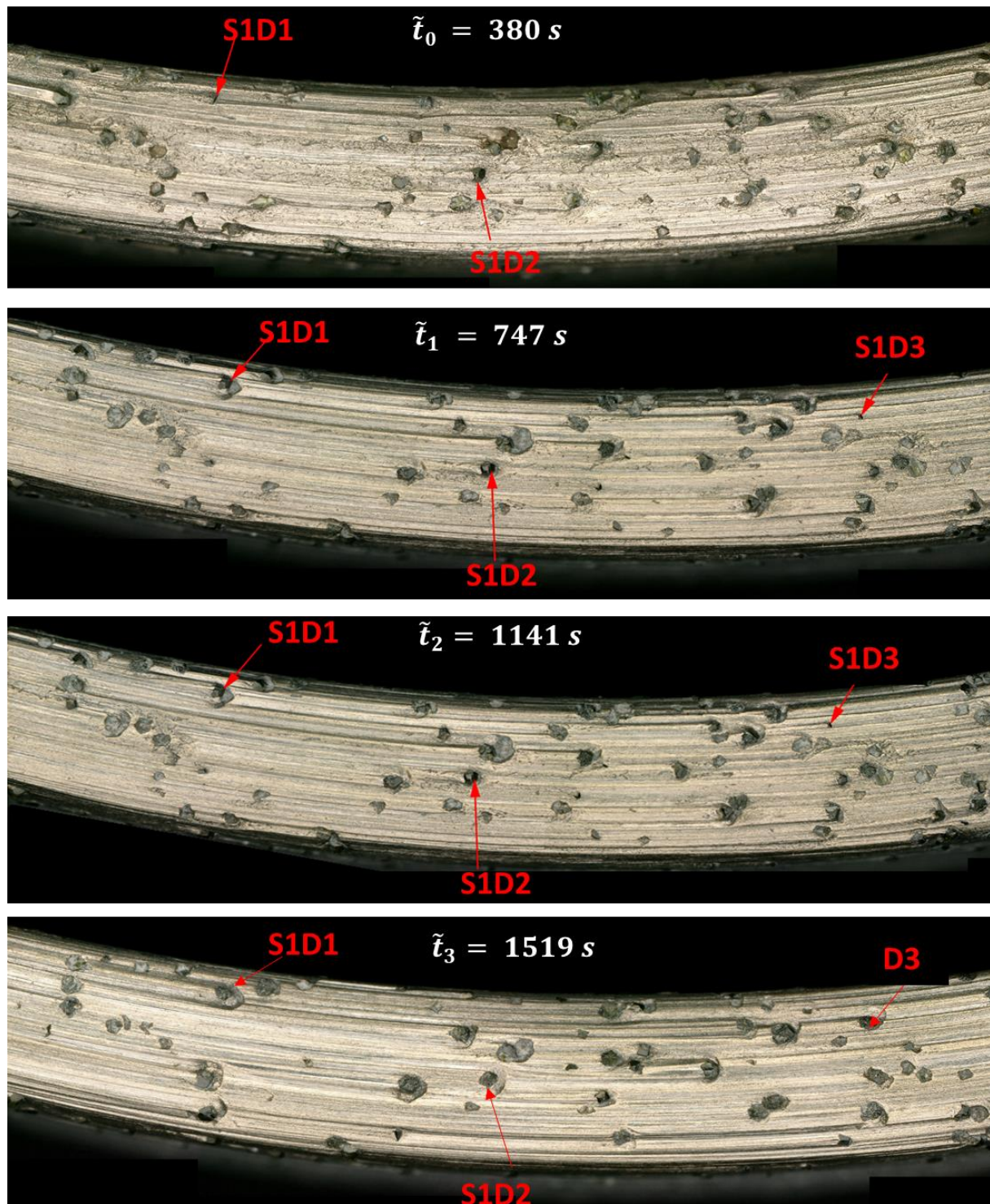


Fig. B-26 Segment surface observed by the optical microscope at different time steps during drilling, and indications of the three diamonds analyzed (kindly granted by USPF)

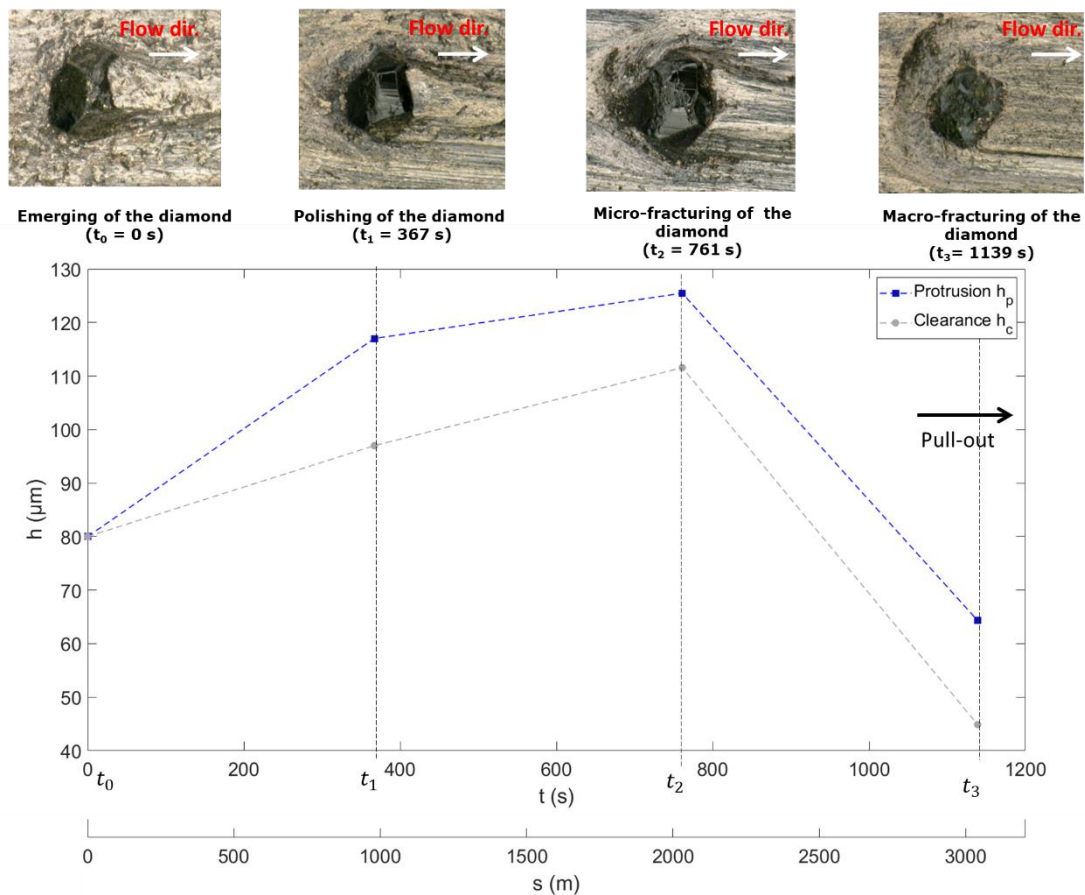


Fig. B-27 Top: Micrographs of the diamond S1D2 (kindly granted by USPF) from its emerging to the pull-out. Bottom: the evolution of the height of the protrusion  $h_p$  and clearance  $h_c$  with time  $t$  and sliding distance  $s$  (sliding velocity = 2.67 m/s, see Tab. B-8)

#### *Emerging + Polishing of diamond (from $t_0 = 0$ s to $t_1 = 367$ s)*

The diamond starts to emerge above the matrix surface in the emerging stage, exerting the best retention. At  $t_0 = 0$  s, protrusion and clearance groove are almost the same. The diamond cutting ability is not yet well developed since the diamond indentation in the workpiece is in its early stage. The matrix is worn away by three-body abrasion contact, allowing the entire diamond to appear with minimum surface damage and best cutting performance.

#### *Micro and Macro-Fracturing of diamond (from $t_1 = 367$ s to $t_3 = 1139$ s)*

During processing, the matrix is continuously subjected to abrasion and erosion in the debris-removing direction until it can no longer support the diamond, which in turn starts to damage in terms of micro-cracks and micro-fractures ( $t_2 = 761$  s). Wear progression leads to a completely damaged diamond ( $t_3 = 1139$  s). The cutting ability is reduced together with clearance and protrusion. If the diamond starts to fracture, the height of the diamond  $d_i$  decreases, leading to a reduction of the wear measured as in Eq. (B.45) and Eq. (B.46).

The diamond fracture explains the reduction in terms of wear rate.

*Pull-put phase (  $t_i > 1139$  s )*

The progressive reduction of the diamond retention leads to the diamond pull out, followed by the two-body abrasion between matrix and rock until new diamonds are exposed to the cutting face.

The same study is made for the other two diamonds S1D1, S1D3, displayed respectively in Fig. B-28, Fig. B-29.

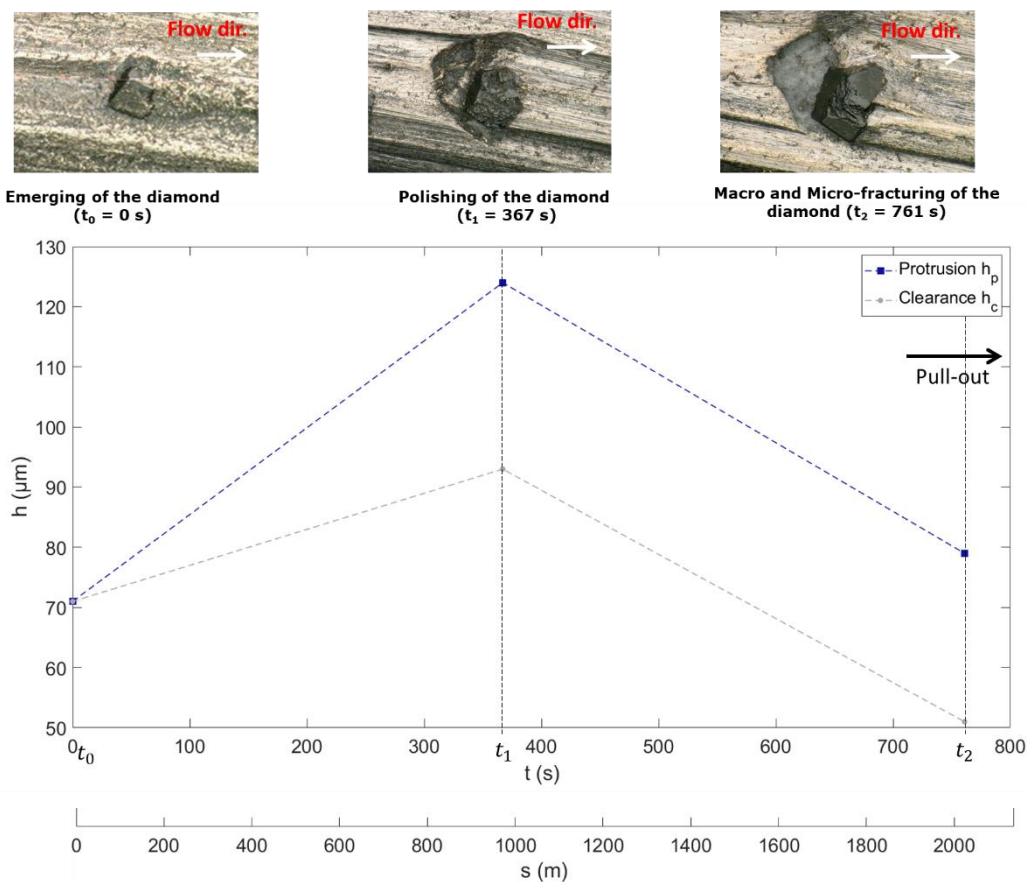


Fig. B-28 Top: Micrographs of the diamond S1D1 (kindly granted by USPF) from its emerging to the pull-out.

Bottom: the evolution of the height of the protrusion  $h_p$  and clearance  $h_c$  with time  $t$  and sliding distance  $s$  (sliding velocity = 2.67 m/s, see Tab. B-8)

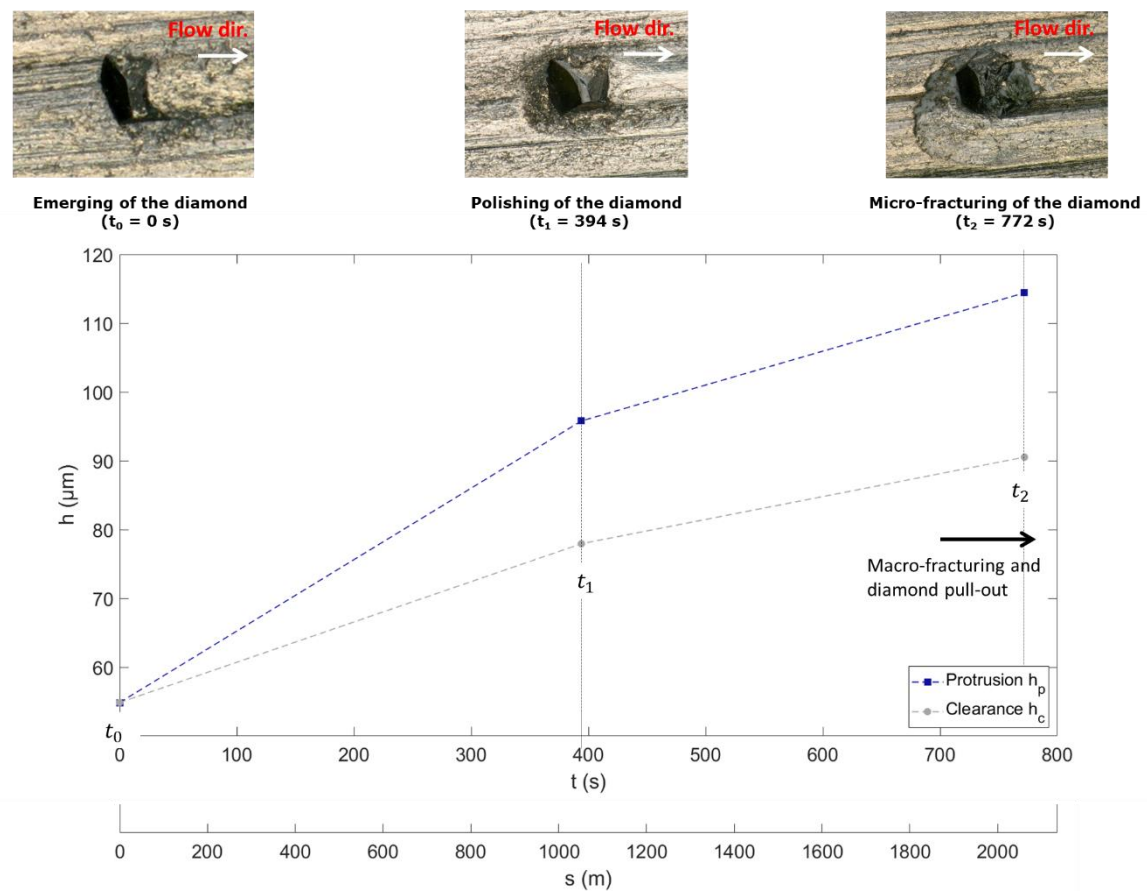


Fig. B-29 Top: Micrographs of the diamond S1D3 (kindly granted by USPF) from its emerging to the micro-fracturing of a diamond. Bottom: the evolution of the height of the protrusion  $h_p$  and clearance  $h_c$  with time  $t$  and sliding distance  $s$  (sliding velocity = 2.67 m/s, see Tab. B-8)

The diamond S1D1 is activated simultaneously as S1D2 ( $\tilde{t}_0 = 380$  s in Fig. B-26) but shows a high wear rate in the polishing stage and an earlier diamond fracture than the S1D2. Diamond S1D3 is activated at  $t_0 = \tilde{t}_1$  (see Fig. B-26). Then, taking  $\tilde{t}_1$  as the reference time, the diamonds protrude with almost the same PWR and CWR as S1D2 from  $\tilde{t}_1$  to  $\tilde{t}_2$  ( $t_1 = 394$  s in Fig. B-29). Then the diamond starts to break, and the matrix continues to protrude. However, the wear rate slightly decreases, as seen for S1D2 because of the diamond fracture.

Previous analysis performed by Umicore has shown a slight dependence on the wear rate to the position of the diamond within the segment: the matrix wear rate is higher in the inner part and decreases going towards the outer edge (Fig. B-30). This appearance may justify the high wear rates obtained for S1D1 compared to the others.

The fracturing of diamond makes it challenging to measure wear rate as it is defined in terms of groove from the diamond tip: if the diamond breaks, the reference point of the measures changes. For this reason, experimental measures prove a reduction in terms of wear rate in time. As this work is focused only on the wear of the matrix, only the first polishing phase is

considered representative of the physics, where wear observation is not much “disturbed” by the fracturing of the diamond.

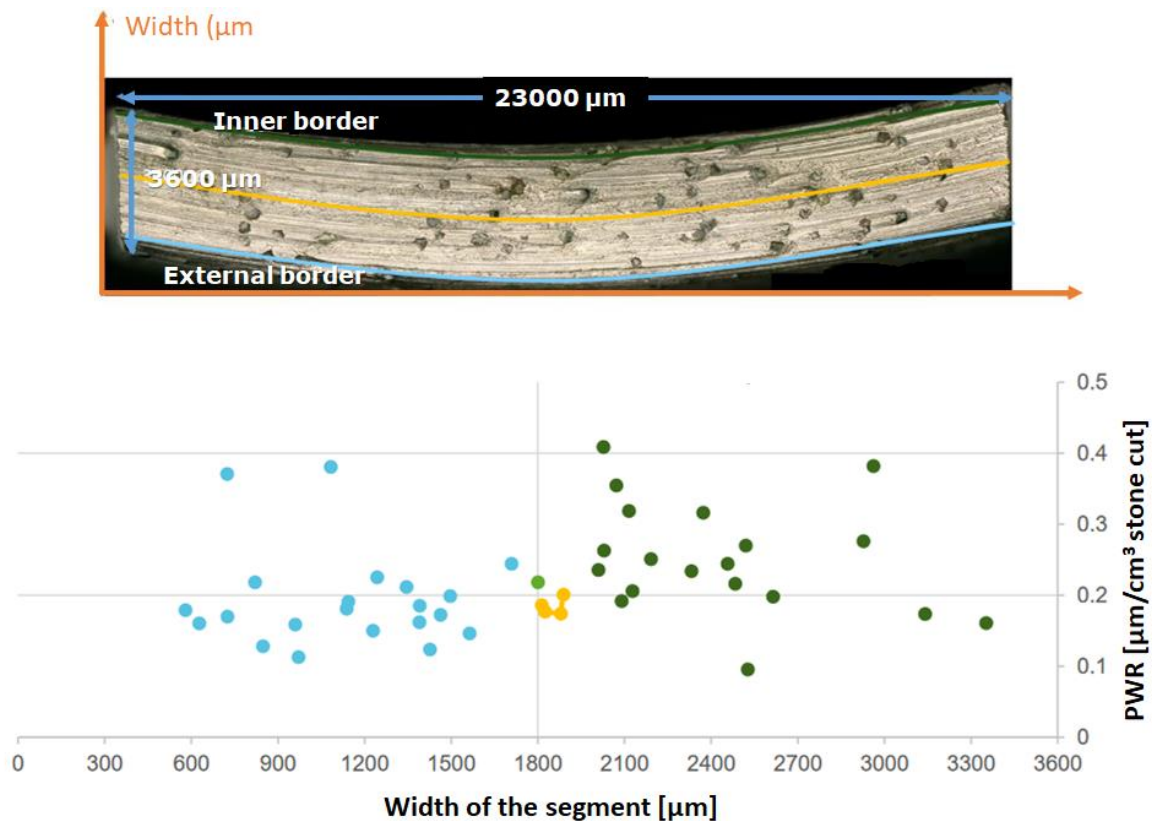


Fig. B- 30 Effect of the diamond position on the PWR measured in  $\mu\text{m}/\text{cm}^3$  stone cut ((kindly granted by USPF)

The protrusion and the clearance wear rate of the central diamond S1D2 are, respectively  $PWR = 0.038 \mu\text{m}/\text{m}$  and  $CWR = 0.017 \mu\text{m}/\text{m}$ . These values are in good agreement with those obtained by [28] in a previous experimental investigation ( $PWR = 0.042 \mu\text{m}/\text{m}$  and  $CWR = 0.020 \mu\text{m}/\text{m}$ ), thus allowing to consider the selected diamond S1D2 representative of the real physics and to use it for the validation of the numerical model.

### B.4.2 Numerical prediction of wear at the diamond scale

The coupling between the Reynolds equation Eq. (B.29) and the wear equation Eq. (B.43), discussed in Chapter B.3, is applied here. This study considers the viscosity of the slurry 3 ( $SF = 32\%$ , flow curves in Fig. B-5 and coefficient of the constitutive equation in Tab. B-6) and the geometrical parameter  $\frac{\delta_D}{h_{c,0}} = 0.01$  as justified in the stationary study performed in section B.2.6. The field properties obtained applying the Reynolds equation change with the solid fraction of the slurry with a clear transition from  $SF = 30\%$  to  $SF = 32\%$  (see the study in section B.2.6.2). It is difficult to define which one of the three slurries is representative of the real one obtained during the cutting operation. The choice of the slurry with  $SF = 32\%$  is

related to its particular non-Newtonian effects close to the diamond particle (Fig. B-17) where the protrusion occurs, and the increase in terms of pressure (Fig. B-15) that is responsible for the wear process as obtained from Eq. (B.43). For these reasons, we assume that the behavior of the slurry is close to the non-newtonian one, justifying the choice made here.

The initial thickness of the slurry is set to  $h_0 = h(x, y, t_0)$ , and is equal to the initial clearance groove found in the experimental observations (Fig. B-12). As this parameter is specific for each diamond, a first model is built considering  $h_{c,0} = 80 \mu m$ , corresponding to the diamond S1D2, which is the most representative of our basic simplifying assumptions, i.e., central and isolated diamond (Fig. B-26). The reader could refer to section B.2.6 for details about the simulation. Results obtained in this section come from a transient analysis to follow the wear process in time.

To better understand the non-linear character of the proposed wear equation, Fig. B-31 plots the attack angle  $\theta_d$  and the specific wear rate  $k_w$  computed as in Section B.3, as a function of the pressure at the time  $t = 0 s$  (corresponding to  $\tilde{t}_1$  of the cutting operation discussed previously in B.4.1) where the conditions in Eqs. (B.44) are fulfilled. As expected,  $k_w$  is not a constant in this range of pressures, indicating that the derived wear law is not, strictly speaking, an Archard law. The variations of  $k_w$  and  $\theta_d$  are caused by the variation of the pressure along the contact surface, which, in turn, is strongly dependent on the geometry: the increase of pressure close to the diamond leads to the increase of the attack angle for the Eqs. (B.38-40) and therefore, for Eq. (B.41), an increase in terms of specific wear rate  $k_w$ .

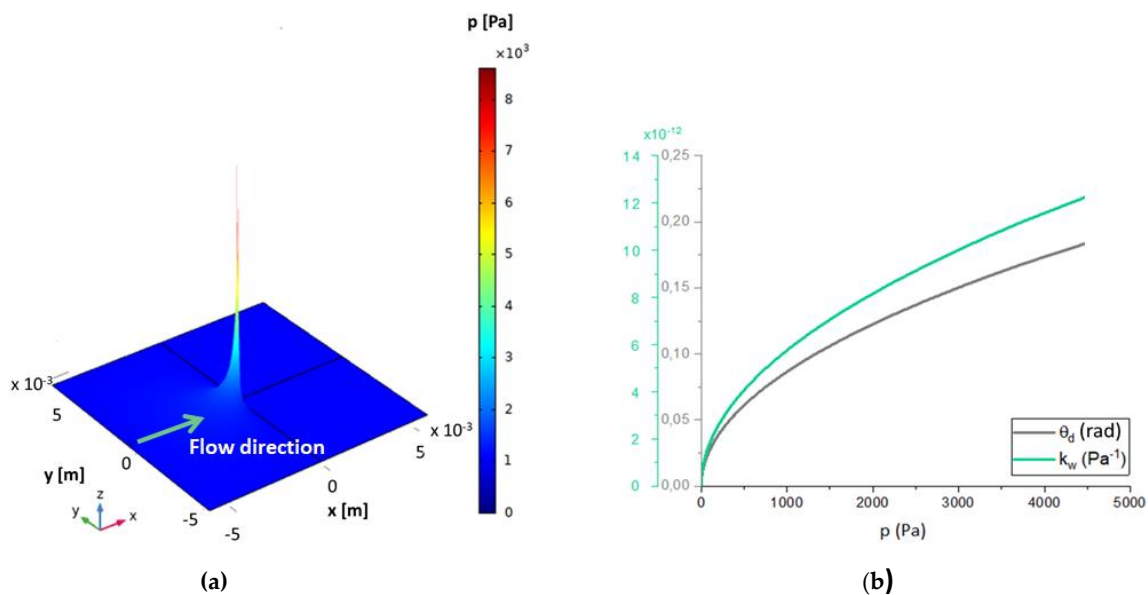


Fig. B-31  $t_0 = 0 s$ : (a) Pressure profile with the indication of the flow direction; (b) evolution on attack angle  $\theta_d$  and specific wear rate  $k_w$  with pressure

High values of attack angle  $\theta_d$  are expected close to the diamond, in the protrusion zone, inducing large values of specific wear rate. Fig. B-32 plots the specific wear rate for  $t_0 = 0 s$ ,  $t_1 = 367 s$  and  $t_3 = 761 s$ .

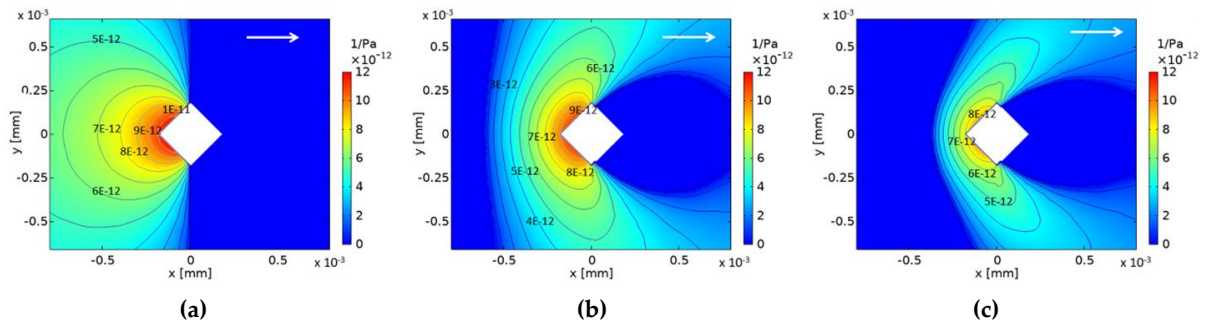


Fig. B- 32 Maps of specific wear rate  $k_w$  at the time: (a)  $t_0 = 0$  s; (b)  $t_0 = 367$  s; (c)  $t_0 = 761$  s

Notice that, as this study concerns only the matrix's wear, the maps corresponding to the diamond positions are not considered; moreover, only the pressure  $p \geq 0$  Pa is considered. The field of pressure is illustrated in Fig.B-33. As the wear of the matrix corresponds to the increase in the gap thickness occupied by the debris flow, a reduction of pressure is observed in time.

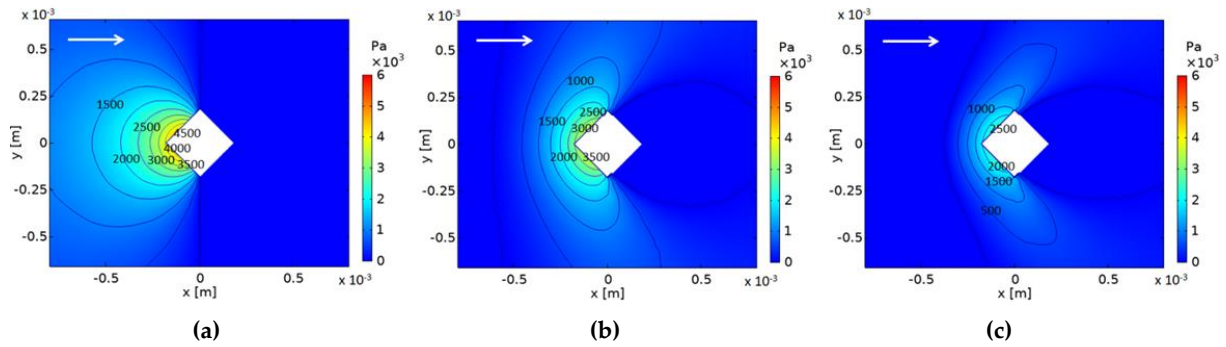


Fig. B-33 Maps of pressure  $p$  at the time (a)  $t_0 = 0$  s; (b)  $t_0 = 367$  s; (c)  $t_0 = 761$  s

Notice that both the specific wear rate  $k_w$  defined as in Eq.(B.41) and the velocity profile  $\|\mathbf{v}_r\|$  (see Eqs. B.34-35) depend on the pressure field obtained by Eq. (B.29). Considering the flow coming from the left to the right direction in Fig. B-33, at  $t_0 = 0$  s the pressure field is generated instantaneously, allowing calculation of the norm of the relative velocity  $\|\mathbf{v}_r\|$  and the specific wear rate  $k_w$ . Then, the numerical model updates the value of  $h$ , which is implemented in the Reynolds equation giving a new field of pressure and the depending variables  $k_w$  and  $\|\mathbf{v}_r\|$ .

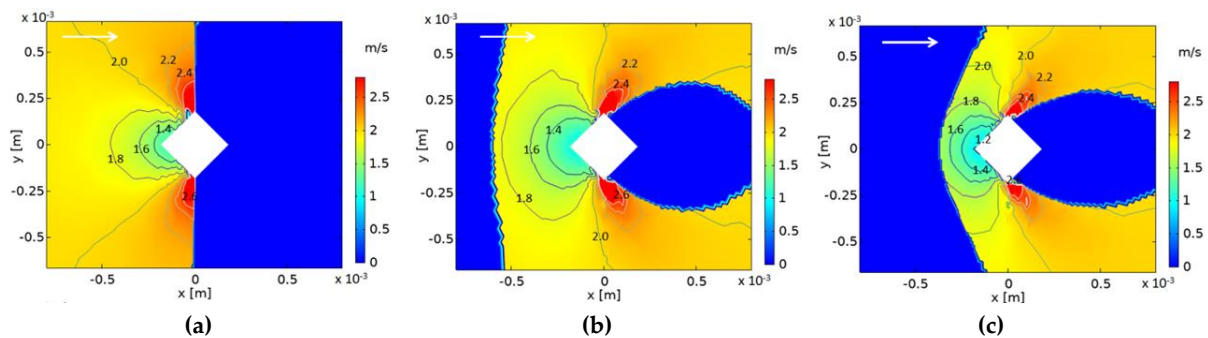


Fig. B- 34 Maps of relative velocity  $\|\mathbf{v}_r\|$  at the time: at the time: (a)  $t_0 = 0$  s; (b)  $t_0 = 367$  s; (c)  $t_0 = 761$  s

Fig. B-35 illustrates the wear of the matrix surface for the same instants in time as the experimental measures discussed in Fig. B-28. A first qualitative comparison shows a good agreement in terms of PWR and CWR; however, the lateral flow is not well developed in the numerical model (Fig. B-35). A possible explanation may be related to the drop of pressure on the side of the diamonds (Fig. B-33) that may lead to the underestimation of  $k_w$  (Fig. B-32). The protrusion zone close to the diamond is due to the combined effect of the pressure (Fig. B-33) and the velocity field (Fig. B-34).

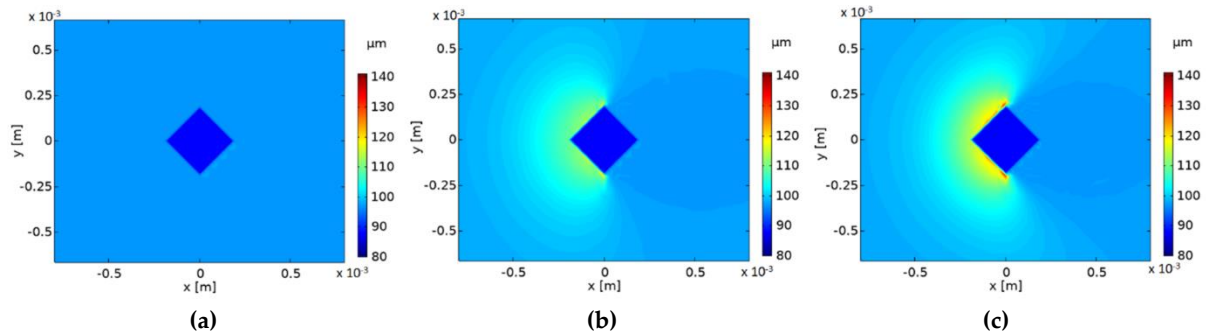


Fig. B-35 Wear of the surface of the matrix computed numerically at the time: (a)  $t_0 = 0$  s; (b)  $t_0 = 367$  s; (c)  $t_0 = 761$  s

One of the main assumptions of the model is that only one single diamond is considered active in the process, and the overall surface is still intact in the early stage of indentation. It means that the model ignores the previous history of wear and the diamond concentration and distribution. The surface of the segment is more complex than what is modeled numerically. Moreover, the fatigue effect due to debris grains' continuous passage may not be entirely well defined numerically.

### B.4.3 Comparison of experimental and numerical results

The qualitative matching in PWR and CWR is nevertheless confirmed quantitatively before diamonds start to fracture, as plotted in Fig. B-36. This good agreement is quite remarkable, given that all the physical parameters of the model were calibrated by independent experimental tests (i.e., scratch test, rheological test, and angularity characterization).

As discussed previously, the diamond is considered intact during the whole cutting process; therefore, we do not observe the reduction of the numerical wear rate beyond 1000-1500 m of sliding and the dramatic drop beyond 2000 m. Also, after reaching a peak, the pressure slightly decreases with time because of the development of the groove on the surface. This behavior leads to a slight reduction of the numerical wear rate that may reach a plateau as  $\frac{dh}{dt} \rightarrow 0$  if  $p \rightarrow 0$  for Eq. B-43.

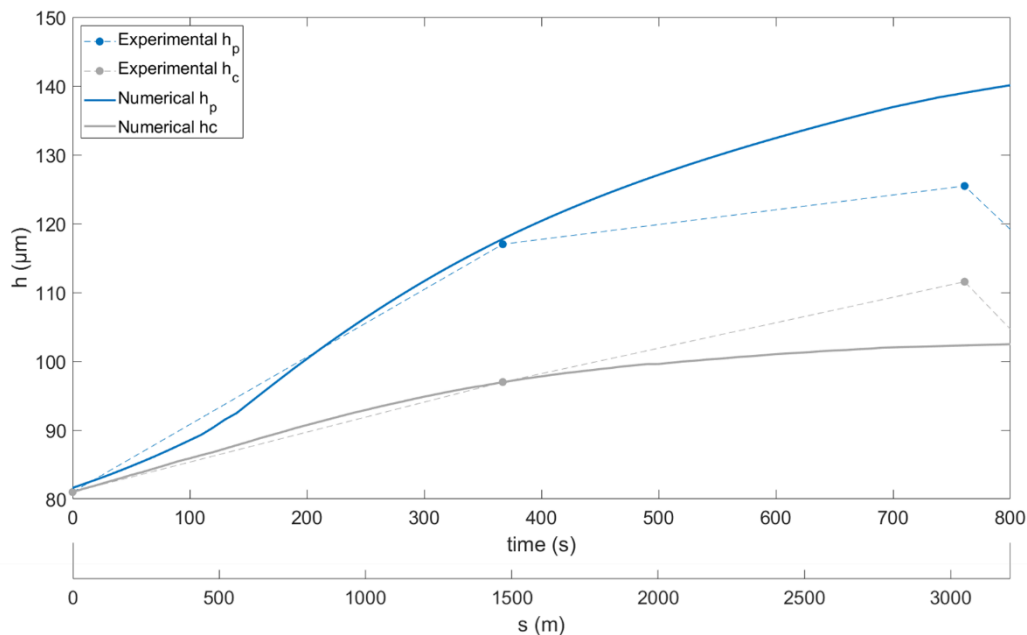


Fig. B- 36 Comparison between the numerical and experimental length of protrusion  $h_p$  and clearance  $h_c$ . The experimental point at  $t_3 = 761$  s is not reliable since diamond is undergoing microcracking that may change the reference of the diamond tip  $p_i$  in the evaluation of the length of wear. The comparison is therefore limited to the diamond polishing ( $t = 367$  s)

As this study aims to the wear analysis and prediction of the binder, we restrict our focus to the first stage of diamond retention, where a quasi-constant wear rate  $dh/dt$  is experimentally expected and numerically confirmed. Fig. B-37 displays the experimental wear rate  $h/t$  obtained as an average value of the three diamonds tested in B.4.1 and the numerical wear rate coming from the proposed methodology.

Keeping in mind that the optimum balance between free-cutting ability and wear of the surface can be reached by looking at the ratio between the PWR and the CWR, the model well matches the experimental values.

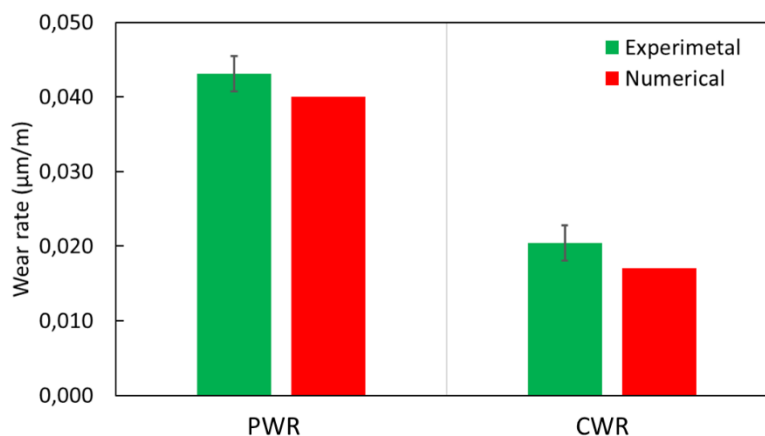


Fig. B- 37 Comparison between experimental and numerical wear rate in the early stage of cutting

Despite the simplifying assumptions on which the model is based, the wear in front of the diamond is well-defined both qualitatively and quantitatively, proving that the model can provide a satisfactory prediction of the wear of the binder considering only the flow properties of the slurry, the mechanical properties of the metallic surface (as characterized via a scratch test) and the typical morphology of the debris grains. This approach is performed without any a posteriori back-calibration on drilling tests and would thus be used with a certain level of confidence for tool design, once confined to other sets of calibration.

Tab. B- 10 Numerical and experimental wear rate in terms of PWR and CWR

	PWR ( $\mu\text{m}/\text{m}$ )	CWR ( $\mu\text{m}/\text{m}$ )	PWR/CWR
Experimental	0.043 (+/-0.003)	0.020 (+/-0.002)	2.11 (+/-0.08)
Numerical	0.04	0.017	2.35



## B.5

# Conclusions

The numerical models presented here can analyze the flow properties of the debris flow and the wear of the matrix surface.

The results obtained on a cobalt-based alloy with a well-defined slurry are in good agreement with the experimental observation of the material surface after the drilling process. The agreement is both qualitative in terms of the wear patterns on the surface and quantitative in terms of protrusion wear rate PWR and clearance wear rate CWR. It proves that, starting from an independent experimental setup consisting of a scratch test, a rheological test, morphological characterization, and making some physically sound scale changes, it is possible to describe and predict wear at the industrial application scale.

The first scale jump from scratch test to grain contact is assumed at equivalent mean pressure considering the scratch hardness as a metallic surface property. The second jump from the local to global contact allows us to compute the specific wear rate considering that the wear of the surface is own to the contribution of each debris grain and treating the slurry as equivalent fluid flow. The specific wear rate is a function of the local pressure exerted by debris grains; it increases with the abrasiveness of debris and decreases with the increase of the hardness of the surface. The sharpness of debris grain has a strong influence on the wear of the matrix. It should be noted that the indenter used in the scratch test is a Rockwell with a perfectly spherical tip of the radius of 100  $\mu\text{m}$ . It is, therefore, one order of magnitude larger than the radius of the abrasives and at least two orders of magnitude larger than their typical asperities. Another important aspect is that, at the diamond scale, no relative velocity is considered between the slurry (treated here as an equivalent fluid) and the matrix surface. The slip effect is considered by looking at the scale of the debris grain in contact with the surface. The geometrical model consisting of a single square-based central diamond is a strong simplification of reality. However, experimental evidence shows that the wear is much more affected by the mechanical properties of the surface than by the geometry of the diamonds. Diamonds retained by the same metallic binder but with differences in orientation and size, as well as in terms of clearance and protrusion with respect to the surrounded matrix, have compatible wear rates.

The numerical study presents some limitations in predicting the lateral wear that can be overcome considering other diamonds and a realistic topology of the segment surface or by

improving some of the basics assumptions. However, results are quite satisfactory in terms of PWR and CWR, meaning that the complex phenomena can be well described numerically by this multiscale approach. Also, the correlation between pressure, attack angle and wear rate is not only consistent with the physics of the cutting process of DIT, but it may also be generalized to other situations where abrasive particles have different normal loads. A great challenge is also to adapt the model to other tribological situations consisting of the wear of a soft surface caused by a flow of abrasive particles.

The strategy here discussed is a useful tool to predict wear at the scale of diamond indentation. The wear equation is based on a multiscale approach, and wear is measured in terms of protrusion and clearance wear rate, which are useful indicators in selecting a metal matrix. However, the numerical model simplifies the complexity of the matrix and does not account for the main properties of the microstructure (grain size, roughness, and ultimate strength), which are responsible for the local phenomena of damage and wear. Locally, wear occurs in terms of grains detachment from the microstructure and their ejection from the system. For a good optimization of the microstructure, its micromechanical behavior should be considered as complementary information of the wear process observed at the contacting surfaces scale. The next Part of this manuscript proposes a methodology to study the contact between the matrix and the debris flow; both treated as assemblies of grains using Discrete Element Methods (DEM).

---

## **PART C**

# **Wear description at the mesoscopic scale**

---



# Part C.

## Wear description at the mesoscopic scale

As concluded in Part B, some important phenomena controlling wear are not accessible at the scale of the diamond and need to be investigated at a smaller one. For this purpose, a numerical model accounting for the nature of the debris grains and the polycrystalline microstructure of the metal matrix should be considered. In this way, the wear of the microstructure can be appropriately studied as a function of the stress cycles induced by the continuous passage of debris and in terms of intergranular de-cohesion and fracture of the matrix. Moreover, the deformable nature of the matrix will be taken into account. Other improvements may be performed to optimize the microstructure, including biphasic or triphasic microstructures, with grains with variable properties in terms of deformability and ductility.

As introduced in section A.3.2, the discrete element methods coupled with mesh-free techniques allow for dealing in a single framework with several grains, both rigid (i.e., the debris grains and the workpiece) and deformable (i.e., the metal matrix microstructure). Hence, the MELODY2D<sup>6</sup> [19] code is used to meet these needs. In this context, cohesive grains boundaries of the metal matrix are points of weakness, defining preferential paths for crack initialization and propagation. This part aims to describe and understand better the wear process at the mesoscale, i.e., the scale of the contact between the matrix surface and the debris flow. Simulations are performed considering a representative volume element (RVE) extracted from a diamond segment.

The first Chapter C.1, describes the numerical tools used for the grains generation and the dynamic simulations as well as the contact-laws through which the bodies interact. The wear process is then analyzed numerically in Chapter C.2, in terms of grains damage, detachment, and ejection, also considering the fatigue effects. Then, an improvement of the model is pursued in Chapter C.3. This last section leads to the calibration of the contact parameters between the matrix grains simulating the  $\mu$ -scratch test and comparing results with the experimental ones introduced in section B.1. Therein, the aim is to offer a perspective of improving the model described in the two previous Chapters C.1 and C.2 and address it towards the specific industrial problem.

---

<sup>6</sup> Multibody ELeMent-free Open code for DYnamic simulations in 2D



## C.1

# Matrix wear at the local scale: Modeling

This chapter describes the numerical framework for the study of damage and wear of the matrix microstructure at the scale of debris grains. The idea is to offer a numerical tool for understanding aspects that are not accessible, either experimentally or numerically at the scale of the model in Part B. The strategy proposed here is ongoing and should be taken as a perspective whose results, discussed in the next chapter, are nevertheless promising. In a more general context, the model proposed here aims to understand better the wear phenomenon caused by a debris flow on a degradable material.

The model is built using an innovative multibody meshfree technique coupled with a Discrete Element Method (DEM) approach (MELODY2D, [19], [113]). The discrete approach allows representing the degradable material as a collection of deformable grains held together through their intergranular cohesion. The continuous passage of debris causes points of weakness in the resistance chains of the matrix, generating the loss of cohesion and the consequent detachment of the grains by fatigue. In this way, the wear is no longer studied from a global point of view but by a local one that looks at the detachment of the grains and their expulsion from the tribological system (defined as in Section A.2.2). As will be explained in section C.1.2, fatigue effects are introduced in the model to account that wear rate is actually a slow and progressive phenomenon. Fatigue effects are not considered in the model proposed in Part B. Further improvements of the strategy may include the connection between the two models and, therefore, implementing the fatigue in the wear equation.

The first Section C.1.1 gives an overview of the model and the main code used to generate the microstructure and debris grains [29]. The damage and wear of the matrix are performed in terms of de-cohesion between grains, leading to their detachment from the binder. Therein, a triangular cohesive zone model (CZM)-fatigue contact law is used, as described in section C.1.

### C.1.1 Description of the model

-The model considers the matrix a polycrystalline degradable material, where grain size and size distribution are chosen according to the experimental observations. Matrix grains are in contact with debris grains, which are also modeled with realistic shapes and sizes using the same code (PACKING2D [29]) as for the matrix.

### C.1.1.1 Geometrical problem and boundary conditions

The mesoscopic model considers a representative volume element accounting for the contact between matrix and debris grains. The code is currently limited to 2D. Despite this simplification of the reality and knowing that the wear process is clearly 3D (see the subdivision in wear zones in Fig. B-25, as well as the displacement of matter predominant in ploughing-like wear mode), the code can overcome such limitations through an artificial deactivation of grains whose displacements are large enough to consider them ejected (cutting mode) or displaced on the lateral sides (ploughing mode).

Considering the tool segment in Fig. B-69, the attention is focused on a small portion of the matrix surface in contact with the debris flow. Although it is currently not possible to quantify experimentally the flow properties exerted by the debris grains on the contacting matrix surface, the model proposed in Part B allows computing the velocity field and the pressure by applying the Eq. (B.16) and the Eq. (B.29) (i.e., the Reynolds equation), respectively. This interconnection between the two models allows to locally analyze any portion of the segment without considering the presence of diamonds by choosing the proper pressure  $p$  in terms of boundary condition. Moreover, the experimental observation by optical microscope allows choosing the thickness of debris grain correctly (see, for example, Fig. B-12). The metal matrix's microstructure is modeled as a collection of deformable grains prolonged by a deformable non-degradable base of the same material. The matrix dimensions must be appropriately chosen to avoid any perturbations at the boundary conditions, guaranteeing continuity between the degradable and the non-degradable part since there is no physical discontinuity between them. It is straightforward that the higher is the degradable thickness, the higher is the number of grains modeled, and the more costly the simulation is. Therefore, the continuum base is necessary to limit the cost of the simulation by reducing the thickness of the degradable part. Based on this required continuity between the two parts, the height of the degradable and non-degradable matrix are respectively  $h_m = 20 \mu\text{m}$  and  $h_b = 30 \mu\text{m}$  (a smaller value of  $h_m$  is also investigated, and results are reported in Annex II). Here again, to guarantee the respect of the periodic boundary conditions and avoid boundary effects optimizing the computation time, the length of the domain is set one order of magnitude larger than the thickness  $h_m$  ( $L_x = 200 \mu\text{m}$ ). Debris grains are modeled as rigid bodies occupying an initial thickness (before the compaction)  $h_{TB} = 50 \mu\text{m}$ . The modeling of matrix and debris grains are described in Section C.1.1.2 and C.1.1.3, respectively.

It should be kept in mind that the previous model in Part B referred to a precise diamond of the microstructure since the idea was to validate the model and use it later to predict wear. In the model presented here, the intent is purely descriptive, even though a challenging perspective is to connect the two models. This first study is limited to sensitivity analysis in the framework of abrasive wear during cutting processes without going into the details of the

particular operating conditions. Therefore, the main input data (matrix and debris flow thickness, field properties) are taken here in terms of order of magnitude for the model.

The main geometrical features are displayed in Fig. C-1 together with the field nodes for the deformable bodies. Notice that, in a meshfree code, the discretization is only required to define the density of field nodes and their possible gradient but does not include any strict connectivity relation between them, as described in [20]. The smaller typical nodal distance is set to  $d_{nodes} = 0.1 \mu m$ .

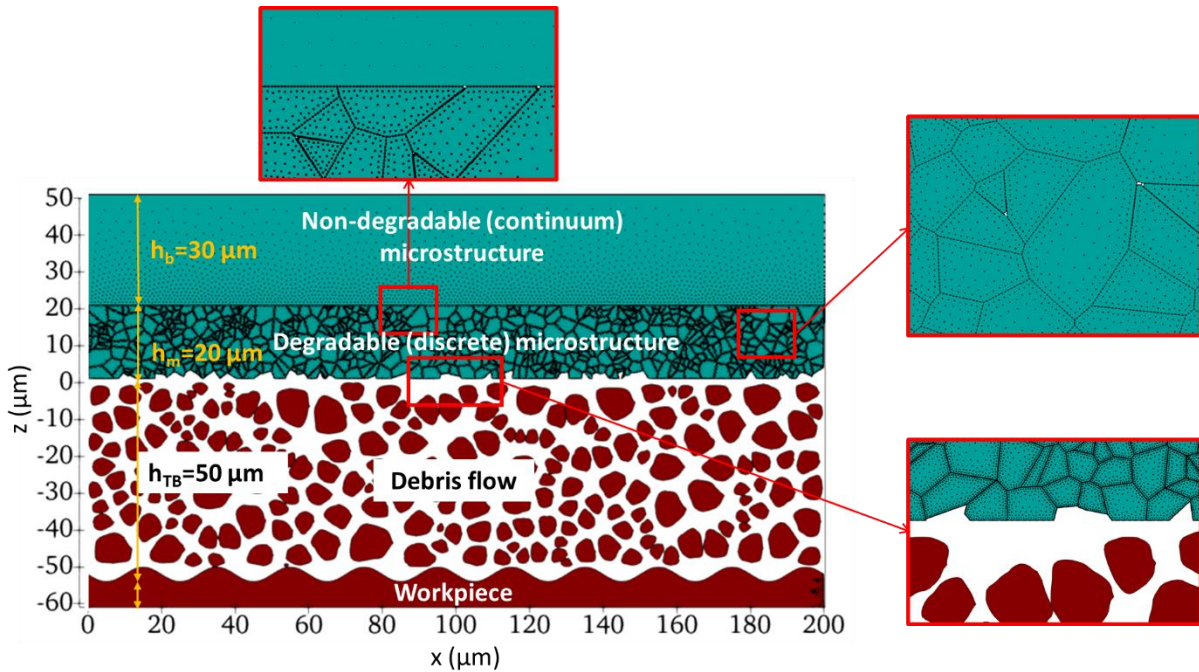


Fig. C-1 Mesoscale model (at  $t = 0$  s) with information about the geometry and the mesh of deformable bodies (non-degradable and degradable microstructure)

In addition to the aforementioned periodic boundary conditions, the upper boundary of the continuum microstructure is fixed. A normal pressure and sliding velocity are imposed on the lower limit of the workpiece, as illustrated in Fig. C-2, which refers to the compacted system. The vertical pressure  $p_n = 3.4 \text{ MPa}$  is taken as the force applied on each segment by the machine, equally distributed on the segment surface. This choice is justified because, at this stage, the macroscopic and mesoscopic models are not connected. However, as introduced above, further studies may use the pressure obtained from the Reynolds equation, Eq. (B-29), to account for the fact that a part of the pressure is carried by diamonds. Notice that, according to our macroscopic model, debris pressure is much smaller than the one carried by diamonds to cut the material.

Performing simulation at the same time scale as the real phenomena leads to unreasonable computational costs; therefore, we impose a larger velocity than the cutting velocity. In a core drill, the tool is subjected to low and constant peripheral speed ( $v_{tool} = 1 - 10 \text{ m/s}$ , see Section

A.2.5), we consider here an average value  $\bar{v}_t = 5 \text{ m/s}$ . The applied numerical sliding velocity is taken an order of magnitude larger than:  $v_t^{num} = 50 \text{ m/s}$ . Since the model is 2D, for the sake of simplicity, we do not consider here the formalism used in Part B that defines the velocity components  $u, v, w$  in the  $x, y$  and  $z$  direction. Therefore, the velocity :  $v_t^{num}$  is the “numerical” velocity applied in the tangential direction, i.e., along the  $x$ -axis. The acceleration of the computation –under well-defined initial assumptions- achieves a proper simulation of the physics as explained in the sub-section C.1.1.4.

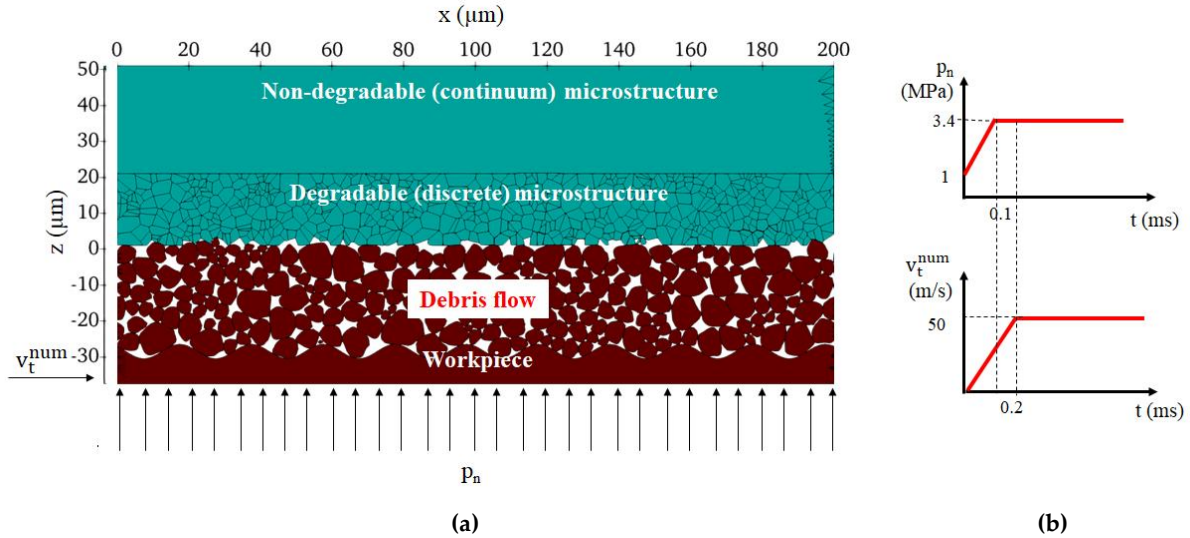


Fig. C-2 (a) Microscale model after compaction (at  $t = 0.1 \text{ s}$ ); (b) definition of the boundary condition imposed on the workpiece

### C.1.1.2 Microstructure grains generation

Grains of the degradable matrix are generated using Packing2D, a numerical code developed in MATLAB, allowing the generation and packing of particles with arbitrary and realistic shapes [29]. They are generated in a given domain divided into subdomains (equal to the number of grains) using the Voronoi Tessellation [114]: starting from a cloud of seeding points  $P_i$ , each point defines a polygon including all the points  $P$  that are closer to  $P_i$ , than to any other seeding point  $P_j$ .

The size and orientation of cells can be statistically controlled by imposing the size distribution and orientation. Neglecting any anisotropy and limiting the coding to a Voronoi sample building, the only useful parameter to set is the size distribution.

Fig. C-3 shows a SEM micrograph of the cobalt powder labeled CO6102 used in the model described in part B, and the size distribution of grains after sintering (features are reported in

Tab. B-9), which follows a lognormal distribution with an average grain size  $d_m = 2.3 \mu\text{m}$  and coefficient of variation<sup>7</sup>  $CV = 0.54$ .

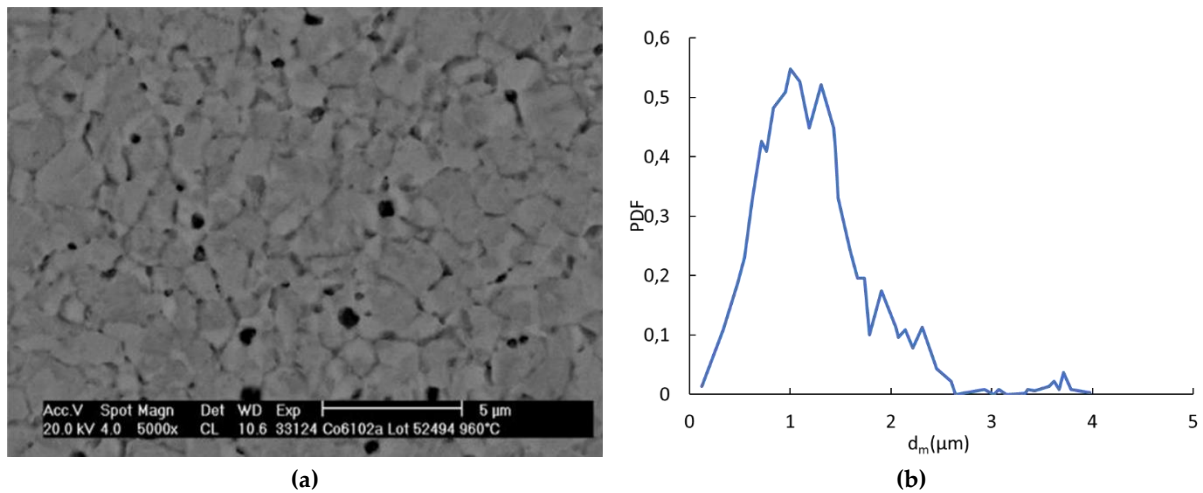


Fig. C-3 (a) SEM micrograph of the microstructure; (b) grain size distribution after sintering [42]

There are two main issues in the classical Voronoi procedure:

- i) If a point  $P_i$  lies on the border of the cloud of points, the corresponding cell may be open as the point  $P_i$  is not seen by any other point  $P_j$  in the domain.
- ii) The standard Voronoi tessellation generates the initial set of seeding points randomly, without including any statistical constraints.

The first drawback is solved considering a bounded Voronoi tessellation [29], which consists of creating a number of points outside the domain and symmetrical to the ones associated with open cells. This procedure allows the creation of closed subdomains and solves the Voronoi tessellation considering only the initial cells as part of the domain.

The second problem was overcome in [29] considering the Inverse Monte Carlo method (IMC) proposed by [115][116], which is a stochastic procedure that improves the statistic of the corresponding Voronoi tessellation introducing random modification in the cloud of points. The procedure is repeated by iterations until the gradual convergence to the desired distribution -under prescribed tolerance- is met. The size distribution of grains generated applying the IMC fits the experimental powder grains broadly, as shown in Fig. C-4.

<sup>7</sup> The coefficient of variation  $CV$  is generally defined as the ratio between the standard deviation and the mean value of the population

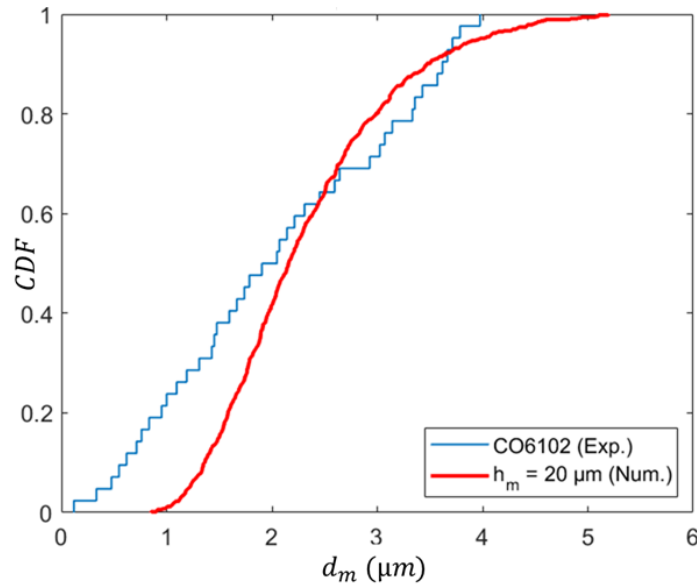


Fig. C-4 Comparison between the experimental (blue) and numerical (red) degradable microstructure

The microstructure obtained following this procedure is illustrated in Fig. C-5, together with the initial clouds of seeding points. This sample is then cleaned from acute angles and small edges that may cause instability problems in the contact resolutions during the simulation.

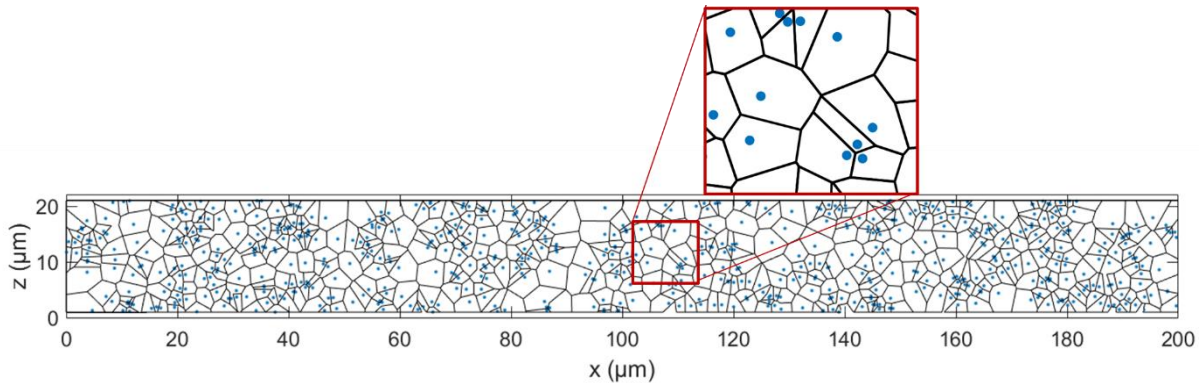


Fig. C-5 Microstructure generated in Packing2D applying the IMC method to the Voronoi Tessellation (black) and initial clouds of seeding points (blue)

This procedure allows implementing some roughness on the surface exposed to the debris flow, cleaning small edges and angles. Finally, the microstructure assumes the form previously observed in Fig. C-1 and Fig. C-2.

### *Roughness characterization*

The surface in contact with the debris flow is characterized by a roughness evolving with time as grains are detached and ejected. In order to relate roughness to wear, it is important to define the main roughness parameters.

Generally, the average roughness of a surface is defined as the arithmetic mean deviation of the surface height from the mean line [117][118]:

$$R_a = \frac{1}{N} \sum_{i=1}^N |z_i'| \quad (C.1)$$

Where  $z_i'$  is the z-coordinate of a point of the surface, measured from the mean line. Despite its simplicity, this parameter alone do not account for the shape and the spatial distribution of peaks and valleys across the surface: two different surfaces may have the same mean roughness  $R_a$  but different topography and different probability distribution of the surface height. Using a probabilistic approach, the surface irregularity, as well as the shape of the surface, can be defined in terms of moments of the profile amplitude density function [117]:

- Root mean square (RMS) parameter  $R_q$ . It represents the standard deviation of the distribution of surface height:

$$R_q = \sqrt{\frac{1}{N} \sum_{i=1}^N |z_i'^2|} \quad (C.2)$$

- Skewness parameter  $R_{sk}$ . It is the third moment of the density function. It is an indicator of the symmetry of the height distribution:

$$R_{sk} = \frac{1}{R_q^3} \left( \frac{1}{N} \sum_{i=1}^N z_i'^3 \right) \quad (C.3)$$

The skewness can be either positive or negative:  $R_{sk} > 0$  indicates a surface profile with high peaks and shallow valleys,  $R_{sk} < 0$  is representative of a surface characterized by rounded peaks and sharp valleys. If  $R_{sk} = 0$  the profile is symmetric to the mean line, i.e., the height distribution follows the normal one.

- Kurtosis parameter  $R_{ku}$ . It is the fourth moment of the density distribution and describes the sharpness of the probability density of the profile:

$$R_{ku} = \frac{1}{R_q^4} \left( \frac{1}{N} \sum_{i=1}^N z_i'^4 \right) \quad (C.4)$$

Unlike skewness, the kurtosis  $R_{ku}$  is always positive. If  $R_{ku} > 3$ , the distribution is narrowly-peaked and has many peaks and valleys; if  $R_{ku} < 3$  the distribution is flat and has relatively few peaks and valleys. If  $R_{ku} = 3$  the distribution is close to the normal one.

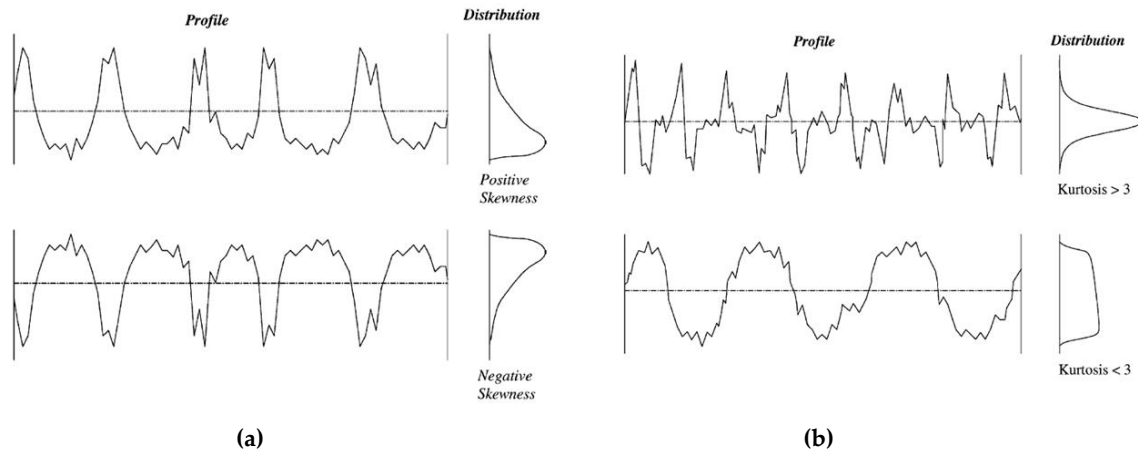


Fig. C-6 (a) Definition of skewness  $R_{sk}$  and (b) kurtosis  $R_{ku}$  together with the respective distribution functions [117]

The initial profile generated in this work is almost flat, with positive skewness ( $R_{sk} = 1.0922$ ) and kurtosis higher than 3 ( $R_{ku} = 3.3404$ ); the main parameters  $R_a$ ,  $R_q$ ,  $R_{sk}$ ,  $R_{ku}$  are reported in Tab. C-1.

Tab. C-1 Initial roughness parameters of the degradable microstructure

$R_a$ ( $\mu\text{m}$ )	$R_q$ ( $\mu\text{m}$ )	$R_{sk}$ (-)	$R_{ku}$ (-)
0.4652	0.5553	1.0922	3.3404

The evolution of the surface profile during the wear process will be analyzed in Chapter C.2.

### C.1.1.3 Debris grains generation

Grains can be modeled by targetting realistic shapes and sizes in Packing2D [29]. An assembly of 200 grains is generated in a rectangular domain ( $50 \times 200 \mu\text{m}$ ). The first version of the code was limited to Gaussian distribution; therefore, it was not able to impose the bimodal distribution as the one observed experimentally in Fig. B-2 (b). However, assuming the median value of the distribution equal to the median one, the target mean size is set equal to  $10 \mu\text{m}$  (i.e., equal to the median value in Fig. B-2 (b)). In this way, the average grain size obtained is  $d_a = 8.98 \mu\text{m}$ . This preliminary study does not aim to predict wear but to set a modeling strategy for understanding the phenomenological features triggering wear by the abrasive debris flow, and the sample generated here seems to satisfy this objective well. A new version of the Packing2D code includes the generation of grains with more complex size distributions and can generate a new packing of grains representing better the bimodal distribution. This new assembly is illustrated in Annex II.

The contour of each grain is discretized by 128 nodes equally distributed, allowing to describe the shape by 64 shape descriptors, defined mathematically in terms of Fourier descriptors  $D_{nF}$  (Fig. C-7). The complete procedure is documented in [29] and briefly reported in Annex II. What is important to know is that each Fourier mode is an indicator of a shape characteristic;

there is, in fact, a strong relationship between the normalized spectrum and the intrinsic properties of grains. The mode  $D_2$  controls the particle elongation ( $D_2 = 0$  for circular particles) while the modes from  $D_3$  to  $D_7$  control the main irregularity, and  $D_{n_F} > 8$  describe the roughness of the particle surface. For  $n_F > 8$  the values of Descriptors  $D_{n_F}$  decrease linearly in a log-log scale, the surface roughness of given granular material can be described only by a slope and intercept, given by the following relation:

$$\Delta_{n_F,1} = 2^{\lambda_1 \cdot \log_2(\frac{n_F}{8}) + \log_2(D_8)} \quad (C.5)$$

For the sake of simplicity, a similar relationship can also be used for the modes from  $D_4$  to  $D_7$ :

$$\Delta_{n_F,1} = 2^{\lambda_2 \cdot \log_2(\frac{n_F}{3}) + \log_2(D_3)} \quad (C.6)$$

Generally, the rate of decay may be different from one population to another. Without any information about the spectrum decay,  $\lambda_1$  (Eq. (C.5)) and  $\lambda_2$  (Eq. (C.5)) can be assumed equal to  $-2$ . In this way, only the parameters  $D_2$ ,  $D_3$  and  $D_8$  need be defined.

The code allows smoothing the surface by choosing the parameter  $N_m$  properly cutting off the high angular frequencies of the spectrum used for the shape definition [119]. The utility of smoothing the surface consists in the possibility of partially replacing the roughness of the contacting bodies by an artificial increase of the coefficient of friction (between two grains in contact by a frictional law). This cost reduction is demonstrated to be valid under certain conditions (i.e., when the attention is only focused on the macroscopic response of the sample) [119]. In our case, we set  $N_m=64$ , meaning that modes  $D_{n_F} > 64$  are ignored.

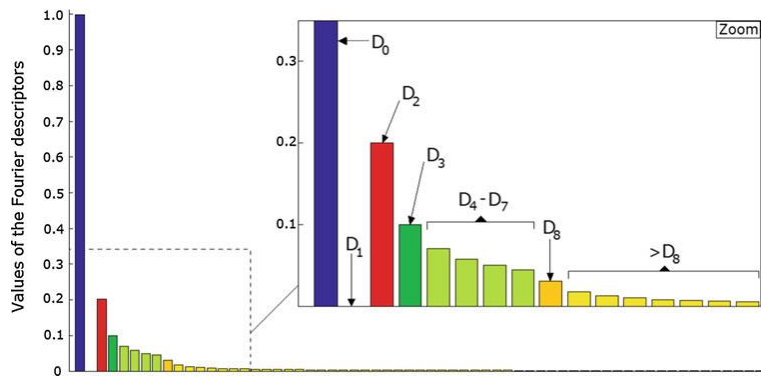


Fig. C-7 Example of normalized amplitude spectrum [29]

In this preliminary study, the angularity is not considered, and debris grains are relatively smooth (Fig. C-1). The Voronoi parameters, the spectrum cut-off  $N_m$  and the target solid fraction  $SF_t$ , as well as the Fourier Descriptors  $D_n$  and  $c_1$  and  $c_2$  are listed in Tab. C-2. The code gives as outputs the sample solid fraction  $SF$ , the equivalent grain diameter  $d_d$ , and the sample coefficient of uniformity  $C_u$ .

Tab. C-2 Packing 2D input and output parameters ( $d_d$  is in  $\mu\text{m}$ , the other parameters are dimensionless)

Voronoi Tessellation		Cell Filling		Fourier Spectrum Properties					Output		
$N_{debris}$	$CV_t$	$SF_t$	$N_m$	$D2$	$D3$	$D8$	$\lambda_1$	$\lambda_2$	$SF$	$d_d$	$C_u$
200	0.8	0.5	32	0.1	0.07	0.01	-2	-2	0.48	10	1.65

The Voronoi tessellation is illustrated in Fig. C-8.

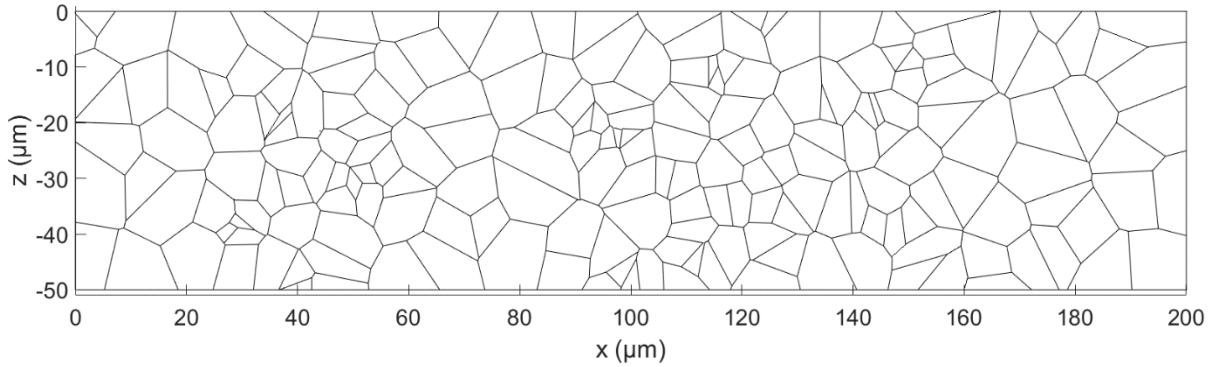


Fig. C-8 Voronoi Tessellation for the debris grains generation in Packing2D

#### C.1.1.4 Computational cost and numerical acceleration

Concerning the optimization of the simulation, a first estimate of the computational cost is given by the critical time step  $\Delta t$  required by the solver, which is a function of the minimum nodal distance  $d_{nodes}$ , the Young modulus ( $E_m = 211 \text{ GPa}$ ) and the density of the matrix ( $\rho_m = 9800 \text{ kg/m}^3$ ):

$$\Delta t = \frac{d_{nodes}}{\sqrt{\frac{E_m}{\rho_m}}} \approx 10^{-11} \text{ s} \quad (C.7)$$

The ratio  $\sqrt{E_m/\rho_m}$  defines the maximum velocity of wave propagation in the deformable microstructure:

$$v_{waves} = \sqrt{\frac{E_m}{\rho_m}} \quad (C.8)$$

Reducing the Young modulus  $E_m$  by a factor of 100, reduces the velocity of elastic waves propagation in Eq. (C.8), and increases the time step  $\Delta t$  in Eq. (C.7) by a factor of 10 and, therefore, accelerates the simulation.

However, relatively small values of  $E_m$  should be avoided because they may change the physics of the problem by increasing too much the compliance of the material. The reduction

of the Young modulus  $E_m$  as well as the increase of sliding velocity  $v_t^{num}$  are required to accelerate the simulation, but they must also assure that the applied velocity  $v_t^{num}$  remain much smaller than the elastic wave velocity  $v_{waves}$  in Eq. (C.8) to preserve the physics of the real problem.

Another dimensionless parameter to preserve in the simulation is the inertial number  $I$  [120] defined as a function of the shear rate  $\dot{\gamma}$  (equal to the ratio between the sliding velocity  $v_t^{num}$  and the thickness occupied by the debris flow  $h_{TB}$ ), the average debris diameter  $d_d$ , the applied pressure  $p_n$  and the density of the debris flow  $\rho_d$ :

$$I = \frac{\dot{\gamma} d_d}{\sqrt{\frac{p_n}{\rho_d}}} \quad (C.9)$$

The increase of the sliding velocity requires changing other parameters of Eq. (C.9) to preserve the same inertial number in the numerical simulation as in experiments: it is possible to increase the pressure  $p_n$  or decrease the debris flow density  $\rho_d$ . As the pressure variation can lead to a significant change in the physics, the debris density is reduced by 100. The main physical and numerical features are listed in Tab. C-3. The difference between the real and the numerical inertial number  $I$  is due to the difference in terms of grain size since the packing obtained as in section C.1.1.3 has an average size  $d_d = 8.98 \mu m$ , which is smaller than the equivalent size computed founded experimentally ( $d_d = 20 \mu m$ ). The numerical value of  $d_d$  is constrained by the fact that, as explained above, the Gaussian distribution with mean equal to the median of the distribution in Fig. B-2 (b) is assumed. Moreover, this difference does not affect the inertia number strongly since it remains in the range defined for dense granular flows ( $10^{-3} < I < 10^{-1}$ ) [120].

Tab. C- 3 Real and numerical features for the numerical acceleration

	$p_n$ [MPa]	$\bar{v}_{tool}$ [m/s]	$E_m$ [MPa]	$\rho_m$ [kg/m <sup>3</sup> ]	$\rho_d$ [kg/m <sup>3</sup> ]	$\frac{v_t}{v_{waves}}$ [-]	$I$ [-]
Real	3.4	5	211000	8900	2700	$\approx 10^{-3}$	0.056
Num.	3.4	50	2110	8900	27	$\approx 10^{-1}$	0.025

## C.1.2 Main contact models

The model accounts for rigid (debris grains and the workpiece) and compliant bodies (degradable and non-degradable matrix), both of them defined by a collection of field nodes located on the contour (contact nodes), allowing for the same contact algorithm and the definition of complex contour shapes.

Rigid bodies follow the classical DEM formulation as they are characterized by a mass, a center of mass and rotational inertia and carry three degrees of freedom (2 displacements and one rotation in the 2D formulation).

Other nodes are located on the bulk of compliant bodies. Each node carries the degrees of freedom in displacement as in the classical FEM theory, defining a displacement field that is interpolated between the nodes by meshfree shape functions.

The contact algorithm is a node-to-segment algorithm, described extensively in [20] and illustrated in Fig. C-9.

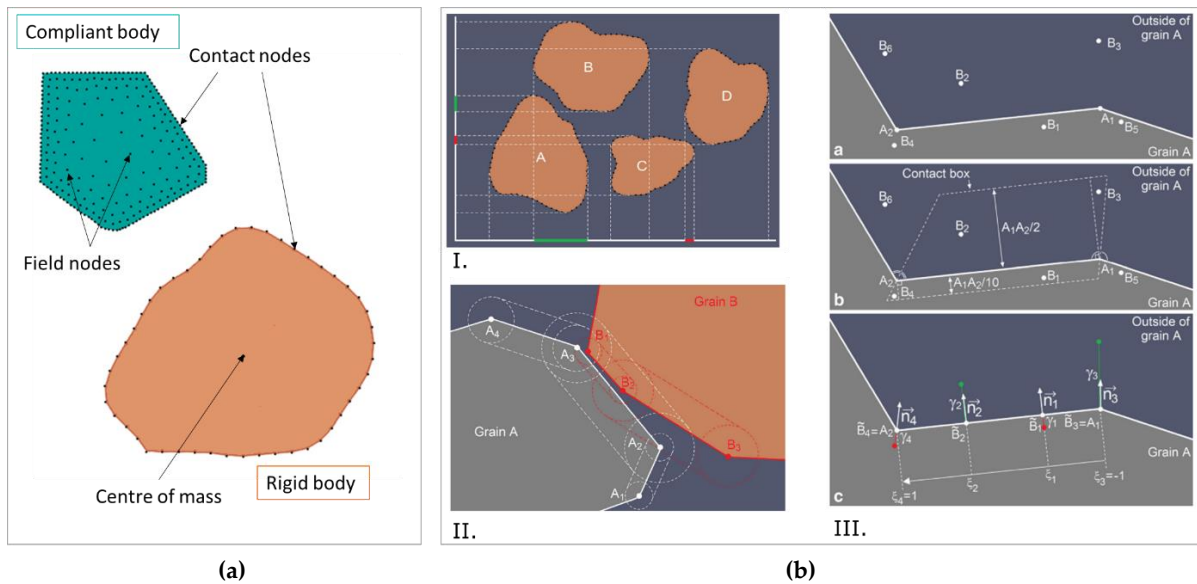


Fig. C-9 (a) Definition of compliant and rigid bodies (inspired by [20]); (b) Definition of the contact algorithm: I: Broad proximity detection (detected contact are in green and in red); II: close detection; III: Contact detection: a. nodes from  $B_1$  to  $B_6$  are detected in stage II as close to the segment  $A_1A_2$ ; b. definition of the contact box to select nodes ( $B_5$  and  $B_6$  are out from the detection box and therefore not considered); c. projection for computing local detection quantities (normal  $\vec{n}$  and tangential  $\vec{t}$  vector, normal  $\gamma_n$  and tangential gap  $\delta_t$ , local coordinate  $\xi_i$  varying from -1 to 1 from the origin to the extremity of the segment) [20]

To account for complex shapes and sharp corners in the initial or deformed configuration [19], it consists of three main stages:

- I) Broad proximity detection: selection of pairs of close grains. Grains are defined as close if they overlap when projected on the x- and y-direction [20].

- II) Close proximity detection: definition of potential contact between any node of the contour of a body B and any segment of another grain A.
- III) Not all the grains defined by close proximity are useful for contact detection. To avoid loss of detection or double detection, only nodes inside a detection box are selected. Such limit is defined for each segment  $A_iA_{i+1}$  and is described by the two bisecting lines arising from  $A_i$  and  $A_{i+1}$  respectively and closed by two lines parallel to the segment  $A_iA_{i+1}$  at a distance  $\frac{A_iA_{i+1}}{2}$  in the outward direction and  $\frac{A_iA_{i+1}}{10}$  in the inward direction. For all the nodes  $B_j$  of the body B in proximity detection with body A the following quantities are computed:
- The normal and tangential vectors ( $\vec{n}$  and  $\vec{t}$ ) on the surface of the body A;
  - The unique projection  $\tilde{B}_j$  of the point  $B_j$  on the contour of A;
  - The normal and tangential gaps ( $\tilde{\delta}_n$  and  $\tilde{\delta}_t$ )

When the local contact configuration is defined from a kinematic point of view, the computation of the contact pressures  $\tilde{p}$  relies on the contact law applied between bodies. In this model, the following contact laws are used:

- (a) Mohr-Coulomb: for the contact between debris grains and grains of the degradable microstructure.
- (b) "Impact Mohr-Coulomb" for the debris grains-workpiece contact and the contact between debris grain themselves.
- (c) "CZM" with fatigue for the degradable and non-degradable contact and the contact between grains of the degradable material.

The following description is limited to (b) and (c) since the Mohr-Coulomb (a) can be seen as a particular case of the impact Mohr-Coulomb (b).

### C.1.2.1 The "Impact Mohr-Coulomb" contact law

The simple Mohr-Coulomb contact law describes the frictional contact between rigid debris grains and deformable matrix grains. It may include a tangential "cohesion"  $\Gamma$  (in addition to the frictional contribution) and a tensile cut-off  $\tilde{\sigma}_{cut-off}$ , both set to zero in the present case, while the friction coefficient is set to  $\varphi = 0.3$ . This kind of contact is illustrated in Fig. C-10(a).

The contact between rigid bodies (contacts between debris grains and between debris grains and the workpiece) includes the dissipation of a part of the impact energy by a smaller stiffness during the unloading. Thus, the interaction by the impact is defined in terms of the ratio between the stiffness during loading  $k_n^+$  and unloading  $k_n^-$ , and is set to 0.1. This contact model

was developed by [121] to account for the energy dissipated naturally during rock flows and is particularly appropriate when complex grains with multiple contacts are considered, as normal damping becomes difficult to calibrate in that case.

Fig. C-10(b) plots this contact law in terms of the normal force  $f_n$  vs. the overlap distance  $\tilde{\delta}_n$ . The increase of the overlap  $\tilde{\delta}_n$  ( $\Delta\tilde{\delta}_n \geq 0$ ) leads to the increment of the force  $f_n$  ( $\Delta f_n = k_n^+ \cdot \Delta\tilde{\delta}_n$ ) up to a given overlap  $\tilde{\delta}_n^*$  defining the impact, which is followed by the unloading (with a reduced stiffness  $k_n^-$ ) until  $f_n = 0$ .

After the impact, the energy restored is defined as:

$$E_r = \frac{k_n^- \cdot \tilde{\delta}_n^{*2}}{2} \quad (C.10)$$

While the maximum energy stored during the loading is:

$$E_t = \frac{k_n^+ \cdot \tilde{\delta}_n^{*2}}{2} \quad (C.11)$$

Therefore, the energy dissipation rate in the normal direction is:

$$\bar{E}_n^2 = \frac{k_n^-}{k_n^+} \quad (C.12)$$

This model has the added advantage of using a single parameter  $\zeta$  for normal energy dissipation without the need to speculate on all phenomena involved (e.g., viscosity, plasticity).

For the sake of simplicity, the contact in the tangential direction follows the same laws as in the normal one with the same stiffness:

$$k_n^{+/-} = k_t^{+/-} \quad (C.13)$$

Frictional forces are opposite to the sliding direction; they are defined as  $f_t = \mu|f_n|$  (Fig. C-10(c)).

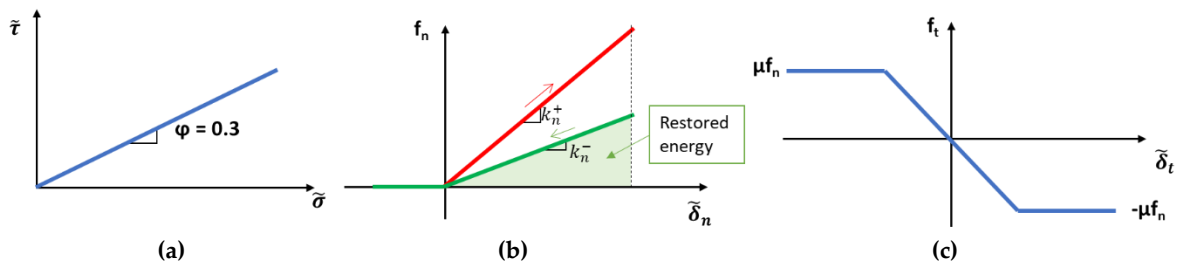


Fig. C- 10 (a) Mohr-Coulomb contact law; (b) Normal contact force vs. overlap; (c) tangential frictional force vs. sliding displacement

## C.1.2.2 "CZM-fatigue" contact law

The cohesive zone model (CZM) is an approach in the fracture mechanics framework regarding fracture formation as a gradual phenomenon [122]. Crack surfaces' separation occurs across an extended crack tip or cohesive zone held by cohesive tractions.

This approach was initially proposed by Hillerborg and co-workers [123] based on the model proposed by Barenblatt [124], [125] to account for the finite strength of brittle materials concerning the Griffith theory of fracture. Dugdale [126] applied a similar model to investigate the yielding and sizing of a crack tip on the plastic zone, while Zhou & Molinari applied the cohesive crack opening process to study the brittle failure in ceramic materials by FEM [127], [128], introducing a type rate-dependent cohesive law [129].

The cohesive zone model is generally used to model fracture of polycrystalline materials [30]–[33], accounting for the influence of microstructure on the macroscopic response. The real microstructure is modeled using the Voronoi tessellation as explained above. The crack interface separation in the tensile direction  $-\tilde{\delta}_n$  (mode I) and in the tangential direction  $-\tilde{\delta}_t$  (Mode II) are calculated from the relative displacement of its nodes once the interface begins to open (Mode I) or slide (Mode II) (Fig. C-11(a)), using the contact detection algorithm explained previously. The model is based on the choice of a particular cohesive law. Different functional forms of the cohesive law are proposed in the literature [31]–[33], [130], [131] (e.g., triangular, exponential, or trapezoidal) in order to establish a relation between the increase of damage and the decrease of stiffness at a given material point of the element. Here, a simple triangular law is used, while a little more complex shape will be defined in the numerical scratch test modeling, discussed in Chapter C.3. The cohesive law is illustrated in Fig. C-11(b) for the tangential direction. It is characterized by an initial elastic regime followed by softening.

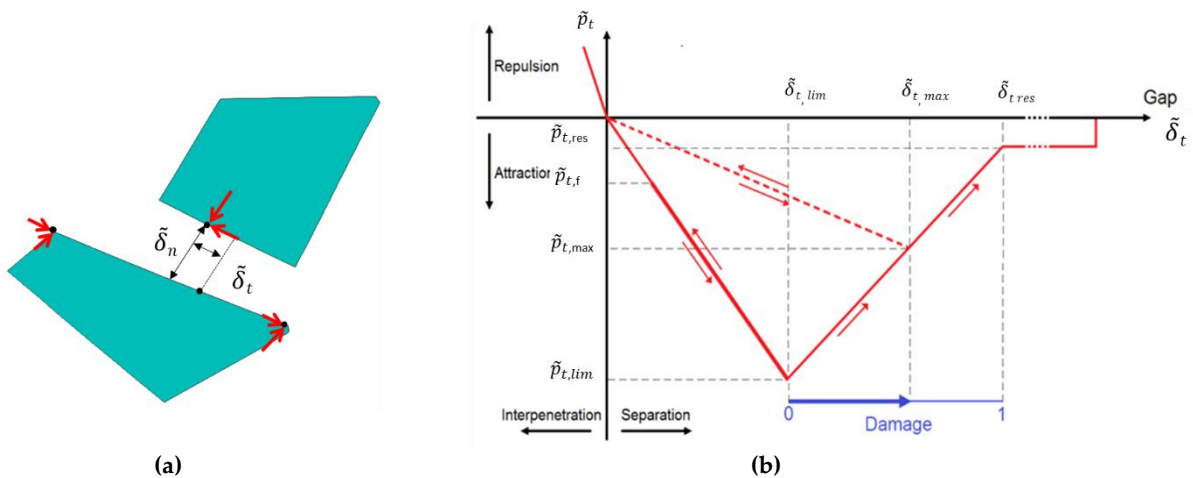


Fig. C-11 (a) Cohesive contact between two grains; (b) Traction – separation law in the tangential direction (the same graph could be plotted for the tensile direction by simply changing the name of the variables)

The same plot can be obtained for normal direction by simply substituting the tangential pressure  $\tilde{p}_t$  with the tensile one  $\tilde{p}_n$  and the tangential gap  $\tilde{\delta}_t$  with the normal one  $\tilde{\delta}_n$ .

The main parameters controlling the triangular shape of the law are:

- $\tilde{p}_{n,lim}$  and  $\tilde{p}_{t,lim}$ : initial ultimate normal and tangential strength
- $k_n^0$  and  $k_t^0$ : initial contact stiffness in the normal and tangential direction
- $\tilde{p}_{n,res}$  and  $\tilde{p}_{t,res}$ : residual tensile and tangential strength at full damage
- $\tilde{\delta}_{n,res}$  and  $\tilde{\delta}_{t,res}$ : ultimate tensile and tangential extension that the contact can sustain

The tangential strength ( $\tilde{p}_{t,lim}$  and  $\tilde{p}_{t,res}$ ) and the maximum tangential extension  $\tilde{\delta}_{t,res}$  are assumed equal to the input counterpart for the tensile direction ( $\tilde{p}_{n,lim}$ ,  $\tilde{p}_{n,res}$  and  $\tilde{\delta}_{n,res}$ ), meaning that the ruptures in mode I and mode II follow the same contact-law.

The ultimate strength ( $\tilde{p}_{n,lim}$  and  $\tilde{p}_{t,lim}$ ) and the residual gap thickness ( $\tilde{\delta}_{n,res}$  and  $\tilde{\delta}_{t,res}$ ) are the strength parameters controlling the cohesive law. Instead of the gap thickness, the CZM in the monotonous condition is generally defined in literature by the critical fracture energy  $G_c$  [30], [131]–[133] defined as the area of the triangular shape of the law, and given by:

$$G_{c,I} = \frac{\tilde{p}_{n,lim} \tilde{\delta}_{n,res}}{2} \quad G_{c,II} = \frac{\tilde{p}_{t,lim} \tilde{\delta}_{t,res}}{2} \quad (C.14)$$

in the normal and tangential direction, respectively.

The shape of the law is generally controlled by the initial stiffness parameters  $k_{n,0}$  and  $k_{t,0}$  [134]. These stiffnesses should be sufficiently large to minimize artificial compliance and interpenetration of contacting bodies. However, the higher the stiffness value, the more time-consuming the simulation. The strength parameters are generally calibrated by experiments [133], [135]; however, there is no standard procedure [131]. The ultimate strength in the wear analysis is discussed in Chapter C.2, while a methodology for the calibration through the experimental  $\mu$ -scratch (see Chapter B.1) is proposed in Chapter C.3.

For the sake of simplicity, the index -  $n$  and -  $t$  (for normal and tangential CZM parameters) are omitted in the remainder of this study.

An internal scalar variable controlling the degree of de-cohesion between grains and, therefore, the detachment of grains is the damage parameter  $D$ , which ranges from 0 (intact contact) to 1 (broken contact). The CZM is initialized at the beginning of the simulation; the damage parameter is measured at each node of each border grain and updated at each time step. If no fatigue effects are considered, the loss of cohesion may happen only in a monotonous way and only if the current stress reaches the ultimate strength  $\tilde{p}_{lim}$ , or, in other words, if the current gap  $\tilde{\delta}_i$  exceeds the limit:  $\tilde{\delta}_i > \tilde{\delta}_{lim}$  defining the maximum gap even

reached ( $\tilde{\delta}_i = \tilde{\delta}_{max}$ ) in the simulation. The increase of the damage parameter leads to the reduction of stiffness and strength, as illustrated in Fig. C-11(b).

Additionally, as the continuous passage of debris grains is the leading cause of the grains detaching from the microstructure, fatigue effects are implemented in the CZM to simulate the fatigue damage degradation. Generally, they are introduced to account locally for the realistic wear rate that is a progressive and slow phenomenon. Implementing fatigue effect allows considering the slow evolution of the damage parameter  $D$ , which progressively degrades the interface between the grains, representing the physics in a more realistic way.

Fatigue damage occurs by elastic degradation ( $\tilde{p} < \tilde{p}_{lim}$ : left side of the curve in Fig. C-11(b)). The main parameters controlling the fatigue damage are:

- $\tilde{p}_f$  : contact stress (either normal or tangential) above which damage may occur by fatigue.
- $dD_f$  fatigue damage evolution parameter: it defines the increment of damage parameter  $D$  between two successive time instants  $i - 1$  and  $i$  in relation to the corresponding increment of contact pressure :

$$dD_f = \frac{D_i - D_{i-1}}{\tilde{p}_i - \tilde{p}_{i-1}} \quad (C.15)$$

$dD_f$  is imposed as a constant during the simulation. It means that smaller is the damage evolution parameter  $dD_f$  and smaller is the increment of the damage parameter after a certain number of stress cycles. In more conventional fatigue models where the stress cycles are all identical, this parameter is generally written in terms of increment of the damage parameter  $D$  per loading cycles  $\Delta N$ :

$$dD_f = \frac{dD}{dN} = \frac{D_i - D_{i-1}}{\Delta N} \quad (C.16)$$

Several formulations can be found in the literature [131], [136]–[139], all of them are defined to describe the experimental power Paris law [140], [141] relating the crack length to the loading cycles through material coefficients obtained experimentally.

A different model accounting for the current stress increment instead of the loading cycles is considered in this work ( $dD_f$  defined by Eq. (C. 15)), because the evolution in time of the contact stress is highly unpredictable, and no “stress cycle” can easily be defined based on local tribological loadings.

Finally, coupling cohesive law with fatigue, failure may happen both in monotonous and fatigue ways.

In summary, for the  $i^{th}$  time step, the output quantities computed and returned are:

- $\tilde{p}_i$ : current contact pressure
- $D_i$ : the updated value of the damage parameter
- $\tilde{\delta}_i$  the updated value of the gap related to the updating position of the node

The numerical procedure is illustrated in the flowchart in Fig. C-12, while the main parameters of the CZMfatigue law are reported in Tab. C-4.

Tab. C-4 User-defined parameters of the CZM-fatigue contact law

CZM shape parameters			CZM fatigue		
$k_0$	$\tilde{p}_{lim}$	$\tilde{\delta}_{res}$	$\tilde{p}_{res}$	$\tilde{p}_f$	$dD_f$
(MPa/ $\mu\text{m}$ )	(MPa)	( $\mu\text{m}$ )	(MPa)	(MPa)	(1/MPa)

The CZM contact law is initialized by setting  $D = 0$  for all contact nodes detected as bonds by the code. The main contact parameters are set and the simulation start. Then, for each time step, if the bond is active it is possible to compute the current gap ( $\tilde{\delta}_{max}$ ) corresponding to the current  $D_i$ ; and therefore, the current normal and tangential stiffness ( $k_0$ ) and the maximum pressure  $\tilde{p}_{max}$ .

Damage may increase by fatigue if the pressure is larger than the fatigue threshold  $\tilde{p}_f$  and the contact pressure of the previous time step  $\tilde{p}_{i-1}$ . The update damage parameter  $D_i$ :

$$D_i = D_{i-1} + \frac{\tilde{p}^i - \tilde{p}_f}{\tilde{p}_{max} - \tilde{p}_f} \cdot dD_f \cdot (\tilde{p}_i - \tilde{p}_{i-1}) \quad (C.17)$$

It means that the damage increment  $D_i - D_{i-1}$  is proportional to the contact stress increment ( $\tilde{p}_i - \tilde{p}_{i-1}$ ) multiplied by the fatigue damage rate  $dD_f$  defined in Eq. (C.12). The increment of the damage is more significant if the load is high than if it is low.

If the current gap  $\tilde{\delta}_i$  is the maximum gap reached in the simulation  $\tilde{\delta}_i = \tilde{\delta}_{max}$  the damage increase in a monotonous way:

$$D_i = \frac{\tilde{\delta}_i - \tilde{\delta}_{lim}}{\tilde{\delta}_{res} - \tilde{\delta}_{lim}} \quad (C.18)$$

Eq. (C.17) allows updating the current reduced value of the stiffness and strength (see Fig. 11 (b)). If the bond is already broken (i.e.  $D_i = 1$ ), the cohesion is set to the residual value  $\tilde{p}_{res}$ .

The complete procedure is described in the pseudo-code in Annex III.

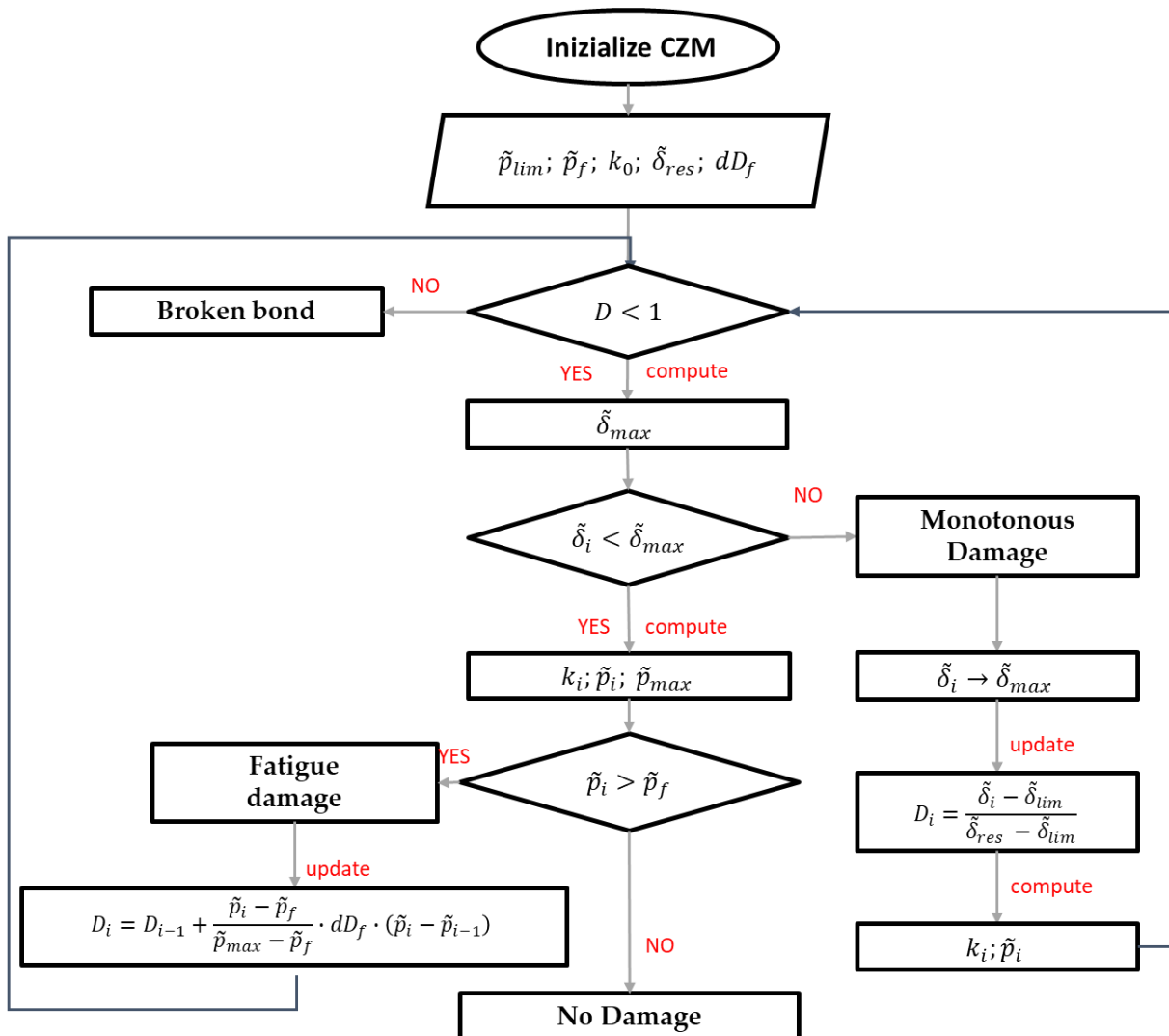


Fig. C-12 Flowchart of the CZM fatigue algorithm

Different studies were performed on the fatigue crack growth using a CZM approach. Most of them aimed to analyze the mechanical resistance of materials and the intergranular fracture in fracture mechanics framework [30]–[32], [130], [142]. Only a few works are addressed to tribological situations. Champagne and co-workers [33] performed the implementation of the CZM on the investigation of friction and wear of a biphasic material. Sadeghi and co-workers focused on rolling contact fatigue dealing with microstructural cracks that develop at the scale of contacting surfaces [137], [143].

The next chapter discusses the results obtained from the model here described in terms of damage and wear.



## C.2

# Matrix wear at the local scale: First results and discussion

Borrowing from fracture mechanics the CZM approach, this Chapter aims to mimic the damage and wear of the metal matrix microstructure caused by the abrasive debris flow.

As explained in the previous section C.1.2.2, damage may occur in a monotonous way (if  $\tilde{\delta} \geq \tilde{\delta}_{max}$ ) or by fatigue ( $\tilde{\delta} < \tilde{\delta}_{max}$ ). The first section of this chapter analyzes the two different types of damage in terms of stress distribution within the degradable material, grain detachment and ejection, while section C.2.2 is focused on the damage by fatigue. A sensitivity analysis is performed to understand the main parameters of the CZM with fatigue and their effect on the grains detachment and wear.

### C.2.1 A first parametric sensitivity analysis of the monotonous CZM

Ignoring fatigue effects, the parameters of the CZM define the shape of the traction-separation curve and, therefore, the strength of the material. The choice of such parameters is not straightforward. Several attempts have been made to calibrate them [131], [133], [144]; however, there is no standard procedure.

A calibration method based on the  $\mu$ -scratch test is proposed in Chapter C.3; this choice is justified by the strong analogy between the scratch test and the wear process caused by the abrasive debris flow, already discussed and used for the model proposed in Part B.

For what concerns this first study, the aim is to offer a tool for understanding the abrasive wear phenomenon from a general perspective. Therefore, a sensitivity analysis is performed to identify the role of the strength parameters of the matrix microstructure (i.e., the parameters defining the shape of the CZM law curve) on the wear process.

Considering the CZM parameters (Tab. C-4), a first attempt was made to calibrate the initial cohesive stiffness  $k_0$ : The stiffness parameters have to be large enough to avoid artificial overlapping between grains, keeping in mind that if the system is "too stiff", it will increase the computation time of the simulation. For these reasons, in the following, the value  $k_0 =$

$10^6 \text{ MPa}/\mu\text{m}$  is assumed as a reasonable compromise. Then, this sensitivity analysis is performed to analyze the effect of the ultimate strength  $\tilde{p}_{lim}$  and the residual gap  $\tilde{\delta}_{res}$ .

A first study is performed considering a full damaging distance  $\tilde{\delta}_{res} = 0.002 \mu\text{m}$  (three orders of magnitude smaller than the average grain size) and the ultimate strength  $\tilde{p}_{lim}$  is successively set to 50 MPa and 800 MPa. Then, setting  $\tilde{p}_{lim} = 50 \text{ MPa}$ , the effect of the residual gap is discussed considering  $\tilde{\delta}_{res} = 0.002 \mu\text{m}$  and  $0.0002 \mu\text{m}$ . For the sake of simplicity, at this stage, the shape of the curve in Fig. C-11 (b) is assumed bilinear; therefore, the residual stress is  $\tilde{p}_{res} = 0 \text{ MPa}$  (the effect of  $\tilde{p}_{res}$  will be analyzed in the calibration based on the scratch test). In all cases, the fatigue parameters are fixed: the fatigue pressure is  $\tilde{p}_f = 10 \text{ MPa}$  and the fatigue damage rate  $dD_f = 0.001 \text{ MPa}^{-1}$ . The parameters are listed in Tab. C-5.

Tab. C-5 CZM fatigue parameters for the matrix-matrix and matrix-base contact used in the sensitivity analysis

CZM shape parameters				CZM fatigue	
$k^0$ (MPa/ $\mu\text{m}$ )	$\tilde{p}_{lim}$ (MPa)	$\tilde{\delta}_{res}$ ( $\mu\text{m}$ )	$\tilde{p}_{res}$ (MPa)	$\tilde{p}_f$ (MPa)	$dD_f$ ( $\text{MPa}^{-1}$ )
$10^6$	50	<b>0.0002</b>	0	10	0.001
	800	<b>0.002</b>			

The effect of the strength parameters  $\tilde{p}_{lim}$  and  $\tilde{\delta}_{res}$  on the functional shape of the cohesive law is represented in Fig. C-13. The increase of the ultimate strength  $\tilde{p}_{lim}$  will increase the elastic domain of the triangular law (Fig. C-13(a)), where the damage can occur only by fatigue. While the increase of the residual gap  $\tilde{\delta}_{res}$  increases the ductile domain (Fig. C-13(b)). Increasing any of these two parameters (ultimate strength  $\tilde{p}_{lim}$  or residual gap  $\tilde{\delta}_{res}$ ) leads to an increase of the critical fracture energy defined in Eq. (C.14).

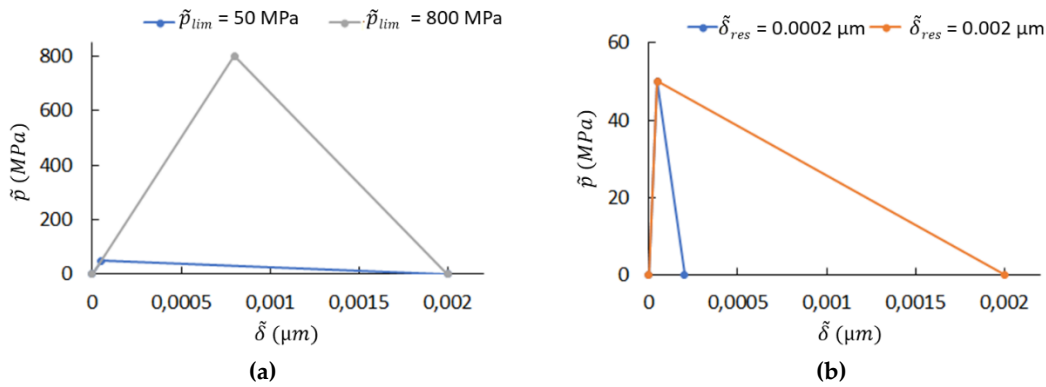


Fig. C-13 Bilinear CZM laws: (a) Effect of the ultimate strength  $\tilde{p}_{lim}$  ( $\tilde{p}_{res} = 0 \text{ MPa}$ ;  $\tilde{\delta}_{res} = 0.002 \mu\text{m}$ ); (b) Effect of the residual gap  $\tilde{\delta}_{res}$  ( $\tilde{p}_{res} = 0 \text{ MPa}$ ;  $\tilde{p}_{lim} = 50 \text{ MPa}$ ) on the shape of the law (in this chart, the tensile strength is taken as positive)

The contact between debris grains and the degradable microstructure is a simple frictional Mohr-Coulomb contact (with cohesion  $\Gamma = 0 \text{ MPa}$ ), while a damping parameter  $\zeta$  is added to account for the dissipated energy during the contact between debris grains and debris grains in contact with the workpiece. The selected parameters are in Tab. C-6.

Tab. C-6 Mohr-Coulomb parameters for the matrix debris contact, and Damped Mohr-Coulomb parameters for the debris-debris and debris-workpiece contact used in the sensitivity analysis

Contact law	$k_0$ (MPa/ $\mu\text{m}$ )	$\varphi$ (rad)	$\Gamma$ (MPa)	$\zeta$ (-)
Mohr-Coulomb	$10^6$	0.3	0	0
Impact Mohr - Coulomb	$10^6$	0.3	0	0.1

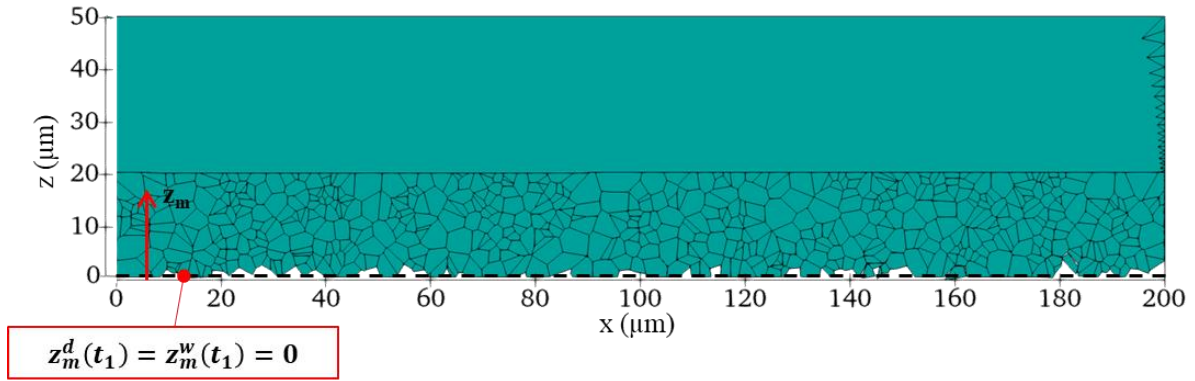
The wear analysis is performed following the damage process of each matrix grain and assuming they are ejected quickly from the system. This assumption is consistent with what is discussed in Part A, as the wear is not caused by the metal grains themselves, and the third body is mostly characterized by debris grains (which are the leading cause of the wear process). This experimental evidence is placed in the numerical simulation by imposing a deactivation condition on the displacement  $l_{de}$  for detached grains, i.e., grains are “ejected” (i.e., disappear from the simulation) when they reach a displacement equal to their equivalent half-size  $d_m/2$ :

$$l_{de} = \frac{d_m}{2} \quad (C.19)$$

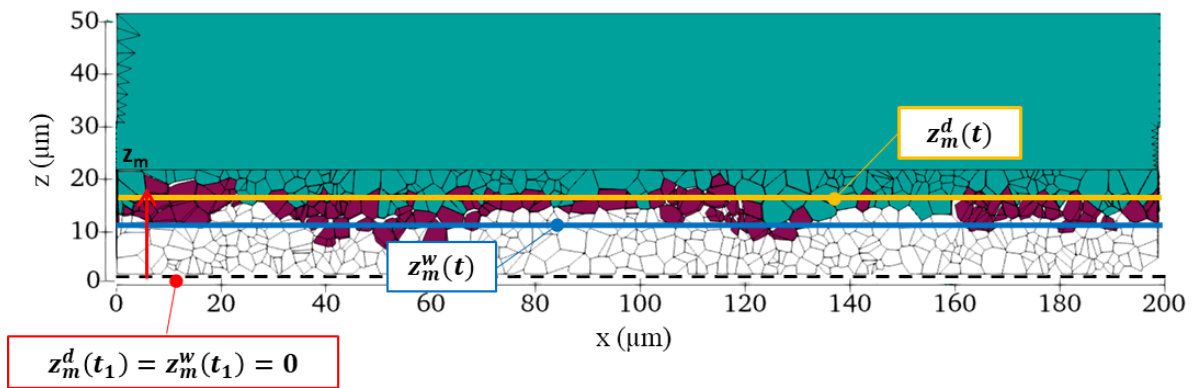
Considering  $d_m = 2.3 \mu\text{m}$  (see Tab. B-9),  $l_{de} = 1.15 \mu\text{m}$ . Moreover, this assumption overcomes the limit imposed by the code that works only in 2D: the lateral displacement of matter during ploughing is simulated in the xz-section through the grains deactivation.

During postprocessing, the position of the damage front in the matrix (termed “damage level”) is measured in terms of the average matrix depth, measured from the contacting surface and ignoring detached grains; that is, based on grains that reached the maximum damage level  $D = 1$  by fatigue (Eq. (C.17)) or monotonously (Eq. (C.18)). This average level is labeled as  $z_m^d(t)$  and is illustrated in Fig. C-14. Similarly, the current matrix surface (termed as “wear level”) is measured in Fig. C-14 as the average matrix depth computed from the contacting surface, but including the detached grains that are still in the system. In other words, the wear level is the average level of the contacting surface and it is named as  $z_m^w(t)$ . Both the damage and wear levels are measured from the onset of the contact ( $z_m = 0 \mu\text{m}$ ) in Fig. C-14.

It is straightforward that, at the early stage of the contact ( $t = t_1$ ), no grains have broken their bonds yet, therefore  $z_m^d(t_1) = z_m^w(t_1)$ , which is the situation in Fig. C-14 (a).



(a)



(b)

Fig. C-14 Schematization of the measure of the damage and wear level ( $z_m^d$  and  $z_m^w$ ) computed from the contacting surface at (a)  $t = t_1$  initial stage of the contact; and (b)  $t = t_i$ : after a certain number of passage of the debris flow. Grains start to lose cohesion reaching the maximum damage possible (in crimson,  $D = 1$ ) and detaching from the microstructure. This phenomenon leads to a variation of the average contact surface and, therefore of the wear level  $z_m^w$  (in blue,  $l_{de} \geq 1.15 \mu\text{m}$ ) and damage level  $z_m^d$  (in yellow,  $D = 1$ ), with respect to the initial profile. Grains in white have been already ejected while the initial profile is plotted in a black dot line

Fig. C-15 (a) plots the level of damage  $z_m^d$  and wear  $z_m^w$  with time for the CZM with ultimate strength  $\tilde{p}_{lim} = 800 \text{ MPa}$ . The wear rate ( $d(z_m^d)/dt$ ) follows the same trend as the fatigue rate ( $d(z_m^w)/dt$ ). Three main stages of wear can be distinguished; a representative instant for each of them is illustrated in Fig. C-15 (b):

- I. Phase I: Initialization. The damage starts to accumulate in the contacting zone, and particles start to detach from the matrix surface. However, the damage rate and the wear rate are negligible.
- II. Phase II: Steady-state. Grains are continuously damaged, detached, and ejected from the system. The damage propagates toward the matrix defining preferential paths for cracking nucleation and grains detachment. This aspect can be related to the fatigue effects and will be analyzed in the following section C.2.2 focused on the wear by fatigue.

- III. Phase III: “Perturbed” steady-state. Matrix grains are removed slower than Phase II because of the presence of the non-degradable material. For this reason, this zone is defined as “perturbed” and has no particular physical meaning.

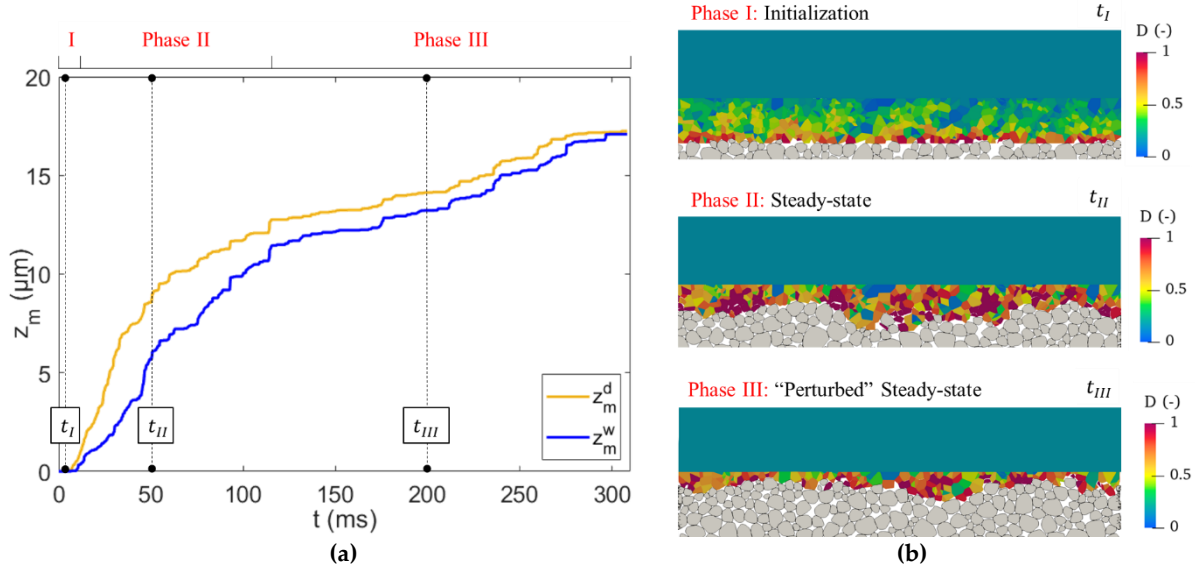


Fig. C-15 (a) Damage and wear curves obtained for the case:  $\tilde{p}_{lim} = 800 \text{ MPa}$ ;  $\tilde{\delta}_{res} = 0.002 \mu\text{m}$ ; (b) Damage maps for three different instants of time ( $t_I, t_{II}, t_{III}$ ) representative of the three phases of the wear process I,II,III

The detachment of grains during the wear process modifies the topography of the contact surface, which evolution can be directly correlated to the three stages of wear rate defined above. To better understand this evidence, Fig. C-16 plots the variation of the four roughness parameters  $R_a, R_q, R_{sk}, R_{ku}$  in time together with the variation of the wear level  $z_m^w$ .

It should be noted that the  $z$ -coordinate defining the roughness parameters in Eqs. (C.1-4) refers to the mean line that is different from the reference used to compute the height of wear  $z_m^w$  (see Fig. C-14). As expected, the average roughness  $R_a$  and the standard deviation  $R_q$  have the same shape profile that can be directly related to the three phases of wear discussed above in Fig. C-15.

After a brief and negligible initialization stage (Phase I), corresponding to stable values of  $R_a$  and  $R_q$ , the steady-state (Phase II) defines a period of rapid wear, during which the average roughness  $R_a$  and the deviation  $R_q$  increase up to a specific value and then decrease. The reduction of the roughness is confirmed in the literature [145]. In this particular case, it can be related to the smoothing of the surface and the truncation of valleys caused by the debris flow.

Although the steady-state can be associated with a large constant wear rate, some local features related to the irregularity of grains and the randomly generated microstructure may cause localized non-linear effects on the evolution of the wear depth with time. It is interesting

to notice that the slight change in the curvature of the level  $z_m^w$  in time corresponds to the peaks of the roughness parameters  $R_a$  and  $R_q$ . The “perturbed” steady-state (Phase III) is characterized by stable  $R_a$  and  $R_q$ ; a small jump on both curves is observed, and it may be related to the irregularities and local phenomenon of the wear. Finally, in the proximity of the non-degradable material, the roughness decreases again, reaching stabilization; however, this last aspect is only related to the presence of the flat non-degradable material and has no physical meaning. Concerning the irregularity of the profile, the skewness parameter  $R_{sk}$  drops down to negative values during Phase II, indicating the formation of sharp valleys where the contact pressure can localize within small contact areas, defining a favorable condition for the wearing. During Phase III, the skewness increases slightly, but it remains negative, reaching a zero value in correspondence with the final plateau of wear. Therefore, the skewness variation can be related to the number of asperities coming into contact that increases initially and decreases as the surface is worn and smoothed [145]. The persistence of negative values of skewness may be related to the slow wear process defined by the high intergranular cohesion (i.e., a large ultimate strength  $\tilde{p}_{lim} = 800 \text{ MPa}$ ), which causes the valleys are smoothed slowly and after several passages of the debris flow. Finally, looking at the kurtosis parameter, it drops down to values  $R_{ku} < 3$  during Phase I and remains almost constant during the steady-state of Phase II, justifying the particular shape of the surface described in Fig. C-15(b). Then, in the perturbed steady-state (Phase III), the kurtosis increases and stabilizes to values close to  $R_{ku} = 3$  with some fluctuations that can be due to the irregularities of the microstructure discussed above.

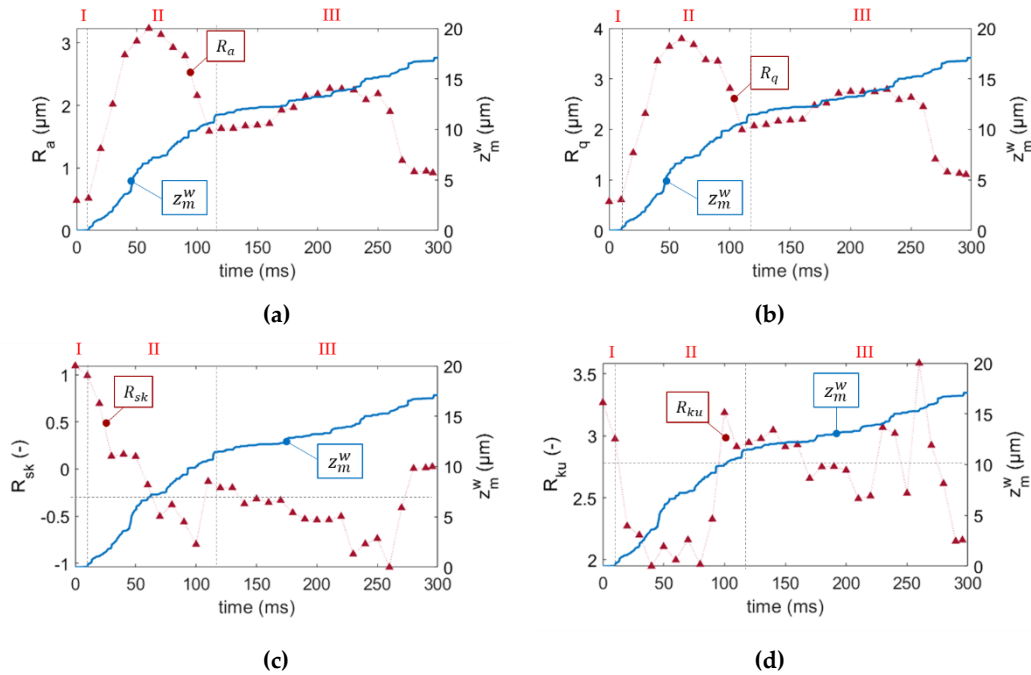


Fig. C-16 Variation of the roughness parameters: (a)  $R_a$ ; (b)  $R_q$ ; (c)  $R_{sk}$ ; (d)  $R_{ku}$  (in dark red) and the depth of wear  $z_m^w$  (in blue) with time if  $\tilde{p}_{lim} = 800 \text{ MPa}$

Changing the ultimate strength to  $\tilde{p}_{lim} = 50 \text{ MPa}$  lead to a faster wear process, as illustrated in Fig. C-17(a). Grains are detached and ejected faster than for  $\tilde{p}_{lim} = 800 \text{ MPa}$ . The initialization is characterized by the accumulation of damage before the material being removed, defining a slow wear rate before the steady-state, during which the wear rate is almost constant. Due to the particular damage distribution within the degradable material (Fig. C-17(b)), the third phase is reduced to a plateau (the wear rate is almost constant) in proximity to the non-degradable material. As already said discussing Fig. C-15, this last phase is unphysical since it is related to contact with the continuous material that does not exist in reality.

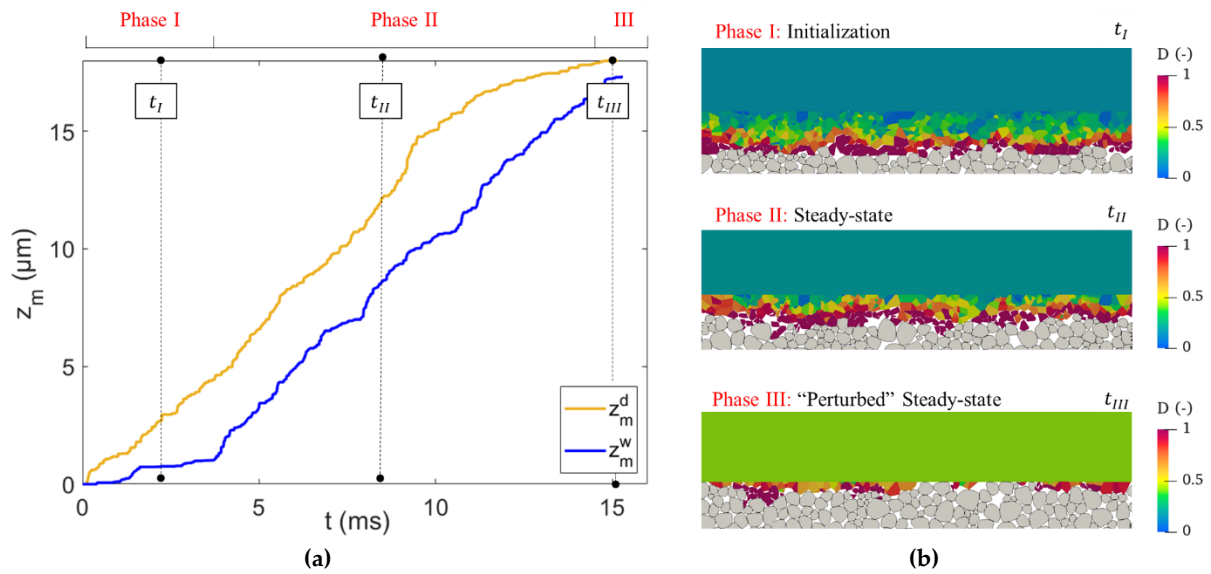


Fig. C-17 (a) Damage and wear curves obtained for the case:  $\tilde{p}_{lim} = 50 \text{ MPa}$ ;  $\tilde{\delta}_{res} = 0.002 \mu\text{m}$ ; (b) Damage maps for three different instant of time representative of the three phases of the wear process I, II, III

The rapidity of grains detachment and wear gives rise to a surface profile evolution which is different from that of the previous case shown in Fig. C-16. It is illustrated in Fig. C-18. The initial incubation of damage (Phase I – initialization in Fig. C-17) increases the irregularity of the surface in terms of  $R_a$  and  $R_q$ , defining favorable conditions to the wear process, as displayed in Fig. C-18. During the steady-state (Phase II), roughness continues to increase and then decreases because of the smoothing of the surface caused by the debris passages.

Concerning the symmetry of the profile, the skewness reduces in Phase I, reaching negative values during the steady-state, meaning the presence of sharp valleys on the profile in contact with the debris flow. Then, the last part of Phase II is characterized by the increase of the skewness up to  $R_{sk} > 0$ , which is consistent with the reduction of the average roughness. At contact with the non-degradable material (Phase III), the skewness decrease again to  $R_{sk} < 0$ , however, as already said, this part is affected by the non-degradable material and should be ignored. The kurtosis profile firstly reduces during the initialization and then increases again during the steady-state reaching values that are consistent with the profile in Fig. -17(b) ( $R_{ku} <$

3). Fig. C-18 shows that the skewness and kurtosis evolutions are characterized by fluctuations that can be explained by the continuously sharpening and smoothing of the contact surface caused by the spatial distribution of damage (damaged grains are equally distributed along the contact surface as illustrated in Fig. C-17 (b), and they can be easily removed and ejected).

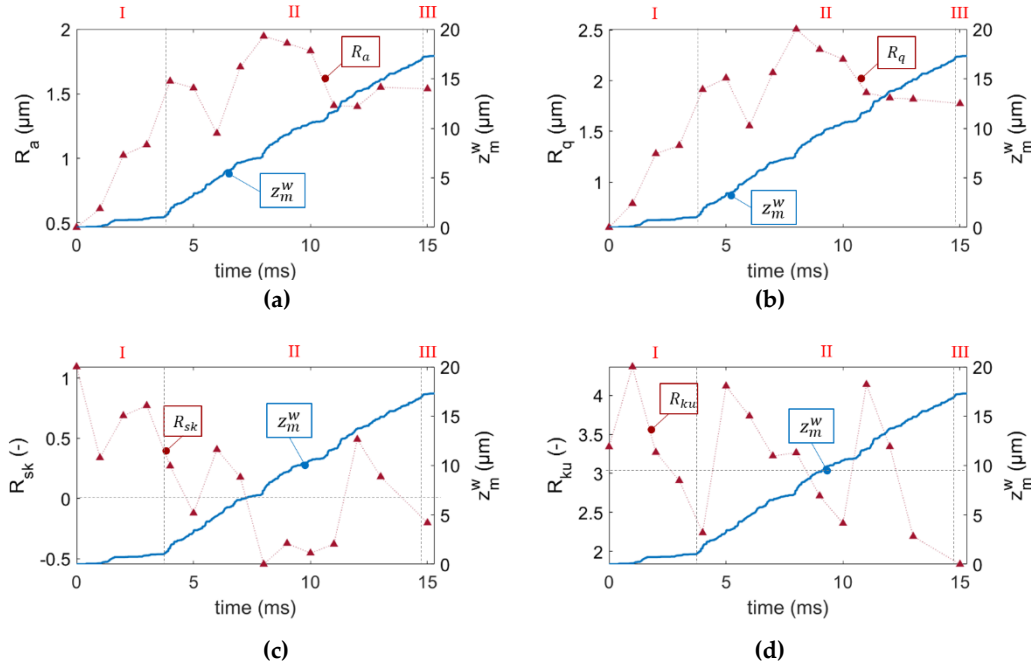


Fig. C-18 Variation of the roughness parameters: (a)  $R_a$ ; (b)  $R_q$ ; (c)  $R_{sk}$ ; (d)  $R_{ku}$  (in dark red) and the depth of wear  $z_m^w$  (in blue) with time if  $\tilde{p}_{lim} = 50 \text{ MPa}$

Fig. C-16 and Fig. C-18 demonstrate that the evolution of the characteristic roughness is strongly related to the mechanical properties of the microstructure and the following wear process. Also, a single parameter is not sufficient to describe the topography of a surface completely.

Moreover, the initialization develops differently in the two cases analyzed ( $\tilde{p}_{lim} = 800 \text{ MPa}$  and  $\tilde{p}_{lim} = 50 \text{ MPa}$ ). The ultimate strength  $\tilde{p}_{lim}$  also has a strong impact on the onset of the contact between the matrix and the debris flow. If  $\tilde{p}_{lim}$  is large enough compared to the applied pressure (i.e. for  $\tilde{p}_{lim} = 800 \text{ MPa}$  as compared with  $p_n = 3.4 \text{ MPa}$ ) the maximum Von Mises stress (Fig.C-19(a)) occurs close to the contact surface, and results agree with continuum elasticity theory. Due to its particular roughness, the local contacting surface is almost horizontal, and the shear stress  $\tilde{\tau}$  is representative of the tangential stress (Fig. 19 (b)). When reducing the ultimate strength ( $\tilde{p}_{lim} = 50 \text{ MPa}$ , as compared with  $p_n = 3.4 \text{ MPa}$ ), the impact with the debris flow allows the stress to propagate within the matrix leading to an early crack initialization. The maximum Von Mises stress (Fig. C-20(a)) occurs at a certain distance from the contacting surface, corresponding to the weak joints where the fracture starts to appear.

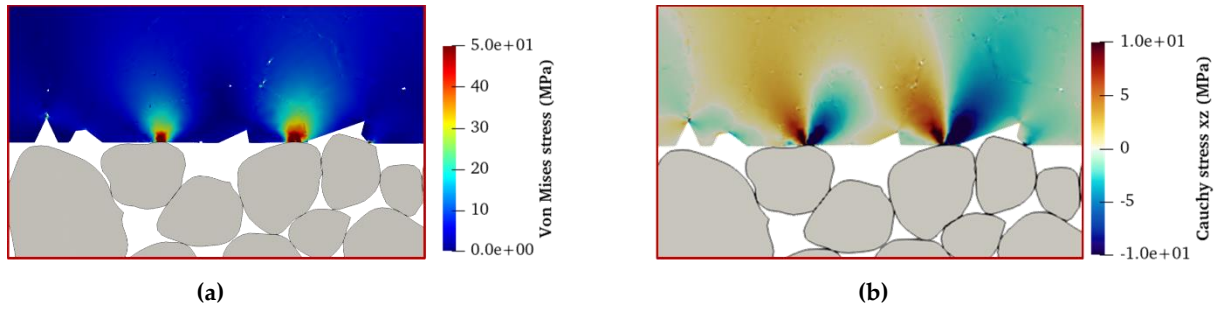


Fig. C-19 Example of stress generated during the onset of the contact ( $\tilde{p}_{lim} = 800 \text{ MPa}$ ;  $\tilde{\delta}_{res} = 0.002 \mu\text{m}$ ) (a) Von Mises stress; (b) tangential xz stress

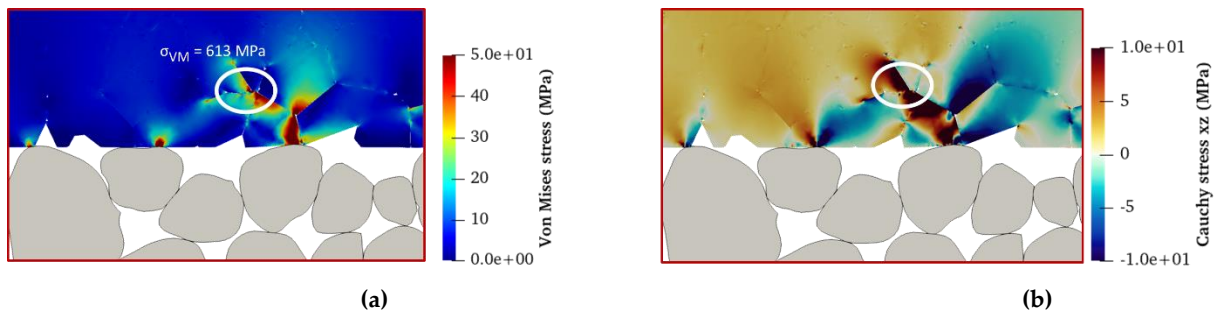


Fig. C-20 Stress on the matrix microstructure generated during the onset of the contact with the first cracking in the microstructure ( $\tilde{p}_{lim} = 50 \text{ MPa}$ ;  $\tilde{\delta}_{res} = 0.002 \mu\text{m}$ ) (a) Von Mises stress; (b) tangential stress

We observe that, in the case  $\tilde{p}_{lim} = 50 \text{ MPa}$ , the source flow (i.e. the detachment of grains from the matrix) occurs too fast to allow for an efficient ejection of the worn material from the interface. Grains are detached too quickly and remain in the system for a while before being ejected; they are free to evolve in the contact during this time, defining a part of the third body. Therefore, in this case, wear is not caused by debris grains but by the grains of the matrix themselves (Fig. C-17(b)). This is in disagreement with experimental observations, which show that the presence of matrix grains in the third body (i.e., in the debris flow) is negligible. The case  $\tilde{p}_{lim} = 50 \text{ MPa}$  can therefore be considered as unphysical. This phenomenon is more evident when decreasing the ultimate strength  $\tilde{\delta}_{res}$  as illustrated in Fig. C-21, where the wear level  $z_m^w(t)$  is plotted for  $\tilde{\delta}_{res} = 0.002 \mu\text{m}$  and  $\tilde{\delta}_{res} = 0.0002 \mu\text{m}$ .

Therefore, the simple damage parameter  $D$  used in the standard CZM law does not account for this character since grains bonds evolve quickly from the intact to the broken state.

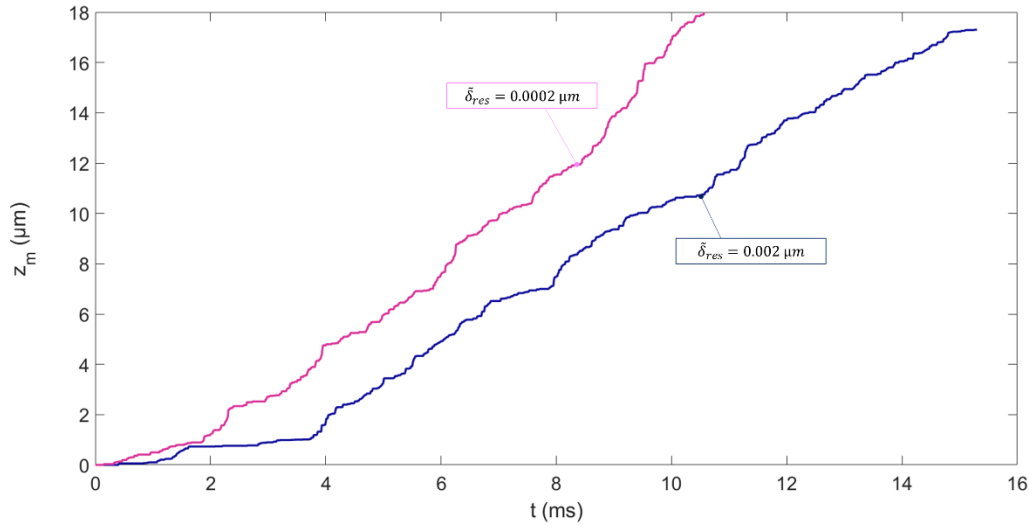


Fig. C-21 Wear curves obtained for  $\tilde{\delta}_{res} = 0.002 \mu m$  and  $\tilde{\delta}_{res} = 0.0002 \mu m$ . In both cases  $p_{lim} = 50 MPa$

On the other side, a large ultimate strength coupled with a low fatigue damage rate  $dD_f$  requires many stress cycles before grains are damaged and then detached, allowing time for the damage to propagate towards the inner part of the degradable microstructure (Fig. C-15 (b)). This observation confirms the benefit of introducing fatigue in the CZM contact-law applied to the wear of the matrix. The following section C.2.2. is focused on the fatigue effect considering an ultimate strength  $\tilde{p}_{lim} = 800 MPa$  and a residual gap  $\tilde{\delta}_{res} = 0.002 \mu m$ .

## C.2.2 Effect of the fatigue damage rate on the wear process

If a large ultimate strength ( $\tilde{p}_{lim} = 800 MPa$ ) is chosen, the matrix damaging occurs mostly by fatigue. The fatigue damage evolution parameter  $dD_f$  defines the rapidity with which the damage parameter  $D$  evolves from 0 to 1 with cycles of contact pressure  $\tilde{p}$ . To quantify this effect in terms of wear rate, simulations are run considering different values for  $dD_f$  as listed in Tab. C-7, while the Mohr-Coulomb parameters are the same as in Tab. C-6.

Tab. C-7 CZM parameters for the fatigue damage rate sensitivity

$k_0$ (MPa/ $\mu m$ )	$\tilde{p}_{lim}$ (MPa)	$\tilde{\delta}_{res}$ ( $\mu m$ )	$\tilde{p}_{res}$ (MPa)	$\tilde{p}_f$ (MPa)	$dD_f$ (MPa <sup>-1</sup> )
10 <sup>6</sup>	800	0.002	0	10	<b>0.1 0.05 0.01</b>
					<b>0.001</b>
					<b>0.0001</b>

Fig. C-22 illustrates the effect of the fatigue damage evolution parameter  $dD_f$  on the wear process. The larger the parameter  $dD_f$ , the faster the grains ejection.

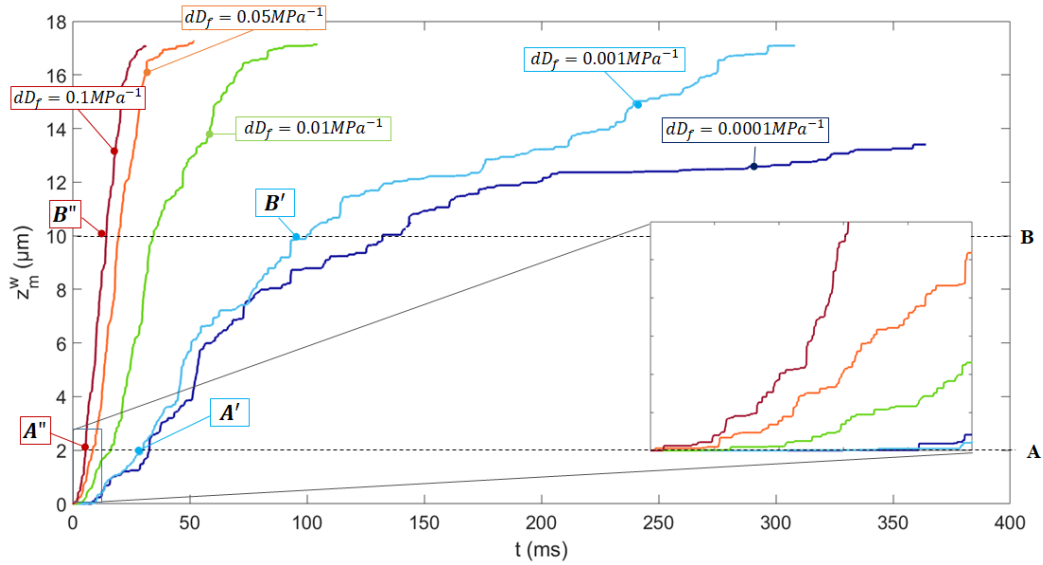


Fig. C-22 Wear curves for different values of  $dD_f$  and zoom on the initialization stage. Indications A and B refer to two particular wear depth  $z_m^w$  of the wear-in: A' and B' are relative to the case  $dD_f = 0.001 \text{ MPa}^{-1}$ ; A'' and B'' correspond to  $dD_f = 0.1 \text{ MPa}^{-1}$

Looking in more details at the three phases of wear (initialization, wear-in and steady-state), the decreasing of the fatigue damage evolution parameter  $dD_f$  leads to an increase in the duration of the initialization stage, which defines the damage incubation. However, the onset of the contact does not appear to be strongly affected by  $dD_f$ ; even for large values, the pressure field follows a Hertzian-like profile, as illustrated in the example of Fig.C-23 in terms of Von Mises and Cauchy tangential stresses for large fatigue damage parameter evolution ( $dD_f = 0.1 \text{ MPa}^{-1}$ ). The stress field in Fig. C-23 is comparable with the stress field in Fig. C-19, corresponding to the case  $dD_f = 0.001 \text{ MPa}^{-1}$ .

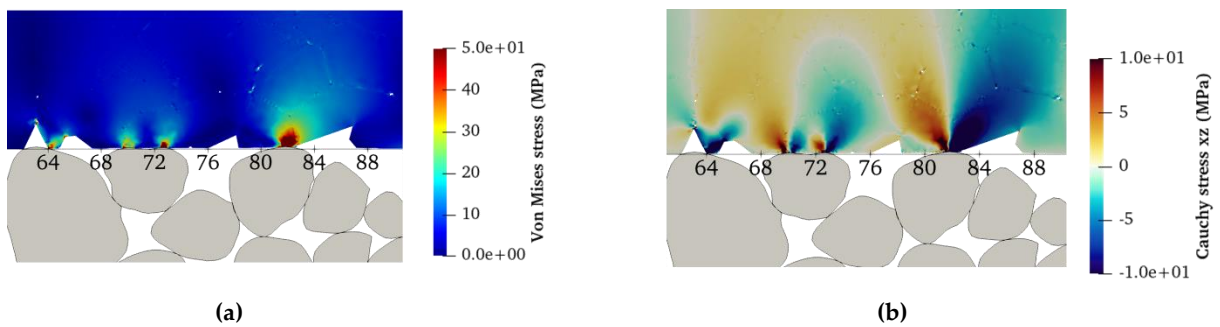


Fig. C-23 Example of stress generated during the onset of the contact ( $\tilde{p}_{lim} = 800 \text{ MPa}$ ;  $\tilde{\delta}_{res} = 0.002 \text{ } \mu\text{m}$ ,  $dD_f = 0.1 \text{ MPa}^{-1}$ ) (a) Von Mises stress; (b) tangential xz stress

Concerning the steady-state, when increasing the fatigue damage evolution parameter  $dD_f$ , it becomes more and more linear with a transition from  $dD_f = 0.001 \text{ MPa}^{-1}$  to  $dD_f = 0.01 \text{ MPa}^{-1}$ . To better understand the role of the  $dD_f$ , figures from Fig. C-24 to Fig.C-27 show the damage distribution  $D$ , the magnitudes of displacements, the von-Mises stress, and the

Cauchy tangential stress corresponding to  $dD_f = 0.001 \text{ MPa}^{-1}$  and  $dD_f = 0.1 \text{ MPa}^{-1}$  taken at two different steps of the wear process (A' and B' for  $dD_f = 0.001 \text{ MPa}^{-1}$ , and A'' and B'' for  $dD_f = 0.1 \text{ MPa}^{-1}$ , as described in Fig. C-22) but corresponding to the same wear depth  $z_w^m$  corresponding to the points A and B in Fig. C-22.

Figs. C-24 and C-25 refers to the wear depth corresponding to point A in Fig. C-22, referring respectively to the case  $dD_f = 0.001 \text{ MPa}^{-1}$  and  $dD_f = 0.1 \text{ MPa}^{-1}$ .

As introduced in section C.2.1, the slow fatigue damage evolution parameter ( $dD_f = 0.001 \text{ MPa}^{-1}$ ) coupled with large ultimate strength ( $\tilde{p}_{lim} = 800 \text{ MPa}$ ) gives time to the damage to propagate in the thickness of the microstructure, defining a preferential path for the crack propagation. This evidence is explained by looking at the displacement map of Fig. C-24, where damaged grains are subjected to significant relative displacements corresponding to the opening of the micro-fractures. This aspect can also be seen in Von Mises and tangential Cauchy stress distribution within the matrix. This particular evidence is responsible for the slow wear process as grains of the contacting surface remain for a certain time before being damaged and ejected.

For a large value of fatigue damage parameter ( $dD_f = 0.1 \text{ MPa}^{-1}$ ), damaged grains are almost distributed along the contact surface; they are detached and ejected faster than for  $dD_f = 0.001 \text{ MPa}^{-1}$ , giving no time for cracks to propagate within the matrix. This situation is also confirmed by the map of grain displacement and stress field: localization of stress is limited to the surface in contact with the debris flow (Fig. C-25).

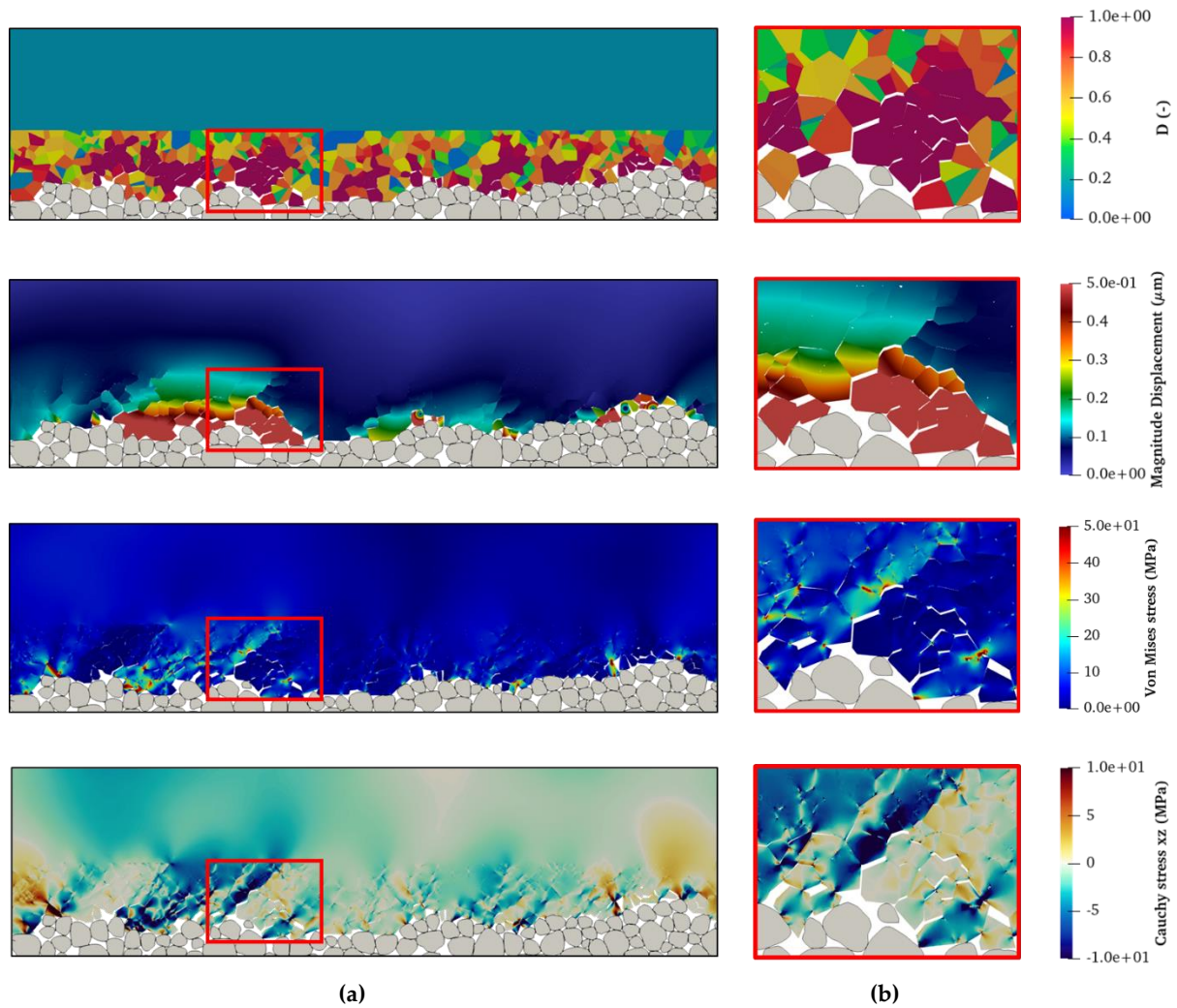


Fig. C-24 Steady-state at the point A' corresponding to the time  $t = 30 \text{ ms}$  and the wear level  $z_m^w = 2 \text{ }\mu\text{m}$  ( $\tilde{p}_{lim} = 800 \text{ MPa}$ ;  $\tilde{\delta}_{res} = 0.002 \text{ }\mu\text{m}$ ,  $dD_f = 0.001 \text{ MPa}^{-1}$ ): **(a)** Maps in terms of body damage parameter  $D$ , Magnitude displacement; Von Mises stress and Cauchy  $-xz$  stress; **(b)** relative zooms on a microcrack highlighted in the red window. The damage propagates within the matrix microstructure generating cracks within the material. The fracture is characterized by high relative displacement; moreover, damaged grains are subjected to large displacements while the stress concentrates on the surrounding non-damaged material

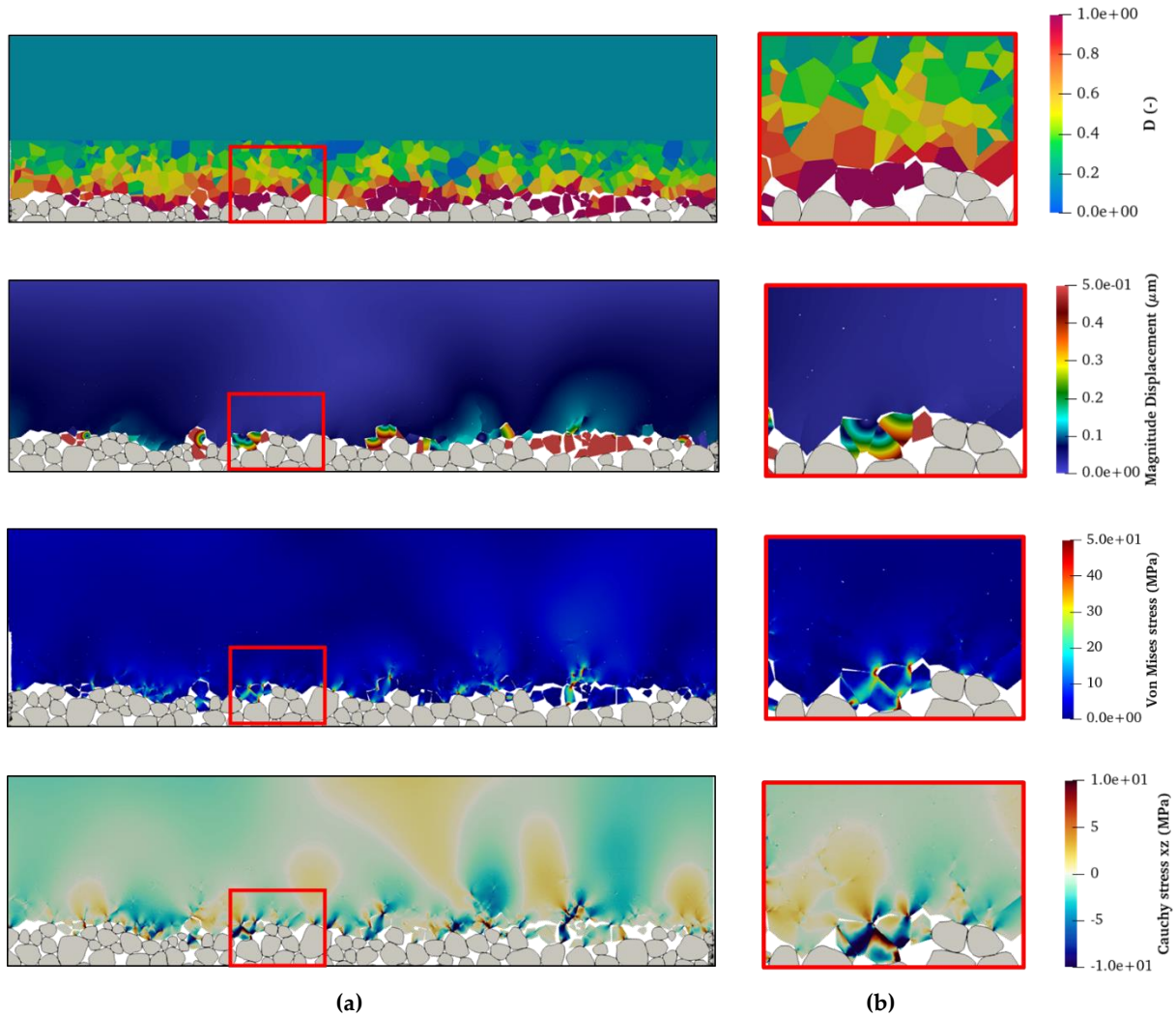


Fig. C-25 Steady-state at the point A'' corresponding to the time  $t = 5.6 \text{ ms}$  and the wear level  $z_m^w = 2 \text{ } \mu\text{m}$  ( $\tilde{p}_{lim} = 800 \text{ MPa}$ ;  $\tilde{\delta}_{res} = 0.002 \text{ } \mu\text{m}$ ,  $dD_f = 0.1 \text{ MPa}^{-1}$ ): **(a)** Maps in terms of body damage parameter  $D$ , Magnitude displacement; Von-Mises stress and Cauchy  $-xz$  stress; **(b)** relative zooms on the red windows (same as in Fig. C-25). There are no particular fractures and microcracks within the matrix microstructure. The fracture is localized on the contacting surface

Going deeper with wear and reaching the point  $z_m^w = B = 10 \text{ } \mu\text{m}$ , the damage, displacement and stress fields referring to B' ( $dD_f = 0.001 \text{ MPa}^{-1}$ ) are illustrated in Fig. C-26. The damage propagation within the material seems to be hindered by the non-degradable material since it defines an upper limit to wearing: grains in contact with it are generally characterized by strong cohesion. This evidence, together with the already investigated evolution of roughness (Fig. C-16) can explain the particular bilinear wear rate observed in Fig. C-22 characterized by a "premature perturbed" steady-state (phase III of wear begins before that most of the grains are ejected, meaning that the wear rate becomes perturbed by the damage that has already reached the upper limit).

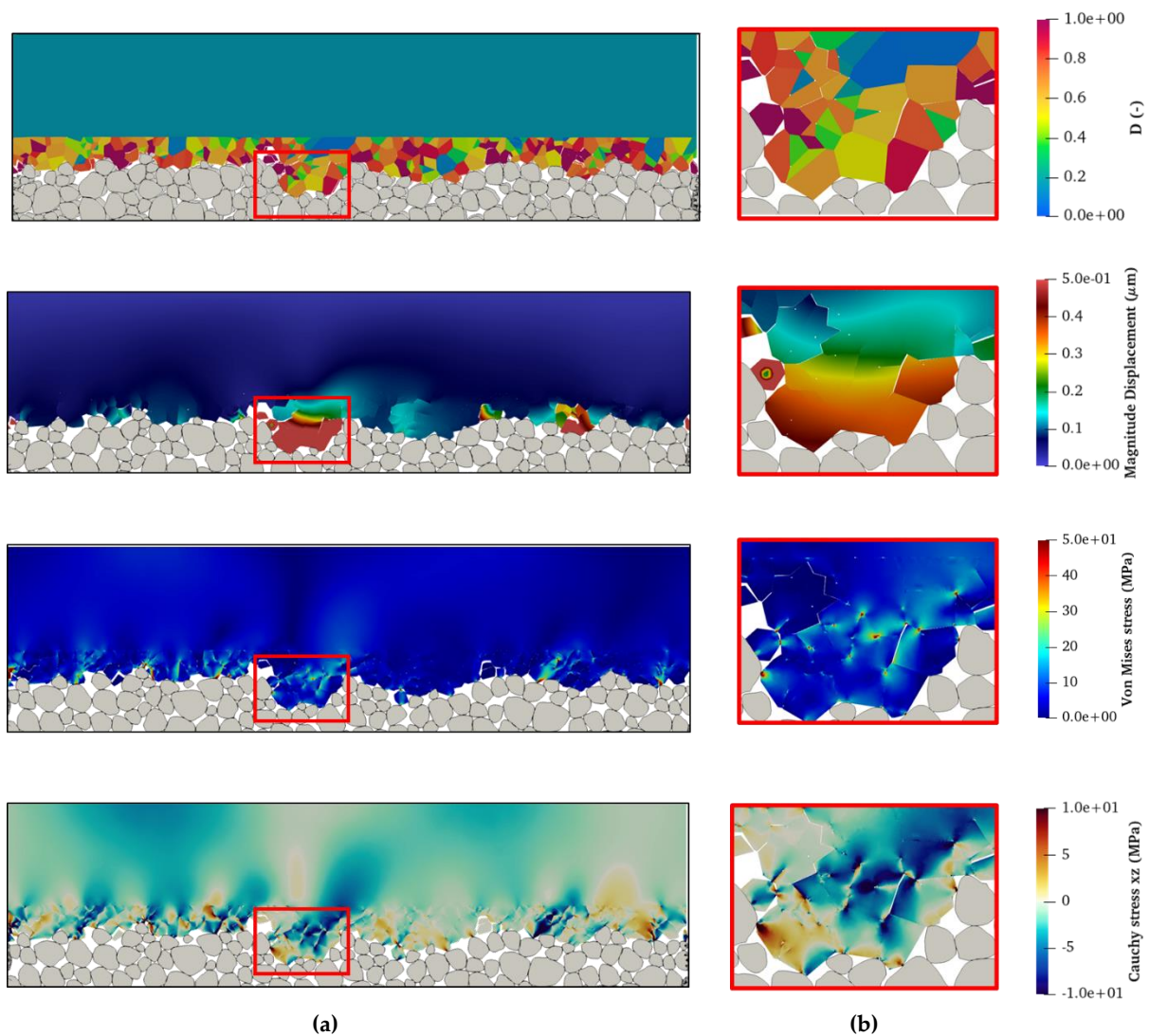


Fig. C-26 “Perturbed” steady-state at the point B' corresponding to the time  $t = 100 \text{ ms}$  and the wear level  $z_m^w = 10 \mu\text{m}$  ( $\tilde{p}_{lim} = 800 \text{ MPa}$ ;  $\delta_{res} = 0.002 \mu\text{m}$ ,  $dD_f = 0.001 \text{ MPa}^{-1}$ ): (a) Maps in terms of body damage parameter  $D$ , Magnitude displacement; Von-Mises stress and Cauchy  $xz$  stress; (b) relative zooms on the red windows. The damage propagates within the matrix microstructure, generating developing microfracture; however, the presence of the non-degradable microstructure imposes a limit to this phenomenon and to the grains detachment

On the other hand, for a large fatigue damage evolution parameter ( $dD_f = 0.1 \text{ MPa}^{-1}$ ), the damage is well distributed on the surface and seems to be non affected by the presence of the non-degradable base (Fig.C-27). Since the fatigue damage parameter is large, the damage increases quickly, the microcracks generated at the contacting surface do not have time to propagate toward the inner microstructure as grains are detached.

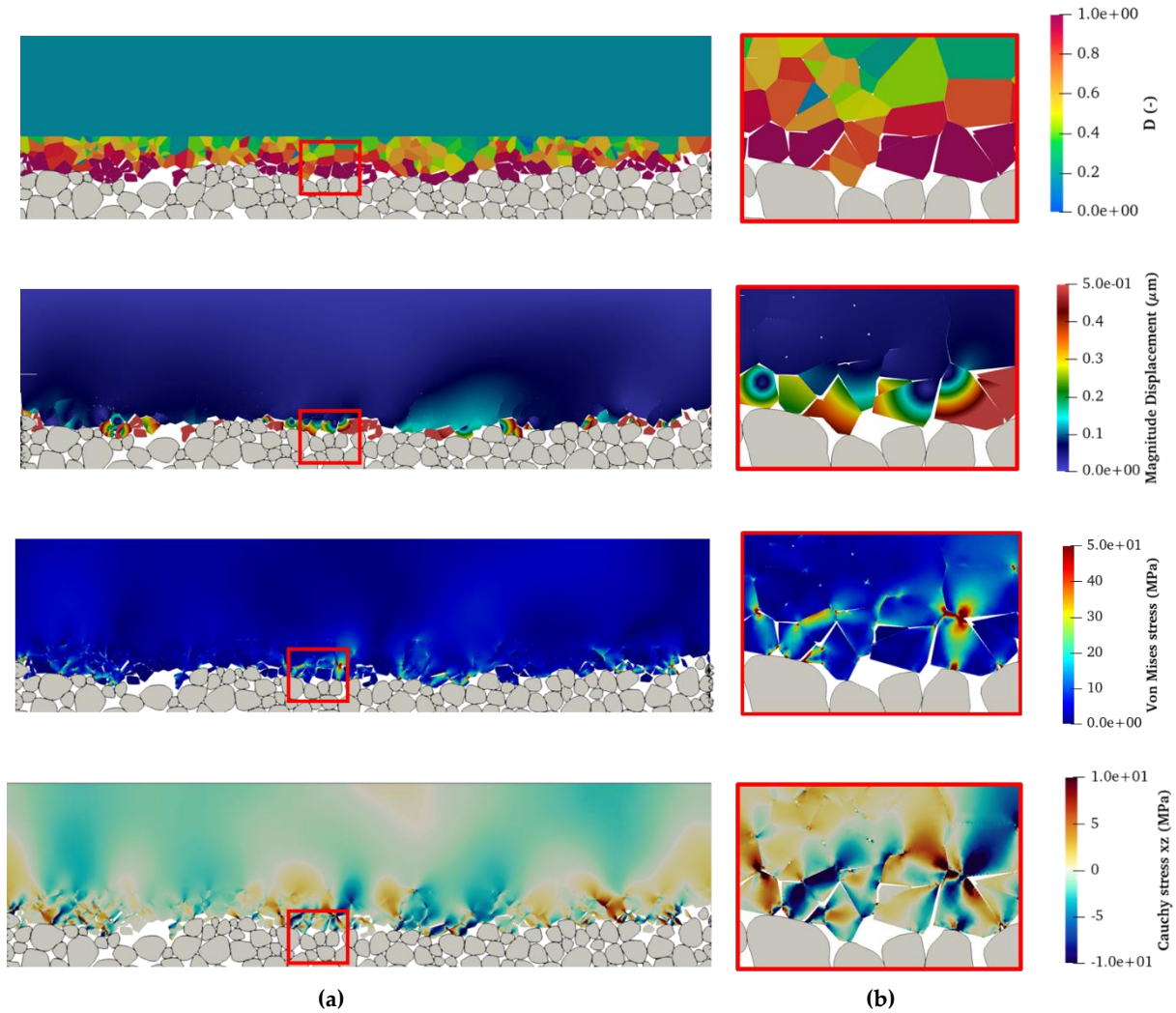


Fig. C-27 Steady-state at the point B'' corresponding to the time  $t = 14.4 \text{ ms}$  and the wear level  $z_m^w = 10 \text{ }\mu\text{m}$  ( $\tilde{p}_{lim} = 800 \text{ MPa}$ ;  $\tilde{\delta}_{res} = 0.002 \text{ }\mu\text{m}$ ,  $dD_f = 0.1 \text{ MPa}^{-1}$ ): (a) Maps in terms of body damage parameter  $D$ , Magnitude displacement; Von Mises stress and Cauchy  $-xz$  stress; (b) relative zooms on the red windows. Damaged grains are distributed on the contacting surface. Detached grains undergo severe displacements; microcracks emerge on the contacting surface but, since the damage increases quickly, they do not have time to propagate within the material

To better understand the propagation of the damage within the matrix microstructure, Fig. C-28 plots the vertical position of each grain as a function of their damage parameter  $D$  for the two conditions A and B of Fig. C-22 and representing the two situations described by  $dD_f = 0.001 \text{ MPa}^{-1}$  (A', B') and  $dD_f = 0.1 \text{ MPa}^{-1}$  (A'', B''). As expected, damaged grains are distributed along the whole vertical direction if  $dD_f = 0.001 \text{ MPa}^{-1}$  (Fig. C-28 (a) and (b)); while they are more localized along the contacting surface if  $dD_f = 0.1 \text{ MPa}^{-1}$ . Moreover, the averaged damage obtained, as the moving average of spatial damage distribution, is almost linear for cases (a) and (b) ( $dD_f = 0.001 \text{ MPa}^{-1}$ ) defining a constant slope  $z_m/D$  of the averaged damage. Graphs (c) and (d), on the other hand, show an initially bilinear and finally linear behavior of the mean damage. This aspect indicates that if the parameter  $dD_f$  is small, the

damage  $D$  is linearly distributed over the whole depth of the degradable part. If the parameter  $dD_f$  is large, the damage evolves quickly and has not time to propagate within the whole degradable material involving, in the first moment, only the part of the degradable surface in contact with the debris flow (c).

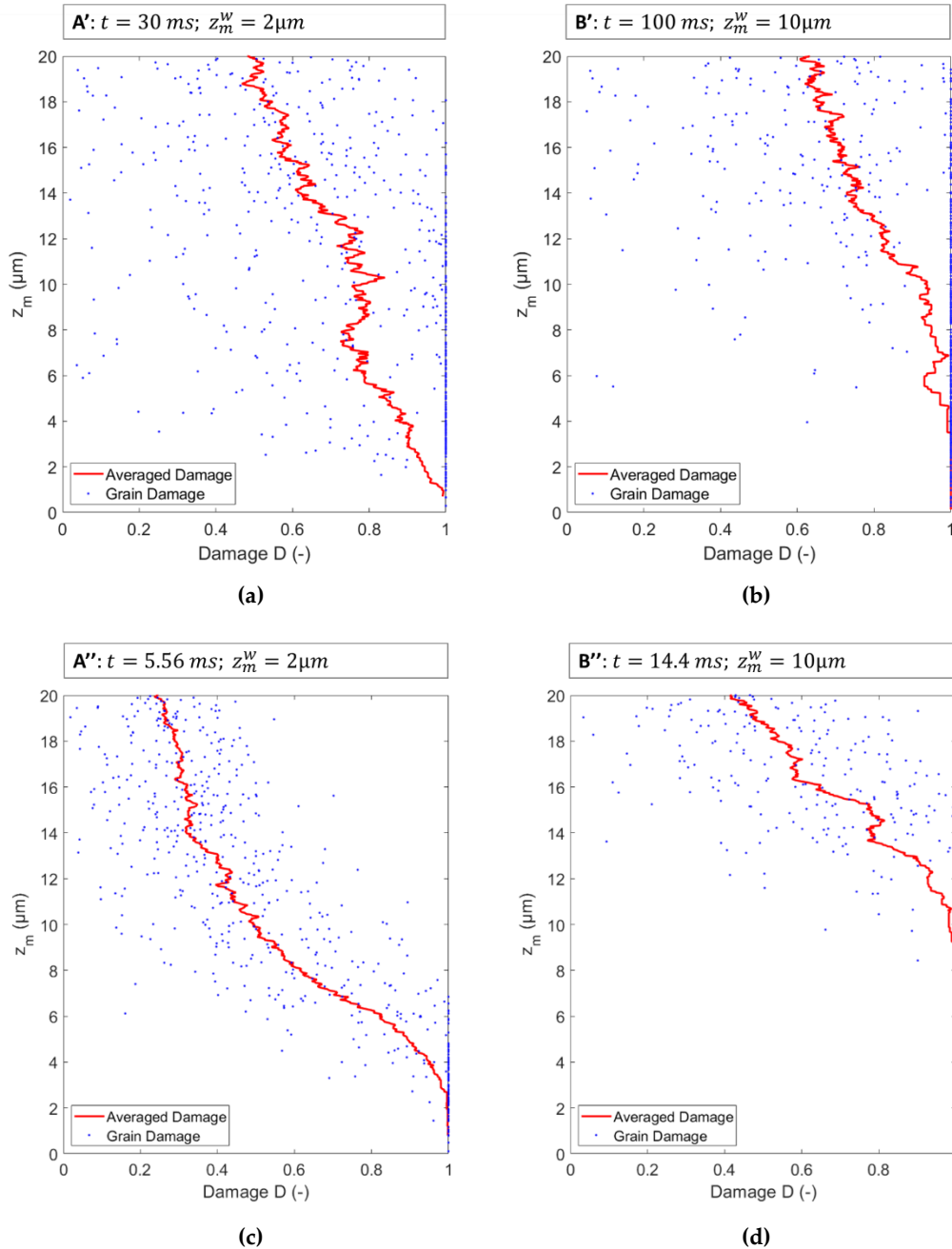


Fig. C-28 Grains vertical position vs. Damage parameter (a)  $A'$   $dD_f = 0.001\text{MPa}^{-1}$ ; (b)  $B'$   $dD_f = 0.001\text{MPa}^{-1}$ ; (c)  $A''$   $dD_f = 0.1\text{MPa}^{-1}$ ; (d)  $B''$   $dD_f = 0.1\text{MPa}^{-1}$ ;

It is interesting to notice that the slope ( $-z_m/D$ ) increases reducing the fatigue damage parameter  $dD_f$  and is almost constant for each value of  $dD_f$ , as illustrated in Fig. C-29.

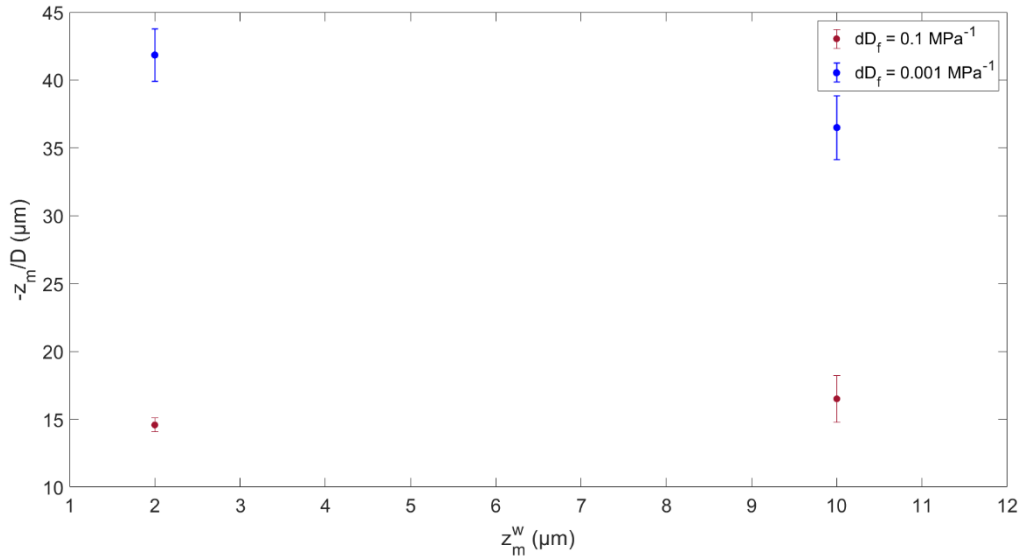


Fig. C-29 Spatial derivate of the damage parameter  $D$  with the depth of the degradable material  $z_m$  as a function of the wear level  $z_m^w$  for the cases observed in Fig. C-28

These results confirm that if the fatigue damage evolution parameter is large, the damage has no time to propagate within the matrix.

Fig. C-30 plots the wear rate defined as  $z_m^w/t$  computed from Fig. C-22 considering the steady-stage phase as a function of the fatigue damage evolution parameter  $dD_f$ . The uncertainty of the measurement is estimated in terms of standard error (defined as the ratio between the standard deviation and the root square of the sample size), which increases for low values of  $dD_f$ . However, the relationship  $z_m^w/t$  vs.  $dD_f$  is well fitted by a power law.

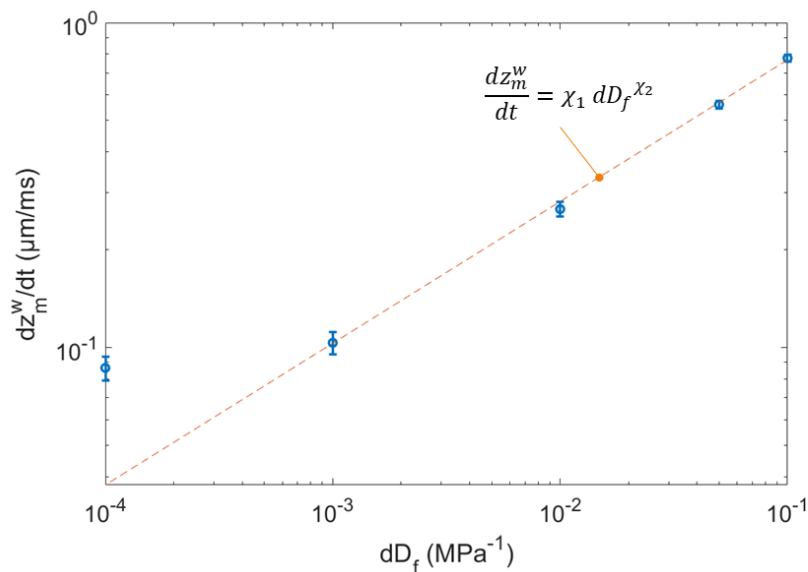


Fig. C-30 Evolution of the wear rate  $\Delta h_m/t$  with the fatigue damage rate  $dD_f$  fitted by a power law ( $\chi_1 = 2.099$ ;  $\chi_2 = 0.4363$ ;  $R^2 = 0.9099$ )

The effect of the damage evolution parameter on the wear rate is analyzed in Fig. C-31 by comparing the number of damaged particles  $Q_m^d$  ( $D = 1$ ) to the ejected ones  $Q_m^w$  ( $l_{de} \geq \frac{d_g}{2}$ ) and observing that grains achieving  $D = 1$  remain in the system before being ejected, most of them are not completely detached, and the wear is still caused by the debris flow, as explained in Part A. The relationship  $Q_m^w$  vs.  $Q_m^d$  changes as a function of the fatigue damage evolution parameter  $dD_f$ , confirming the transition observed in Fig. C-18 from  $dD_f = 0.001 \text{ MPa}^{-1}$  to  $dD_f = 0.01 \text{ MPa}^{-1}$ .

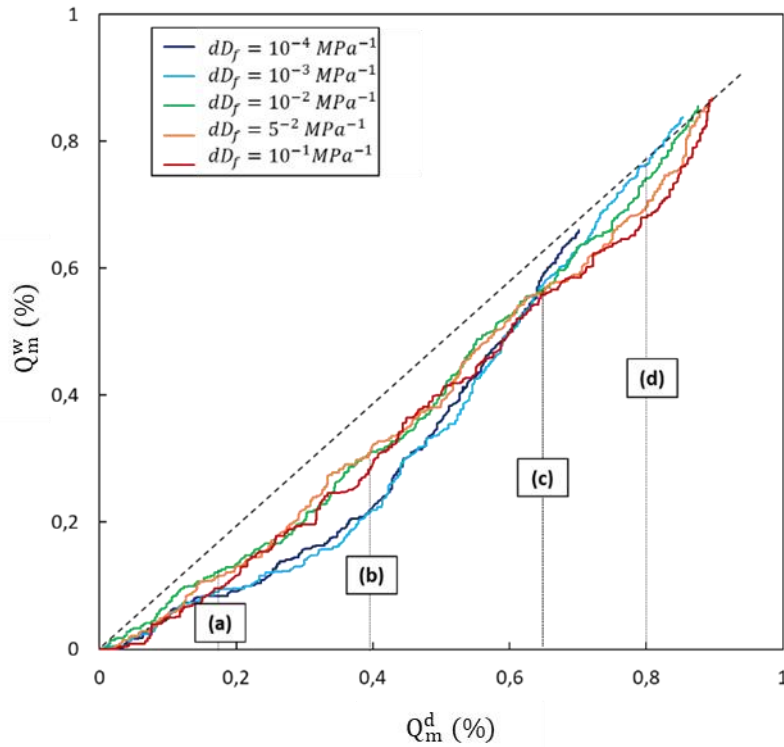


Fig. C-31 Relationship between damaged particles  $Q_m^d$  ( $D = 1$ ) and ejected particles  $Q_m^w$  ( $l_{de} \geq \frac{d_g}{2}$ )

To better understand the effect of the damage on the debris ejection, Fig. C-32 illustrates the damage of the microstructure for different instant times corresponding to the points (a), (b), (c), (d), which are chosen from Fig. C-31 ((a):  $Q_m^d = 0.17$ , (b):  $Q_m^d = 0.4$ , (c):  $Q_m^d = 0.6$ , (d):  $Q_m^d = 0.8$ ) on the curves with  $dD_f = 0.1 \text{ MPa}^{-1}$  and  $dD_f = 0.001 \text{ MPa}^{-1}$

- (a)  $Q_m^d = 0.17$ : there is no significant influence of the damage rate on the amount of ejected particles. However, the distribution of the damage  $D$  depends on the established fatigue damage parameter: If the damage parameter  $D$  increases fast, it does not have time to propagate towards the inside of the matrix, and the damaged grains stay mostly on the surface in contact with the debris flow. If the damage parameter increases slowly, the damage propagates within the matrix surface, defining a preferential path for further cracking and detaching.

- (b)  $Q_m^d = 0.4$ : the amount of ejected particles is smaller for the lower damage rate. The roughness of the surface may explain the two different behaviors observed for low and large fatigue damage evolution parameter  $dD_f$ . In the former case, the damage is localized in clusters whose ejection is prevented by the neighboring undamaged grains.
- (c)  $Q_m^d = 0.64$ : the ratio of ejected and damaged grains is almost the same for the different fatigue damage evolution parameter; Then, for  $Q_m^d > 0.64$ , the trend is reversed with respect to that observed for  $Q_m^d < 0.64$
- (d) For  $Q_m^d = 0.8$ , the number of damaged particles increases with decreasing the damage rate. This evidence is consistent with what is observed previously. If the fatigue damage parameter is large, the damage is equally distributed on the contact surface that shows several peaks and valley on the profile ( $R_{ku} > 3$ ) which are smoothed at the end of the wear-in. As already said, grains are strongly bonded to the non-degradable surface, and their detachment happens slowly. If the fatigue damage parameter is large, the damage distribution follows different paths and propagate within the matrix surface.

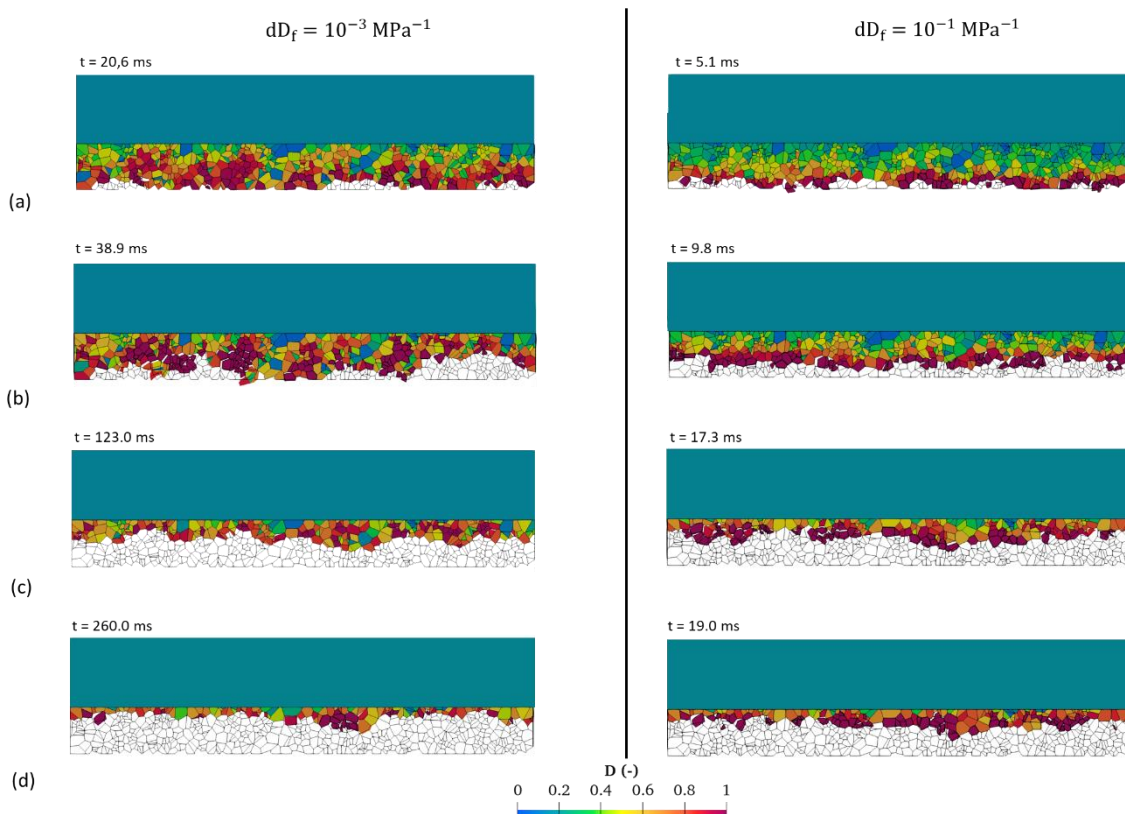


Fig. C- 32 Evolution of the damage profile for two different fatigue damage rate:  $dD_f = 0.001 \text{ MPa}^{-1}$  (left)  $dD_f = 0.1 \text{ MPa}^{-1}$  (right) at four different stages of  $Q_m^d$  from Fig. C-25: (a)  $Q_m^d = 0.17$ ; (b)  $Q_m^d = 0.4$ ; (c);  $Q_m^d = 0.6$ , (d)  $Q_m^d = 0.8$

Although it is difficult to extract quantitative information from this model and the several parameters that need to be defined, the model can describe the mechanisms involved in the wear process at the local scale. The wear by fatigue plays an important role in the mechanisms of damage and detaching of particles.

Results here presented showed a strong relationship between the evolution of the surface topography, the contact parameters and the wear process. What is not yet clear is whether the roughness is directly related to the strength of the contact (i.e., the CZM –fatigue parameters) and is, therefore, a cause of the wear process or if it is a consequence of it. Such observation and results should be validated considering a large degradable matrix, which will require a more expensive computation but will be useful for a better understanding of the wear processes involving small fatigue damage evolution parameters  $dD_f$ .

A methodology to set the parameters of the CZM is discussed in the next Chapter C.3 using the strong analogy between the wear caused by a debris flow and that generated by an indenter, already discussed in Part B for the writing of the wear equation.



## C.3

# Towards a quantitative approach

The previous Chapters, C.1 and C.2 defined a model for describing the wear of a softer polycrystalline material caused by a harder debris flow. The grain size distribution of the metal microstructure was consistent with the experimental one, but the CZM contact laws' strength parameters did not correspond to any measurement made on the targetted microstructure. Performing a calibration based on the mesoscopic model is possible but costly since it requires performing fatigue simulations, including a large number of compliant grains and a long-wear process. Moreover, the comparison with the experimental test may not be so evident.

The idea of this chapter is to calibrate the ultimate strength  $\tilde{p}_{lim}$  and the residual stress  $\tilde{p}_{res}$  of the CZM law, bypassing the wear model described previously and performing a numerical multi-scratch test whose results can be compared with the experiments introduced in Chapter B.1.

As MELODY is restricted to plane strain kinematics, the intention is limited to the calibration; it cannot claim to describe numerically the wear modes induced by the indentation and scratching (discussed in section A.2.4). Despite its simplicity, the model can, however, describe micromechanical phenomena such as irreversible deformations and residual stress induced by scratching.

The first section C.3.1 completes section B.1.2 and adds some complementary information regarding the multi-scratch test, which is useful for the calibration. The second section C.3.2, describes the model in terms of geometry, boundary conditions, and contact laws. The third section C.3.2, discusses and compares numerical results with what is already explained in C.3.1, investigating the micromechanical response of the matrix during scratching.

### C.3.1 Experimental observation on the $\mu$ -scratch test

The  $\mu$ -scratch test was introduced in section B.1.2 to define a characteristic hardness  $H_s^*$ , which was further used to derive the wear equation. Important features that can be extracted during the second stage of the test, and for each indenter pass, are the penetration depth  $h_{p,s}$ , the residual depth  $h_{r,s}$ , and friction coefficient  $\mu_{r,s}$ . These quantities are plotted in Fig. C-33 for successive passages  $n_s$  of the indenter along the same scratch path  $L_s$ .

The rate of penetration depth  $h_{p,s}$  (Fig. C-32 (a)) and residual depth (Fig. C-32 (b)) reduces with the number of scratches  $n_s$ , as a consequence of the strain hardening introduced previously in section B.1.2.

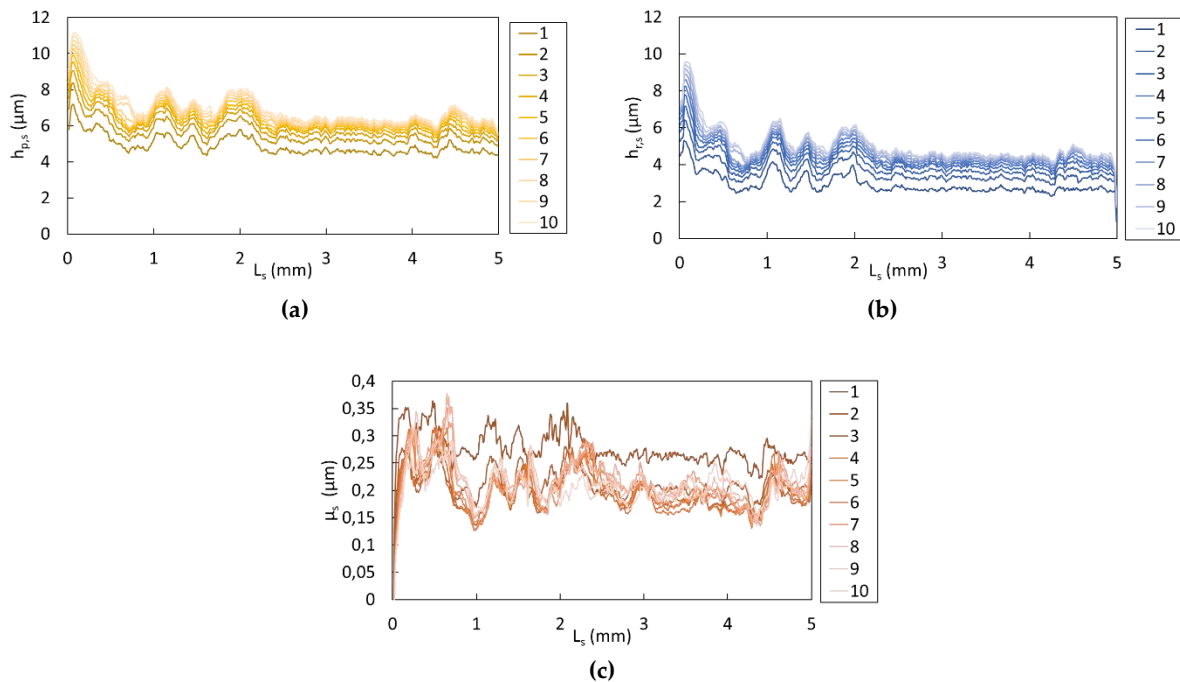


Fig. C-33 Measure of **(a)** penetration depth  $h_{p,s}$ ; **(b)** residual depth  $h_{r,s}$ ; **(c)** coefficient of friction  $\mu_s$ ; for successive passages  $n_s$  of the indenter along the same the scratch path  $L_s$

The respective mean values of  $\bar{h}_{p,s}$ ,  $\bar{h}_{r,s}$  and  $\bar{\mu}_s$  are computed as arithmetic means of the profiles in Fig. C-33, excluding perturbations at the beginning of each scratch (small values of  $L_s$ ), and are displayed in Fig. C-34. As expected, the variation of penetration and residual depths with the number of scratches is not linear, while the friction coefficient first reduces with the number of scratches and then seems to increase again, reaching a plateau. The mean values of  $\bar{h}_{r,s}$  and  $\bar{\mu}_s$  are used in the next section to calibrate the ultimate strength  $p_{lim}$  of the CZM contact-law.

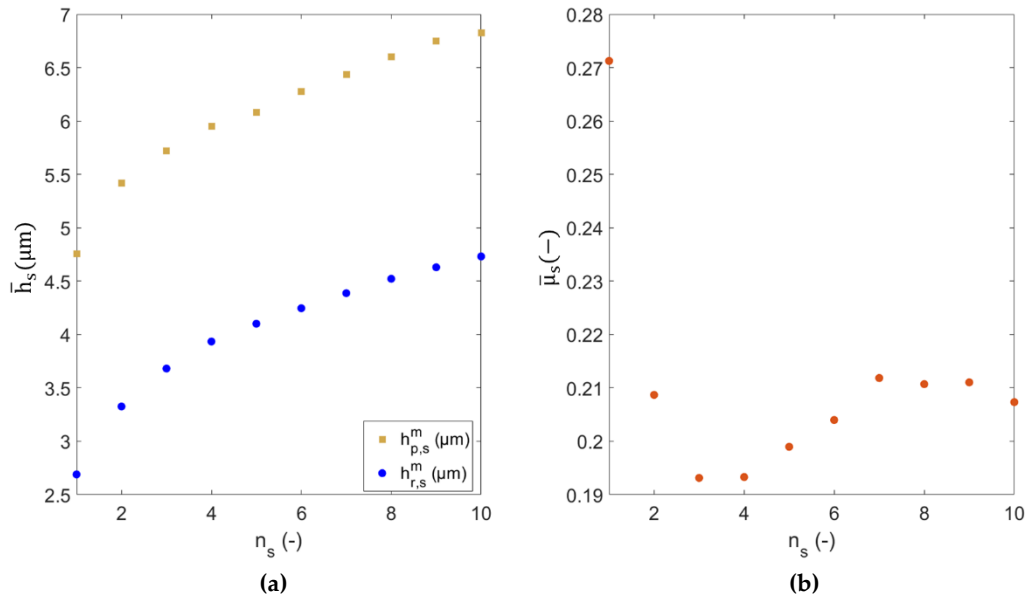


Fig. C-34 (a) mean values of penetration and residual depth  $\bar{h}_s$  (b) mean value of friction coefficient  $\bar{\mu}_s$

### C.3.2 Numerical scratch test

The numerical scratch test is briefly introduced; the main contact laws and features of the degradable microstructure discussed in Chapter C.1 are still valid with some implementations that are discussed here.

#### C.3.2.1 Geometry and boundary conditions

The model reproduces the second stage of the experimental scratch test explained in B.1: the indenter slides several times (always in the same direction) on the surface under constant normal load  $F_s$ , and scratching velocity  $v_s$  (Fig. B-6(b)).

The geometry of the model consists of a degradable matrix (generated in the same manner as in the previous section) in contact with the circular tip of the indenter on the upper free surface and supported by a deformable but non-degradable base (Fig. C-35). Following the model exposed in C.1 and C.2, grains of the microstructure are deformable while the indenter is rigid. The metal matrix's microstructure is modeled in the same way as explained in C.1.1 but considering a larger thickness  $h_m = 40 \mu\text{m}$  than the previous model to account for the propagation of stress within the matrix induced by a large indenter ( $R_s = 100 \mu\text{m}$ ). The lower base has a thickness  $h_b = 30 \mu\text{m}$ , as in the mesoscale model. The length of the domain is limited to  $L_x = 200 \mu\text{m}$  to optimize the simulation time, and periodic boundary conditions are imposed on the lateral borders to guarantee the continuity of the indenter motion and allow successive pass. The main geometrical features are displayed in Fig. C-35. The applied scratching velocity is set to  $v_s^{num} = 200 \text{ m/s}$ .

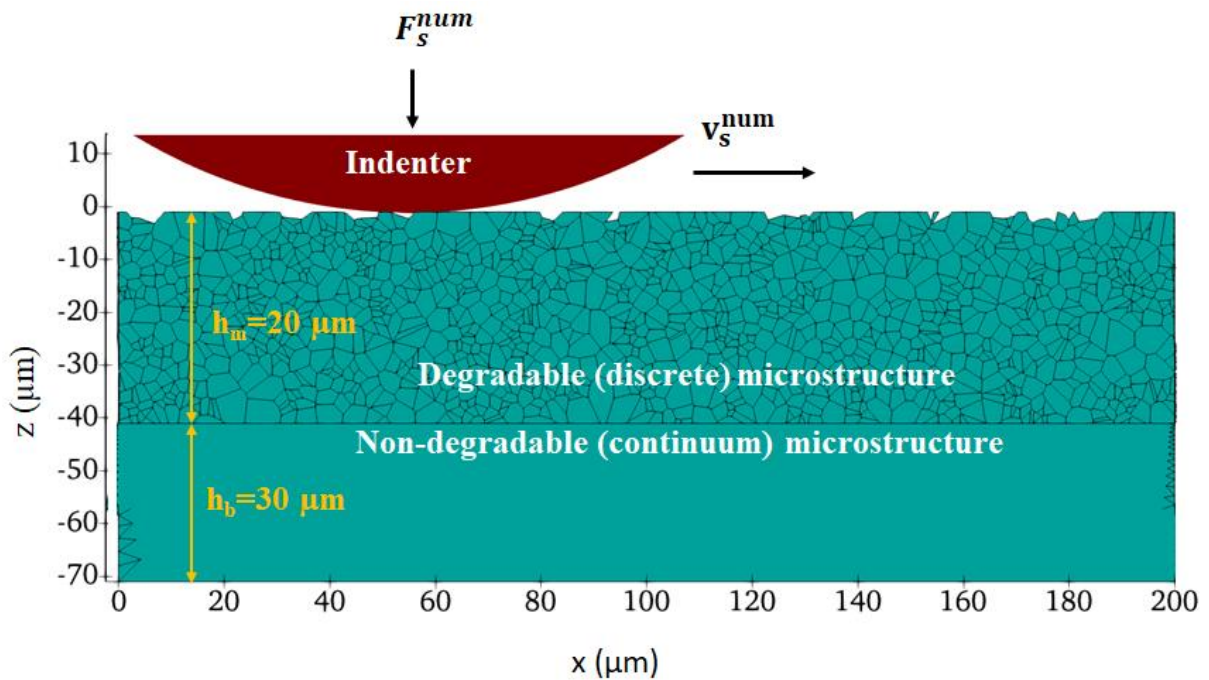


Fig. C-35 2D Microscratch model with the indication of the thickness of the matrix  $h_m$  and the base  $h_b$ , as well as of the applied normal force  $F_s^{num}$  and velocity  $v_s^{num}$  on the indenter

The grains size distribution is reported in Fig. C-36 and compared with the experimental one, which is used in the mesoscale model.

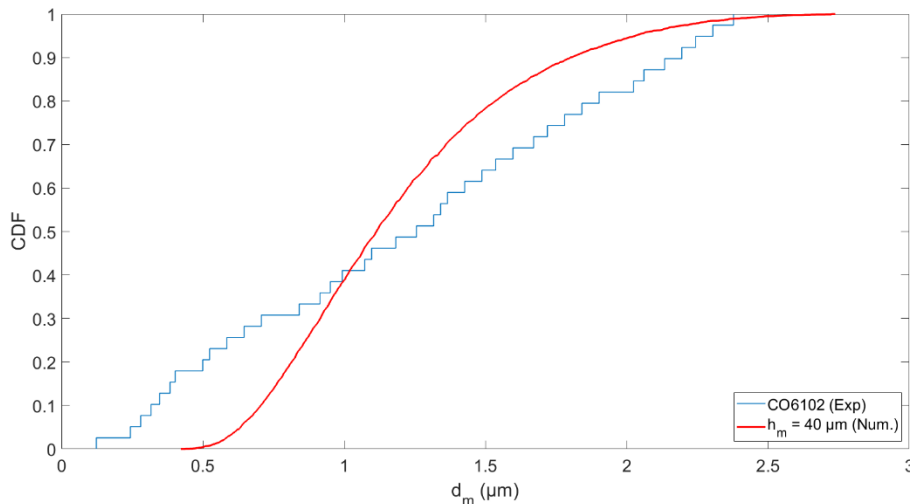


Fig. C-36 Comparison between the experimental (blue) and numerical (red) degradable microstructure

The velocity applied is larger than the real velocity imposed during the experimental scratch test; however, the quasi-static regime is guaranteed during the simulation. Remembering that such a condition is verified if the sliding velocity is much smaller than the wave propagation, defined as in Eq. (C.8), a large wave velocity is obtained considering the real young modulus

of the metal microstructure ( $E_m = 211 \text{ GPa}$ ); therefore the velocity  $v_s^{num} = 200 \text{ m/s}$  is larger than the scratch test velocity but is always smaller than wave propagation ( $v_{wave} \approx 4900 \text{ m/s}$ ).

In order to determine the appropriate vertical load to be applied to the indenter, Hertz equivalent pressure is considered. The applied load in the 2D simulations is chosen such that the Hertz equivalent pressure be identical to that obtained in the 3D case during experiments. Assuming the indenter-surface contact is equal to the contact between a sphere of radius  $R_s$  - equal to the tip radius of the indenter ( $R_s = 100 \mu\text{m}$ )- and an elastic half-space, the 3D Hertz theory allows finding the maximum experimental contact pressure  $p_{max,3D}$  as:

$$p_{max}^{3D} = \frac{3}{2} \cdot \frac{F_s}{\pi \cdot a_s^2} \quad (C.19)$$

Where  $F_s = 10 \text{ N}$  is the load applied on the indenter, and  $a_s$  is the half contact width computed, in the elastic framework, as:

$$a_s = \left( \frac{3}{2} \cdot \frac{R_s \cdot F_s}{E^*} \right)^{\frac{1}{3}} \quad (C.20)$$

$E^*$  is the effective Young modulus, computed as a function of the Young modulus  $E$  and the Poissons coefficients  $\nu$  of the indenter and the matrix, respectively denoted with index  $i$  and  $m$ :

$$\frac{1}{E^*} = \frac{1}{2} \left( \frac{1 - \nu_i^2}{E_i} + \frac{1 - \nu_m^2}{E_m} \right) \quad (C.21)$$

As the indenter tip is far more rigid than the matrix, the Eq. (C.21) can be simplified as:

$$\frac{1}{E^*} \cong \frac{1}{2} \left( \frac{1 - \nu_m^2}{E_m} \right) = 2.17 \cdot 10^{-6} \text{ MPa}^{-1}$$

Where  $E_m = 210 \text{ GPa}$  and  $\nu_m = 0.31$ .

The maximum pressure in 2D writes as:

$$p_{max}^{2D} = \left( \frac{E^{*2D} \cdot F_s^{num}}{\pi \cdot R_s} \right)^{\frac{1}{2}} \quad (C.22)$$

Where the 2D effective Young modulus  $E_{2D}^*$  is defined as:

$$\frac{1}{E^*} = \frac{1 - \nu_i}{E_i} + \frac{1 - \nu_m}{E_m} \cong \frac{1 - \nu_m}{E_m} = 3.33 \cdot 10^{-6} \text{ MPa}^{-1}$$

Under the assumption of the equivalent pressure:

$$p_{max}^{2D} = p_{max}^{3D} = 2.18 \cdot 10^4 \text{ MPa} \quad (C.23)$$

The 2D normal load  $F_s^{num}$  acting on the tip of the indenter is computed from Eq. (C.22) as:

$$F_s^{num} = \frac{p_{max}^{3D}{}^2 \cdot \pi \cdot R_s}{E^{*2D}} = 4.95 \cdot 10^5 \text{ N} \cdot \text{m}^{-1}$$

The main quantities are summarized in Tab. C-8.

Tab. C-8 Main features for the application of the Hertz theory at equivalent pressure

	$F_n$	$1/E^*$	$a_s$	$p_{max}$
3D	10 [N]	$2.17 \cdot 10^{-6} \text{ MPa}^{-1}$	10.48 $\mu\text{m}$	2.18 $10^4 \text{ MPa}$
2D	$4.96 \cdot 10^5 \text{ [N/m]}$	$3.33 \cdot 10^{-6} \text{ MPa}^{-1}$	14.5 $\mu\text{m}$	

### C.3.2.2 Contact models

In the scratch test model, the following contact laws are used:

- i) CZM with fatigue for the degradable and non-degradable contact and the contact between grains of the degradable material.
- ii) Frictionless (i.e., purely cohesive) Mohr-Coulomb for the indenter-matrix grains contact

The CZM + fatigue contact-law here introduced slightly differs from the one discussed in C.1.2.1 by introducing a residual cohesion  $\tilde{p}_{res}$  that still exist within an interface even when the damage  $D$  has reached 1. This cohesion is active for any contact between matrix grains after complete damage and even after possible separation and re-contact. It represents the remaining surface energy after breakage and allows to mimic ductility of the matrix in a simple way [146]. Moreover, as the scratch is limited to few passages of the indenter, the attention is limited to the strength  $\tilde{p}_{lim}$  and to this residual cohesion  $\tilde{p}_{res}$ , which define the monotonous damage as explained in Fig. C-11. If the  $\tilde{p}_{res} \neq 0$ ; the shape of the law is no more triangular and considers the post-peak ductile deformation of the material under multi-pass loads, as illustrated in Fig. C-37(a).

The contact between the indenter and the degradable material is purely cohesive; therefore, no Coulomb friction is included, but surface adhesion between the indenter and the matrix is accounted for by a purely cohesive term  $\Gamma$ . In this way, the friction coefficient  $\mu^{num}$  is obtained

as an output from the simulation and measured as the ratio between the tangential force  $F_t^{num}$  and the applied normal force  $F_s^{num}$ :

$$\mu_s^{num} = \frac{F_t^{num}}{F_s^{num}} \quad (C.24)$$

This friction coefficient is generally named apparent friction coefficient [147][148]. The purely cohesive contact law is illustrated in Fig.C-37 (b).

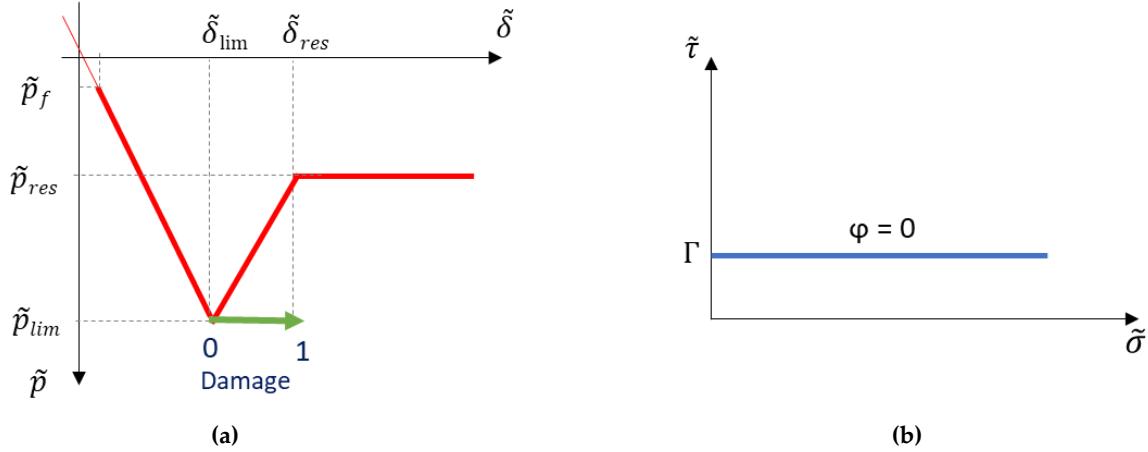


Fig. C-37 Contact laws used in the model: (a) CZM contact law with residual strength  $\tilde{p}_{res} \neq 0$ ; (b) purely cohesive Mohr-Coulomb with Coulomb friction  $\varphi = 0$

### C.3.3 Comparison between experimental and numerical results

The calibration is performed varying systematically the strength  $\tilde{p}_{lim}$  and the residual cohesion  $\tilde{p}_{res}$  of the CZM contact-law and the cohesion  $\Gamma$  between the indenter and the grains of the microstructure. Another necessary parameter already used in the mesoscopic model is the deactivation length  $l_{de}$ . It is here investigated to mimic the 3D effect of ploughing (i.e., the shifting of the material on the side of the indenter) and avoid some undesirable contacts between the indenter and detached grains that can modify the physics of the problem.

Numerical results are then compared with the experimental ones in terms of friction coefficient and wear depth.

As shown in section B.1.2, the behavior under the first scratch may be affected by initial conditions and may not represent the behavior of the surface under continuous abrasive flow. Therefore, the numerical friction coefficient  $\bar{\mu}_s^{num}$  obtained as in Eq. (C-24) is compared with the experimental  $\bar{\mu}_s$  plotted in Fig. C-33(b), ignoring the first passage  $n_s = 1$ . The comparison in terms of wear depth requires additional observations.

The experimental test consists of the indentation followed by the release of the indenter; however, since the numerical test aims not to give the numerical values for the mean residual depth but to give a characteristic feature for the calibration, the release of the indenter is not performed. In the numerical simulation, the indentation depth is calculated following the vertical position of the indenter tip during scratches  $h_s^{num}$ . For each passage, the mean value is calculated in terms of average numerical indentation depth  $\bar{h}_s^{num}$ . Finally, the numerical depth of wear  $\bar{h}_{s-1}^{num}$  is calculated as the difference between the mean indentation depth  $\bar{h}_{s-1}^{num}$  at the scratch  $n_s$  with respect to the initial one  $\bar{h}_1^{num}$  at  $n_s = 1$ :

$$\bar{h}_{s-1}^{num} = |\bar{h}_s^{num} - \bar{h}_1^{num}| \quad (C.25)$$

This value is compared with the experimental depth of wear  $\bar{h}_{s-1}$  obtained in the same way as in Eq. (C.25) starting from the mean residual depth  $\bar{h}_{r,s}$  plotted in Fig. C-34 (a):

$$\bar{h}_{s-1} = \bar{h}_{r,s} - \bar{h}_{r,1} \quad (C.26)$$

The calibration starts with imposing the strength parameters  $\tilde{p}_{lim}$  and  $\tilde{p}_{res}$  and the deactivation length  $l_{de}$  and by varying the cohesion  $\Gamma$  between the surface and the indenter. Then, the activation length is varied by keeping the strength parameters fixed and for an optimal cohesion value. Finally, for fixed values of cohesion  $\Gamma$  and deactivation length  $l_{de}$ , the study is performed analyzing the effect of the  $\tilde{p}_{lim}$  and  $\tilde{p}_{res}$ .

Notice that, for computational time reasons, the numerical scratch test is limited to the first 3-4 scratches (compared to 10 scratched performed experimentally).

### C.3.3.1 Effect of the cohesion $\Gamma$ between the matrix and the indenter

The effect of the cohesion on friction and wear is studied considering the contact parameters reported in Tab. C-9 and Tab. C-10 for the CZM and the Mohr-Coulomb contact laws.

Tab. C-9 CZM fatigue parameters for the matrix-matrix and matrix-base contact

$k_0$ (MPa/ $\mu\text{m}$ )	$\tilde{p}_{lim}$ (GPa)	$\tilde{\delta}_{res}$ ( $\mu\text{m}$ )	$\tilde{p}_{res}$ (GPa)	$\tilde{p}_f$ (MPa)	$dD_f$ (MPa <sup>-1</sup> )
10 <sup>8</sup>	12	0.002	6	10	0.003

Tab. C-10 Mohr-Coulomb parameters for the matrix indenter contact

$k_0$ (MPa/ $\mu\text{m}$ )	$\varphi$ (rad)	$\Gamma$ (GPa)
10 <sup>8</sup>	0	3; 4.5; 6

In this first analysis, the deactivation length is set to infinity, meaning that grains remain in the system for the whole simulation time. Three successive scratches are performed numerically in the same direction. For purely illustrative reasons, Fig. C-38 plots the evolution of the indentation depth  $h_s^{num}$  and the friction coefficient  $\mu_s^{num}$  along with the scratch distance  $L_x$  and for the different scratch passages  $n_s$ . During the first and second scratch, the indentation depth  $h_s^{num}$  is almost constant, while it increases linearly with the distance traveled  $x$  during the third scratch. The friction coefficient  $\mu_s^{num}$  is subjected to rather large fluctuations due to the evolution in time of the contact tangential force  $F_{t,2D}$ .

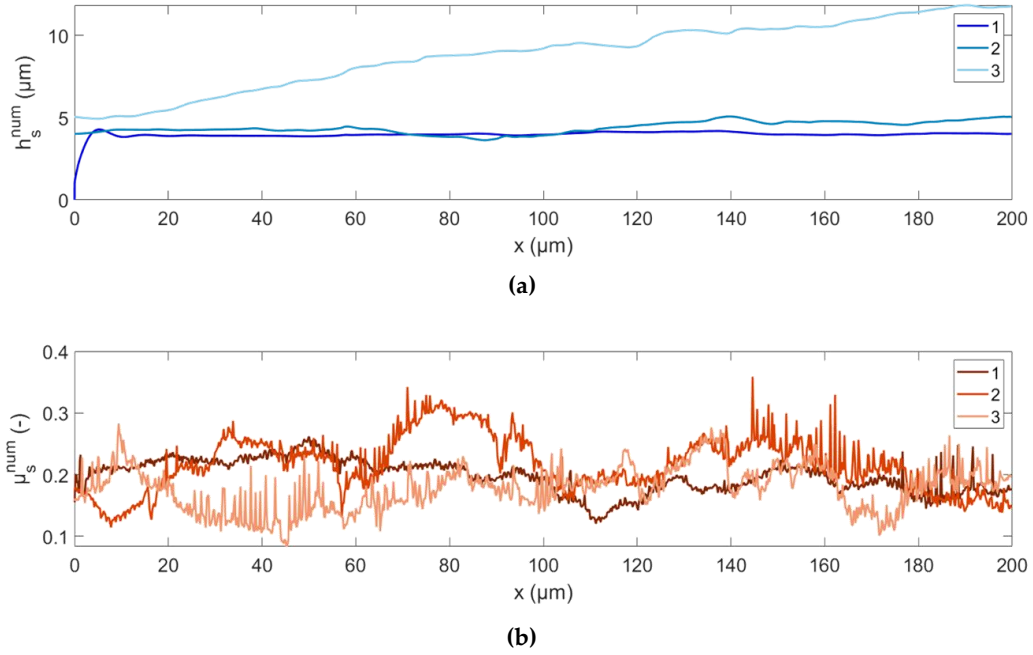


Fig. C-38 (a) numerical indentation depth  $h_s^{num}$ ; (b) numerical friction coefficient  $\mu_s^{num}$  along the scratch distance  $x$  for different scratch pass  $n_s = 1, 2, 3$  ( $\Gamma = 4.5 \text{ MPa}$ )

From curves in Fig. C-38, the mean friction coefficient  $\bar{\mu}_s^{num}$  and the mean wear depth  $\bar{h}_{s-1}^{num}$  are computed numerically by Eq. (C.24) and Eq. (C.25), respectively. The same procedure is repeated by running simulations with a different value of cohesion  $\Gamma$  as listed in Tab. C-8. For all of them, the mean values  $\bar{h}_{s-1}^{num}$  and  $\bar{\mu}_s^{num}$  are calculated and compared with the respective experimental values  $\bar{h}_{s-1}$  and  $\bar{\mu}_s$  as illustrated in the histograms of Fig. C-39.

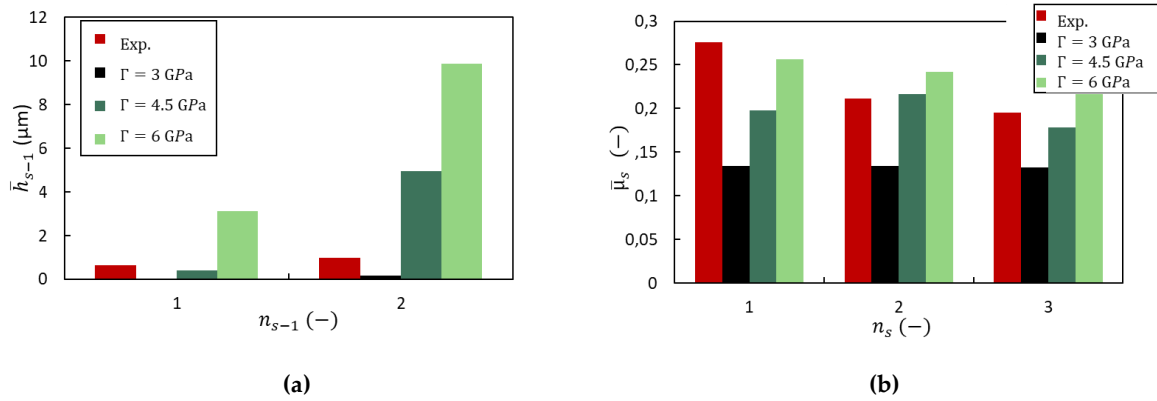


Fig. C-39 Comparison between experimental and numerical results varying the cohesion  $\Gamma$  between the indenter and the matrix: (a) mean wear depth  $\bar{h}_{s-1}$ ; (b) mean friction coefficient  $\bar{\mu}_s$ .

Generally, the larger the cohesion, the larger the depth of wear and the friction coefficient. The more representative results are obtained for  $\Gamma = 4.5 \text{ GPa}$ , and this value will therefore be used in the remainder of this study.

### C.3.3.2 Effect of the deactivation length $l_{de}$ of grains detached

The following simulations aim to set a value of the deactivation length  $l_{de}$  able to mimic the 3D behavior (i.e. the lateral flow) during scratching and avoid contacts between ejected grains and the indenter. The deactivation is imposed in terms of the vertical displacement  $\Delta z$  of each grain with respect to its initial position at time  $t = 0 \text{ s}$ . Considering CZM parameters listed in Tab.C-9 and the Mohr-Coulomb parameters in Tab.C-11, three different deactivation lengths  $l_{de}$  are used:

- I.  $l_{de}: \Delta z \rightarrow \infty$ : No deactivation is imposed, this is the case already discussed in the previous section C.3.3.1
- II.  $l_{de}: \Delta z = d_m$ : Grains are deactivated when they reach a vertical displacement equal to their equivalent average size  $d_m$
- III.  $l_{de}: \Delta z = d_m/2$ : Grains are deactivated when they reach a vertical displacement equal to half of their equivalent average size  $d_m$

Tab. C-11 Mohr-Coulomb parameters for the matrix indenter contact

$k_0(\text{MPa}/\mu\text{m})$	$\varphi$ (rad)	$\Gamma$ (GPa)
$10^8$	0	4.5

Fig.C-40 compares the mean experimental values of wear depth  $\bar{h}_{s-1}$  and friction coefficient  $\bar{\mu}_s$  with the numerical ones when varying the deactivation length  $l_{de}$  as explained above. The depth of wear increases when the deactivation length is decreased (Fig. C-40 (a)): in case III.

mentioned above ( $l_{de}: \Delta z = d_m/2$ ) grains are deactivated quickly, while no significant difference is observed between cases I. and II. The comparison in terms of friction coefficient shows no significant difference in behavior between the three cases, especially during the first passage.

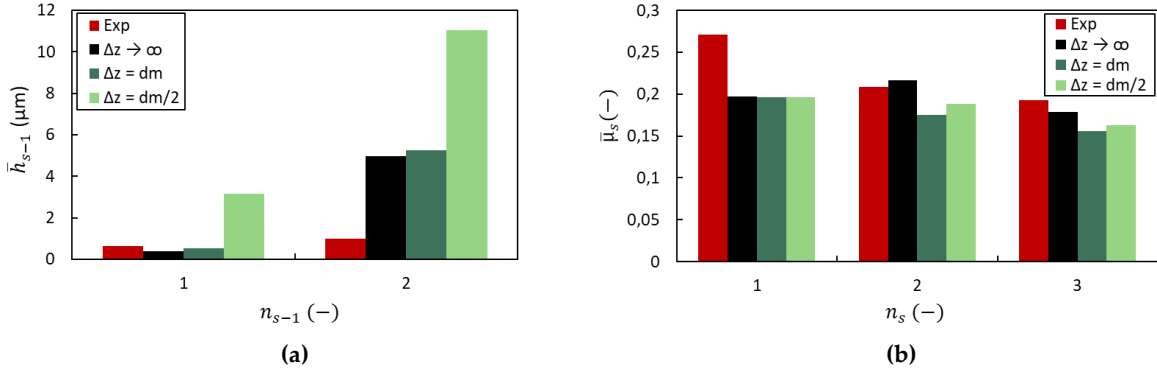


Fig. C-40 Comparison between experimental and numerical results varying the deactivation length  $l_{de}$  in terms of  $\Delta z$  between the indenter and the matrix: (a) wear depth  $\bar{h}_{s-1}$ ; (b) mean friction coefficient  $\bar{\mu}_s$ . The comparison is limited to the first three scratches  $n_s = 1, 2, 3$

Fig. C-41 compare the Von Mises stress induced by the indenter on the microstructure at three different times  $t$ :

- $t = 1 \text{ ms}$ : the indenter has completed the first passage and is back to its initial position. The stress field is almost Hertzian; however, the scratch induces residual stresses within the material that are evident. Cases I. (Fig. C-41 (a)) and II. (Fig. C-41 (b)) show no significant differences, while case III (Fig. C-41 (c)) shows a different surface roughness due to the fast deactivation of grains and more severe wear than the other two.
- $t = 2 \text{ ms}$ : the indenter has completed the second pass. When  $l_{de}: \Delta z \rightarrow \infty$  and therefore with no deactivation, detached grains can be in contact with the indenter, while they should be ejected. In the same way, the rapid deactivation of the grains ( $l_{de}: \Delta z = d_m$ , case III.) changes the roughness of the surface and overestimates the depth of wear.
- $t = 2.5 \text{ ms}$ : the indenter is in the middle of the third scratch pass. If there is no deactivation, a bed of grains is formed between the indenter and the metal matrix. This third body changes the mechanics of the contact. On the other side, if detached grains are ejected faster from the scratch path ( $l_{de}: \Delta z = d_m$ ), the wear depth continues to increase quickly.

An optimum situation is the one defined by the intermediate case II ( $l_{de}: \Delta z = d_m$ ). This parameter, together with the cohesion  $\Gamma = 4.5 \text{ MPa}$  chosen in the previous section C.3.3.1 is used for the calibration of the strength parameters  $\tilde{p}_{lim}$  and  $\tilde{p}_{res}$  discussed in the next section C.3.3.3.

Another important aspect to notice from Fig. C-41 is the formation of the above-mentioned residual stresses and the following crack path within the material. This aspect will be discussed further in this chapter.

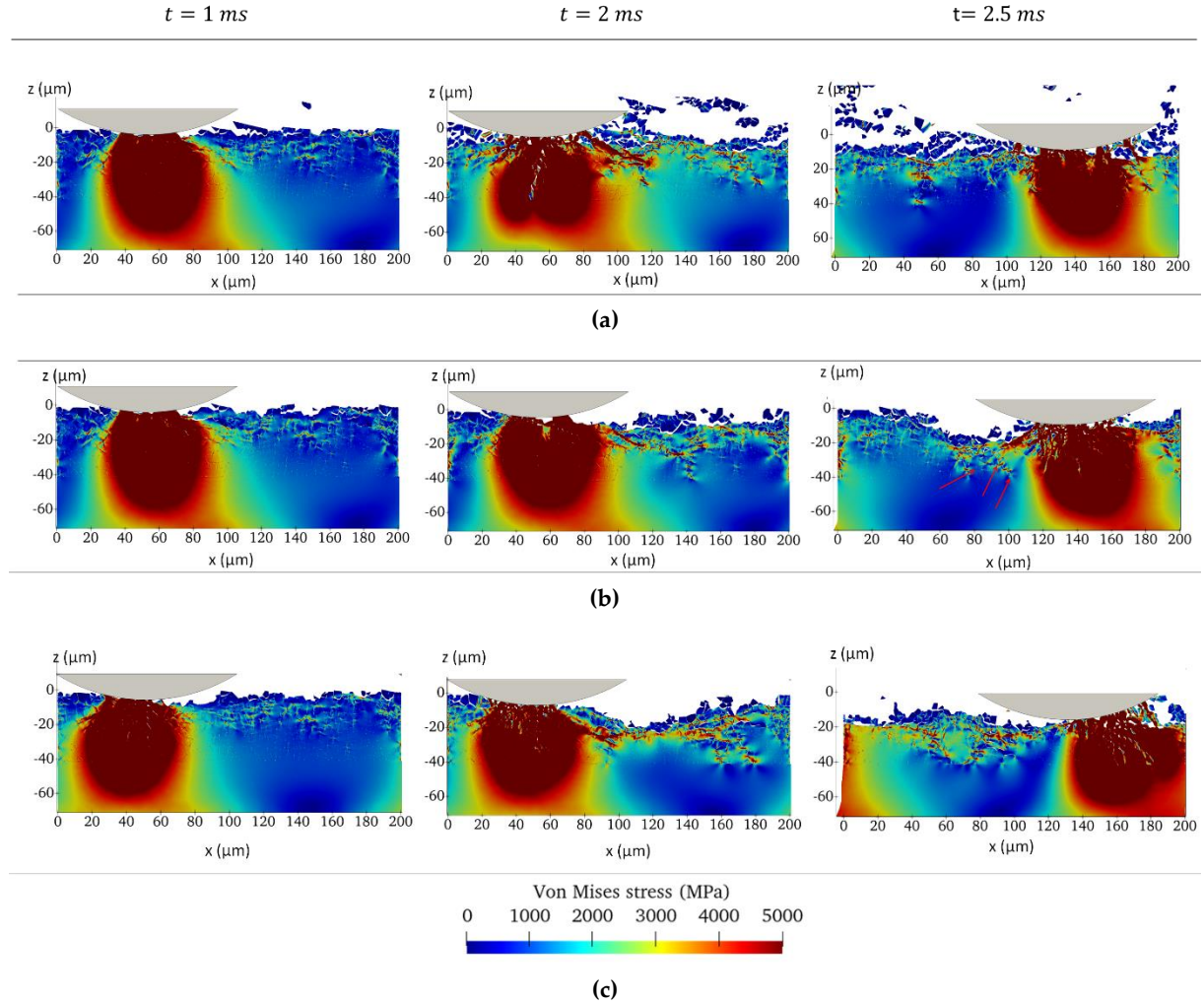


Fig. C- 41 Von Mises stress distribution at three different times  $t = 1 \text{ ms}$ ,  $t = 2 \text{ ms}$ ,  $t = 2.5 \text{ ms}$  for different values of deactivation length  $l_{de}$ : (a)  $\Delta z \rightarrow \infty$ ; (b)  $\Delta z = d_m$ ; (c)  $\Delta z = d_m/2$

### C.3.3.3 Effect of the strength parameters $\tilde{p}_{lim}$ and $\tilde{p}_{res}$ of the CZM law

Considering the cohesion matrix-indenter  $\Gamma = 4.5 \text{ GPa}$  and the deactivation length  $l_{de}$ :  $\Delta z = d_m$ , different numerical studies are performed to calibrate the strength  $\tilde{p}_{lim}$  and the residual cohesion  $\tilde{p}_{res}$ . The Mohr-Coulomb parameters are in Tab. C-11, the CZM parameters are chosen as in Tab. B-12.

Tab. C-12 CZM fatigue parameters for the matrix-matrix and matrix-base contact

$k_0$ (MPa/ $\mu\text{m}$ )	$k^0$ (MPa/ $\mu\text{m}$ )	$\tilde{p}_{lim}$ (GPa)	$\tilde{\delta}_{res}$ ( $\mu\text{m}$ )	$\tilde{p}_{res}$ (GPa)	$\tilde{p}_f$ (MPa)	$dD_f$ (MPa $^{-1}$ )
$10^8$	$10^8$	12; 24; 36	0.002	6; 9	10	0.003

Fig. C-42 and Fig. C-43 illustrates the effect of the ultimate strength  $\tilde{p}_{lim}$  and the residual stress  $\tilde{p}_{res}$  on the depth of wear  $\bar{h}_{s-1}$  and the mean coefficient  $\bar{\mu}_{s-1}$ , respectively. Whatever is the ultimate strength  $\tilde{p}_{lim}$ , the case  $\tilde{p}_{res} = 6 \text{ GPa}$  overestimate the wear depth  $\bar{h}_{s-1}$ , while  $\tilde{p}_{res} = 9 \text{ GPa}$  underestimate it, with an evident increase of wear when decreasing the value of  $\tilde{p}_{lim}$ . The strength parameters do not play a significant role in the activation of the friction coefficient  $\bar{\mu}_s$ , meaning that it is mostly controlled by the cohesion between the indenter and the matrix (Fig. C-42 (b)).

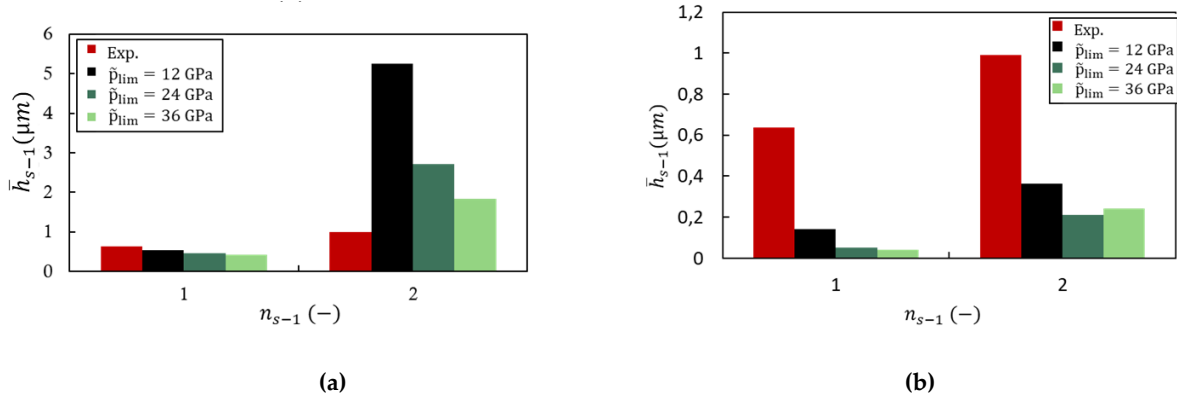


Fig. C-42 Comparison between experimental and numerical mean depth of wear  $\bar{h}_{s-1}$  varying the strength parameters: (a) Effect of the ultimate strength parameter  $\tilde{p}_{lim}$  considering the residual depth  $\tilde{p}_{res} = 6 \text{ GPa}$ ; (b) Effect of the ultimate strength parameter  $\tilde{p}_{lim}$  considering the residual depth  $\tilde{p}_{res} = 9 \text{ GPa}$  (in both cases  $\Gamma = 4.5 \text{ GPa}$ ;  $l_{de} \cdot \Delta z = d_m$ )

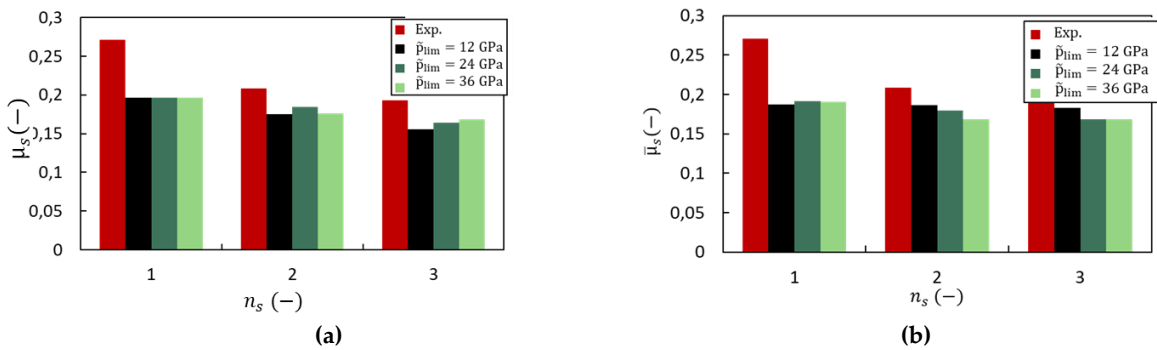


Fig. C-43 Comparison between experimental and numerical mean friction coefficient  $\bar{\mu}_s$  varying the strength parameters: (a) Effect of the ultimate strength parameter  $\tilde{p}_{lim}$  considering the residual depth  $\tilde{p}_{res} = 6 \text{ GPa}$ ; (b) Effect of the ultimate strength parameter  $\tilde{p}_{lim}$  considering the residual depth  $\tilde{p}_{res} = 9 \text{ GPa}$  (in both cases  $\Gamma = 4.5 \text{ GPa}$ ;  $l_{de} \cdot \Delta z = d_m$ )

The study performed here allows calibrating the parameters of the cohesive contact law for a specific material. In this particular case, the matrix microstructure is generated randomly but controlling the grain size distribution. This allows us to use the strength parameters here obtained to perform wear simulations under abrasive debris flow of a specific case of study.

In particular, the calibration performed showed that the wear depth is mainly controlled by the strength parameters  $\tilde{p}_{lim}$  and  $\tilde{p}_{res}$ ; their combined effect on the wear depth  $\bar{h}_{s-1}$  can be approximated by performing a multiple linear regression that writes, if  $n_{s-1} = n_2 - n_1$  as:

$$\bar{h}_{s-1}: (\bar{h}_2 - \bar{h}_1) = \alpha_0 + \alpha_1 \tilde{p}_{lim} + \alpha_2 \tilde{p}_{res} + \alpha_3 \tilde{p}_{lim} \tilde{p}_{res} \quad (C.27)$$

If  $n_{s-1} = n_3 - n_1$ , it as the form:

$$\bar{h}_{s-1}: (\bar{h}_3 - \bar{h}_1) = \beta_0 + \beta_1 \tilde{p}_{lim} + \beta_2 \tilde{p}_{res} + \beta_3 \tilde{p}_{lim} \tilde{p}_{res} \quad (C.28)$$

The coefficients parameters  $\alpha_i$  and  $\beta_i$  are synthesized in Tab. C-13; while the application of the multiple regressions is displayed in Fig. C-44. It should be noted that the idea is to give a reasonable order of magnitude of such parameters and not to predict wear.

Tab. C-13 Coefficients and respective errors of the multiple linear regressions obtained from Eqs. (C.25)-(C.26)

	$n_2 - n_1$		$n_3 - n_1$		
	Coeff.	Err.	Coeff.	Err.	
$\alpha_0$	0.682	0.0431	$\beta_0$	19.277	2.6618
$\alpha_1$	0.0140	0.0016	$\beta_1$	-0.417	0.1027
$\alpha_2$	-0.017	0.0057	$\beta_2$	-2.098	0.3480
$\alpha_3$	-0.003	0.0002	$\beta_3$	0.046	0.0134

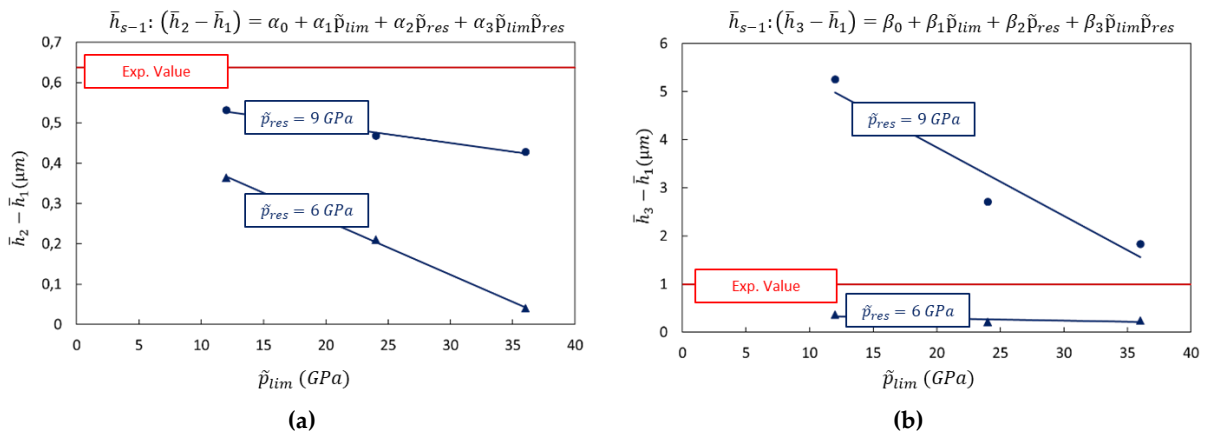


Fig. C-44 Multiple linear regression applied on numerical results of the wear depth and comparison with the experiments: -Experimental results; -Multiple regression applied on numerical results: ●  $\tilde{p}_{res} = 9 \text{ GPa}$ ; ▲  $\tilde{p}_{res} = 6 \text{ GPa}$ : (a)  $n_{s-1} = n_2 - n_1$ ; (b)  $n_{s-1} = n_3 - n_1$

Despite the small number of numerical data, it is possible to note that the multiple regression can represent well the combined effect of  $\tilde{p}_{lim}$  and  $\tilde{p}_{res}$  on the depth of wear  $\bar{h}_{s-1}$  after the second and third scratches. In particular, the residual pressure  $\tilde{p}_{res}$  plays a decisive role in it, while the variation in terms of ultimate strength  $\tilde{p}_{lim}$  does not affect results significantly. From this first analysis, it emerges that representative values can be the following:

- $\tilde{p}_{lim} \approx 9 \text{ GPa}$
- $\tilde{p}_{res} \approx 8.5 \text{ GPa}$

Which slightly overestimate the depth  $\bar{h}_2 - \bar{h}_1$  but gives a good estimation of  $\bar{h}_3 - \bar{h}_1$  according to Eq.(C-26) and Eq.(C.27), minimizing the error with respect to the experimental value as:

$$\left| (\bar{h}_2 - \bar{h}_1)^{num} - (\bar{h}_2 - \bar{h}_1)^{exp} \right| \approx 0.2 \mu m$$

$$\left| (\bar{h}_3 - \bar{h}_1)^{num} - (\bar{h}_3 - \bar{h}_1)^{exp} \right| \approx 0.002 \mu m$$

An improvement of the model may be obtained by increasing the number of the numerical scratches and testing other combinations of strength parameters  $\tilde{p}_{lim}$  and  $\tilde{p}_{res}$  improving the regression. For what concerns this analysis, it is important to notice that the residual strength plays a key role in the wear resistance, and the CZM should include the ductile-plastic behavior of the material.

It should also be noted that the strength parameters obtained from this calibration are much larger than those discussed at the mesoscale ( $\tilde{p}_{lim} = 800 \text{ MPa}$ ;  $\tilde{p}_{res} = 0 \text{ MPa}$ ); however, from what observed previously, wear also occurs by fatigue when  $\tilde{p} < \tilde{p}_{lim}$ .

Further study may improve this approximation by performing other numerical simulations of the scratch test and introducing optimized values of  $\tilde{p}_{lim}$  and  $\tilde{p}_{res}$  on the wear test at the mesoscale together with a correct fatigue damage parameter  $dD_f$ , chosen by exploiting results already discussed in section C.2.

The effect of scratching the material surface induces residual stress within the degradable microstructure observed after the indenter's passage. For illustrative purposes, the case illustrated in Fig. C-45 refers to the case  $\tilde{p}_{lim} = 12 \text{ GPa}$  and  $\tilde{p}_{res} = 6 \text{ GPa}$  at the end of the first, the second and the third scratch ( $n_s = 1, n_s = 2, n_s = 3$ ).

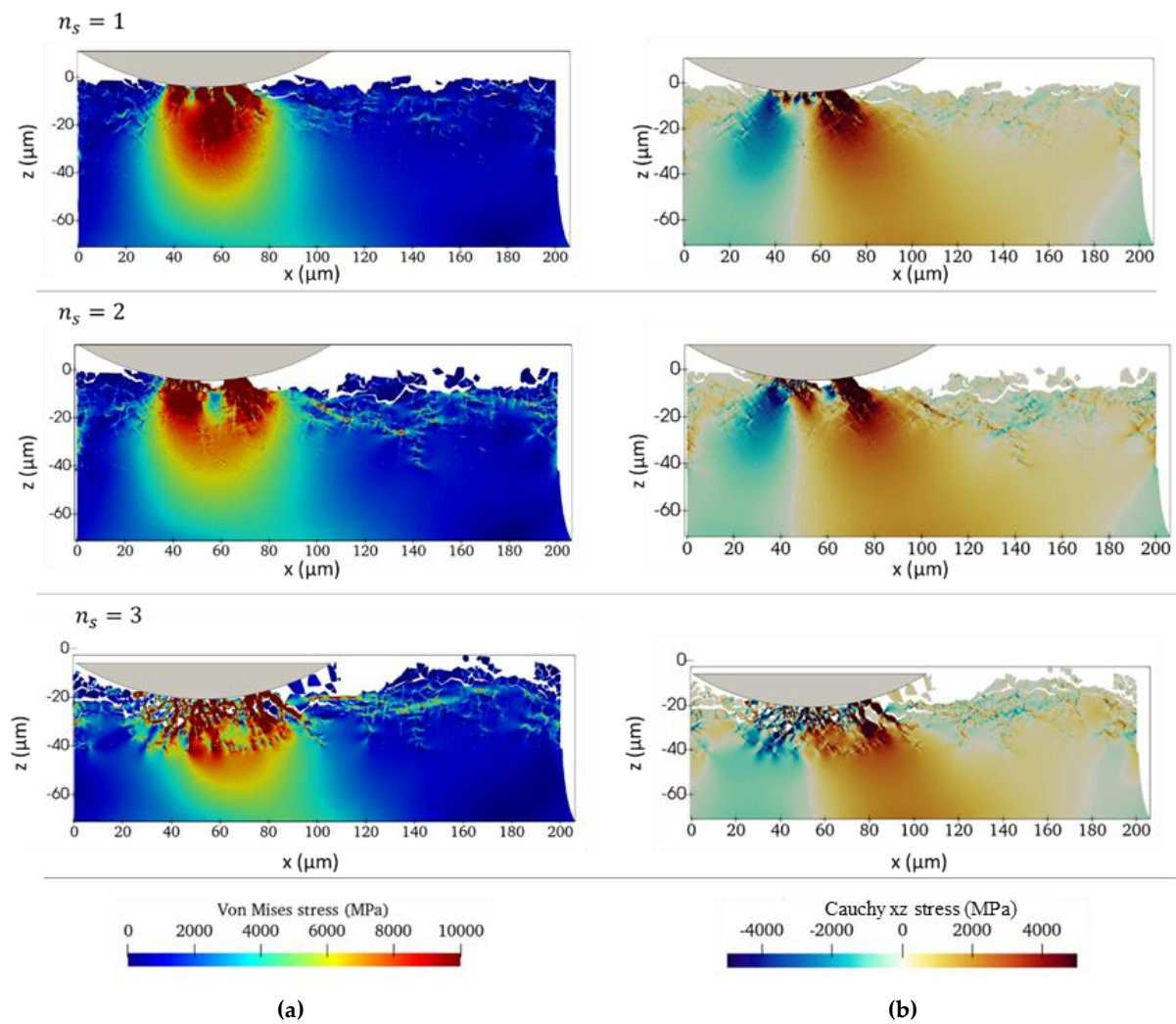


Fig. C-45 (a) Von-Mises stress and (b) Cauchy  $xz$  stress at the end of the first, the second, and the third scratch ( $n_s = 1, n_s = 2, n_s = 3$ )

Results are in good agreement with those obtained by Raje and co-workers [137], [143], [149] on the discrete modeling of a bearing contact. Several joints will rupture in subsurface regions due to the residual stresses that remain in the matrix microstructure after the indenter passage.

## C.4

# Conclusions

The framework described in this part C aims to describe wear at the local scale. Debris and metal matrix grains are modeled with realistic shape and size using a 2D software coupling meshfree and discrete elements techniques (MELODY2D).

Although the code is limited in 2 dimensions and despite the large number of user-defined parameters involved in the contact laws between discrete bodies, it is a useful tool for understanding phenomena not accessible at the industrial application scale.

Whatever the chosen contact parameters, the wear process seems to be always defined by three main stages: initialization, steady-state and perturbed steady-state. The duration of each of them and the more or less linear trend of the second phase depend on the CZM parameters chosen.

In practice, the physics of the problem is strictly related to them:

- If the ultimate strength  $\tilde{p}_{lim}$  is large enough, wear occurs mostly by fatigue, and it is faster if the fatigue damage parameter  $dD_f$  is larger.
- A small value of ultimate strength  $\tilde{p}_{lim}$  combined with a small value of the residual gap  $\tilde{\delta}_{res}$  leads to a rapid wear process since the decreasing of  $\tilde{p}_{lim}$  may induce monotonous damage or lead to a faster increment of the damage parameter if damage occurs by fatigue. The decrease of  $\tilde{\delta}_{res}$  may induce a brittle rupture of the contacting surface and a faster increase of the damage parameter in a monotonous way.
- The fatigue damage evolution parameter  $dD_f$  defines the damage propagation within the microstructure by changing the roughness of the contacting surface, the way of cracking initialization, and the following grain detachment and wear. It is a crucial parameter in the wear analysis; therefore, it should be appropriately chosen. The study conducted in this work shows that there is a sort of transition from  $dD_f = 0.01 \text{ MPa}^{-1}$  to  $dD_f = 0.001 \text{ MPa}^{-1}$ .
- Low fatigue damage parameters  $dD_f$  are defined by an important steady-state at a low wear rate. This peculiarity can be related to the particular damage distribution within

the material and the roughness of the surface. However, a limit to the damage propagation and the wear process is imposed by the non-degradable material in contact with the degradable part (necessary to reduce the cost of the simulation). Therefore, it will be useful to consider a larger matrix and analyze the effect of the non-degradable material on the damage and wear.

- A high fatigue damage parameter  $dD_f$  may lead to the formation of the third body of abrasive particles that can abrade the metallic surface, defining another wear process different from the one observed since the wear is actually caused by debris grains and not by the metallic grains themselves. This change in wear generation also occurs with small values of the strength parameters (the ultimate strength  $\tilde{p}_{lim}$  and the residual gap  $\tilde{\delta}_{res}$ )

Therefore, an optimal solution is to avoid small fatigue damage parameters and ensure that the strength parameters are large enough to account for the fatigue effects and ensure that wear is caused by the debris flow.

To optimize the cost of the simulation, CZM parameters can be calibrated on a different model representing almost the same phenomenon, that is, in this case, the abrasive wear caused by the passages of harder particles. In this way, the calibration conducted by performing  $\mu$ -scratch test shows that the depth of wear depends mostly on the strength parameters of the CZM (if the cohesion between matrix and indenter is properly chosen).

Despite the few numerical data, it is possible to perform a multiple linear regression to observe the combined effect of ultimate strength  $\tilde{p}_{lim}$  and residual strength  $\tilde{p}_{res}$  on wear. The strength parameters obtained by this calibration are quite larger than those used in the mesoscopic model. However, as wear occurs mostly by fatigue in that case, these two parameters should be combined with the effect of the fatigue damage rate, already discussed qualitatively. Concerning fatigue, it may also be interesting to analyze the effect of the threshold  $\tilde{p}_f$  (fatigue pressure) defining the threshold above which damage occurs by fatigue.





# General conclusions

This work aims to develop a strategy to model the wear of the metal matrix used as a binder in diamond tools for stone cutting. The wear process is caused by the flow of abrasive debris (consisting of chips of the workpiece and the water used to carry them out) and should be controlled to optimize the life of the tool.

In a more general context, the wear of the matrix surface can be seen a three-body contact problem involving the stone, the tool and the stone debris (third body). It can be simplified considering the tribological circuit where the matrix and the workpiece are two degradable first bodies, the third body consists of debris grains (particles detached from the workpiece that are continuously renewed and recirculate in the flow), while matrix grains are ejected quickly. Therefore, the wear of the matrix is caused by the debris grains and not by the metal grains themselves.

Due to the multiscale nature of the problem and the large number of variables involved, the industrial demand is met by developing a new numerical approach, which implies two main goals, realized in two (currently) parallel models:

- prediction of the matrix wear at the scale of the diamond with a macroscopic model,
- description of the local wear mechanisms at the scale of the debris flow with a mesoscopic model.

A fully numerical approach should consider the interconnection between the two models since they look at two different scales giving two complementary information.

Generally, the wished model should hold for any metal matrix (monophase, biphasic, triphasic,...). To achieve this goal, a first calibration and validation are required. In this work, the two models are applied to a cobalt metal matrix microstructure (monophase, 100% Cobalt) whose mechanical response is, at least at the macroscale, known qualitatively and quantitatively, allowing the validation of such a model and offering purposes for further developments, as suggested in the next dedicated section.

In the macroscopic model, one single diamond is considered, that remains intact during the whole process. This is not actually verified in literature since the wear of the matrix is also affected by the size and distribution of diamonds; also, diamonds can undergo several fractures during processing. However, choosing an “isolated diamond” (i.e., not shielded by the others) and considering only the first phase of diamond polishing (i.e., the first stage of the cutting process, where the matrix undergoes wear and the diamond is still intact) allows a fair

comparison between the numerical model and the experimental results performed on a drilling machine.

Considering an independent experimental set-up consisting of a scratch test, a rheological test, and morphological characterization, to calibrate the macroscopic model, and making some physically sound scale changes, it is possible to describe and predict wear at the industrial application scale. These scale changes induce the main contribution of this model, consisting in the reformulation of the Archard equation to account for aspects that are not considered in the original formulation, i.e., the spatial variability of the specific wear rate and the multipass nature of the contact (accounted by the analogy with the scratch test).

The new formulation of wear rate accounts for the abrasiveness of the debris grains and their characteristic size, the characteristic hardness of the matrix and the pressure and velocity field of third body. The application of such a model on the reference situation (cobalt matrix) can well describe, qualitatively and quantitatively, the wear rate measured experimentally in terms of height of protrusion (in front of the diamond) and clearance (upstream); however, the lateral flow is not yet completely developed numerically, therefore the model is open to several improvement.

Moreover, although the model is based on a multiscale approach, the results are strictly related to the diamond scale (macroscopic scale) without accounting for the main properties of the microstructure (grain size, roughness, and ultimate strength). For a good optimization of the microstructure, its micromechanical behavior should be considered as complementary information of the wear process observed at the contacting surface scale. The mesoscopic model describes the local phenomena of damage and wear at the scale of the debris flow. Simulations are performed using an open source code developed in the lab and considering a representative volume element (RVE) extracted from a diamonds segment. Here debris grains are represented as rigid bodies controlled in shape and size, while the matrix is defined in a realistic way as a polycrystalline deformable material. The upper limit to the degradable part is imposed by a deformable and non-degradable base of the same material as the degradable part. The wear of the microstructure is studied as a function of the stress cycles induced by the continuous passage of debris and in terms of intergranular de-cohesion and fracture, which are in turn affected by the parameters used for the cohesive law.

The grains detachment is controlled by an internal parameter representing the damage, evolving during the simulation from 0 (intact bond) to 1 (broken bond). The continuous passage of debris causes points of weakness in the resistance chains of the matrix, generating the loss of cohesion and the consequent detachment of the grains by fatigue. In this way, the wear is no longer studied from a global point of view but by a local one that looks at the detachment of the grains.

Moreover, fatigue effects are introduced in the cohesive contact law to account for the wear rate being a slow and progressive phenomenon. If the damage occurs mostly in a monotonous way, grains are detached quickly, but they remain in the system modifying the physics of the

problem since the wear is no longer caused by debris grains but by the matrix grains themselves. If the ultimate strength of the cohesive law is much larger than the applied normal pressure, the damage occurs by fatigue.

The main difficulty of this model is related to the definition of contact parameters that have a strong impact on the results of the numerical simulation and, therefore, on the representation of the physics. The calibration of the main strength parameters of the cohesive law can be achieved by performing numerical simulations of the scratch test.



## Further possible developments

The proposed multiscale approach requires further developments that concern both models independently (the macroscopic and the mesoscopic model) and their interconnection. Some of the most important developments, according to the author, are detailed below.

- Setting: improvements are required in the two models.
  - The two experiments on which the macroscopic model is based can be improved to better represent the industrial conditions. The rheological test can be extended to high values of shear rate to mimic the ones reached during the cutting process. The scratch test can be extended increasing the number of scratches to verify if the exponential law used to define the characteristic hardness after a large number of passage has been chosen correctly.
  - The mesoscopic model in the present state features a somewhat important number of parameters that have to be chosen by the user. They concern, in particular, the contact law parameters used for the frictional contact between the debris grains and the degradable microstructure and the fatigue parameters of the cohesive law used for the contact between the grains of the degradable matrix, as well as between the degradable and non-degradable part. After the sensitivity analysis performed in this thesis, the adaptation of the model to the particular case of the study would validate the approach. To do it, the calibration performed on the scratch test allows defining the strength parameters of the cohesive law, while the fatigue parameters need to be chosen properly based on the results already obtained in Chapter C.2. Moreover, the boundary conditions applied to the modeled matrix can be chosen by considering the macroscopic model. In this way, it is possible to apply the corresponding flow properties obtained by applying the Reynolds equation as boundary conditions in the mesoscopic model.
- Validation to be consolidated: the macroscopic model is built considering the wear of a cobalt matrix microstructure around a specific diamond. Therefore, the model needs to be validated considering other diamonds retained by the same microstructure in order to consider the effect of diamond size and orientation in the wear process. Moreover, the model is limited to the prediction of clearance and protrusion since the lateral flow is not well developed numerically.

- **Extension:** Once the macroscopic model is validated, the study can be extended to other metal matrix microstructures. Other microstructures can also be studied numerically at the mesoscale. Herein, the effect of debris angularity can be analyzed deeper, controlling the shape and size distribution of debris grains. A great challenge is also to adapt the model to other tribological situations consisting of the wear of a surface caused by a flow of abrasive particles.
- **Fully numerical coupling:** This is an important area of development that can be done once the two models are set and validated. The numerical coupled approach will start from the same experimental set-up consisting of the micro scratch test and the rheological test. The first will be used to calibrate the cohesive model parameters, while the second is useful to define the rheology of the debris flow used in the macroscopic model to solve the Reynolds equation, which in turn gives the flow properties that can be implemented as boundary conditions in the mesoscopic model, as illustrated in the schema of Figure. 1. The mesoscopic model setting in terms of boundary conditions is the first important step for coupling the two models. Moreover, once the calibration and the validation of the mesoscopic model are completed, it can also be used to define the constitutive behavior of the contact surface between the debris flow and the metal matrix, as well as the microscopic behavior of the matrix at the grain boundary scale. This will allow writing a wear equation based on the numerical model with the advantage of accounting for more information on the mechanical behavior of the microstructure than what was obtained from the experimental scratch test. Finally, the wear equation can be solved in the macroscopic model to define wear rate as a function of the local values of pressure and velocity and the properties of the microstructure observed at the mesoscale.

## Further possible developments

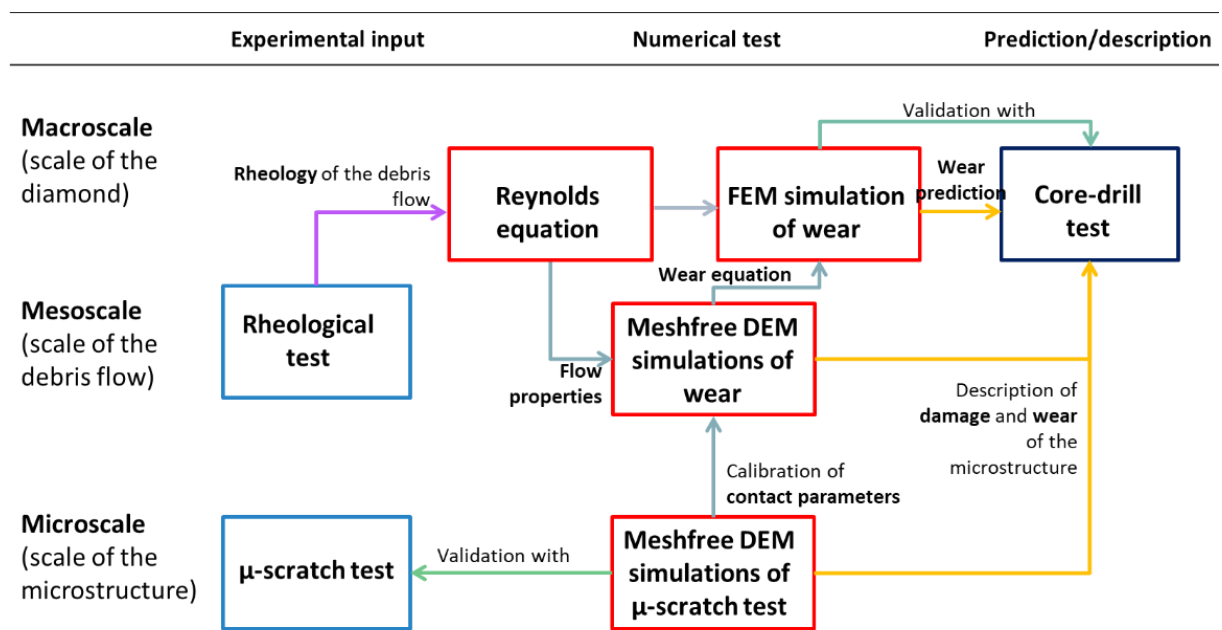


Figure 1 Perspective of the strategy that can be used for the wear analysis



## Annex I.

# Definition of particles sharpness

The method used to define the radius of the characteristic asperity  $r_d^*$  in the specific wear rate is discussed here. This method was initially proposed by [108] to create the complex contour of irregular particles and was then implemented by [29] to generate grains with a realistic shape.

The method consists of filling the real particle volume with spheres of different diameters. The positions and diameters of the spheres relative to the surface of the particle are taken by choosing a point randomly on the real particle surface (a 'node') and developing a tangent sphere internally along its normal direction to the maximal size possible, reaching the contours of the real particle (Fig. I-1). This process is repeated for other points on the surface.

The total number of spheres and the precision of the reproduced particle shape is controlled through three primary parameters  $d_{min}$ ,  $P_{max}$  and  $r_{min}$  defined such that:

- i.  $d > d_{min}$  If the distance  $d$  between the node and the surface of a proximal sphere is lower than a predetermined threshold  $d_{min}$  then a new sphere will not be created.
- ii.  $P < P_{max}$  For selected nodes  $p$ , the process is repeated until a maximum percentage  $P_{max}$ .
- iii.  $r > r_{min}$  Spheres with a radius  $r$  smaller than a predetermined threshold are eliminated.

This procedure reduces the time-consuming process and avoids artificial roughness for rounded particles.

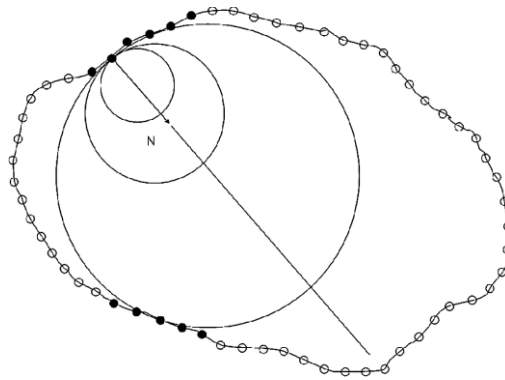


Fig. I-1 Expansion of a sphere along with the normal  $N$  at a surface point inside the boundaries of the real particle [108]

If  $d_{min} = 0$  the resolution of the created contour is maximum. A significant increase in  $r_{min}$  increases the roundness of the particle. If the sharpness is essential, it is preferable to keep this parameter low and use other criteria to reduce spheres. In particular, the total number of spheres can be merely limited by controlling the number of nodes selected by the  $P_{max}$  parameter. Respect of the original definition of  $P$ , the code is developed considering its complementary part, i.e.  $\bar{P} = 1 - P$  is the number of unchosen points. Fixing the percentage of unselected points to 0.01, Fig. I-2, Fig. I-3 and Fig. I-4 show the effect of varying  $d_{min}$  and  $r_{min}$  and  $\bar{P}_{max}$  on the number of circles.

As expected, the number of circles increases decreasing  $d_{min}$  and  $\bar{P}_{max}$  and increasing  $r_{min}$ . The line in red is the contour of the grain: the greater the number of circles, the better they define the contour.

In this study, the following threshold parameters are chosen:

$$d_{min} = 0.05 \mu m$$

$$P_{max} = 0.01$$

$$r_{min} = 0.01 \mu m$$

## Annex I. Definition of particles sharpness

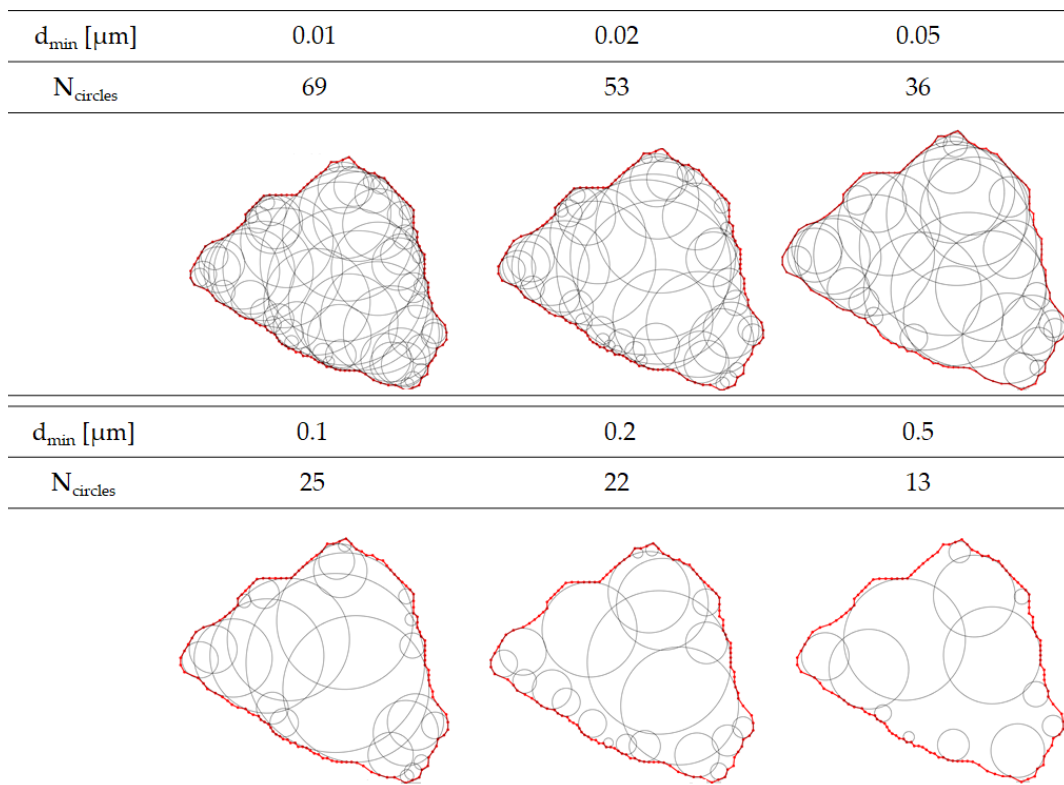


Fig.I-2 Effect of  $d_{min}$  of the definition of circles ( $r_{min} = 0.05 \mu\text{m}$ ;  $P_{max} = 0.01$ )

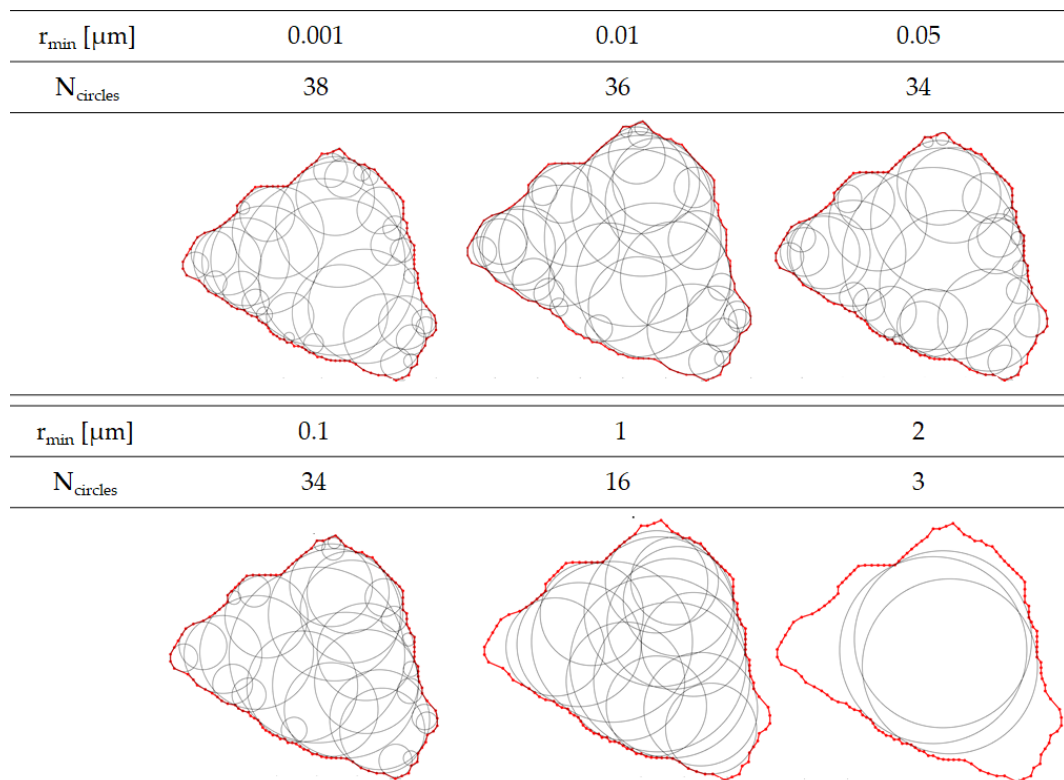


Fig. I-3 Effect of  $r_{min}$  of the definition of circles ( $d_{min} = 0.01 \mu\text{m}$ ,  $\bar{P}_{max} = 0.01$ )

## Annex I. Definition of particles sharpness

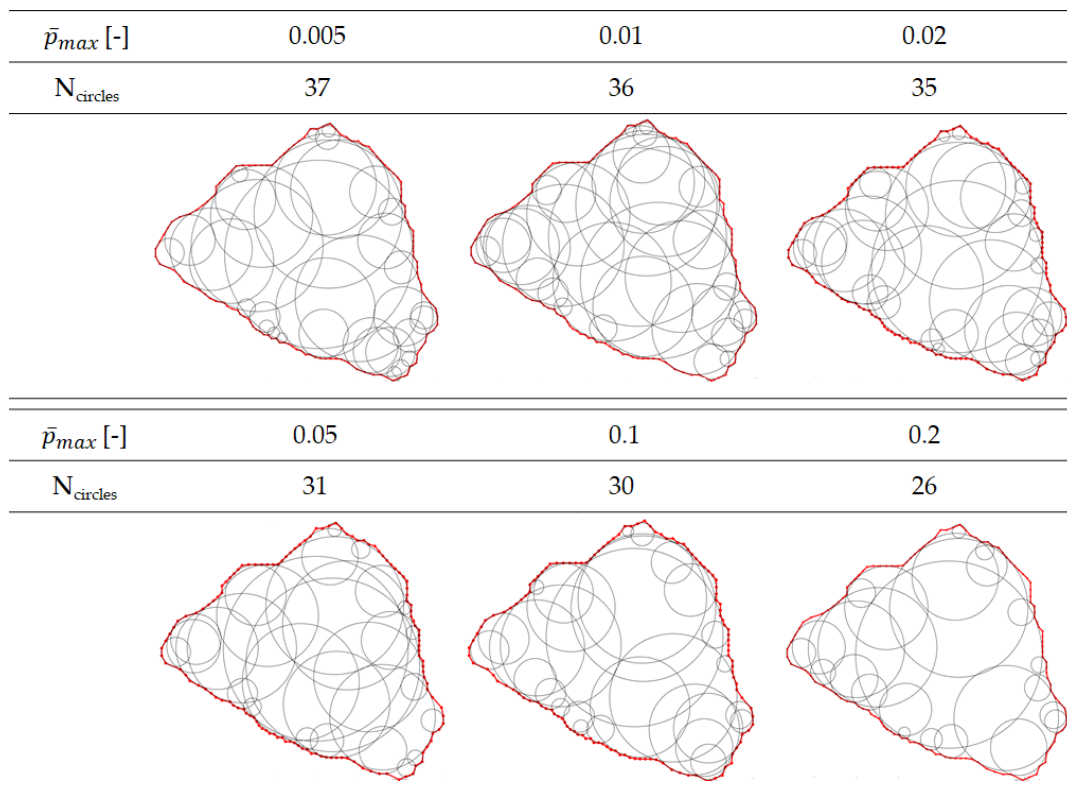


Fig. I-4 Effect of  $\bar{p}_{max}$  of the definition of circles ( $d_{min} = 0.01 \mu m$ ;  $r_{min} = 0.05 \mu m$ )

## Annex II.

# Generation of a realistic sample

Fourier Descriptors are the amplitudes  $\{D_n\}$  of the normalized amplitude spectrum obtained by DFT [29], as illustrated in Fig.C-7. The main procedure consists of the discretization of the grain contour by a number  $N$  of points, separated by a constant angle  $\vartheta_i$  to the center  $O$ :

$$\vartheta_i = \frac{2\pi}{N} \quad (II.1)$$

Thus, each point  $P_i$  is defined by an angle  $\vartheta_i$  and a radial distance  $r_i = OP_i$ . The average radius is given by:

$$r_0 = \frac{1}{N} \sum_{i=1}^N [r_i] \quad (II.2)$$

The amplitudes  $D_n$  of the spectrum are defined as:

$$D_n = \frac{\sqrt{A_n^2 + B_n^2}}{r_0} \quad (II.3)$$

Where  $A_n$  and  $B_n$  are the Fourier Coefficients, defined as:

$$A_n = \frac{1}{N} \sum_{i=1}^N (r_i \cdot \cos(i \cdot \vartheta_i)) \quad (II.4a)$$

$$B_n = \frac{1}{N} \sum_{i=1}^N (r_i \cdot \sin(i \cdot \vartheta_i)) \quad (II.4b)$$

The spectrum of debris grain is obtained by discretizing the contours of the 34 grains extracted from Fig. B-2(a) (already used to define the characteristic asperity  $r_d^*$  (Fig. B-22)) into 128 points  $P_i$ , each of them defined by a constant angle  $\vartheta_i$  (see Eq. (II.1)) and a radial distance  $r_i$ .

Fig. II-1 illustrated the first 64 modes of the measured Fourier spectrum and the averaged.

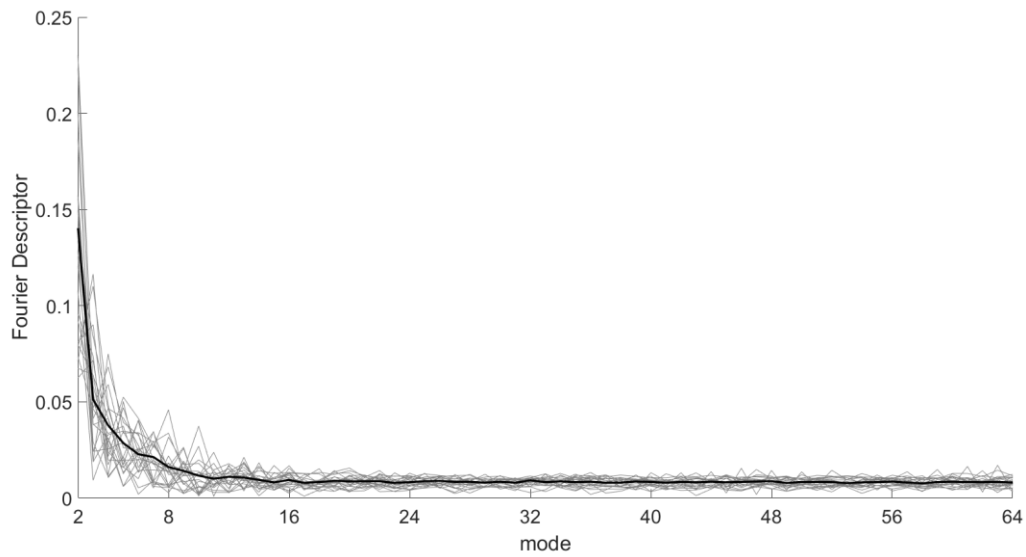


Fig. II-1 Measured Fourier spectra and average spectrum (bold black line)

Tab. II-1 compares the main shape descriptors  $D_2$ ,  $D_3$ ,  $D_8$  as well as the decays  $\lambda_1$  and  $\lambda_2$  coming from the spectrum here propose and those described in Chapter C.1 (and then used in the application discussed in C.2). Grains obtained from the spectrum are more elongated and irregular than those described in Part C.

Tab. II-1 Definition of shape descriptors used in Part C and those obtained from the spectrum

	Fourier Spectrum Properties				
	$D_2$	$D_3$	$D_8$	$\lambda_1$	$\lambda_2$
Previous application	0.1	0.05	0.01	-2	-2
New sample	0.14	0.05	0.016	-2	-2

The spectrum can be implemented in the code PACKING2D to generate a sample of realistic grains. Moreover, the new version of the code allows the implementation of grain size distributions more complicated than the Gaussian distribution. Therefore, it is possible to generate grains following the bimodal distribution defined in Fig. B-2 (b). Fig. II-2 compares the numerical size distribution with the experimental, while Fig. II-3 displays the final grains package obtained from the code.

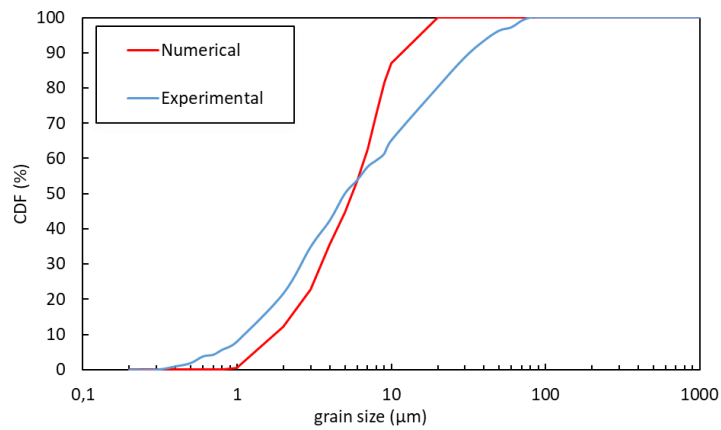


Fig. II-2 Comparison between the experimental (in blue) and the numerical (in red) grain size distribution of debris grains

The debris sample obtained from the spectrum is more uniform than the one discussed in section C.1.1.2. The package obtained is realistic and, together with the calibration discussed in Chapter C.3, can be used to further improve the mesoscopic model.

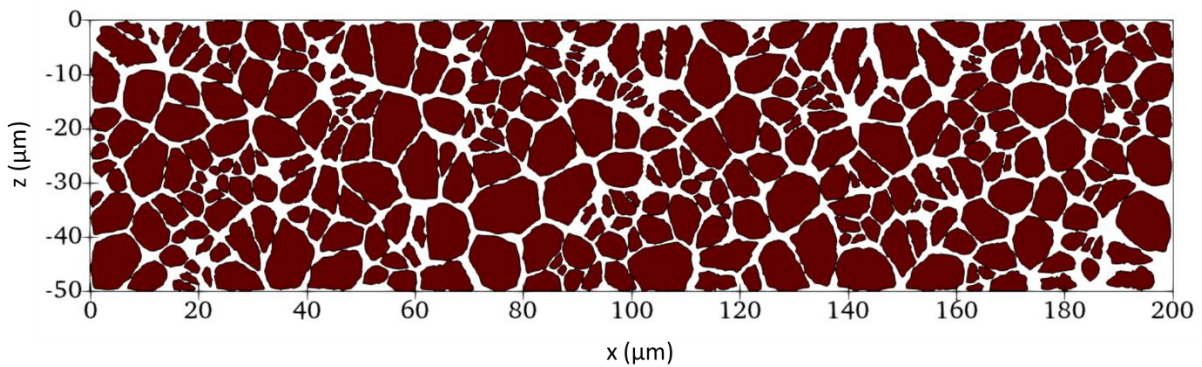


Fig. II-3 Sample generated from the spectrum analysis



## Annex III.

# The pseudo-code for the solving of the CZM-fatigue contact law

The implementation and solving of the CZM in the MELODY code is based on the contact algorithm explained in Section C.1.2.

This annex aims to describe in detail the contact algorithm solved in the code. As already said in Section C.1.2, the contact law takes:

Five contact-related input quantities:

- the normal gap  $\tilde{\delta}_n$
- the tangential gap  $\tilde{\delta}_t$
- the damage parameter  $D$  attached to the node of B (such damage is the result of the previous history of the simulation, and ranging from 0 to 1)
- the previous normal contact pressure  $\tilde{p}_{n,prev}$
- the previous tangential contact pressure  $\tilde{p}_{t,prev}$
- Eight contact law input parameters
  - the initial contact stiffness  $k_{ini}$
  - the initial ultimate normal strength  $\tilde{p}_{n,lim}$
  - the ultimate tensile extension that the contact can sustain called  $\tilde{\delta}_{n,res}$
  - the residual tensile strength at full damage, called  $\tilde{p}_{n,,res}$
- the ratio of strength and extensions in the tensile and tangential directions, called  $NT_{ratio}$
- the threshold of fatigue pressure  $\tilde{p}_f$  it is possible to have fatigue-related damage of the bond
- the fatigue-damage evolution parameter in the tensile direction, called  $dD_{f,n}$

- the fatigue-damage evolution parameter in the tangential direction, called  $dD_{f,t}$
- Four output quantities
  - the tensile (or compressive) contact pressure  $\tilde{p}_n$
  - the tangential contact pressure  $\tilde{p}_t$
  - an updated value of the damage parameter  $D$
- an updated value of the tangential gap  $\tilde{\delta}_t$

The ratio between the tensile and tangential quantities  $NT_{ratio}$  allows to compute the tangential strengths ( $\tilde{p}_{t,lim}$ ,  $\tilde{p}_{t,res}$ ) and maximum tangential extension ( $\tilde{\delta}_{t,res}$ ) from their input counterparts for the tensile direction (respectively  $\tilde{p}_{n,lim}$ ,  $\tilde{p}_{n,res}$  and  $\tilde{\delta}_{n,res}$ ). A simple choice is to take  $NT_{ratio} = 1$ , and in this case, the strengths and maximum extensions are identical in both directions.

When starting a MELODY simulation, the user may use the keyword "INITIALIZECZM". In such a case, the code will detect all the contacts within the simulation, which should be considered as bonds, and put an initial value of the damage parameter  $D$  equal to 0 for all those contact nodes. It means that these bonds are intact in the initial state. Then the simulation starts. The algorithm is described hereafter in commented pseudo-code.

**% CASE A**

```

If  $D < 1$                                      % The bond is not broken, CASE A

From the value of  $D$ , compute  $\tilde{\delta}_{n,max}$           % This is the current maximum tensile
extension (since this value evolves with the damage parameter, see Fig. C-11 (b)).

From this value, and using  $NT_{ratio}$ , compute  $\tilde{\delta}_{t,max}$  % Its tangential counterpart

    If  $\tilde{\delta}_n < \tilde{\delta}_{n,max}$  and  $\tilde{\delta}_t < \tilde{\delta}_{t,max}$       % CASE A1: Elastic part of the bond: damage may
    only occur by fatigue, but not by monotonous loading:
    Compute the current tensile and tangential stiffnesses
    Compute the maximum tensile and tangential strengths ( $\tilde{p}_{n,max}$  and  $\tilde{p}_{t,max}$ )
    Compute the new tensile/compressive contact pressure  $\tilde{p}_n$ 
    Compute the new tangential contact pressure  $\tilde{p}_t$ 

    If  $\tilde{p}_n > p_{n,f}$  and  $\tilde{p}_n > \tilde{p}_{n,prev}$  % Tensile contact stress is large enough to have fatigue,
    and it is also larger than that of the previous time step.
    Increase the damage parameter  $D$  by applying:
    
```

$$D \leftarrow D + \frac{\tilde{p}_n - \tilde{p}_{n,f}}{\tilde{p}_{n,max} - \tilde{p}_{n,f}} \cdot dD_{n,f} \cdot (\tilde{p}_n - \tilde{p}_{n,prev})$$

% It means that the damage increment is proportional to the contact stress increment ( $\tilde{p}_n - \tilde{p}_{n,prev}$ ), multiplied by a certain material parameter  $dD_{n,f}$ , and that this damage is also more important if the load is high than if it is low (hence the term  $\frac{\tilde{p}_n - \tilde{p}_{n,f}}{\tilde{p}_{n,max} - \tilde{p}_{n,f}}$ )

Additionally, If  $\tilde{p}_t > \tilde{p}_{t,f}$  and  $\tilde{p}_t > \tilde{p}_{t,prev}$  % Tangential contact stress is large enough to have fatigue, and it is also larger than that of the previous time step

Increase the damage parameter  $D$  by applying:

$$D \leftarrow D + \frac{\tilde{p}_t - \tilde{p}_{t,f}}{\tilde{p}_{t,max} - \tilde{p}_{t,f}} \cdot dD_{t,f} \cdot (\tilde{p}_t - \tilde{p}_{t,prev})$$

% Same formula but in the tangential direction. Hence we potentially cumulate fatigue damage in the normal and tangential directions.

Contact is solved, algorithm returns the new values of  $\tilde{p}_n$ ,  $\tilde{p}_t$ , and  $D$ . The value of  $\tilde{\delta}_t$  is unmodified.

Else, if  $\tilde{\delta}_n > \tilde{\delta}_{n,max}$  and  $\tilde{\delta}_t < \tilde{\delta}_{t,max}$  % **CASE A2:** The current maximum extension of the bond in the tensile direction is exceeded, there is thus monotonous damage of the bond in that direction and we must increase  $D$ . Meanwhile, the tangential direction is ignored because its limit is not reached.

Update  $\tilde{\delta}_{n,max}$  (which takes the value of  $\tilde{\delta}_n$ )

Increment the damage parameter  $D$  using the following formula:

$$D \leftarrow \frac{\tilde{\delta}_n - \tilde{\delta}_{lim}}{\tilde{\delta}_{res} - \tilde{\delta}_{lim}}$$

Compute the new tensile and tangential stiffnesses.

Compute and return the new values of  $\tilde{p}_n$  and  $\tilde{p}_t$ . Return also  $D$ . The value of  $\tilde{\delta}_t$  is unmodified.

Else, if  $\tilde{\delta}_n < \tilde{\delta}_{n,max}$  and  $\tilde{\delta}_t > \tilde{\delta}_{t,max}$  % **CASE A3:** Same as before, but in tangential direction only.

Update  $\tilde{\delta}_{t,max}$  (which takes the value of  $\tilde{\delta}_t$ )

Increment the damage parameter  $D$  using the following formula:

$$D \leftarrow \frac{\tilde{\delta}_t - \tilde{\delta}_{t,lim}}{\tilde{\delta}_{t,res} - \tilde{\delta}_{t,lim}}$$

Compute the new tensile and tangential stiffnesses.

Compute and return the new values of  $\tilde{p}_n$  and  $\tilde{p}_t$ . Return also  $D$ . The value of  $\tilde{\delta}_t$  is unmodified.

Else, if  $\tilde{\delta}_n > \tilde{\delta}_{n,max}$  and  $\tilde{\delta}_t > \tilde{\delta}_{t,max}$  % **CASE A4**: In that case, the current maximum extension of the bond is exceeded both in the tensile and in the tangential directions, the updated damage parameter  $D$  is then the maximum between those obtained in the cases A2 and A3.

If  $\tilde{\delta}_n/\tilde{\delta}_{n,max} > \tilde{\delta}_t/\tilde{\delta}_{t,max}$  % Tensile direction is more damaging  
Apply algorithm of case A2

If  $\tilde{\delta}_n/\tilde{\delta}_{n,max} < \tilde{\delta}_t/\tilde{\delta}_{t,max}$  % Tangential direction is more damaging  
Apply algorithm of case A3

Else, if  $D \geq 1$  % The bond is broken, **CASE B**

Apply the much more classical cohesive contact law, as if the bond had never existed in the first place. The value of cohesion is  $\tilde{p}_{n,res}$  in the tensile direction and  $\tilde{p}_{t,res}$  in the tangential direction.

To summarize:

- Either the bond is already broken, and everything happens as for any other contact
- Or the bond is still active (i.e., not completely damaged), its damage can increase:
  - by fatigue (based on the increment of contact pressure with respect to the previous time step);
  - by monotonous loading in the tensile direction;
  - by monotonous loading in the tangential direction

## Annex IV.

# Effect of the matrix thickness

In this annex, the effect of the gap thickness is investigated. Two different degradable microstructure are randomly generated using the code explained in section C.1.2 using the same input parameter but differing in terms of matrix thickness  $h_m$  (10 and 20  $\mu\text{m}$ ).

Fig. IV-1(a) and (b) illustrate a qualitative comparison between the two microstructures. The sample built with  $h_m = 20 \mu\text{m}$  (Fig. IV-1(b)) is the one already discussed and illustrated in Fig. C-1 and Fig. C-2. The size distributions of both microstructures are in good agreement with the experimental grain size distribution.

Moreover, the two microstructure are comparable in terms of surface topography, measured in terms of average roughness  $R_a$ , rms  $R_q$ , skewness  $R_{sk}$  and kurtosis  $R_{ku}$  defined in equations (C.1)-(C.4). The comparison in terms of roughness parameters is defined in Tab. IV-1

Tab. IV-1 Comparison between roughness parameters of metal matrix randomly generated in PACKING2D differing in terms of thickness  $h_m$

	$R_a$ ( $\mu\text{m}$ )	$R_q$ ( $\mu\text{m}$ )	$R_{sk}$ (-)	$R_{ku}$ (-)
$h_m = 20 \mu\text{m}$	0.4802	0.5736	1.0951	3.2680
$h_m = 10 \mu\text{m}$	0.4500	0.5384	1.1126	3.0142

The wear is analyzed by performing simulations as explained in detail in Chapter C.2. The contact law parameters are listed in Tab. IV-2 and Tab. I -3 for the CZMfatigue and Mohr-Coulomb contact law, respectively.

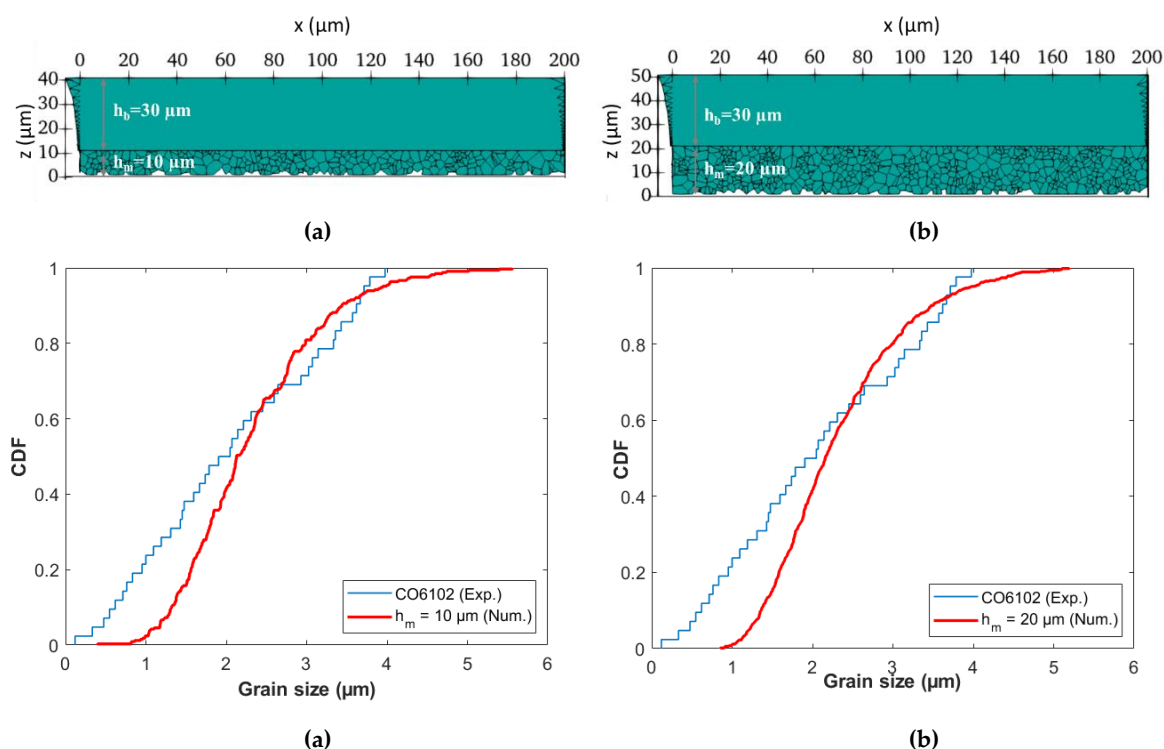


Fig. IV-1 Qualitative and quantitative comparison between two degradable microstructure of different thickness  $h_m$ : (a) degradable microstructure  $h_m = 10 \mu\text{m}$ ; (b) non-degradable microstructure  $h_b = 30 \mu\text{m}$ ; (c) Comparison between the experimental (blu) and numerical (red) degradable microstructure  $h_m = 10 \mu\text{m}$ ; (d) Comparison between the experimental (blu) and numerical (red) degradable microstructure  $h_m = 20 \mu\text{m}$  (same as in Fig. C-4, reported here for the sake of comparison with the matrix  $h_m = 10 \mu\text{m}$ )

Tab. IV-2 CZM fatigue parameters

$k_0$ (MPa/ $\mu\text{m}$ )	$\tilde{p}_{lim}$ (MPa)	$\tilde{\delta}_{res}$ ( $\mu\text{m}$ )	$\tilde{p}_{res}$ (MPa)	$\tilde{p}_f$ (MPa)	$dD_f$ ( $\text{MPa}^{-1}$ )
$10^6$	800	0.002	0	10	0.05

Tab. IV-3 Mohr - Coulomb parameters

Contact law	$k_0$ (MPa/ $\mu\text{m}$ )	$\varphi$ (rad)	$\Gamma$ (MPa)	$\zeta$ (-)
Mohr-Coulomb	$10^6$	0.3	0	0
Damped Mohr - Coulomb	$10^6$	0.3	0	0.1

The influence of the matrix thickness  $h_m$  on the wear rate  $z_m^w/t$  is plotted in Fig. IV-2. As expected, smaller is the thickness  $h_m$  and smaller is the wear rate.

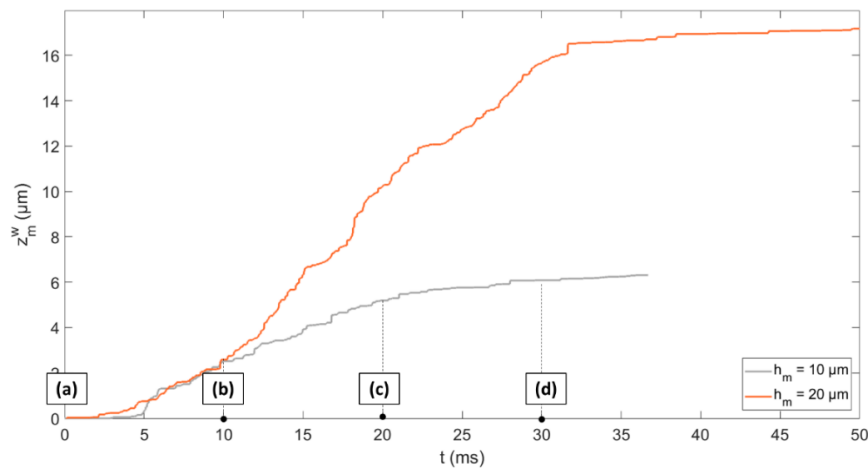


Fig. IV-2 Effect of the degradable thickness  $h_m$  on the wear rate and definition of the instants (a), (b), (c) and (d)

The three main stages of wear defined in Chapter C.2 (initialization, steady-state and perturbed steady-state) are evident in Fig. IV-2 for both microstructure and are defined by the propagation of the damage within the metal matrix. In particular, since the thickness of the degradable material is small, the damage reaches the non-degradable part quickly. This aspect is also evident considering the damage map for the four instants defined in Fig. IV -2 as (a), (b), (c) and (d) (Fig. I IV -3).

The large damage evolution parameter ( $dd_f = 0.05 \text{ MPa}^{-1}$ ) defines the rapidity with which grains detach and the damage propagation within the microstructure. For what already discussed in C.2, since  $dd_f$  is large enough, grains are detached quickly and the damage has no time to propagate within the matrix. However, since the thickness of the degradable part is small, the damage propagation is interrupted by the non-degradable part, perturbing the steady-state as can already be observed from  $t = 10 \text{ s}$  in Fig. IV -3 (b). Therefore, the thickness  $h_m = 10 \mu\text{m}$  is not sufficient to describe the damage and wear propagation.

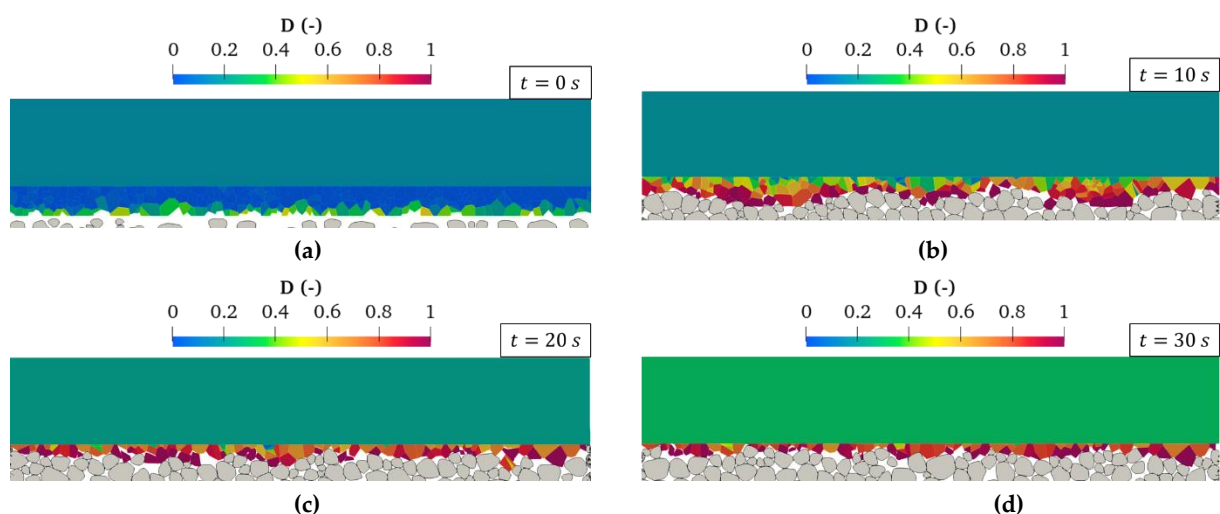


Fig.IV-3 Evolution of damage D on the degradable material for (a)  $t = 0 \text{ s}$ ; (b)  $t = 10 \text{ s}$ ; (c)  $t = 20 \text{ s}$ ; (d)  $t = 30 \text{ s}$



# Bibliography

- [1] J. Konstanty, "Chapter 2 - Machining with diamonds — Theoretical model," J. B. T.-P. M. D. T. Konstanty, Ed. Amsterdam: Elsevier Science, 2005, pp. 21–38.
- [2] M. Mostofi, T. Richard, L. Franca, and S. Yalamanchi, "Wear response of impregnated diamond bits," *Wear*, vol. 410–411, pp. 34–42, 2018, doi: <https://doi.org/10.1016/j.wear.2018.04.010>.
- [3] D. N. Wright, H. Wapler, and H. K. Tönshoff, "Investigations and Prediction of Diamond Wear when Sawing," *CIRP Ann.*, vol. 35, no. 1, pp. 239–244, 1986, doi: [https://doi.org/10.1016/S0007-8506\(07\)61879-4](https://doi.org/10.1016/S0007-8506(07)61879-4).
- [4] K. Gahr, "Microstructure and Wear of Materials." .
- [5] K. Kato, "Micro-mechanisms of wear - wear modes," pp. 277–295, 1992.
- [6] K. Kato, "Classification of wear mechanisms/models," *Proc. Inst. Mech. Eng. Part J J. Eng. Tribol.*, vol. 216, no. 6, pp. 349–355, Jun. 2002, doi: [10.1243/135065002762355280](https://doi.org/10.1243/135065002762355280).
- [7] I. Hutchings and P. Shipway, "6 - Wear by hard particles," I. Hutchings and P. B. T.-T. (Second E. Shipway, Eds. Butterworth-Heinemann, 2017, pp. 165–236.
- [8] D. Aquaro and E. Fontani, "Erosion of Ductile and Brittle Materials," *Meccanica*, vol. 36, no. 6, pp. 651–661, 2001, doi: [10.1023/A:1016396719711](https://doi.org/10.1023/A:1016396719711).
- [9] A. Misra and I. Finnie, "On the size effect in abrasive and erosive wear," *Wear*, vol. 65, no. 3, pp. 359–373, 1981, doi: [https://doi.org/10.1016/0043-1648\(81\)90062-4](https://doi.org/10.1016/0043-1648(81)90062-4).
- [10] D. V De Pellegrin and G. W. Stachowiak, "Assessing the role of particle shape and scale in abrasion using 'sharpness analysis': Part II. Technique evaluation," *Wear*, vol. 253, no. 9, pp. 1026–1034, 2002, doi: [https://doi.org/10.1016/S0043-1648\(02\)00233-8](https://doi.org/10.1016/S0043-1648(02)00233-8).
- [11] D. V. De Pellegrin and G. W. Stachowiak, "Simulation of three-dimensional abrasive particles," *Wear*, vol. 258, no. 1-4 SPEC. ISS., pp. 208–216, 2005, doi: [10.1016/j.wear.2004.09.040](https://doi.org/10.1016/j.wear.2004.09.040).
- [12] G. B. Stachowiak and G. W. Stachowiak, "The effects of particle characteristics on three-body abrasive wear," *Wear*, vol. 249, no. 3–4, pp. 201–207, 2001, doi: [10.1016/S0043-1648\(01\)00557-9](https://doi.org/10.1016/S0043-1648(01)00557-9).
- [13] M. Woldman, E. Van Der Heide, T. Tinga, and M. A. Masen, "The influence of abrasive body dimensions on single asperity wear," *Wear*, vol. 301, no. 1–2, pp. 76–81, 2013, doi: [10.1016/j.wear.2012.12.009](https://doi.org/10.1016/j.wear.2012.12.009).
- [14] J. Konstanty, "Factors Affecting Diamond Retention in Stone Sawblade Segments," *Key Eng. Mater. - KEY ENG MAT*, vol. 250, pp. 13–20, Sep. 2003, doi: [10.4028/www.scientific.net/KEM.250.13](https://doi.org/10.4028/www.scientific.net/KEM.250.13).
- [15] X. Zhao and L. Duan, "A Review of the Diamond Retention Capacity of Metal Bond Matrices," *Metals (Basel)*, vol. 8, p. 307, Apr. 2018, doi: [10.3390/met8050307](https://doi.org/10.3390/met8050307).
- [16] J. Borowiecka-jamrozek and J. Lachowski, "An Analysis of the Retention of a Diamond Particle in a Metallic Matrix after Hot Pressing," *Arch. Foundry Eng.*, vol. 17, Mar. 2017, doi: <https://doi.org/10.1016/j.afe.2017.03.001>.

- 10.1515/afe-2017-0003.
- [17] S. W. Webb, "Diamond retention in sintered cobalt bonds for stone cutting and drilling," *Diam. Relat. Mater.*, vol. 8, no. 11, pp. 2043–2052, 1999, doi: [https://doi.org/10.1016/S0925-9635\(99\)00167-3](https://doi.org/10.1016/S0925-9635(99)00167-3).
- [18] Y. Berthier, "Maurice Godet's Third Body," in *The Third Body Concept Interpretation of Tribological Phenomena*, vol. 31, D. Dowson, C. M. Taylor, T. H. C. Childs, G. Dalmaz, Y. Berthier, L. Flamand, J.-M. Georges, and A. A. B. T.-T. S. Lubrecht, Eds. Elsevier, 1996, pp. 21–30.
- [19] G. Mollon, "A multibody meshfree strategy for the simulation of highly deformable granular materials," *Int. J. Numer. Methods Eng.*, vol. 108, no. 12, pp. 1477–1497, 2016, doi: <https://doi.org/10.1002/nme.5258>.
- [20] G. Mollon, "A unified numerical framework for rigid and compliant granular materials," *Comput. Part. Mech.*, vol. 5, no. 4, pp. 517–527, 2018, doi: [10.1007/s40571-018-0187-6](https://doi.org/10.1007/s40571-018-0187-6).
- [21] N. Fillot, I. Jordanoff, and Y. Berthier, "Kinetics of particle detachment: contribution of a granular model," in *Transient Processes in Tribology*, vol. 43, G. Dalmaz, A. A. Lubrecht, D. Dowson, and M. B. T.-T. S. Priest, Eds. Elsevier, 2003, pp. 63–73.
- [22] N. Fillot, I. Jordanoff, and Y. Berthier, *Simulation of Wear Through Mass Balance in a Dry Contact*, vol. 127. 2004.
- [23] N. Fillot, I. Jordanoff, and Y. Berthier, "Modelling third body flows with a discrete element method—a tool for understanding wear with adhesive particles," *Tribol. Int.*, vol. 40, no. 6, pp. 973–981, 2007, doi: <https://doi.org/10.1016/j.triboint.2006.02.056>.
- [24] S. Li and W. K. Liu, "Meshfree and particle methods and their applications," *Appl. Mech. Rev.*, vol. 55, no. 1, pp. 1–34, 2002, doi: [10.1115/1.1431547](https://doi.org/10.1115/1.1431547).
- [25] D. Dowson, "A generalized Reynolds equation for fluid-film lubrication," *Int. J. Mech. Sci.*, vol. 4, no. 2, pp. 159–170, 1962, doi: [https://doi.org/10.1016/S0020-7403\(62\)80038-1](https://doi.org/10.1016/S0020-7403(62)80038-1).
- [26] O. Reynolds, "On the Theory of Lubrication and Its Application to Mr. Lowe's Experiments," *Philos. Trans. R. Soc. London*, vol. 177, pp. 157–234, 1886, [Online]. Available: [https://scholar.google.com/scholar?q=related:zTMHxIMaYncJ:scholar.google.com/&hl=en&as\\_sdt=0,39&as\\_ylo=1886&as\\_yhi=1886#0](https://scholar.google.com/scholar?q=related:zTMHxIMaYncJ:scholar.google.com/&hl=en&as_sdt=0,39&as_ylo=1886&as_yhi=1886#0).
- [27] J. F. Archard, "Contact and Rubbing of Flat Surfaces," *J. Appl. Phys.*, vol. 24, no. 8, pp. 981–988, Aug. 1953, doi: [10.1063/1.1721448](https://doi.org/10.1063/1.1721448).
- [28] A. Deborde and T. Commeau, "Design of high performance binder by understanding the protrusion and clearance dynamics of diamonds during the cutting process+."
- [29] G. Mollon and J. Zhao, "Fourier–Voronoi-based generation of realistic samples for discrete modelling of granular materials," *Granul. Matter*, vol. 14, pp. 621–638, Sep. 2012, doi: [10.1007/s10035-012-0356-x](https://doi.org/10.1007/s10035-012-0356-x).
- [30] T. Luther and C. Könke, "Polycrystal models for the analysis of intergranular crack growth in metallic materials," *Eng. Fract. Mech.*, vol. 76, no. 15, pp. 2332–2343, 2009, doi: [10.1016/j.engfracmech.2009.07.006](https://doi.org/10.1016/j.engfracmech.2009.07.006).
- [31] M. F. S. F. De Moura, J. P. M. Gonçalves, J. A. G. Chousal, and R. D. S. G. Campilho, "Cohesive

- and continuum mixed-mode damage models applied to the simulation of the mechanical behaviour of bonded joints," *Int. J. Adhes. Adhes.*, vol. 28, no. 8, pp. 419–426, 2008, doi: 10.1016/j.ijadhadh.2008.04.004.
- [32] M. Paggi and P. Wriggers, "Numerical modelling of intergranular fracture in polycrystalline materials and grain size effects," *Frat. ed Integrità Strutt. ed Integrità Strutt.*, vol. 5, no. 17, pp. 5–14, 2011, doi: 10.3221/igf-esis.17.01.
- [33] M. Champagne *et al.*, "Modeling wear for heterogeneous bi-phasic materials using discrete elements approach To cite this version : HAL Id : hal-01003460 Modeling wear for heterogeneous bi-phasic materials using discrete elements approach," 2017.
- [34] J. Konstanty, "Chapter 1 - Introduction," in *Powder Metallurgy Diamond Tools*, J. Konstanty, Ed. Amsterdam: Elsevier Science, 2005, pp. 1–19.
- [35] J. Konstanty, "Sintered diamond tools: Trends, challenges and prospects," *Powder Metall.*, vol. 56, pp. 184–188, 2013, doi: 10.1179/1743290113Y.0000000058.
- [36] J. Konstanty, "Production parameters and materials selection of powder metallurgy diamond tools," *Powder Metall.*, vol. 49, no. 4, pp. 299–306, Dec. 2006, doi: 10.1179/174329006X113508.
- [37] J. D. Dwan, "Production of Diamond Impregnated Cutting Tools," *Powder Metall.*, vol. 41, no. 2, pp. 84–86, Jan. 1998, doi: 10.1179/pom.1998.41.2.84.
- [38] R. M. Goktan and N. Yilmaz, "Diamond Tool Specific Wear Rate Assessment in Granite Machining by Means of Knoop Micro-Hardness Process Parameters," *Rock Mech. Rock Eng.*, vol. 50, pp. 1–17, May 2017, doi: 10.1007/s00603-017-1240-0.
- [39] J. Konstanty, "Chapter 3 - Diamond tool design and composition," in *Powder Metallurgy Diamond Tools*, J. Konstanty, Ed. Amsterdam: Elsevier Science, 2005, pp. 39–68.
- [40] E. O. Hall, "The Deformation and Ageing of Mild Steel: {III} Discussion of Results," *Proc. Phys. Soc. Sect. B*, vol. 64, no. 9, pp. 747–753, Sep. 1951, doi: 10.1088/0370-1301/64/9/303.
- [41] N. J. Petch, "The Cleavage Strength of Polycrystals," 1953.
- [42] T. . COMMEAU, A. . NOUVEAU, and A. . DEBORDE, "Usure de matrices métalliques dans un flux de debris," pp. 1–11, 2017.
- [43] J. Borowiecka-Jamrozek, "Engineering structure and properties of materials used as a matrix in diamond impregnated tools," *Arch. Metall. Mater.*, pp. 5–8, 2013.
- [44] Y. S. Liao and S. Y. Luo, "Effects of matrix characteristics on diamond composites," *J. Mater. Sci.*, vol. 28, no. 5, pp. 1245–1251, 1993, doi: 10.1007/BF01191959.
- [45] Y. S. Liao and S. Y. Luo, "Wear characteristics of sintered during circular sawing diamond composite," vol. 157, pp. 325–337, 1992.
- [46] K. Kato and K. Adachi, "Wear mechanisms," in *Modern Tribology Handbook: Volume One: Principles of Tribology*, CRC press, 2000, pp. 273–300.
- [47] A. Ramalho and J. C. Miranda, "The relationship between wear and dissipated energy in sliding systems," vol. 260, pp. 361–367, 2006, doi: 10.1016/j.wear.2005.02.121.
- [48] S. Fouvry, P. Kapsa, H. Zahouani, and L. E. O. Vincent, "Wear analysis in fretting of hard

- coatings through a dissipated energy concept  $DC \sim ne \sim nr$ ," vol. 1648, no. 96, 1997.
- [49] S. U. Fouvry and P. Kapsa, "An energy description of hard coating wear mechanisms &," no. April 2000, 2001.
- [50] E. Rabinowicz, L. A. Dunn, and P. G. Russell, "A study of abrasive wear under three-body conditions," *Wear*, vol. 4, no. 5, pp. 345–355, 1961, doi: 10.1016/0043-1648(61)90002-3.
- [51] S. W. Watson, F. J. Friedersdorf, B. W. Madsen, and S. D. Cramer, "Methods of measuring wear-corrosion synergism," *Wear*, vol. 181–183, no. PART 2, pp. 476–484, 1995, doi: 10.1016/0043-1648(95)90161-2.
- [52] M. Godet, "The third-body approach: A mechanical view of wear," *Wear*, vol. 100, no. 1, pp. 437–452, 1984, doi: [https://doi.org/10.1016/0043-1648\(84\)90025-5](https://doi.org/10.1016/0043-1648(84)90025-5).
- [53] Y. Berthier, "Experimental evidence for friction and wear modelling," *Wear*, vol. 139, no. 1, pp. 77–92, 1990, doi: [https://doi.org/10.1016/0043-1648\(90\)90210-2](https://doi.org/10.1016/0043-1648(90)90210-2).
- [54] A. Ersoy, S. Buyuksagic, and U. Atici, "Wear characteristics of circular diamond saws in the cutting of different hard abrasive rocks," *Wear*, vol. 258, no. 9, pp. 1422–1436, 2005, doi: <https://doi.org/10.1016/j.wear.2004.09.060>.
- [55] M. Petrica, E. Badisch, and T. Peinsitt, "Abrasive wear mechanisms and their relation to rock properties," *Wear*, vol. 308, no. 1–2, pp. 86–94, 2013, doi: 10.1016/j.wear.2013.10.005.
- [56] J. Konstanty, T. Kim, and S.-B. Kim, "Resistance to Abrasive Wear of Materials Used as Metallic Matrices in Diamond Impregnated Tools," *Mater. Sci. Forum - MATER SCI FORUM*, vol. 534–536, pp. 1125–1128, Jan. 2007, doi: 10.4028/www.scientific.net/MSF.534-536.1125.
- [57] H. Sin, N. Saka, and N. P. Suh, "Abrasive wear mechanisms and the grit size effect," *Wear*, vol. 55, no. 1, pp. 163–190, 1979, doi: [https://doi.org/10.1016/0043-1648\(79\)90188-1](https://doi.org/10.1016/0043-1648(79)90188-1).
- [58] R. Gåhlin and S. Jacobson, "The particle size effect in abrasion studied by controlled abrasive surfaces," *Wear*, vol. 224, no. 1, pp. 118–125, 1999, doi: [https://doi.org/10.1016/S0043-1648\(98\)00344-5](https://doi.org/10.1016/S0043-1648(98)00344-5).
- [59] J. Larsen-Badse, "Influence of grit size on the groove formation during sliding abrasion," *Wear*, vol. 11, no. 3, pp. 213–222, 1968, doi: [https://doi.org/10.1016/0043-1648\(68\)90559-0](https://doi.org/10.1016/0043-1648(68)90559-0).
- [60] G. W. Stachowiak, "Particle angularity and its relationship to abrasive and erosive wear," *Wear*, vol. 241, no. 2, pp. 214–219, 2000, doi: [https://doi.org/10.1016/S0043-1648\(00\)00378-1](https://doi.org/10.1016/S0043-1648(00)00378-1).
- [61] P. A. Swanson and A. F. Vetter, "The Measurement of Abrasive Particle Shape and Its Effect on Wear," *A S L E Trans.*, vol. 28, no. 2, pp. 225–230, 1985, doi: 10.1080/05698198508981615.
- [62] K. Kato, K. Hokkirigawa, T. Kayaba, and Y. Endo, "Three dimensional shape effect on abrasive wear," *J. Tribol.*, vol. 108, no. 3, pp. 346–349, 1986.
- [63] M. Woldman, E. van der Heide, D. J. Schipper, T. Tinga, and M. A. Masen, "Investigating the influence of sand particle properties on abrasive wear behaviour," *Wear*, vol. 294–295, pp. 419–426, 2012, doi: <https://doi.org/10.1016/j.wear.2012.07.017>.
- [64] I. M. Krieger and T. J. Dougherty, "A Mechanism for Non-Newtonian Flow in Suspensions of Rigid Spheres," *Trans. Soc. Rheol.*, vol. 3, no. 1, pp. 137–152, 1959, doi: 10.1122/1.548848.

- [65] K. Hokkirigawa, K. Kato, and Z. Z. Li, "The effect of hardness on the transition of the abrasive wear mechanism of steels," *Wear*, vol. 123, no. 2, pp. 241–251, 1988, doi: [https://doi.org/10.1016/0043-1648\(88\)90102-0](https://doi.org/10.1016/0043-1648(88)90102-0).
- [66] K. Hokkirigawa and K. Kato, "An experimental and theoretical investigation of ploughing , cutting and wedge formation during abrasive wear," pp. 51–57, 1988.
- [67] J. Konstanty, "Theoretical analysis of stone sawing with diamonds," *J. Mater. Process. Technol.*, vol. 123, no. 1, pp. 146–154, 2002, doi: [https://doi.org/10.1016/S0924-0136\(02\)00071-7](https://doi.org/10.1016/S0924-0136(02)00071-7).
- [68] M. T. Siniawski, S. J. Harris, and Q. Wang, "A universal wear law for abrasion," *Wear*, vol. 262, no. 7–8, pp. 883–888, 2007, doi: [10.1016/j.wear.2006.08.017](https://doi.org/10.1016/j.wear.2006.08.017).
- [69] S. J. Bull and D. S. Rickerby, "Multi-pass scratch testing as a model for abrasive wear," *Thin Solid Films*, vol. 181, no. 1, pp. 545–553, 1989, doi: [https://doi.org/10.1016/0040-6090\(89\)90523-3](https://doi.org/10.1016/0040-6090(89)90523-3).
- [70] T. Kayaba, K. Hokkirigawa, and K. Kato, "Analysis of the abrasive wear mechanism by successive observations of wear processes in a scanning electron microscope," *Wear*, vol. 110, no. 3, pp. 419–430, 1986, doi: [https://doi.org/10.1016/0043-1648\(86\)90115-8](https://doi.org/10.1016/0043-1648(86)90115-8).
- [71] W. Brostow, G. Darmarla, J. Howe, and D. Pietkiewicz, "Determination of wear of surfaces by scratch testing," *E-Polymers*, no. 025, pp. 1–8, 2004, doi: [10.1515/epoly.2004.4.1.255](https://doi.org/10.1515/epoly.2004.4.1.255).
- [72] M. Woldman, E. Van Der Heide, T. Tinga, and M. A. Masen, "A Finite Element Approach to Modeling Abrasive Wear Modes," *Tribol. Trans.*, vol. 60, no. 4, pp. 711–718, 2017, doi: [10.1080/10402004.2016.1206647](https://doi.org/10.1080/10402004.2016.1206647).
- [73] Y. Zhou, P. D. Funkenbusch, and D. J. Quesnel, "Stress distributions at the abrasive - matrix interface during tool wear in bound abrasive grinding - a finite element analysis," *Wear*, vol. 209, no. 1–2, pp. 247–254, 1997, doi: [10.1016/S0043-1648\(96\)07490-X](https://doi.org/10.1016/S0043-1648(96)07490-X).
- [74] B. Li, P. M. Amaral, L. Reis, C. A. Anjinho, L. G. Rosa, and M. de Freitas, "3D-modelling of the local plastic deformation and residual stresses of PM diamond-metal matrix composites," *Comput. Mater. Sci.*, vol. 47, no. 4, pp. 1023–1030, 2010, doi: [10.1016/j.commatsci.2009.12.001](https://doi.org/10.1016/j.commatsci.2009.12.001).
- [75] C. M. Suh, K. S. Bae, and M. S. Suh, "Wear behavior of diamond wheel for grinding optical connector ferrule - FEA and wear test - FEA a," *J. Mech. Sci. Technol.*, vol. 22, no. 11, pp. 2009–2015, 2008, doi: [10.1007/s12206-008-0407-8](https://doi.org/10.1007/s12206-008-0407-8).
- [76] J. Xu, A. H. Sheikh, and C. Xu, "3-D Finite element modelling of diamond pull-out failure in impregnated diamond bits," *Diam. Relat. Mater.*, vol. 71, pp. 1–12, 2017, doi: [10.1016/j.diamond.2016.11.006](https://doi.org/10.1016/j.diamond.2016.11.006).
- [77] H. Heshmat, "The Rheology and Hydrodynamics of Dry Powder Lubrication," *Tribol. Trans.*, vol. 34, no. 3, pp. 433–439, Jan. 1991, doi: [10.1080/10402009108982054](https://doi.org/10.1080/10402009108982054).
- [78] C. F. I. I. Higgs and J. Tichy, "Granular Flow Lubrication: Continuum Modeling of Shear Behavior ," *J. Tribol.*, vol. 126, no. 3, pp. 499–510, 2004, doi: [10.1115/1.1691437](https://doi.org/10.1115/1.1691437).
- [79] A. Vakis *et al.*, "Modeling and simulation in tribology across scales: An overview," *Tribol. Int.*, vol. 125, Feb. 2018, doi: [10.1016/j.triboint.2018.02.005](https://doi.org/10.1016/j.triboint.2018.02.005).

- [80] P. A. . Cundall and O. D. L. Strack, "Cundall\_Strack.Pdf," *Geotechnique*, vol. 29, no. 1. pp. 47–65, 1979.
- [81] H.-P. Cao, M. Renouf, F. Dubois, and Y. Berthier, "Coupling Continuous and Discontinuous Descriptions to Model First Body Deformation in Third Body Flows," *J. Tribol.*, vol. 133, no. 4, Oct. 2011, doi: 10.1115/1.4004881.
- [82] A. Saulot, M. Renouf, and Y. Berthier, "FEM-DEM Dialogue for Tribological Understanding." pp. 581–583, Oct. 20, 2008, doi: 10.1115/IJTC2008-71173.
- [83] J. S. Chong, E. B. Christiansen, and A. D. Baer, "Flow of viscous fluid through a circular aperture," *J. Appl. Polym. Sci.*, vol. 15, no. 2, pp. 369–379, Feb. 1971, doi: <https://doi.org/10.1002/app.1971.070150210>.
- [84] P. K. Senapati, D. Panda, and A. Parida, "Predicting Viscosity of Limestone-Water Slurry," *J. Miner. Mater. Charact. Eng.*, vol. 08, Jan. 2009, doi: 10.4236/jmmce.2009.83018.
- [85] S. K. Mishra, P. K. Senapati, and D. Panda, "Rheological Behavior of Coal-Water Slurry," *Energy Sources*, vol. 24, no. 2, pp. 159–167, Feb. 2002, doi: 10.1080/00908310252774471.
- [86] C. Gauthier, S. Lafaye, and R. Schirrer, "Elastic recovery of a scratch in a polymeric surface: experiments and analysis," *Tribol. Int.*, vol. 34, no. 7, pp. 469–479, 2001, doi: [https://doi.org/10.1016/S0301-679X\(01\)00043-3](https://doi.org/10.1016/S0301-679X(01)00043-3).
- [87] T. A. Adler and R. P. Walters, "Wear and scratch hardness of 304 stainless steel investigated with a single scratch test," *Wear*, vol. 162–164, pp. 713–720, 1993, doi: [https://doi.org/10.1016/0043-1648\(93\)90071-S](https://doi.org/10.1016/0043-1648(93)90071-S).
- [88] M. G. Gee, A. Gant, and L. Van der Berg, "Fine scale abrasion testing of hardmetals and ceramics," 1999.
- [89] M. G. Gee, "Low load multiple scratch tests of ceramics and hard metals," *Wear*, vol. 250, no. 1, pp. 264–281, 2001, doi: [https://doi.org/10.1016/S0043-1648\(01\)00591-9](https://doi.org/10.1016/S0043-1648(01)00591-9).
- [90] M. Ö. Bora, O. Coban, T. Sinmazcelik, V. Günay, and M. Zeren, "Instrumented indentation and scratch testing evaluation of tribological properties of tin-based bearing materials," *Mater. Des.*, vol. 31, no. 6, pp. 2707–2715, 2010, doi: 10.1016/j.matdes.2010.01.033.
- [91] S. Graça, R. Colaço, and R. Vilar, "Micro-to-nano indentation and scratch hardness in the Ni-Co system: Depth dependence and implications for tribological behavior," *Tribol. Lett.*, vol. 31, no. 3, pp. 177–185, 2008, doi: 10.1007/s11249-008-9350-1.
- [92] A. Kareer, X. D. Hou, N. M. Jennett, and S. V. Hainsworth, "The interaction between Lateral size effect and grain size when scratching polycrystalline copper using a Berkovich indenter," *Philos. Mag.*, vol. 96, no. 32–34, pp. 3414–3429, 2016, doi: 10.1080/14786435.2016.1240881.
- [93] B. J. Hamrock and D. Dowson, "Isothermal Elastohydrodynamic Lubrication of Point Contacts: Part 1—Theoretical Formulation," *J. Lubr. Technol.*, vol. 98, no. 2, pp. 223–228, Apr. 1976, doi: 10.1115/1.3452801.
- [94] B. J. Hamrock and D. Dowson, "Isothermal Elastohydrodynamic Lubrication of Point Contacts: Part II—Ellipticity Parameter Results," *J. Lubr. Technol.*, vol. 98, no. 3, pp. 375–381, Jul. 1976, doi: 10.1115/1.3452861.
- [95] B. J. Hamrock and D. Dowson, "Isothermal Elastohydrodynamic Lubrication of Point Contacts:

- Part III—Fully Flooded Results,” *J. Lubr. Technol.*, vol. 99, no. 2, pp. 264–275, Apr. 1977, doi: 10.1115/1.3453074.
- [96] B. J. Hamrock and D. Dowson, “Isothermal Elastohydrodynamic Lubrication of Point Contacts: Part IV—Starvation Results,” *J. Lubr. Technol.*, vol. 99, no. 1, pp. 15–23, Jan. 1977, doi: 10.1115/1.3452973.
- [97] J. A. Tichy, “Hydrodynamic lubrication theory for the Bingham plastic flow model,” *J. Rheol. (N. Y. N. Y.)*, vol. 35, no. 4, pp. 477–496, May 1991, doi: 10.1122/1.550231.
- [98] C. Dorier and J. Tichy, “Behavior of a bingham-like viscous fluid in lubrication flows,” *J. Nonnewton. Fluid Mech.*, vol. 45, no. 3, pp. 291–310, 1992, doi: [https://doi.org/10.1016/0377-0257\(92\)80065-6](https://doi.org/10.1016/0377-0257(92)80065-6).
- [99] W. Habchi, I. Demirci, D. Eyheramendy, E. C. De Marseille, and G. E. Morales-espejel, “A Finite Element Approach of Thin Film Lubrication in Circular EHD Contacts A Finite Element Approach of Thin Film Lubrication in Circular EHD Contacts,” no. October 2017, 2007, doi: 10.1016/j.triboint.2007.01.017.
- [100] B. Najji, B. Bou-Said, and D. Berthe, “New Formulation for Lubrication With Non-Newtonian Fluids,” *J. Tribol.*, vol. 111, no. 1, pp. 29–34, Jan. 1989, doi: 10.1115/1.3261875.
- [101] J. B. Shukla, S. Kumar, and P. Chandra, “Generalized reynolds equation with slip at bearing surfaces: Multiple-layer lubrication theory,” *Wear*, vol. 60, no. 2, pp. 253–268, 1980, doi: [https://doi.org/10.1016/0043-1648\(80\)90226-4](https://doi.org/10.1016/0043-1648(80)90226-4).
- [102] C. Barus, “Isothermals, isopiestic and isometrics relative to viscosity,” *Am. J. Sci.*, vol. 45, no. 266, pp. 87–96, 1893, doi: 10.2475/ajs.s3-45.266.87.
- [103] C. J. A. Roelands, W. O. Winer, and W. A. Wright, “Correlational Aspects of the Viscosity-Temperature-Pressure Relationship of Lubricating Oils(Dr In dissertation at Technical University of Delft, 1966),” *J. Lubr. Technol.*, vol. 93, no. 1, pp. 209–210, Jan. 1971, doi: 10.1115/1.3451519.
- [104] I. A. Frigaard and C. Nouar, “On the usage of viscosity regularisation methods for visco-plastic fluid flow computation,” *J. Nonnewton. Fluid Mech.*, vol. 127, no. 1, pp. 1–26, 2005, doi: <https://doi.org/10.1016/j.jnnfm.2005.01.003>.
- [105] T. C. Papanastasiou, “Flows of Materials with Yield,” *J. Rheol. (N. Y. N. Y.)*, vol. 31, no. 5, pp. 385–404, Jul. 1987, doi: 10.1122/1.549926.
- [106] S. Frey, F. Link, M. Naccache, and C. Fonseca, “Finite element investigation of inertia and viscous effects on regularized Herschel–Bulkley flows,” *J. Brazilian Soc. Mech. Sci. Eng.*, vol. 38, Jan. 2016, doi: 10.1007/s40430-015-0473-7.
- [107] Y. Waddad, V. Magnier, P. Dufrénoy, and G. De Saxcé, “Multiscale thermomechanical modeling of frictional contact problems considering wear – Application to a pin-on-disc system,” *Wear*, vol. 426–427, no. September 2018, pp. 1399–1409, 2019, doi: 10.1016/j.wear.2018.12.063.
- [108] J.-F. Ferrellec and G. McDowell, “A simple method to create complex particle shapes for DEM,” *Geomech. Geoengin. An Int. J.*, vol. 3, pp. 211–216, Sep. 2008, doi: 10.1080/17486020802253992.
- [109] D. V De Pellegrin and G. W. Stachowiak, “Sharpness of abrasive particles and surfaces,” *Wear*,

- vol. 256, no. 6, pp. 614–622, 2004, doi: <https://doi.org/10.1016/j.wear.2003.10.004>.
- [110] C. Gear, “The Numerical Integration of Ordinary Differential Equations of Various Orders,” *Math. Comput.*, vol. 21, May 1969, doi: 10.2307/2004155.
- [111] J. R. Cash, “On the integration of stiff systems of O.D.E.s using extended backward differentiation formulae,” *Numer. Math.*, vol. 34, no. 3, pp. 235–246, 1980, doi: 10.1007/BF01396701.
- [112] J. Konstanty, “Chapter 7 - Wear properties of the matrix,” J. B. T.-P. M. D. T. Konstanty, Ed. Amsterdam: Elsevier Science, 2005, pp. 113–127.
- [113] G. Mollon, “A numerical framework for discrete modelling of friction and wear using Voronoi polyhedrons,” *Tribol. Int.*, vol. 90, pp. 343–355, 2015, doi: 10.1016/j.triboint.2015.04.011.
- [114] S. Fortune, “A sweepline algorithm for Voronoi diagrams,” *Algorithmica*, vol. 2, no. 1–4, pp. 153–174, 1987, doi: 10.1007/BF01840357.
- [115] D. Gross and M. Li, “Constructing microstructures of poly- and nanocrystalline materials for numerical modeling and simulation,” *Appl. Phys. Lett.*, vol. 80, no. 5, p. 746, 2002, doi: 10.1063/1.1432448.
- [116] T. Xu and M. Li, “Topological and statistical properties of a constrained Voronoi tessellation,” *Philos. Mag.*, vol. 89, no. 4, pp. 349–374, Feb. 2009, doi: 10.1080/14786430802647065.
- [117] E. S. Gadelmawla, M. M. Koura, T. M. A. Maksoud, I. M. Elewa, and H. H. Soliman, “Roughness parameters,” *J. Mater. Process. Technol.*, vol. 123, no. 1, pp. 133–145, 2002, doi: 10.1016/S0924-0136(02)00060-2.
- [118] I. Hutchings and P. Shipway, “2 - Surface topography and surfaces in contact,” I. Hutchings and P. B. T.-T. (Second E. Shipway, Eds. Butterworth-Heinemann, 2017, pp. 7–35.
- [119] G. Mollon, A. Quacquarelli, E. Andò, and G. Viggiani, “Can friction replace roughness in the numerical simulation of granular materials?,” *Granul. Matter*, vol. 22, no. 2, p. 42, 2020, doi: 10.1007/s10035-020-1004-5.
- [120] G. Midi, “On dense granular flows,” *Eur. Phys. J. E*, vol. 14, pp. 341–365, Aug. 2004, doi: 10.1140/epje/i2003-10153-0.
- [121] V. Richefeu, G. Mollon, D. Daudon, and P. Villard, “Dissipative contacts and realistic block shapes for modeling rock avalanches,” *Eng. Geol.*, vol. 149–150, pp. 78–92, 2012, doi: 10.1016/j.enggeo.2012.07.021.
- [122] G. Alfano and M. A. Crisfield, “Finite element interface models for the delamination analysis of laminated composites: Mechanical and computational issues,” *Int. J. Numer. Methods Eng.*, vol. 50, no. 7, pp. 1701–1736, 2001, doi: 10.1002/nme.93.
- [123] A. Hillerborg, M. Modéer, and P.-E. Petersson, “Analysis of crack formation and crack growth in concrete by means of fracture mechanics and finite elements,” *Cem. Concr. Res.*, vol. 6, no. 6, pp. 773–781, 1976, doi: [https://doi.org/10.1016/0008-8846\(76\)90007-7](https://doi.org/10.1016/0008-8846(76)90007-7).
- [124] G. I. Barenblatt, “The formation of equilibrium cracks during brittle fracture. General ideas and hypotheses. Axially-symmetric cracks,” *J. Appl. Math. Mech.*, vol. 23, no. 3, pp. 622–636, 1959, doi: 10.1016/0021-8928(59)90157-1.
- [125] G. I. Barenblatt, “Barenblatt,” *Adv. Appl. Mech.*, vol. 7, no. C, pp. 55–129, 1962.

- [126] D. S. Dugdale, "Yielding of steel sheets containing slits," *J. Mech. Phys. Solids*, vol. 8, no. 2, pp. 100–104, 1960, doi: 10.1016/0022-5096(60)90013-2.
- [127] F. Zhou and J. F. Molinari, "Dynamic crack propagation with cohesive elements: a methodology to address mesh dependency," *Int. J. Numer. Methods Eng.*, vol. 59, no. 1, pp. 1–24, 2004, doi: <https://doi.org/10.1002/nme.857>.
- [128] F. Zhou, J. F. Molinari, and K. T. Ramesh, "A cohesive model based fragmentation analysis: Effects of strain rate and initial defects distribution," *Int. J. Solids Struct.*, vol. 42, no. 18–19, pp. 5181–5207, 2005, doi: 10.1016/j.ijsolstr.2005.02.009.
- [129] F. Zhou, J. F. Molinari, and T. Shioya, "A rate-dependent cohesive model for simulating dynamic crack propagation in brittle materials," *Eng. Fract. Mech.*, vol. 72, no. 9, pp. 1383–1410, 2005, doi: 10.1016/j.engfracmech.2004.10.011.
- [130] F. Moroni and A. Pirondi, "A procedure for the simulation of fatigue crack growth in adhesively bonded joints based on the cohesive zone model and different mixed-mode propagation criteria," *Eng. Fract. Mech.*, vol. 78, no. 8, pp. 1808–1816, 2011, doi: 10.1016/j.engfracmech.2011.02.004.
- [131] S. Jimenez and R. Duddu, "On the parametric sensitivity of cohesive zone models for high-cycle fatigue delamination of composites," *Int. J. Solids Struct.*, vol. 82, pp. 111–124, 2016, doi: 10.1016/j.ijsolstr.2015.10.015.
- [132] M. Elices, G. V. Guinea, J. Gómez, and J. Planas, "The cohesive zone model: Advantages, limitations and challenges," *Eng. Fract. Mech.*, vol. 69, no. 2, pp. 137–163, 2001, doi: 10.1016/S0013-7944(01)00083-2.
- [133] Y. J. Wang and C. Q. Ru, "Determination of two key parameters of a cohesive zone model for pipeline steels based on uniaxial stress-strain curve," *Eng. Fract. Mech.*, vol. 163, pp. 55–65, 2016, doi: 10.1016/j.engfracmech.2016.06.017.
- [134] X. P. Xu and A. Needleman, "Numerical simulations of fast crack growth in brittle solids," *J. Mech. Phys. Solids*, vol. 42, no. 9, pp. 1397–1434, 1994, doi: 10.1016/0022-5096(94)90003-5.
- [135] P. A. Gustafson and A. M. Waas, "The influence of adhesive constitutive parameters in cohesive zone finite element models of adhesively bonded joints," *Int. J. Solids Struct.*, vol. 46, no. 10, pp. 2201–2215, 2009, doi: 10.1016/j.ijsolstr.2008.11.016.
- [136] P. Robinson, U. Galvanetto, D. Tumino, G. Bellucci, and D. Violeau, "Numerical simulation of fatigue-driven delamination using interface elements," *Int. J. Numer. Methods Eng.*, no. January 2005, doi: 10.1002/nme.1338.
- [137] N. Raje, W. Lafayette, and R. G. Rateick, "A Statistical Damage Mechanics Model for Subsurface Initiated Spalling in Rolling Contacts Fatigue," *J. Tribol.*, vol. 130, no. October, pp. 1–11, 2008, doi: 10.1115/1.2959109.
- [138] L. F. Kawashita and S. R. Hallett, "International Journal of Solids and Structures A crack tip tracking algorithm for cohesive interface element analysis of fatigue delamination propagation in composite materials," *Int. J. Solids Struct.*, vol. 49, no. 21, pp. 2898–2913, 2012, doi: 10.1016/j.ijsolstr.2012.03.034.
- [139] M. F. S. F. De Moura and J. P. M. Gonçalves, "Cohesive zone model for high-cycle fatigue of adhesively bonded joints under mode I loading," *Int. J. Solids Struct.*, vol. 51, no. 5, pp. 1123–

- 1131, 2014, doi: 10.1016/j.ijsolstr.2013.12.009.
- [140] P. Paris, "A rational analytic theory of fatigue," 1961.
- [141] P. Paris and F. Erdogan, "A Critical Analysis of Crack Propagation Laws," *J. Basic Eng.*, vol. 85, pp. 528–533, 1963.
- [142] L. M. Fernández-Cañadas, I. Iváñez, and S. Sanchez-Saez, "Influence of the cohesive law shape on the composite adhesively-bonded patch repair behaviour," *Compos. Part B Eng.*, vol. 91, pp. 414–421, 2016, doi: 10.1016/j.compositesb.2016.01.056.
- [143] N. Raje and F. Sadeghi, "Statistical numerical modelling of sub-surface initiated spalling in bearing contacts," *Proc. Inst. Mech. Eng. Part J J. Eng. Tribol.*, vol. 223, no. 6, pp. 849–858, 2009, doi: 10.1243/13506501JET481.
- [144] T. Ferracin, C. M. Landis, F. Delannay, and T. Pardoën, "On the determination of the cohesive zone properties of an adhesive layer from the analysis of the wedge-peel test," *Int. J. Solids Struct.*, vol. 40, no. 11, pp. 2889–2904, 2003, doi: 10.1016/S0020-7683(03)00076-3.
- [145] A. Ghosh and F. Sadeghi, "A novel approach to model effects of surface roughness parameters on wear," *Wear*, vol. 338–339, pp. 73–94, 2015, doi: 10.1016/j.wear.2015.04.022.
- [146] K. A. Kounoudji, M. Renouf, G. Mollon, and Y. Berthier, "Role of Third Body on Bolted Joints' Self-Loosening," *Tribol. Lett.*, vol. 61, no. 3, 2016, doi: 10.1007/s11249-016-0640-8.
- [147] E. Felder and J. Bucaille, "Mechanical analysis of the scratching of metals and polymers with conical indenters at moderate and large strains," vol. 39, pp. 70–87, 2006, doi: 10.1016/j.triboint.2005.04.005.
- [148] M. Varga, S. Leroch, S. J. Eder, H. Rojacz, and M. Rodríguez, "Influence of velocity on high-temperature fundamental abrasive contact : A numerical and experimental approach," *Wear*, vol. 426–427, no. September 2018, pp. 370–377, 2019, doi: 10.1016/j.wear.2018.12.013.
- [149] F. Sadeghi, B. Jalalahmadi, T. S. Slack, N. Raje, and N. K. Arakere, "A review of rolling contact fatigue," *J. Tribol.*, vol. 131, no. 4, pp. 1–15, 2009, doi: 10.1115/1.3209132.



## FOLIO ADMINISTRATIF

### THESE DE L'UNIVERSITE DE LYON OPEREE AU SEIN DE L'INSA LYON

NOM : QUACQUARELLI

DATE de SOUTENANCE :

Prénoms : Adriana

TITRE : A multi-scale modeling approach for diamond tools wear

NATURE : Doctorat

Numéro d'ordre : 2021LYSEI040

Ecole doctorale : Mécanique, Energetique, Génie Civil, Acoustique

Spécialité : Mécanique

#### RESUME :

Dans le domaine des outils de coupe, les outils diamantés (DIT: carottage, scies à ruban et circulaires) sont largement utilisés pour traiter et dimensionner les matériaux fragiles. Les DIT sont composés de cristaux de diamant abrasifs noyés dans une matrice métallique par frittage. Lors des opérations de découpe, la matrice retient les diamants qui, du fait de leur dureté, peuvent indenter la pièce. Des débris du matériau découpé se formeront inévitablement, définissant, avec l'eau utilisée pour les ejecter, une suspension dense. Ce flux de débris est très abrasif pour la matrice et peut l'user. Bien que ce processus d'usure soit nécessaire pour renouveler les diamants, il doit être contrôlé en termes de taux d'usure pour atteindre un équilibre optimal entre la durée de vie et la capacité de coupe. Si plusieurs tentatives ont été faites pour analyser l'usure des diamants, le processus d'usure impliquant la matrice n'est pas encore bien compris. Par conséquent, l'objectif principal ici est de construire une stratégie numérique multi-échelles pour prédire et décrire l'usure abrasive en tenant compte des interactions tribologiques complexes impliquant la matrice, les diamants et les flux de débris. Cette stratégie repose sur deux modèles principaux: (1) le modèle macroscopique, construit à l'échelle du diamant et résolu par la méthode des éléments finis (FEM); le modèle mésoscopique (2), construit à l'échelle des débris et résolu avec le code MELODY aux éléments discrete-meshfree pour étudier l'usure localement, en tenant compte du caractère discret des grains de débris et de la microstructure déformable polycristalline de la matrice métallique. Dans le contexte de la demande industrielle, le modèle macroscopique (1) donne des résultats encourageants en termes de taux d'usure et peut être utilisé comme modèle prédictif dans la sélection de la matrice métallique optimal. Le modèle mésoscopique (2) est un modèle descriptif donnant accès à des phénomènes importants de contrôle de l'usure qui ne sont pas accessibles à l'échelle du diamant et doivent être étudiés à un plus petit. Enfin, la stratégie proposée ici peut être utilisée pour prédire (1) et décrire (2) l'usure non seulement dans le cadre du DIT mais aussi pour l'adapter à d'autres situations tribologiques similaires consistant en l'usure d'une surface provoquée par un écoulement d'abrasif.

MOTS-CLÉS : usure abrasive; outils de coupe, modélisation de l'usure; approche multi-échelle, modèle de zone cohésive, fatigue

Laboratoire (s) de recherche : Laboratoire de mécanique des Contacts et des Structures (LaMCoS)

Directeur de thèse: Dr. Nicolas Fillot

Président de jury :  
S. FOUVRY

Composition du jury :

J. F. MOLINARI	Professeur des Universités (EPFL- Switzerland)	Rapporteur
V. MAGNIER	Maître de Conférences HDR (LaMcube - Université de Lille)	Rapporteur
A. MEZIANE	Professeur des Universités (I2M - Université de Bordeaux)	Examinatrice
S. FOUVRY	Directeur de Recherche CNRS (LTDS - Ecole Centrale de Lyon)	Examinateur
N. FILLOT	Maître de Conférences HDR (INSA de Lyon)	Directeur de thèse
G. MOLLON	Maître de Conférences (INSA de Lyon)	Co-directeur de thèse